

AD-A119 719 NAVAL RESEARCH LAB WASHINGTON DC
THE USE OF ION IMPLANTATION FOR MATERIALS PROCESSING. (U)
JUL 82 F A SMIDT
UNCLASSIFIED NRL-MR-4821

F/G 20/8

NL

3

1

2

3

4

5

6

7

8

9

10

11

12

13

14

15

16

17

18

19

20

21

22

23

24

25

26

27

28

29

30

31

32

33

34

35

36

37

38

39

40

41

42

43

44

45

46

47

48

49

50

SECURITY CLASSIFICATION OF THIS PAGE (When Data Entered)

REPORT DOCUMENTATION PAGE		READ INSTRUCTIONS BEFORE COMPLETING FORM												
1. REPORT NUMBER NRL Memorandum Report 4821	2. GOVT ACCESSION NO. AD-A119 719	3. RECIPIENT'S CATALOG NUMBER												
4. TITLE (and Subtitle) THE USE OF ION IMPLANTATION FOR MATERIALS PROCESSING - ANNUAL PROGRESS REPORT FOR THE PERIOD 1 OCTOBER 1980 - 30 SEPTEMBER 1981		5. TYPE OF REPORT & PERIOD COVERED Progress report for period 1 Oct. 1980 - 30 Sept. 1981												
7. AUTHOR(s) F.A. Smidt, Coordinator		6. PERFORMING ORG. REPORT NUMBER												
8. PERFORMING ORGANIZATION NAME AND ADDRESS Naval Research Laboratory Washington, DC 20375		9. CONTRACT OR GRANT NUMBER(s)												
11. CONTROLLING OFFICE NAME AND ADDRESS Office of Naval Research Arlington, VA 22217		10. PROGRAM ELEMENT, PROJECT, TASK AREA & WORK UNIT NUMBERS Complete list follows on next page.												
14. MONITORING AGENCY NAME & ADDRESS (if different from Controlling Office)		12. REPORT DATE July 2, 1982												
		13. NUMBER OF PAGES 205												
		15. SECURITY CLASS. (of this report) UNCLASSIFIED												
		16a. DECLASSIFICATION/DOWNGRADING SCHEDULE												
16. DISTRIBUTION STATEMENT (of this Report) Approved for public release; distribution unlimited.														
17. DISTRIBUTION STATEMENT (of the abstract entered in Block 20, if different from Report)														
18. SUPPLEMENTARY NOTES														
19. KEY WORDS (Continue on reverse side if necessary and identify by block number) <table border="0"> <tr> <td>Amorphous surfaces</td> <td>Fretting fatigue</td> <td>Sputtering</td> </tr> <tr> <td>Atomic collisions</td> <td>Index of refraction</td> <td>Silicon</td> </tr> <tr> <td>Corrosion</td> <td>Ion implantation</td> <td>Polarization measurements</td> </tr> <tr> <td>Defect structure of FeCrO_3</td> <td>Materials processing</td> <td>M2 High speed steel</td> </tr> </table> (Continues)			Amorphous surfaces	Fretting fatigue	Sputtering	Atomic collisions	Index of refraction	Silicon	Corrosion	Ion implantation	Polarization measurements	Defect structure of FeCrO_3	Materials processing	M2 High speed steel
Amorphous surfaces	Fretting fatigue	Sputtering												
Atomic collisions	Index of refraction	Silicon												
Corrosion	Ion implantation	Polarization measurements												
Defect structure of FeCrO_3	Materials processing	M2 High speed steel												
20. ABSTRACT (Continue on reverse side if necessary and identify by block number) <p>An interdisciplinary program on the use of ion implantation for materials processing is being conducted at NRL. This report describes the important factors in ion implantation science and technology and reports progress in the use of ion implantation to modify wear, fatigue, corrosion, and optical properties of materials.</p>														

DD FORM 1 JAN 73 1473

EDITION OF 1 NOV 65 IS OBSOLETE
S/N 0102-014-6601

SECURITY CLASSIFICATION OF THIS PAGE (When Data Entered)

10. Program Element, Project, Task Area & Work Unit Numbers

66-0300; 62761 NavMat; WF-61-544-007

66-0424; RR022-08-44 ONR

66-0424; 62376 NAPC/NavAir

66-0425; RR022-08-44 ONR

63-1019; RR022-08-44 ONR

63-1020; RR022-01-47 ONR

61-0037; RR018-01-43 ONR

66-0444; RR012-02-41 ONR

66-0446; RR012-02-41 ONR

66-0447; RR012-02-41 ONR

63-1100; RR022-11-41 ONR

63-1314; RR022-11-41 ONR

63-0445; RR012-02-41 ONR

19. Key Words (Continued)

M50

Machining

Ti-6Al-4V

Rutherford backscattering

Accession For	
NTIS GRA&I	<input checked="checked" type="checkbox"/>
DTIC TAB	<input type="checkbox"/>
Unannounced	<input type="checkbox"/>
Justification	
By _____	
Distribution/	
Availability Codes	
Dist	Avail and/or Special
A	



CONTENTS

PREFACE - F. A. Smidt	v
SUMMARY	1
RESEARCH PROGRESS	
I. ION IMPLANTATION SCIENCE AND TECHNOLOGY	1
A. USE OF ION BEAM ANALYSIS IN METAL MODIFICATION BY MEANS OF ION IMPLANTATION	6
G. K. Hubler	
B. SELF-ION SPUTTERING YIELDS FOR COPPER, NICKEL AND ALUMINUM	37
R. G. Allas, A. R. Knudson, J. M. Lambert, P. A. Treado and G. W. Reynolds	
C. LASER IRRADIATION OF Ni: DEFECT STRUCTURES AND SURFACE ALLOYS	49
L. Buene, D. C. Jacobson, S. Nakahara, J. M. Poate, C. W. Draper and J. K. Hirvonen	
D. MIGRATION CURRENT AND IMPLANT DENSITIES IN STEADY- STATE ION IMPLANTATION	58
I. Manning	
II. WEAR AND FATIGUE	70
A. PRELIMINARY EVALUATION OF ION IMPLANTATION AS A SURFACE TREATMENT TO REDUCE WEAR OF TOOL BITS	70
F. A. Smidt, J. K. Hirvonen, and S. Ramalingam	
B. THE EFFECT OF ION IMPLANTATION ON FRETTING FATIGUE IN Ti-6Al-4V	126
R. G. Vardiman, D. Creighton, G. Saliver, A. Effatian, and B. B. Rath	
III. CORROSION	139
A. ELECTROCHEMICAL BEHAVIOR OF AN AMORPHOUS Fe-Ti-C SURFACE IN TITANIUM-IMPLANTED STEEL	139
G. K. Hubler, P. Trzaskoma, E. McCafferty, and I. L. Singer	

IV. OTHER EXPLORATORY RESEARCH AREAS	151
A. ELECTRICAL AND STRUCTURAL CHARACTERIZATION OF IMPLANTATION DOPED SILICON BY INFRARED REFLECTION	151
G. K. Hubler, P. R. Malmberg, C. N. Waddell, W. G. Spitzer and J. E. Fredrickson	
B. EFFECTS OF THERMAL ANNEALING ON THE REFRACTIVE INDEX OF AMORPHOUS SILICON PRODUCED BY ION IMPLANTATION	175
J. E. Fredrickson, C. N. Waddell, W. G. Spitzer, and G. K. Hubler	
C. DEFECT PROCESSES IN THIN FILMS OF METAL OXIDES	186
R. H. Basse1 and I. Manning	
D. A THEORETICAL STUDY OF THE DEFECT STRUCTURE OF PRASEODYMIUM CHROMITE	188
J. H. Harding and R. H. Basse1	
BIBLIOGRAPHY	196

THE USE OF ION IMPLANTATION FOR MATERIALS PROCESSING

Preface - F. A. Smidt

This report is the third in a series of Progress Reports of work conducted at the Naval Research Laboratory (NRL) on the use of ion implantation for materials processing. The objective of the programs is to develop ion implantation as a viable surface treatment technique for use in applications of interest to the Navy. Attainment of this objective requires both applications oriented research, to demonstrate the benefits of ion implantation, and fundamental research, to provide an understanding of the physical and metallurgical changes taking place in the implanted region of a material.

The work reported here represents a coordinated effort in three divisions at NRL, the Condensed Matter and Radiation Sciences Division (Code 6600), the Chemistry Division (Code 6100) and the Material Science and Technology Division (Code 6300). The work is coordinated through the Ion Implantation Steering Committee consisting of Dr. J. K. Hirvonen (Code 6670), Dr. J. N. Butler (Code 6670), Dr. J. S. Murday (Code 6170), Dr. B. B. Rath (Code 6320), and Dr. F. A. Smidt (Code 6004), Chairman. The work includes in-house basic research conducted under the auspices of the Office of Naval Research, applied research performed for several Navy and DOD sponsors (NAVAIR, DARPA, NAVMAT, AFML, SSPO, NAVSEA) and collaborative work with scientists at other laboratories.

The purpose of this report is to make available in one source the results from all studies at NRL related to the use of ion implantation for materials processing so as to provide a more comprehensive picture of the scope and interrelationship of the research. The report consists of four sections describing the research and a cumulative bibliography of published papers and reports.

THE USE OF ION IMPLANTATION FOR MATERIALS PROCESSING

ANNUAL PROGRESS REPORT FOR THE PERIOD
1 OCTOBER 1980 - 30 SEPTEMBER 1981

SUMMARY

I. ION IMPLANTATION SCIENCE AND TECHNOLOGY

Research reported in this section contributes to our general understanding of the ion implantation process and the development and refinement of techniques for ion implantation processing.

A. Use of Ion Beam Analysis in Metal Modification by Means of Ion Implantation

G. K. Hubler

Ion implantation is being investigated as a technique for the beneficial modification of surface sensitive, life-limiting properties of metals including resistance to corrosion, wear, and fatigue. Ion implantation has the advantage that it can produce a graded alloy from the surface to the unchanged underlying bulk alloy so that both the surface alloy and bulk alloy can be independently optimized. The technique also offers the ability to produce unique metastable surface alloys. Implantation energies in the range of 10 to 200 keV are typically used for implantation which produces changes to depths of a few hundred nanometers. These implantation depths are well suited for study by means of ion beam analysis techniques. This paper reviews examples of mechanical and corrosion property changes induced by ion implantation and describes in each case how ion beam surface layer analysis provided information useful to the present understanding of the effects observed.

B. Self-Ion Sputtering Yields for Copper, Nickel and Aluminum

R. G. Allas, A. R. Knudson, J. M. Lambert, P. A. Treado, and G. W. Reynolds

Self-ion sputtering yields were determined for copper, nickel, and aluminum at 60 keV, 90 keV, and 120 keV. The sputtering yields were determined by Rutherford backscattering measurements of the energy shifts of a deeply implanted xenon marker layer and by measuring the distribution and amount of sputtered material on a catcher foil using backscattering and particle induced x-ray emission. The effect of dose rate and net fluence on the yield were examined. Optical monitoring of the light intensity emitted by the sputtered particle confirmed no measurable change in the yield using self ion bombardment. The self-ion sputtering yields measured in this study are less

Manuscript submitted March 24, 1982.

than predicted by theory but are self consistent within experimental error independent of measurement technique. Additional measurement of self-ion sputtering yields in this energy range are needed for applications in materials modification.

C. Laser Irradiation of Nickel: Defect Structures and Surface Alloying

L. Buene, D. C. Jacobson, S. Nakahara, J. M. Poate, C. W. Draper, and J. K. Hirvonen

Surface layers of Ni crystals have been melted with Q-switched Nd-YAG laser radiation. The epitaxially regrown surface layers show significant differences between $\langle 100 \rangle$ and $\langle 111 \rangle$ crystals cut from the same boule. The $\langle 100 \rangle$ crystals exhibit a dislocation cell structure with a dislocation density of $10^{11} - 10^{12} \text{ cm}^{-2}$. The $\langle 111 \rangle$ crystals contain a laterally uniform dislocation network resulting in a much higher dislocation density for the $\langle 111 \rangle$ surface. The elements Ag, Au, Pd, Sn and Ta have been implanted into Ni single crystals at surface concentrations of up to 20 at%. All the as-implanted systems demonstrate solid solubility. We have used these implanted systems to study the alloys formed by laser melting of Ni. In all systems, with the exception of Ag, 100 percent of the atoms are trapped on lattice sites.

D. Migration Currents and Implanted Densities in Steady-State Ion Implantation

I. Manning

Several atomic collision and migration processes occurring during ion implantation were examined. The case first considered is that of A atoms bombarding a target of B and C atoms ($A \rightarrow BC$). Allowance is made for the possibility of atomic migration currents within the target of A, B, and C atoms, and expressions are obtained for these currents. The only major assumptions made in the analysis are that atoms are conserved and that the system is in steady state. Whenever preferential sputtering is large enough to substantially alter the surface concentrations of B and C atoms, there must also be substantial migration currents of these atoms. Migration currents may well be significant in other cases as well. The results are illustrated by considering Ar bombarding SiPt, where the Si and Pt migration currents are found to be around one-half the bombarding flux. The analysis is also applied to rederiving expressions for the surface density of implanted ions, the energy deposited into target damage, and the density of PKA's at the surface. The analysis is easily extended to apply to implantation of a single-component target ($A \rightarrow B$) and to self-ion implantation of a two-component target ($A \rightarrow AB$).

II. WEAR AND FATIGUE

Research reported in this section involves the application of ion implantation processing to the improvement of wear and fatigue properties of surfaces and fundamental investigations conducted to improve our understanding of the effects of implantation on wear and fatigue mechanisms.

A. Preliminary Evaluation of Ion Implantation as a Surface Treatment to Reduce Wear of Tool Bits

F. A. Smidt, J. K. Hirvonen and S. Ramalingam

The process of ion implantation is reviewed and concepts for use as a surface hardening technique for extending the life of machine tools are explored. It is concluded that for high speed steel tool materials a system based on implantation of Ti ions with subsequent reaction to form TiC in the surface layers should have merit. Exploratory tests showed that in machining tests of 4140 steel, an implanted M2 lathe tool bit required about 10 percent less power and had a wear rate approximately one half that of the unimplanted tool. Tests of end mills proved inconclusive because the optimum Ti level for the implant was not reached.

B. The Effect of Ion Implantation on Fretting Fatigue in Ti-6Al-4V

R. G. Vardiman, D. Creighton, G. Salivar, A. Effatian, and B. B. Rath

The effect of fretting on the fatigue life of titanium alloys is known to be severely deleterious. A preliminary study shows ion implantation to hold great promise for improving fretting fatigue life in Ti-6Al-4V.

Carbon implanted at 75 keV to a dose of 2×10^{17} atoms/cm² gives a peak concentration of 30 atomic percent at approximately 1700 Angstroms depth. Incoherent particles of TiC averaging 100 Angstroms in size were found by TEM. Fatigue samples were subjected to fretting on one surface at a normal stress of 20.7 MPa. Significant improvement in lifetime was found. No difference in the mode of failure was observed between implanted and unimplanted specimens.

III. CORROSION

Research reported in this section involves the application of ion implantation processing to improvement of the corrosion and oxidation resistance of surfaces and fundamental investigations conducted to improve our understanding of the effects of the implantation on corrosion mechanisms.

A. Electrochemical Behavior of an Amorphous Fe-Ti-C Surface in Titanium-Implanted Steel

G. K. Hubler, P. Trzaskoma, E. McCafferty, and I. L. Singer

Implantation of Ti at high fluences into 52100 steel produced an amorphous surface containing Ti, Fe, and C. This amorphous surface provides modest improvements in corrosion resistance in 1N H₂SO₄ and 0.1N NaCl, as indicated by potentiodynamic polarization scans. In both solutions the anodic current density is about 10 percent that of unimplanted 52100 steel up to anodic overpotentials of about 800 mV. Pitting corrosion, which is initiated at lower overpotentials, leads to undermining and peeling of the implanted layer at higher overpotentials. Detailed optical and microstructural studies of pit initiation in a nital/picral/methanol etch suggest that pitting begins at surface flaws, which are either carbides or impurity inclusions.

IV. OTHER EXPLORATORY RESEARCH AREAS

Research reported in this section includes exploratory investigations of the potential of ion implantation in areas other than wear/fatigue and corrosion.

A. Electrical and Structural Characterization of Implantation Doped Silicon by Infrared Reflection

G. K. Hubler, P. R. Malmberg, C. N. Waddell, W. G. Spitzer, and J. E. Fredrickson

A physical model is presented for calculating infrared reflection interference spectra from ion implanted and annealed crystalline materials. The utility of the method is illustrated by presenting best fit spectra for a $\langle 111 \rangle$ silicon sample implanted with 2.7 MeV phosphorous to a fluence of 1.74×10^{16} ions/cm² and isothermally annealed at 500°C. Non-linear least-squares fitting of reflection data yields structural and electrical information about the implanted region with reasonable precision. The physical quantities determined are (i) the depth of the amorphous layer produced by implantation both before and during isothermal annealing, the thickness of the recrystallized material, and the width of any transition regions, (ii) the dielectric properties of the amorphous and recrystallized material, and (iii) the characteristics of the free carrier plasma which yield the carrier density profile, the mobility near the carrier density maximum, and the carrier activation efficiency. Up to nine fitting parameters are necessary to describe these physical quantities. A critical discussion of the sensitivity of data fit to variation in the parameter is given to establish the uniqueness of fitted parameters. The infrared method is nondestructive, is applicable to other dopants and semiconductors, and provides information complementary to both ion channeling and resistivity profiling techniques.

B. Effects of Thermal Annealing on the Refractive Index of Amorphous Silicon Produced by Ion Implantation

J. E. Fredrickson, C. N. Waddell, W. G. Spitzer, and G. K. Hubler

Precise infrared reflection measurements of the refractive index of silicon show that there are two well-defined optical states of amorphous silicon produced by ion implantation. One is the as-implanted amorphous state which is the high refractive index state produced by high fluence implantation of Si or P ions into Si samples. The other state, which has a refractive index intermediate between the as-implanted and crystalline values, is induced by thermal annealing and is thermally stable until epitaxial recrystallization occurs. A comparison is made to the optical properties of amorphous Si produced by other means.

C. Defect Processes in Thin Films of Metal Oxides

R. H. Bassel and I. Manning

A brief note is presented describing the objective and scope of a study of oxidation processes in thin films of perovskites using the computer codes CERES and HADES. An illustration of the work is shown in the following section.

D. A Theoretical Study of the Defect Structure of Praseodymium Chromite

J. H. Harding and R. H. Bassel

Theoretical calculations in the compound PrCrO_3 using the Harwell INDRES code are presented. The results show that all simple diffusion mechanisms involve high activation energies. It is further predicted that the most important defect in the chromium sublattice will be electronic disorder.

BIBLIOGRAPHY

A cumulative bibliography of papers related to ion implantation for materials processing authored or co-authored by NR' staff members is provided.

Section I.A

USE OF ION BEAM ANALYSIS IN METAL MODIFICATION
BY MEANS OF ION IMPLANTATION

G. K. Hubler

Materials Modification and Analysis Branch
Condensed Matter and Radiation Sciences Division
Naval Research Laboratory

This work was supported by the Office of Naval Research.

Use of Ion Beam Analysis in Metal Modification by means of Ion Implantation

G. K. Hubler
U.S. Naval Research Laboratory
Washington, DC 20375

ABSTRACT

Ion implantation is being investigated as a technique for the beneficial modification of surface sensitive, life-limiting properties of metals, including resistance to corrosion, wear, and fatigue. Ion implantation can produce a graded alloy from the surface to the unchanged underlying bulk alloy so that both the surface alloy and bulk alloy can be independently optimized, and the technique promises the ability to produce unique metastable surface alloys. With typical implantation energies in the range of 10 to 200 keV, implantation depths are less than a few hundred nanometers. These implantation depths are well suited for study by means of ion beam analysis techniques. This paper reviews examples of mechanical and corrosion property changes induced by ion implantation and describes in each case how ion beam surface layer analysis provided information useful to the present understanding of the effects observed.

INTRODUCTION

Ion implantation is being actively investigated as a technique for the beneficial modification of surface-sensitive, life-limiting properties of metals and alloys, including resistance to corrosion, wear, and fatigue.¹ Ion implantation is attractive from a materials surface processing point of view because it can produce a graded alloy from the surface to the unchanged underlying bulk alloy so that both the surface and the bulk alloys are independently optimized. This allows the materials engineer to circumvent the dilemma often encountered where several desirable material properties such as high strength and superior corrosion resistance are mutually exclusive for alloys produced by standard metallurgical techniques. The rising interest in ion implantation is part of a materials research effort stimulated first by the semiconductor and aerospace industries and in recent years by new requirements placed on materials performance from a variety of high technology areas that are an outgrowth of world-wide energy and material shortages. New materials requirements for nuclear power generation, coal gasification, solar and geothermal energy sources are examples of the areas that have promoted research on new materials processing techniques and protective coatings.² The growing shortage of strategic metals has prompted research on new methods of improving properties of the abundant materials such as iron.³

The rapid growth of metal modification by ion implantation can be traced to the pioneering work by the group at the Atomic Energy Research Establishment, Harwell, England, headed by G. Dearnaley. In the early seventies the Harwell group demonstrated the unique capabilities offered by ion implantation in materials research⁴ and herein lies the reason for its acceptance in the materials research community. It provides a tool to tailor the elemental composition of an alloy surface to suit the experiment, in contrast to the normal procedure of choosing an experiment that is compatible with the elemental composition of conventional alloys which are constrained to the limits imposed by solid solubilities and diffusivities. This attractive feature

makes ion implantation useful in its own right as a research tool, without invoking the many possible practical applications of the technique, some of which are already being developed.^{5,6} An excellent overview of the effects of ion implantation on the tribological and corrosion properties of metals has been published by Hirvonen.¹

It is not surprising that ion beam analysis is the primary method for investigating the elemental composition of ion implanted metals. The reasons are numerous. With typical implantation depths of a few tens nanometers, there is a quite natural union of ion implantation and impurity concentration profiling by means of ion beams because the sensitivity and depth resolution of ion beam methods are optimized in the near surface region encompassing the implanted layer. The implanted ion fluence is usually two to four orders-of-magnitude larger for metals than in semiconductor applications so that the ion beam techniques developed for profiling impurities in semiconductors proceed with higher counting rates when used for profiling ion-implanted surface alloys.

Conversely, some techniques which were unworkable in semiconductors because of prohibitively low cross sections, are readily applied to high fluence implantation into metals. Perhaps most importantly, ion beam analysis techniques are still the quantitative standard against which other profiling techniques, destructive or nondestructive, are compared. Ion beam analysis techniques are divided in this review into two categories; nuclear reaction analysis (NRA) and Rutherford backscattering (RBS) analysis. Experimental details of these analysis techniques can be found in the cited references. In addition, the "Ion Beam Handbook for Material Analysis"⁸ contains useful tables of reaction cross sections, stopping powers, and formulas as an aid in analysis of data and in choosing the best method to analyze a particular problem. Bird has also compiled nuclear cross sections for ion beam analysis applications.⁶

It has only been in the 1970's that a significant number of articles, books, and conference sessions^{4,9-11} have appeared on nonsemiconductor applications of ion implantation. The first international conference entitled "Ion Beam Modification of Materials" was held in Budapest in September, 1978.¹² Following this conference, sessions devoted to metals were held at the Materials Research Society Annual Meeting in Cambridge, Massachusetts, Nov., 1979¹³ and at the second Ion Beam Modification of Materials Conference at Albany New York in July, 1980.¹⁴ In these conferences,¹²⁻¹⁴ 60% of the papers on ion-implanted metals relied on ion beam surface layer analysis techniques for measuring the elemental composition of the implanted surfaces.

The intent of this overview is to give an introduction to the application of ion beam analysis in the field of ion beam modification of surface sensitive properties of metals. The emphasis is on the specific engineering properties such as wear, fatigue, oxidation, and corrosion of metals and alloys and examples are presented in each area showing how ion beam surface layer analysis has provided information useful to the present understanding of the effects observed. The examples chosen are representative of work in this field and are those with which the author is familiar. A considerable effort has been made to include numerous references to other ion beam analysis work on engineering alloys. Important related areas not specifically reviewed here include hydrogen and helium profiling,^{15,16} radiation damage in reactor materials,¹⁷ electron beam material modification,¹⁸ and ion implantation metallurgy.¹⁹ The fundamental processes of alloy formation, radiation damage, defect trapping, impurity segregation, etc., that are the subject of the aforementioned areas are intimately related to materials modification of engineering alloys. For the interested reader, reviews of these areas may be found in the indicated references and in a recent book covering most fundamental and applied topics in ion implantation of metals.²⁰

FRICITION, WEAR, AND HARDNESS

The $^{14}\text{N(d,}\alpha\text{)}^{12}\text{C}$ reaction has been used by Dearnaley et al.²¹ to measure nitrogen retention during implantation as a function of implantation temperatures for several steels and by Lo Russo et al.²² to measure the implanted nitrogen retention in steel in a wear scar during an unlubricated pin-on-disk type wear experiment. Lo Russo found 20% of the implanted nitrogen retained in the wear scar even after 5 μm of material was removed during the wear process. Hartley²³ has measured improvements in the friction behavior of steels by Ag and Pb implantation and measured the distribution of Ag and Pb across the wear scar by means of Rutherford backscattering (RBS) in combination with an ion microbeam. While wear tests have not yet been carried out, Baumvol et al.²⁴ used ion bombardment to diffuse rather thick layers of Sn evaporated onto pure Fe substrates with a nitrogen ion beam and measured the Sn depth profile by means of RBS. It is expected that the 10% Sn concentration over a 3 μm depth that results from ion bombardment will improve fretting resistance of the iron. Preece et al.²⁵ have used ion channeling to study the defects produced during implantation of B into Cu and Ni single crystals and have related the RBS result to changes in the hardness. Comprehensive reviews of the effects of ion implantation on mechanical properties exist in the literature by Hartley²⁶ and Herman.²⁷

The first example of the use of ion beam analysis in material modification is a microhardness study on boron-implanted beryllium carried out by Kant et al.²⁸ to determine the feasibility of producing hardened, low-wear beryllium surfaces such as those on precision gas bearings. Hard oxide coatings which are presently used sometimes have adhesion problems which ion implanted layers avoid because of their nonabrupt interface. Increasing the hardness of surfaces in contact in a sliding wear situation is the most common material treatment for reducing wear rates. An implanted layer 0.8 μm in thickness was achieved by overlapping four Gaussian distributed implantations at energies between 90 and 250 keV and for fluences between 1×10^{17} and 10×10^{17} B/cm^2 to produce layers of average atomic concentration for different samples between 10% and 60%. Knoop indenter microhardness tests on the implanted surfaces revealed relative hardness increases over unimplanted Be of a factor of 4 in the as-implanted case, and a factor of 6 after vacuum annealing at 650°C for 20 min.

Figure 1 is the helium ion RBS spectrum (3 MeV, 90°) of unimplanted Be and Be implanted under the stated conditions. The main features of the implanted sample spectrum are a drop in the Be yield caused by the presence of B and an implanted B distribution riding on top of the Be yield. The actual B profile is not readily measured from the raw data. To obtain a clearer picture of the B profile, a subtraction method was used to reduce the data wherein a point by point subtraction is performed between the spectra in figures 1a and 1b to obtain the data points in figure 2a.^{29,30} The RBS spectrum analysis program of Ziegler³¹ was employed to model the B distribution in Fig. 2b and the Be distribution (not shown) in the implanted layer and the smooth curve in Fig. 2a was calculated. The B profile generated by this self-consistent trial and error calculation method shows that the B distribution is uniform between 300 and 700 nm at a concentration of 60 at.% which is near the desired concentration for production of the hardest known phase BeB_2 . Further annealing studies have shown that there is insignificant diffusion of the B at the anneal temperatures used in the hardness studies suggesting that BeB_2 in precipitates are responsible for the increased hardness.

In another wear application of ion implantation the surface hardness of a through-hardened bearing steel has been increased by implantation of Ti ions at 190 keV to a fluence of 4.8×10^{17} Ti/cm^2 . The composition of the martensitic AISI 52100 steel

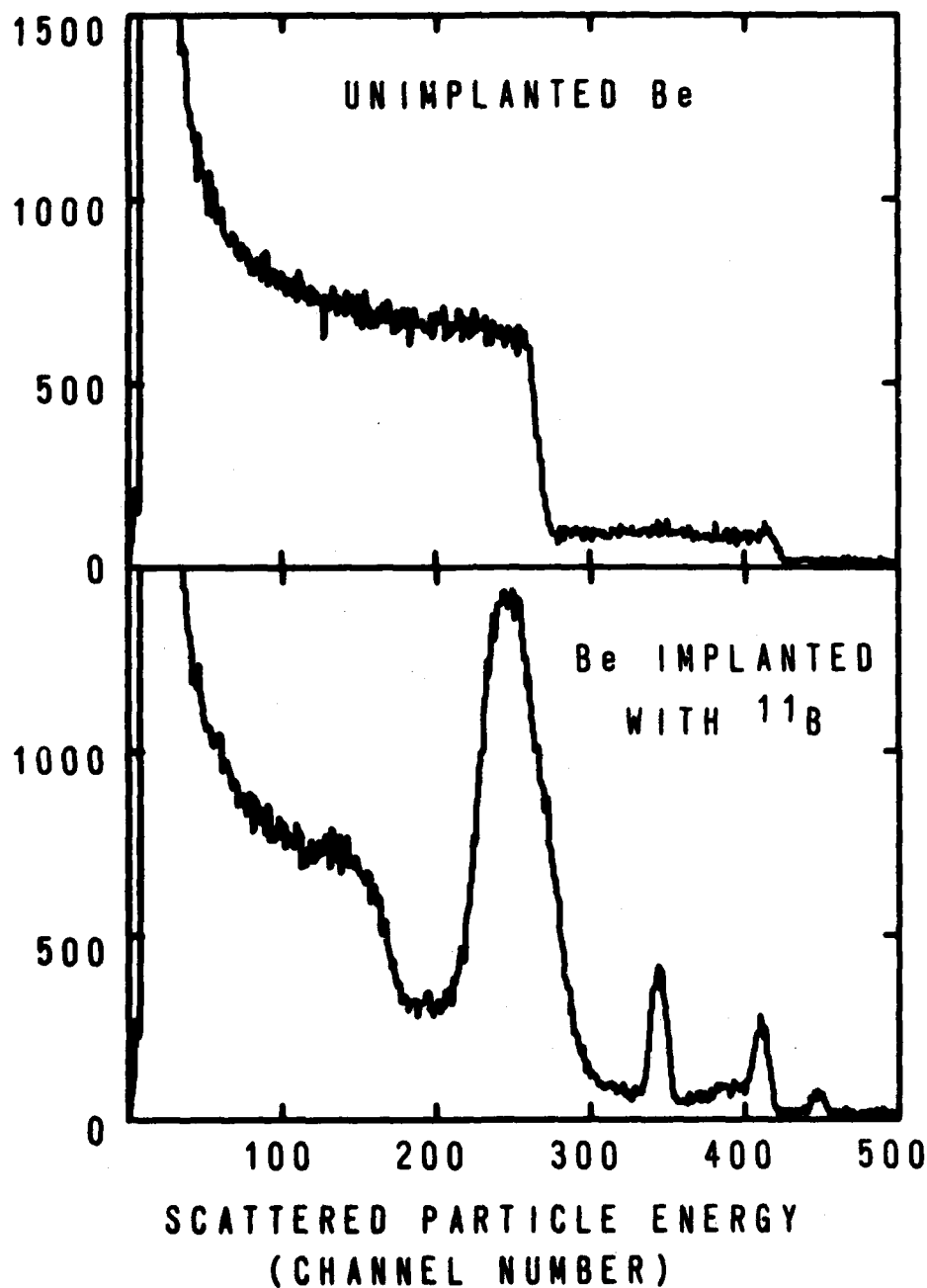


Figure 1. Helium ion RBS spectra (3 MeV, 90°) for a.) (top) unimplanted Be and, b.) (bottom) Be implanted with B to high fluences (see text). The impurity peaks in 1b are C, O, and F. A point by point subtraction of spectrum 1a from spectrum 1b is plotted as the crosses in Fig. 2a for the region between channels about 100 and 350. (After Kant et al., ref. 28).

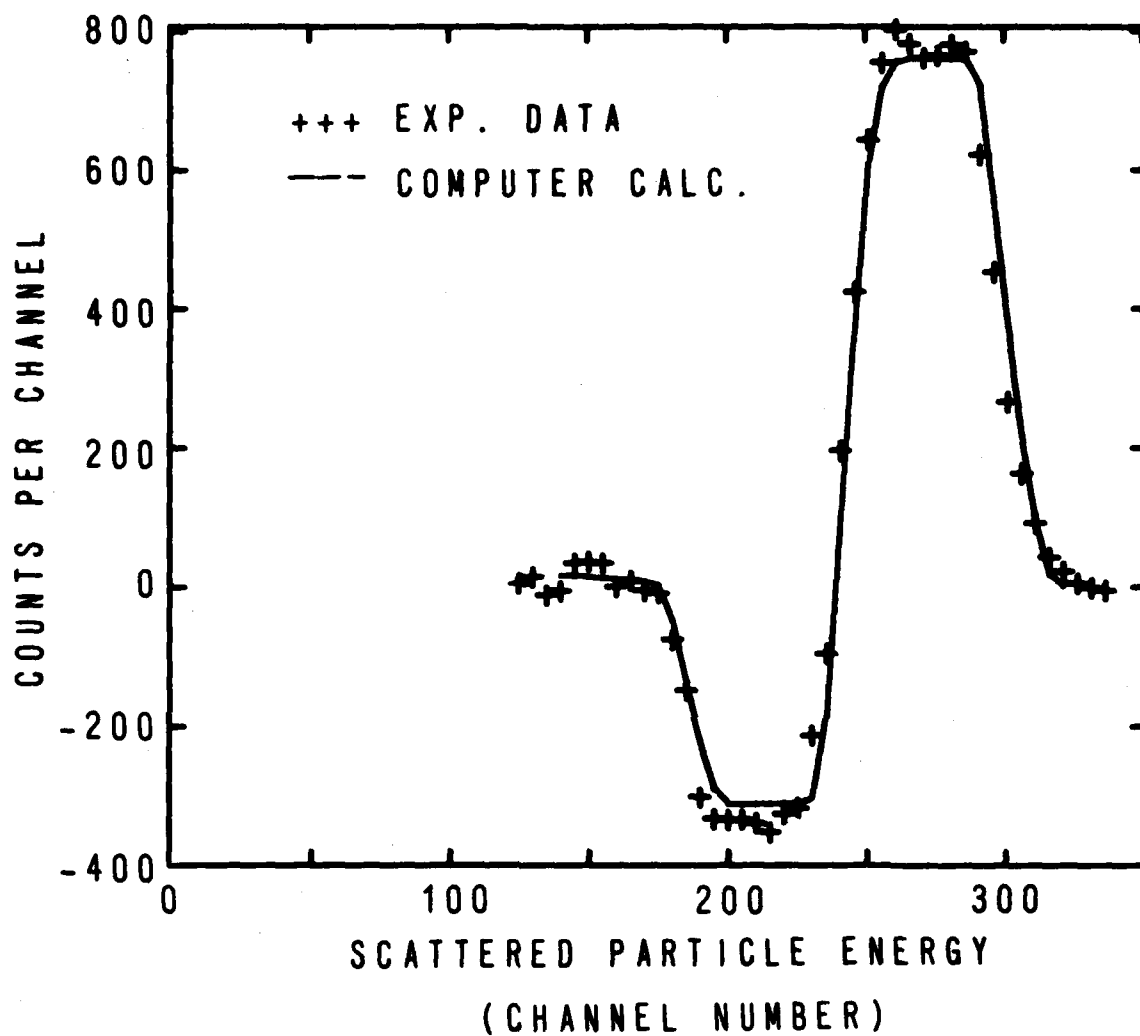


Figure 2a. Calculation of B profile from RBS data. Crosses are generated by a point by point subtraction of RBS data in Fig. 1a from 1b, and the smooth curve is a calculation of the subtracted data assuming the boron profile in Fig. 2b.

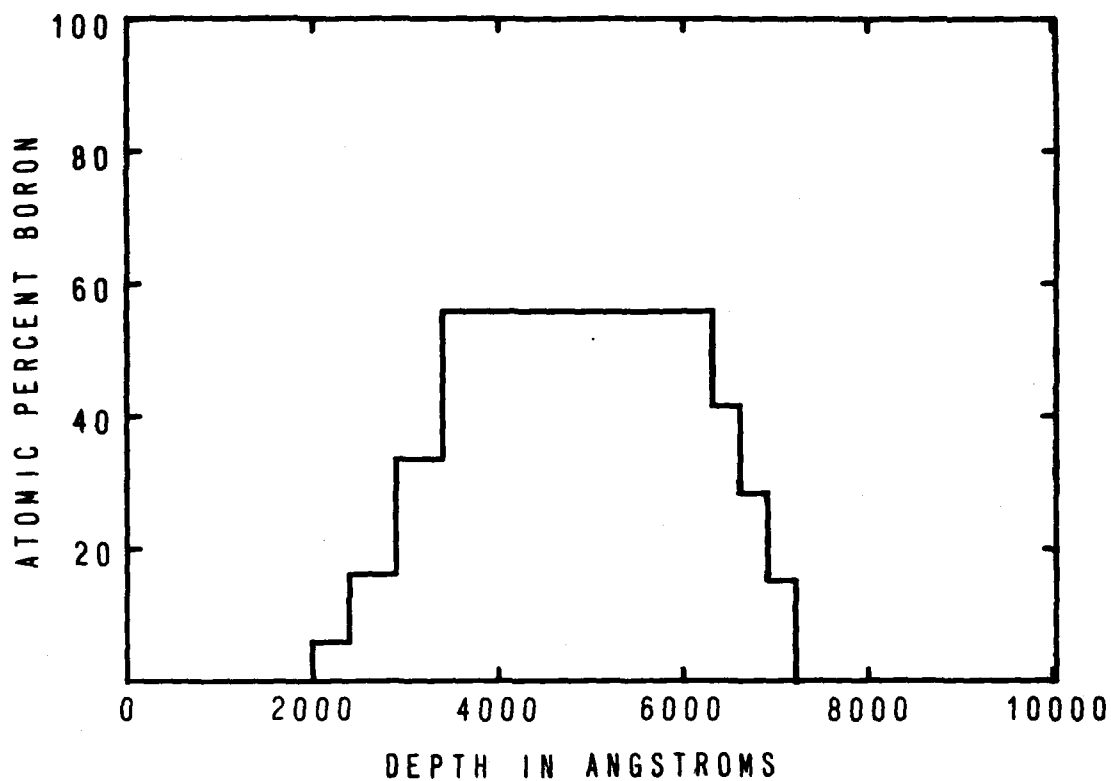


Figure 2b. Calculation of B profile from RBS data. Assumed boron profile which when combined with assumed Be profile (not shown) yields the calculated smooth curve in Fig. 2a. (After Kant et al., ref. 28).

used in these experiments is chiefly Cr (1.5 wt.%), C (0.8 wt.%) with the remainder Fe. Carosella et al.³² measured substantial improvement in sliding wear rates in both good lubrication and poor lubrication wear conditions as well as a factor of two decrease in the friction of poorly lubricated 52100 on 52100 steel. These results were especially interesting because normally the very reactive Ti metal increases friction and wear when coupled with steels by increasing adhesion between the contacting surfaces. Singer et al.³³ subsequently measured hardness increases of a factor of 6 in the near surface region of the same implant steel by adapting an abrasive wear technique to measure the hardness of thin layers.

To characterize the implanted layer, ion beam techniques developed by Gossett^{34,35} were employed to measure Ti and C profiles shown in Figure 3. The Ti profile was measured by making use of a narrow resonance in the $^{48}\text{Ti}(p,\gamma)^{49}\text{V}$ reaction at a bombarding energy of 1007 keV. The gamma decay from the 7.582-MeV level in the ^{49}V nucleus to the 153-keV second excited state was detected with a large volume Ge(Li) detector. As the proton energy is increased in steps above the resonance energy, the depth where resonant reactions occur is also increased and the yield is measured at each step. For the depths profiled here about 20 steps are required to complete a profile. The $^{12}\text{C}(^3\text{He},^4\text{He})^{11}\text{C}$ reaction was used to obtain the high depth resolution necessary to profile the thin surface layer of carbon. In this method, the α particles are detected at an angle of 135° in a position sensitive detector in the focal plane of a magnetic spectrometer. The background of elastically scattered ^3He particles are eliminated by the magnetic field because of their higher magnetic rigidity, and protons from competing $^3\text{He},p$ reactions are eliminated by placing a thin carbon foil over the detector to displace the alpha particles and protons about 40 keV in energy which allows them to be discriminated against in the detector energy spectrum. The position spectrum of the detector yields the C profile directly with a depth resolution of better than 10 nm.

The Ti profile in figure 3 indicates that the surface Ti concentration is about 25 at.% and that the profile has nearly reached the sputter limited saturation dose because of the absence of a well defined concentration maximum. The profile of carbon shows a surprisingly high near-surface concentration that diminishes smoothly in depth. The shape of the carbon profile suggests that indiffusion from a high surface coverage of carbon is the mechanism responsible for its presence. Concurrently the microstructures of Ti implanted into high purity iron single crystals was investigated by Knapp, Follstaedt and Picraux.³⁶ Their work demonstrated that the carbon entered from the ambient vacuum during implantation and TEM results showed that the presence of high carbon concentrations promoted the formation of an amorphous Fe-Ti-C layer. A series of channeling spectra were obtained using 1.8 MeV ^4He along the $\langle 100 \rangle$ direction, with glancing emission detection angle to enhance depth resolution. Four channeling spectra are shown in Fig. 4 for Ti fluences ranging from 1×10^{16} to 2×10^{17} atoms/cm². A random spectrum is also shown for each Ti fluence. The shapes of the random spectra are modified by two factors as the fluence is increased. First, the atomic percentage of Fe in the implanted region is reduced, which reduces the height of the random spectra. Second direct scattering from Ti atoms overlaps the Fe scattering, beginning at the energy corresponding to the surface Ti, marked on the depth scale of Fig. 4. This Ti signal increases the random spectra, counteracting the loss of Fe signal. It should be noted that the Ti signal can also be a component of the channeled spectra at depths below the Ti mark.

The channeling spectra are characterized by a peak at the surface which grows in height (a measure of disorder) and depth as the Ti fluence is increased. In light of the TEM results previously discussed, the disorder peaks in the spectra of Fig. 4 are

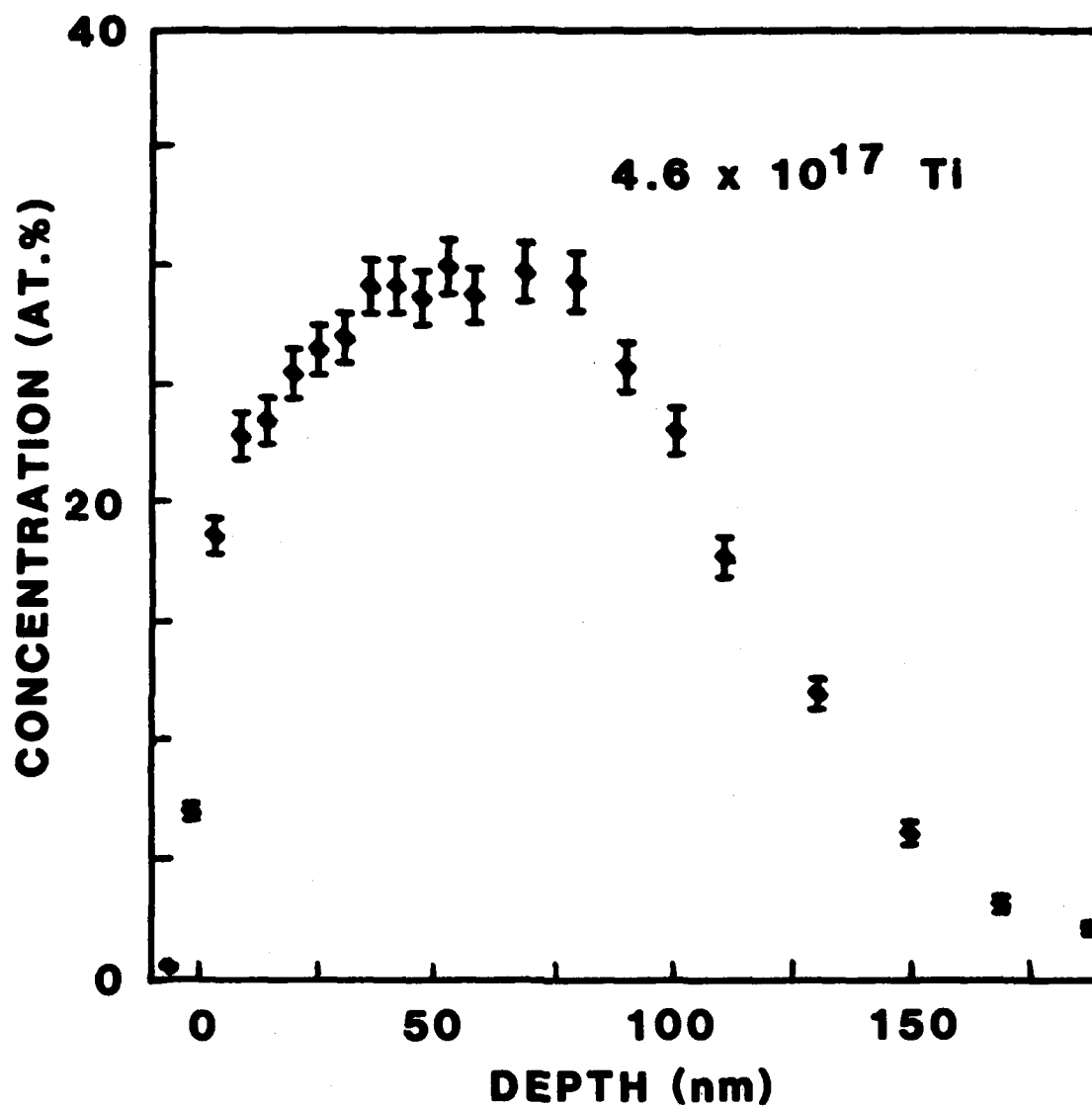


Figure 3a. Nuclear reaction analysis profile of Ti implanted ($4.6 \times 10^{17} \text{ Ti/cm}^2$, 190 keV) into AISI 52100 steel by means of the $^{48}\text{Ti}(p,\gamma)^{49}\text{V}$ resonance reaction. (After Carosella et al., ref. 32, and Gossett et al. ref. 34).

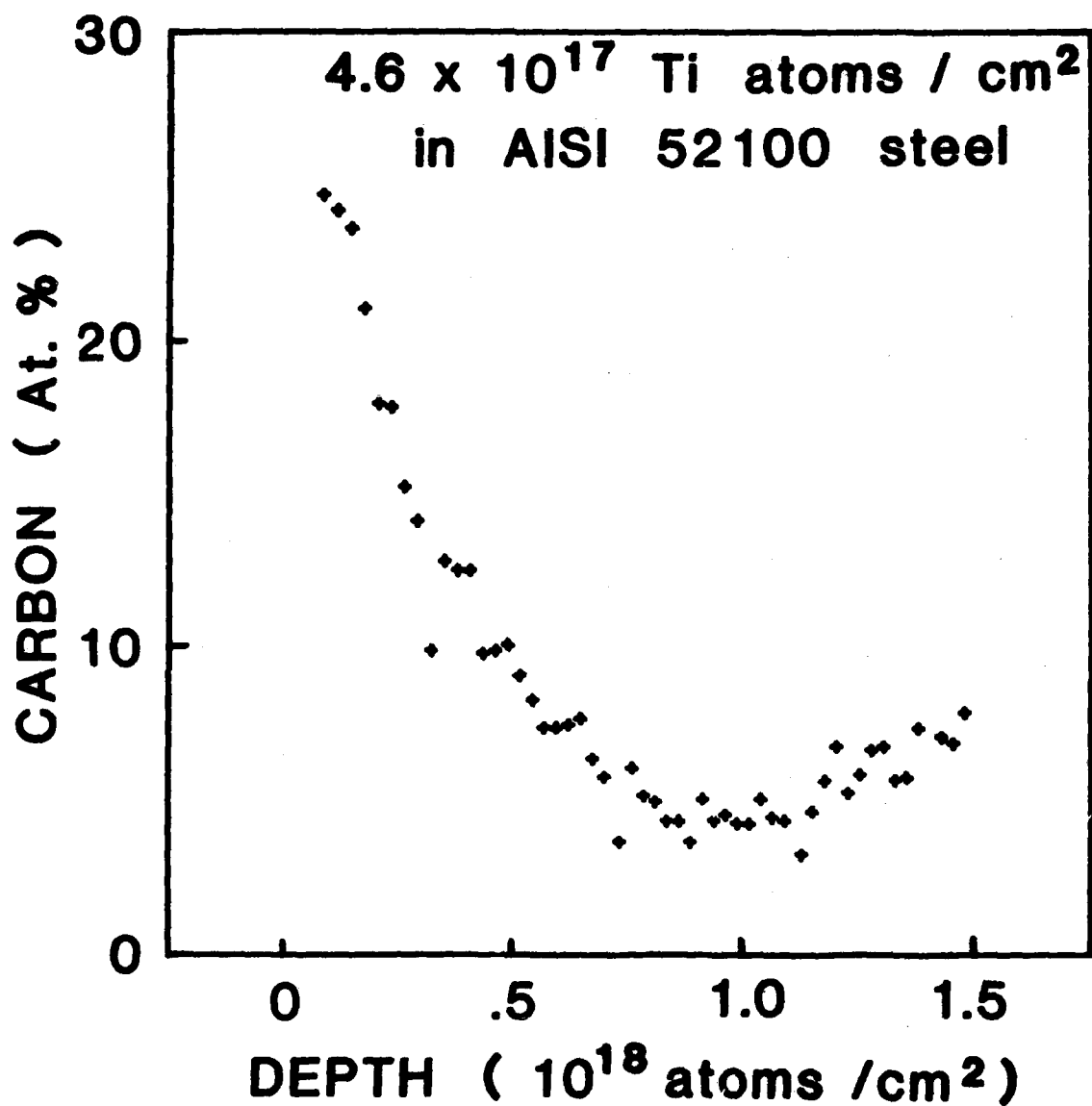


Figure 3b. Nuclear reaction profile of carbon in Ti implanted AISI 52100 steel by means of $^{12}\text{C}(^3\text{He}, ^4\text{He})^{11}\text{C}$ reaction showing that a substantial amount of carbon enters the steel during implantation. (After Gossett, this conference.)

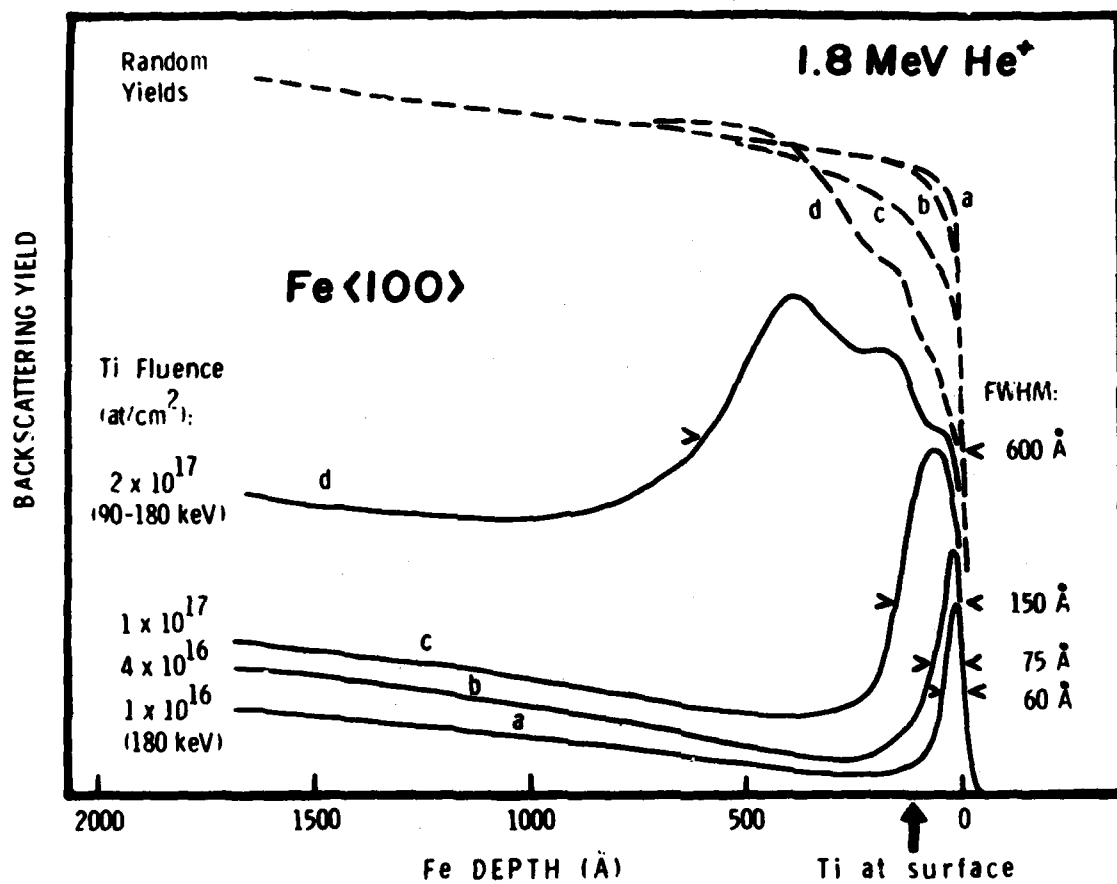


Figure 4. Helium ion channeling spectra obtained along the Fe <100> axis for several fluences of implanted Ti. (After Knapp, Follstaedt, and Picraux, ref. 36).

interpreted as being associated with a partially amorphous region rather than to the presence of precipitates. This amorphous region is seen to grow inward from the surface as a function of Ti fluence. As the Ti fluence is increased, the crystalline fraction is reduced, as seen by the increasingly higher yields, until at 2×10^{17} Ti/cm² the surface region is nearly totally amorphous. Thus, the channeling and TEM are complementary and both give results consistent with the same microstructure for the near surface amorphous layer.

Subsequent TEM investigations by Singer and coworkers of Ti implanted 52100 surfaces revealed an amorphous Fe-Ti-C structure as well.³⁷ It appears that the improved surface hardness and reduced friction of Ti implanted 52100 steel is associated with the production of a thin amorphous layer. The improved surface hardness can account for the improvements in wear resistance, and the lowering of adhesion between two dissimilar metal surfaces (amorphous 52100 vs normal 52100) may account for the lowered friction.

FATIGUE

The application of ion implantation to metal fatigue has been very recent with only two articles published prior to 1978.³⁸ Consequently there is only one result of the application of ion beams to this problem in the literature, although more results are presently being generated in ongoing work on Ti alloys.³⁹ For additional background, there is an excellent discussion of the effects of ion implantation on metal fatigue in a recent review by Herman.²⁷

In this example Hu et al. employed a rotating fatigue test to measure fatigue life improvements in AISI 1018 steel (0.18 wt.%C).⁴⁰ The fatigue test standard specimens were implanted with N₂⁺ ions at 150 keV to a fluence of 1×10^{17} ions/cm². In this widely used laboratory test for measuring fatigue properties one end of a sample of circular cross-section with a reduced-diameter central region is gripped in a chuck and a load is applied at the other end. Points along the reduced diameter central region are alternately forced into tension and compression by rotation of the sample at 5000 rpm. Data are generated by measuring the number of cycles-to-failure (sample breaks) at a stress that is 90% of the yield stress for several samples to ensure good statistics.

The fatigue results showed that both unimplanted and as-implanted samples failed at about 10^6 cycles, whereas samples implanted and aged for 4 months at room temperatures or aged at 100°C for 6 hr (to simulate 4 months at room temp.) failed at about 10^8 cycles—a two-order-of-magnitude improvement. To characterize the surface, depth, concentration profiles of the implanted nitrogen were measured utilizing the ¹⁴N(d,α)¹²C nuclear reaction in combination with a high-resolution magnetic spectrometer to energy-analyze the emitted α particles.

The deuteron beam energy is 900 keV and the energy of the reaction product alpha particles emitted at an angle 135° is about 6 MeV. The reaction excitation function is very flat in this region so that no corrections to the profile other than system resolution need to be considered. The nitrogen distribution in Fig. 5-1 for the as-implanted sample appears reasonably symmetric and buried at a depth of about 80 nm with a peak concentration of approximately 30 at.%. There was little difference observed in the depth distribution profiles of an as-implanted nitrogen sample (Fig. 5-1) and the same sample thermally aged for 20 min. at 100°C (not shown) indicating that the nitrogen which is not in precipitate form is presumably being trapped by damage in the irradiated layer.

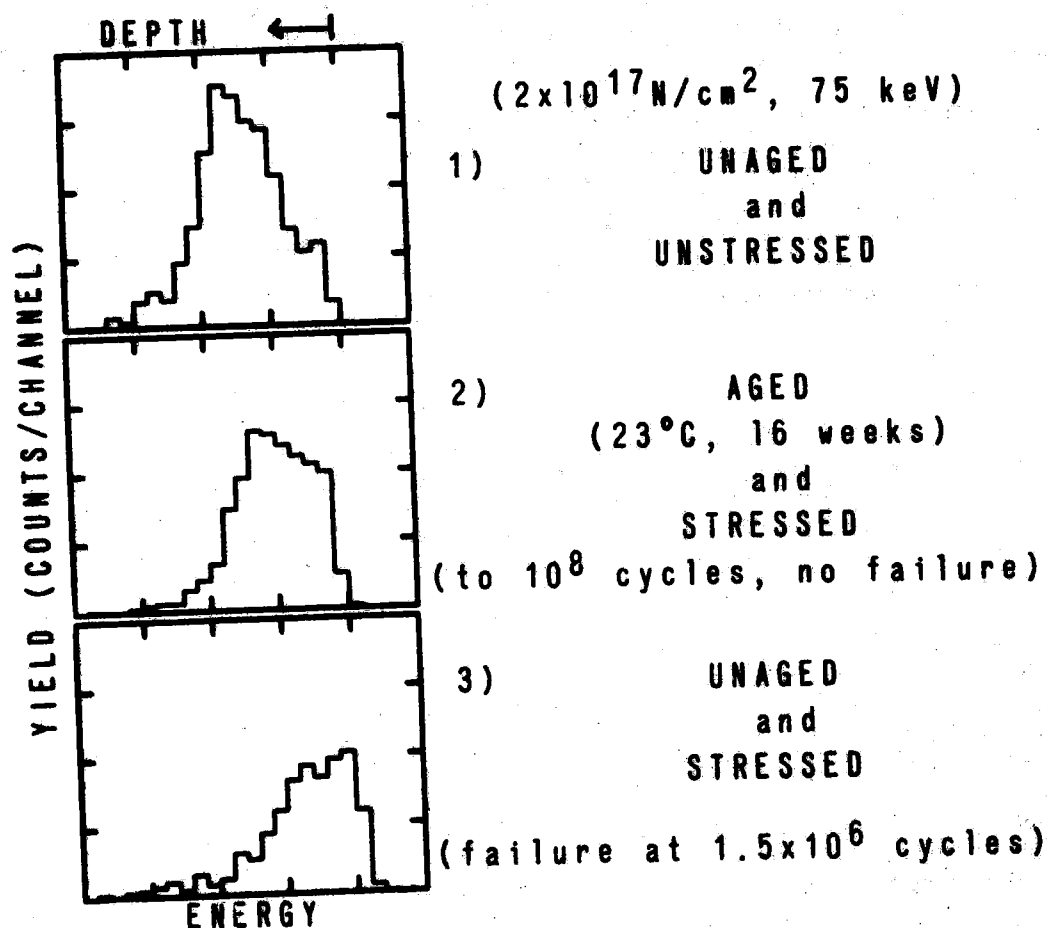


Figure 5. Nuclear reaction analysis profiles of nitrogen implanted into AISI 1018 steel by means of the $^{14}\text{N(d,}\alpha)^{12}\text{C}$ reaction after various post implantation treatments. (After Hu et al., ref. 40).

However, samples that had undergone mechanical stress did show significant redistribution of the nitrogen towards the surface (Figs. 5-2, 5-3), presumably due to stress-induced diffusion. The redistribution was seen in a sample that was aged (23°C for 16 weeks) and showed much longer lifetime (Fig. 5-2), as well as for a sample that was freshly implanted and showed no significant increase in lifetime, relative to unimplanted samples (Fig. 5-3). This non result, in the sense that there is little difference in the nitrogen profiles between short lifetime and long lifetime implanted samples, is useful in that it provides new insight into the fatigue mechanism. It is indirect evidence that nitrogen locally diffuses over small distances to nearby defects. Also, a TEM study on the similar samples showed that both the as-implanted and aged specimens have qualitatively similar microstructures.

Hu et al. points out that the results of these experiments serve to emphasize the profound influence of the near surface on the macroscopic behavior of metals. This study has established that fatigue lifetime can be extended by more than two orders of magnitude by treating only the first 100 nm of the surface of 1018 steel, and nuclear reaction profiling indicated that aging does not cause significant migration of nitrogen from the implanted layer. It is clear that the understanding of these effects is incomplete. Hu et al. speculate that perhaps a process similar to strain aging is occurring where implanted nitrogen interacts with defects in such a way as to inhibit the motion of dislocations. However, the required diffusion of nitrogen to reaction sites proceeds at a low rate and thus requires several weeks at room temperature or several hours at 100°C to be effective.

OXIDATION

The most widely used nuclear reaction for oxidation studies is the $^{16}\text{O}(\text{d,p})^{17}\text{O}$ reaction which measures the total amount of oxygen taken up in an oxide film in analogous fashion to measuring the weight gain of oxidized samples. This reaction lowers the sensitivity of the weight gain method several orders of magnitude. Oxide thickness and stoichiometry are not usually obtained, however, because of the poor depth resolution associated with the protons. Using $^{16}\text{O}(\text{d,p})$ reaction in combination with a magnetic spectrometer improves the depth resolution so that the oxygen may be quantitatively profiled.⁴¹ Very often RBS is employed to measure oxide thickness and stoichiometries by measuring the height and energy width of a well defined step in the RBS signal from an oxidized pure metal—the step being caused by a decrease in the metallic signal due to the presence of oxygen in the oxide. The most active researchers on the effects of ion implantation on oxidation have been Dearnaley and coworkers producing several informative reviews in this field⁴²⁻⁴⁴ and an article on the use of microbeams in corrosion science.⁴⁵ Ion beams have been used to study the effects of ion implantation on the oxidation of the pure metals Ti,⁴⁶ Cr,⁴⁷ Fe,⁴⁸ Ni,⁴⁹ Cu,^{50,51} Zr,⁵² and a number of alloys including S.S.⁴³ In addition, the ion microprobe in conjunction with taper sectioning of specimens has been used to study the oxidation of FeCr,⁵³ Zircaloy, and FeNi Cr⁵⁴ alloys. In this technique, the ion microbeam is scanned along the taper section and nuclear reaction yields from oxygen and other impurities measured. This allows examination of thick oxide scales.

An example of the use of ion beam analysis in the modification of oxidation behavior of metals by ion implantation is that of Ba implanted Ti first reported by Benjamin and Dearnaley⁴⁸ and further studied by Lucke et al.⁵⁵ Figures 6a and 6b show helium ion RBS spectra (2 MeV, 135°) for pure Ti oxidized for 2h at 600°C in air and for Ti implanted with Ba ions to a fluence of 2×10^{16} ions/cm² at an energy of 100 keV and oxidized for the same time. There is a notable decrease in oxide thickness for

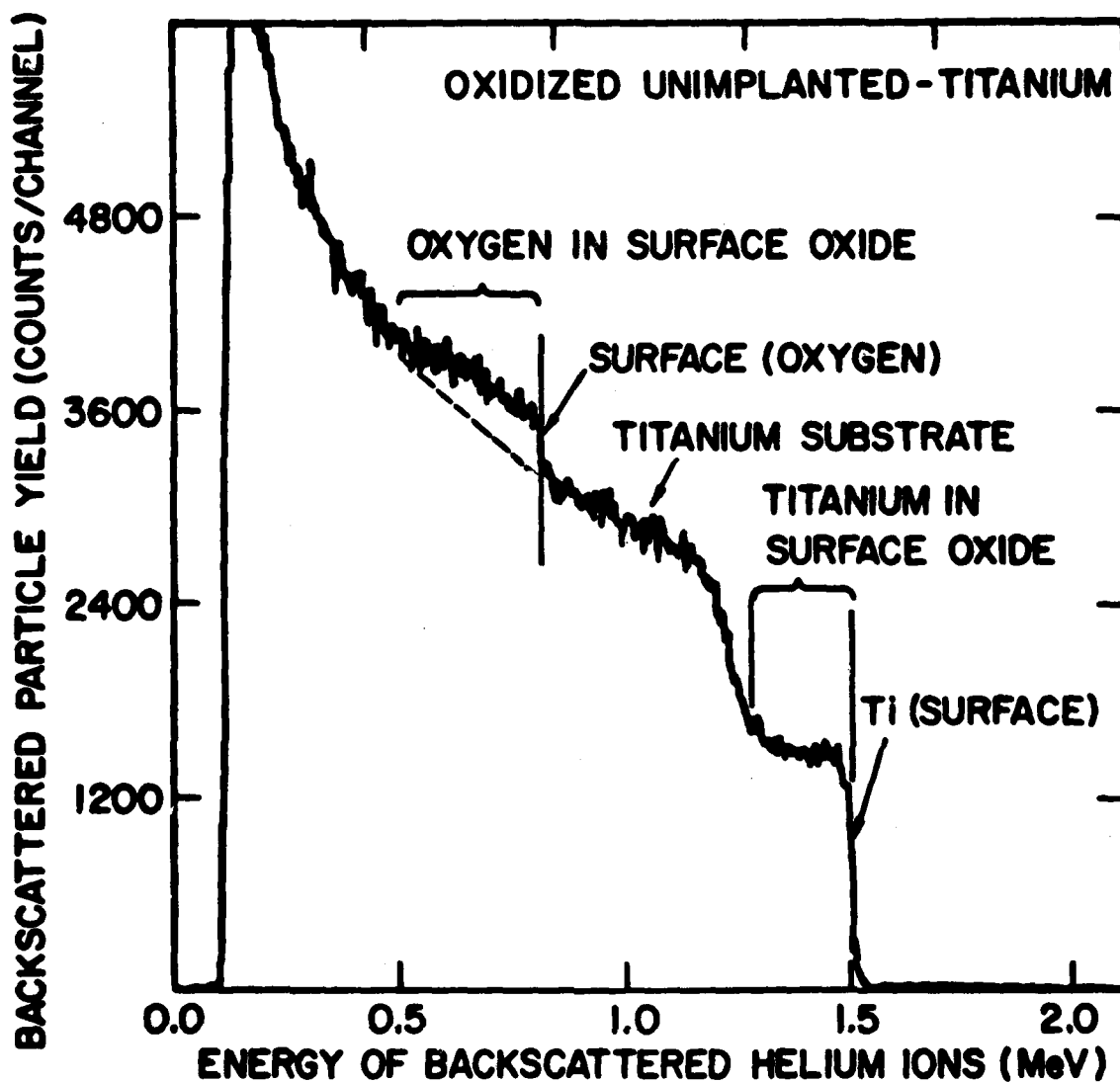


Figure 6a. Helium ion RBS spectra (2 MeV, 135°) for pure Ti oxidized for 2h at 600°C in air.

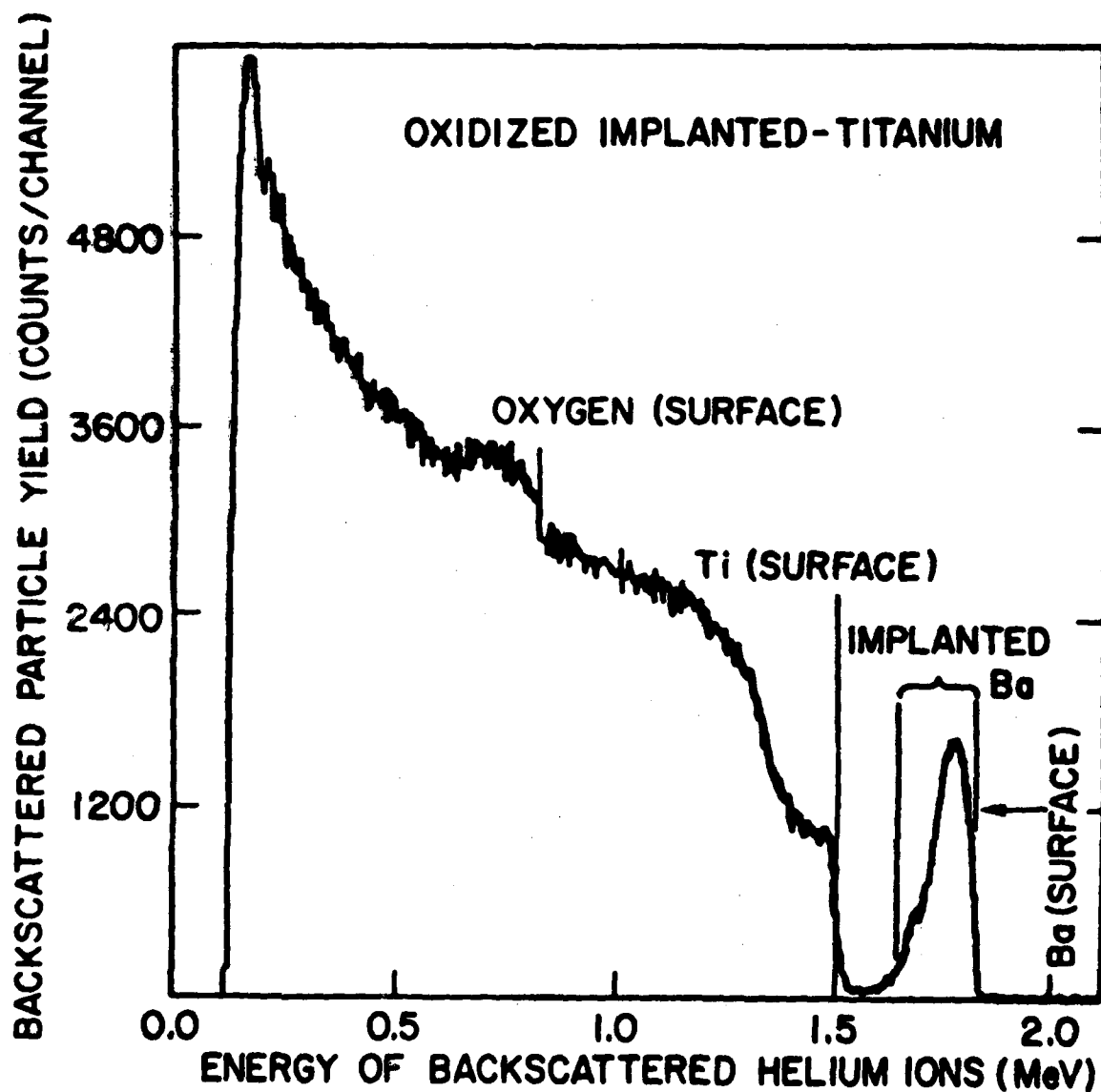


Figure 6b, Helium ion RBS spectra (2 MeV, 135°) for Ti implanted with Ba ions (2×10^{16} Ba/cm², 100 keV) and oxidized under the same conditions as in a.). (After Lucke et al., ref. 55).

the Ba implanted sample. Oxide thicknesses were determined by measuring the depth of the Ti plateau within the oxide for a series of samples oxidized for different times at 600°C. The normal parabolic oxidation rate for oxide growth on Ti was found to be inhibited by a factor of 80 and the beneficial effect on the oxidation rate peaked at a Ba fluence of 2×10^{16} atoms/cm². In the RBS spectrum of Fig. 6b the Ba distribution, which was Gaussian in shape prior to oxidation (not shown), has a shoulder on the low energy edge. TEM investigation of this region revealed BaTiO₃ grains approximately 200 nm in diameter. The positive identification of BaTiO₃ grain formation in these samples is consistent with the model of Benjamin and Dearnaley⁴⁶ for the oxidation inhibition of Ba implanted Ti in which it is postulated that during the initial stages of oxidation, Ba rapidly migrates to grain boundaries and dislocation cores and forms a very stable BaTiO₃ structure which blocks further oxygen in-diffusion.

Additional information was obtained from the oxygen profiles shown in Figure 7. The depth concentration profiles of oxygen were measured utilizing the ¹⁶O(d,p)¹⁷O nuclear reaction in combination with a magnetic spectrometer to analyze the emitted protons.⁴¹ The deuteron energy was 900 keV and the reaction product protons were detected at an angle of 135°. The unimplanted oxide in Fig. 7a is about 1 μm after exposure to air at 600°C for 24h while the oxide thickness on the Ba-implanted sample is about 150 nm. Furthermore, there is an abrupt decrease in the oxygen yield at the metal-oxide interface which does not appear in unimplanted samples with similar oxide thicknesses (not shown). This step could be an indication that the oxide in the implanted samples acts as a diffusion barrier to oxygen in-diffusion. Clearly further work is necessary to clarify the mechanism of oxidation inhibition in this system, but considerable insight has been gained by the application of ion beams to the problem.

AQUEOUS CORROSION

In an early study of the effects of ion implantation on aqueous corrosion Sartwell and coworkers employed low-energy proton-excited x rays in combination with Ar ion sputtering to profile Cr, Ni, and Al implanted ion distributions in pure Fe.⁵⁶ Nearly all subsequent ion beam work has involved RBS in studies of the corrosion behavior of ion-implanted Fe,⁵⁷⁻⁵⁹ Ti,⁶⁰⁻⁶² Al,⁶³⁻⁶⁵ and S.S.⁶⁶ where large improvements in corrosion resistance are claimed. Akano and coworkers⁶⁷ have used RBS and the ¹⁶O(d,p)¹⁷O reaction to study the effects of ion implantation on the oxygen over-potential of Ni anodes. For additional information a very complete review of this field has been published by Ashworth, Procter, and Grant.⁶⁸

The application of ion beams to corrosion science is illustrated by a direct application to a specific corrosion problem, and by two examples of corrosion studies. In this application main shaft bearings for turbojet engines are being implanted to impart corrosion resistance to the rolling element surfaces.⁶ A major cause of bearing rejection is pitting corrosion arising when chlorides and water accumulate in the engine lubricants of aircraft in intermittent use.⁶⁹ The corrosion pits act as initiation sites for fatigue spalling which can lead to catastrophic engine failure. The bearing alloys being investigated are AISI M50 and AISI 52100. The composition of AISI 52100 has been previously mentioned. The composition of M50, which has a martensitic structure, is chiefly 0.85 C, 0.25 Mn, 4.0 Cr, 1.2 V, and 4.3 Mo by wt.%. Pitting corrosion tests have shown that implantation of Cr, Cr+Mo, Cr+P or Ta strikingly improve the general corrosion and pitting corrosion resistance of these steels.⁷⁰ The high doses used in these experiments ($> 10^{17}$ /cm²) preclude accurate calculation of depth profiles because sputtering and ion beam mixing effects predominate. To obtain profiles, the elemental composition of Cr and Cr+Mo implanted samples was investigated by Gossett with

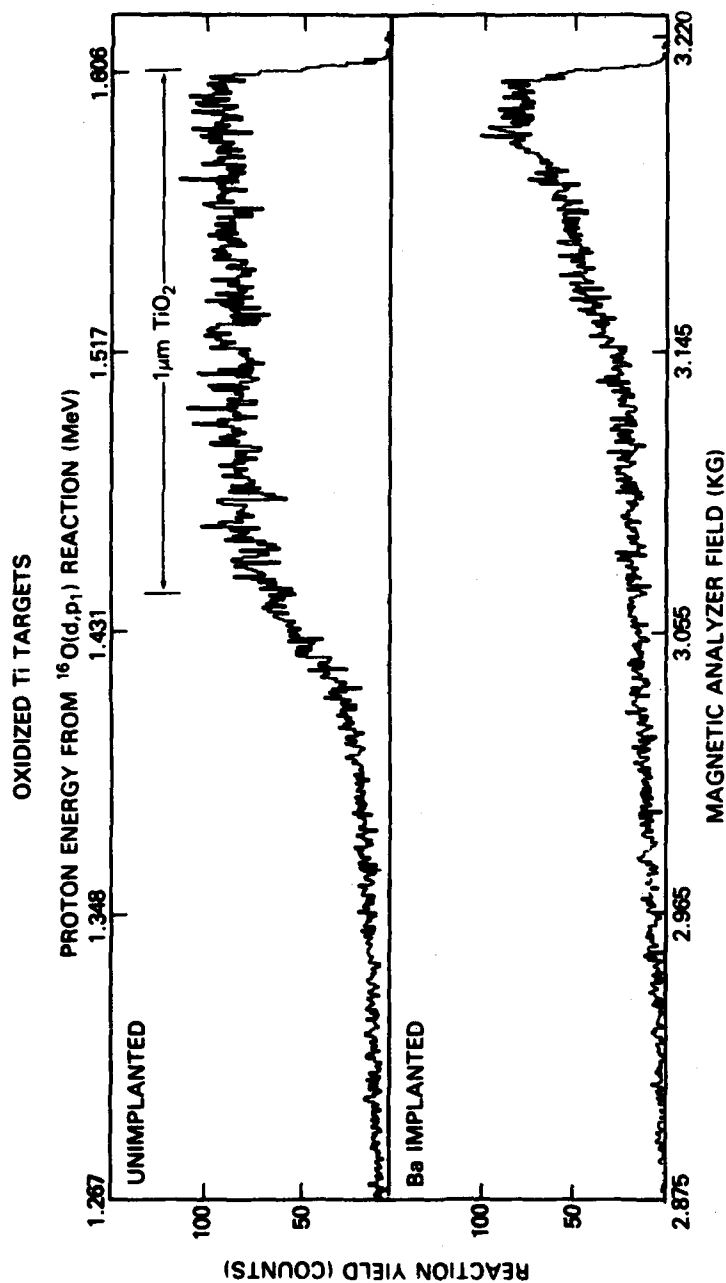


Figure 7. Nuclear reaction analysis profiles of oxygen in oxidized pure Ti by means of $^{16}\text{O}(\text{d},\text{p})^{17}\text{O}$ nuclear reaction for a) unimplanted Ti oxidized for 24h at 600°C in air and, b.) Ti implanted with Ba ($2 \times 10^{16}\text{Ba}/\text{cm}^2$, 100 keV) and oxidized under the same conditions as in a.). (After Hirvonen and Lucke, ref. 41).

nuclear reaction profiling³⁴ and RBS. In the NRA method, Gossett summed the yields of 10 different γ -ray peaks in a large volume Ge(Li) detector energy spectrum that are unique to a narrow resonance in the $^{52}\text{Cr}(p,\gamma)^{53}\text{Mn}$ reaction at a proton energy of 1005 keV. Profiles of Cr were obtained in the presence of Fe, Mn, and V in the same manner as previously discussed for the $^{48}\text{Ti}(p,\gamma)^{49}\text{V}$ reaction. Two concentration profiles are shown in Fig. 8 for $2 \times 10^{17} \text{ Cr/cm}^2$ at 150 keV and for a dual implantation of $2 \times 10^{17} \text{ Cr/cm}^2$ at 150 keV plus $3.5 \times 10^{16} \text{ Mo/cm}^2$ at 100 keV. The single implant in Fig. 8a shows that the normal Gaussian shape for implanted profiles has been altered by sputtering such that the Cr concentration at the surface is about 20 at.%. Further implantation with Mo ions has depleted the Cr concentration by sputtering, but the Cr surface concentration remains at an acceptable level for corrosion resistance. Profiles such as these are instrumental in optimizing implantation parameters. In this case, the surface has been converted into a high Mo content stainless steel which is known to process high localized corrosion resistance in the bulk form.

The next example is a study of hydrogen absorption in high purity polycrystalline iron foils.⁷¹ Hydrogen absorption greatly reduces the mechanical properties of structural alloys and the motivation for these experiments is to determine if ion implantation is useful for reducing hydrogen absorption. In these experiments a 0.4 mm thick Fe foil is implanted with Pt ions to a fluence of $1.5 \times 10^{16} \text{ ions/cm}^2$ at 100 keV. The foil becomes a membrane between two electrochemical cells. In one cell the membrane is cathodically charged to evolve H_2 at the surface and in the process a surface coverage of H atoms is generated which causes in-diffusion of H atoms. In the second cell, the H atoms which have diffused through the membrane are anodically oxidized. The measured anodic current is a direct measure of the hydrogen flux through the membrane. Implantation with He or Fe ions had no effect on the measured hydrogen flux, nor did Pt ions in the as-implanted state. RBS spectra shown in Fig. 9 were taken with 2.5 MeV α particles detected in a magnetic spectrometer at a scattering angle of 135° . The effective depth resolution for this system is 4 nm. The RBS profiles of Pt were taken as a function of the time of immersion in room temperature 1N H_2SO_4 . It is clear that initially the surface Pt concentration is negligible; however, after 20 seconds the surface concentration of Pt has reached a maximum level and further time in the acid results in rapid loss of Pt atoms. The RBS profiles correlated well with hydrogen permeation flux measurements performed after immersion in acid for various times and showed a substantial reduction of hydrogen flux when the surface concentration of Pt was a maximum. Through measurements of the dependence of permeation flux on the charging current and charging potential it was established that the implanted Pt catalyzed the $\text{H} + \text{H} \rightarrow \text{H}_2$ reaction on the surface, effectively reducing the H partial pressure which results in reduced H permeation. These results support the notion that ion implantation can effectively reduce hydrogen absorption in metals, but in this case, only after the surface has been sensitized by dipping into a strong acid.

The work of Hubler and McCafferty⁶⁰ serves as a final example of how implantation can not only provide corrosion resistance but also bear on specific corrosion mechanisms. It has been known for some time that small amounts of Pd (about 0.1 at.%) in bulk alloys produces a very large reduction in the corrosion rate of Ti in boiling acids.⁷² The present experiments consisted of measuring the relative corrosion rates of unimplanted and Pd-implanted Ti exposed to boiling 1M sulphuric acid. Samples of pure (99.79%) polished, polycrystalline Ti were implanted with Pd (10^{16} Pd/cm^2 at 90 keV) and Xe ($3.5 \times 10^{15} \text{ Xe/cm}^2$ at 90 keV) resulting in a buried Pd distribution with a peak concentration of approximately 5 at.% and a surface concentration less than 0.1 at.%. The Xe atoms provided a "marker" for elastic backscattering analyses against which to register the amount of Ti removed from the

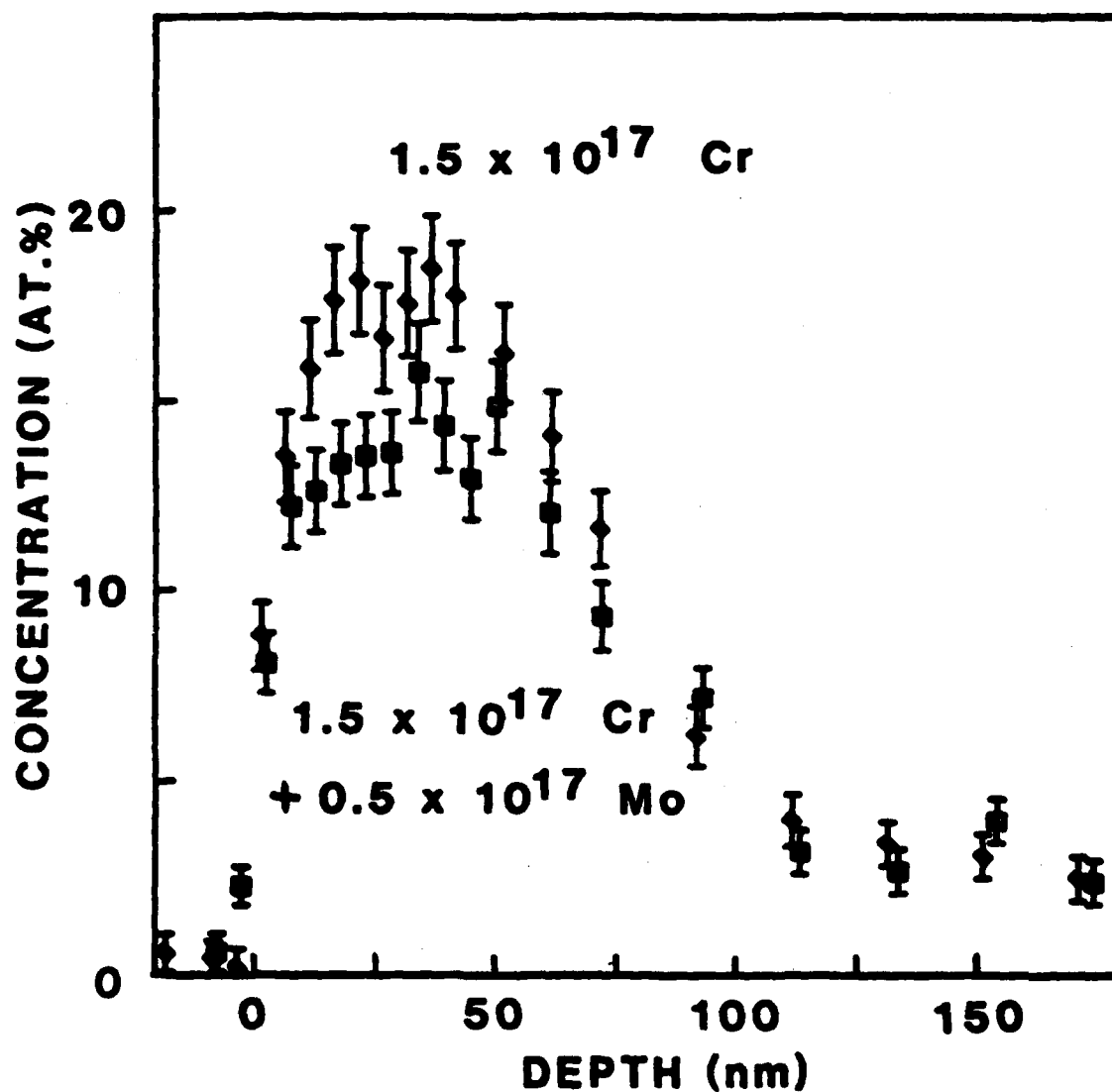


Figure 8. Nuclear reaction analysis profiles of Cr implanted into AISI M50 steel by means of the $^{52}\text{Cr}(p,\gamma)^{53}\text{Mn}$ resonance reaction for implantation conditions of 1.5×10^{17} Cr/cm² at 150 keV (solid diamonds) and 1.5×10^{17} Cr/cm² at 150 keV plus 0.5×10^{17} Mo/cm² at 100 keV (solid squares). M50 steel contains 4 at.% Cr in the bulk. (After Gossett, ref. 34).

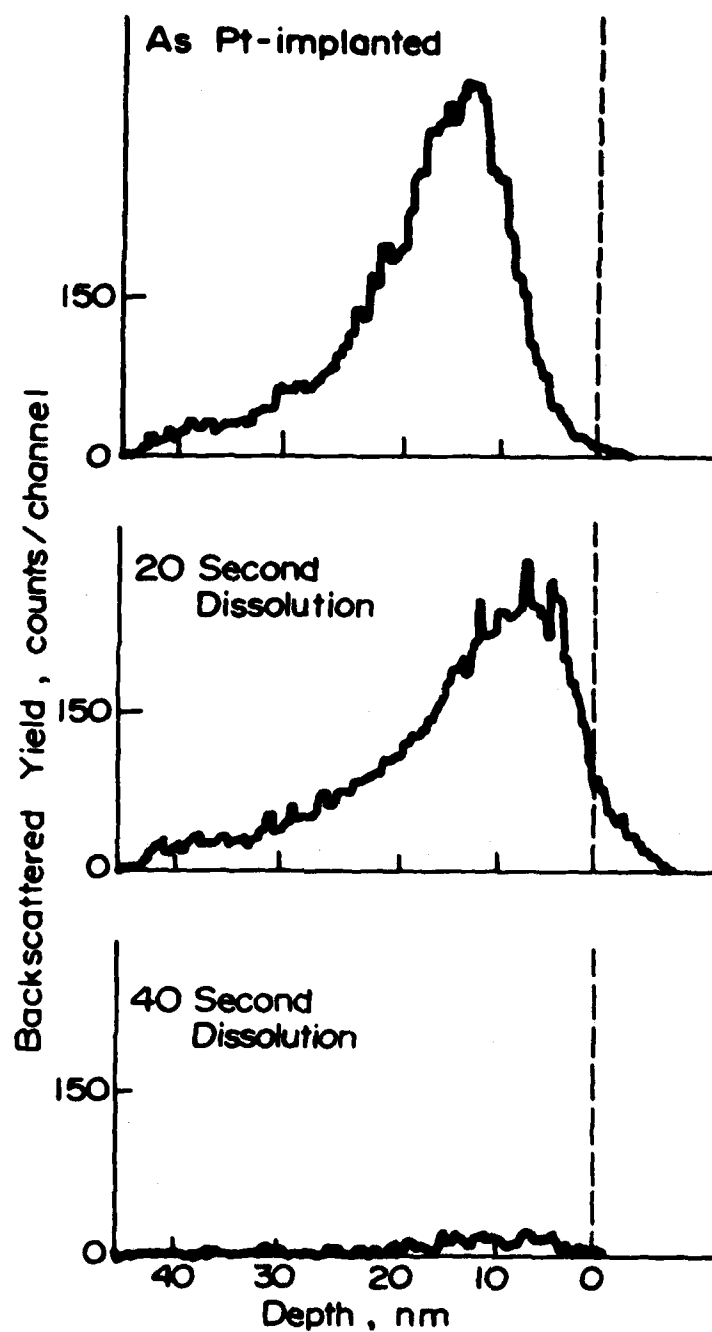


Figure 2. High-resolution helium-ion RBS spectra (2.5 MeV, 135°) of implanted Pt (1.5×10^{16} Pt/cm², 100 keV) in Fe as a function of time of immersion of the implanted sample in 1M H₂SO₄ at room temperature. (After Zamanzadeh et al., ref. 71).

front surface as a function of exposure time to the acid solution. Fig. 10 shows the Pd profiles as a function of time obtained with high-resolution elastic backscattering under the same conditions as in the previous example. The Pd profiles have been redrawn to reflect the measured amount of Ti atoms dissolved from the surface. It can be seen that as the exposure time increases, the titanium above the buried palladium-implanted layer is quickly dissolved away until the surface reaches the buried palladium layer. During this process the palladium concentration at the surface begins to grow and stabilizes at about 20 at.% after 48 min.

Corrosion potential versus time data in boiling 1M H_2SO_4 showed a rapid transition in time from a corrosion potential near that of pure Ti to a potential close to that of pure Pd and steady state corrosion potential was reached after less than 1h. The measured reduction in the corrosion rate of Ti in boiling 1M H_2SO_4 was a factor of 5000. The long-lasting protection is explained by the preferential dissolution of Ti over that of Pd, leaving Pd distributed at the surface, even after a greater thickness of material has been removed than the depth of the original implanted Pd.

OTHER STUDIES

A number of other studies of primary importance to ion implantation of metals and engineering alloys which do not fit under the previous categories deserve mentioning. Carbon buildup from cracked hydrocarbons on the surface of the sample during implantation has been investigated by Moller by means of the $C^{12}(d,p)C^{13}$ reaction.⁷³ Feldman and coworkers used the same reaction on C^{12} and C^{13} to study the lattice location of carbon in iron by ion channeling,⁷⁴ and Johnson and coworkers used RBS analysis and TEM to identify a phase transition to martensite induced by the implantation of Sb into stainless steel.⁷⁵ The latter systems are clearly of interest in understanding the mechanical properties of steels. Grant et al. have studied amorphous layers created by implantation of P or Dy into stainless steel by ion channeling,⁷⁶ and several workers have studied dislocations in Al induced by ion implantation of Zn, N, or Ni ions by means of ion dechanneling measurements.⁷⁷⁻⁷⁹ The latter experiments could in theory be applied to fatigue studies of pure metal single crystals in order to directly measure changes in dislocation densities of fatigued metals in the near surface region.

RBS and ion channeling have been used in wide ranging studies of the fundamental processes which occur as a result of ion implantation. The following is a listing of key papers, reviews, and chapters in books on the indicated subject areas for the interested reader. These are; metastable alloy formation encompassing super saturated solid solutions and amorphous metals,^{80,81} impurity immobilization⁸² and defect trapping⁸³ by ion implantation damage and doping, ion beam induced migration and reactions,⁸⁴⁻⁸⁶ all of which can be classified under the general heading of ion implantation metallurgy.⁸⁷⁻⁸⁹

A final example comes from the work of Reynolds and coworkers who studied the composition of Cr-implanted polycrystalline iron by means of optical emission from highly excited sputtered atoms during Ar ion bombardment.⁹⁰ It is an extension of work by White et al.⁹¹ and was motivated by the desire to obtain in situ information on the surface composition during ion implantation, and to develop a new quantitative surface analysis technique. An iron sample was implanted with 90 keV chromium to a fluence of $4.1 \times 10^{17}/cm^2$ and then sputtered by a 50 keV Ar ion beam. The optical emission of both Cr and Fe were monitored continuously and plotted as a function of time. The concentration of Cr in the surface alloy was calibrated by Ar sputtering on pure Fe and Cr targets. The measured Cr concentration profile in Fig. 11 is compared

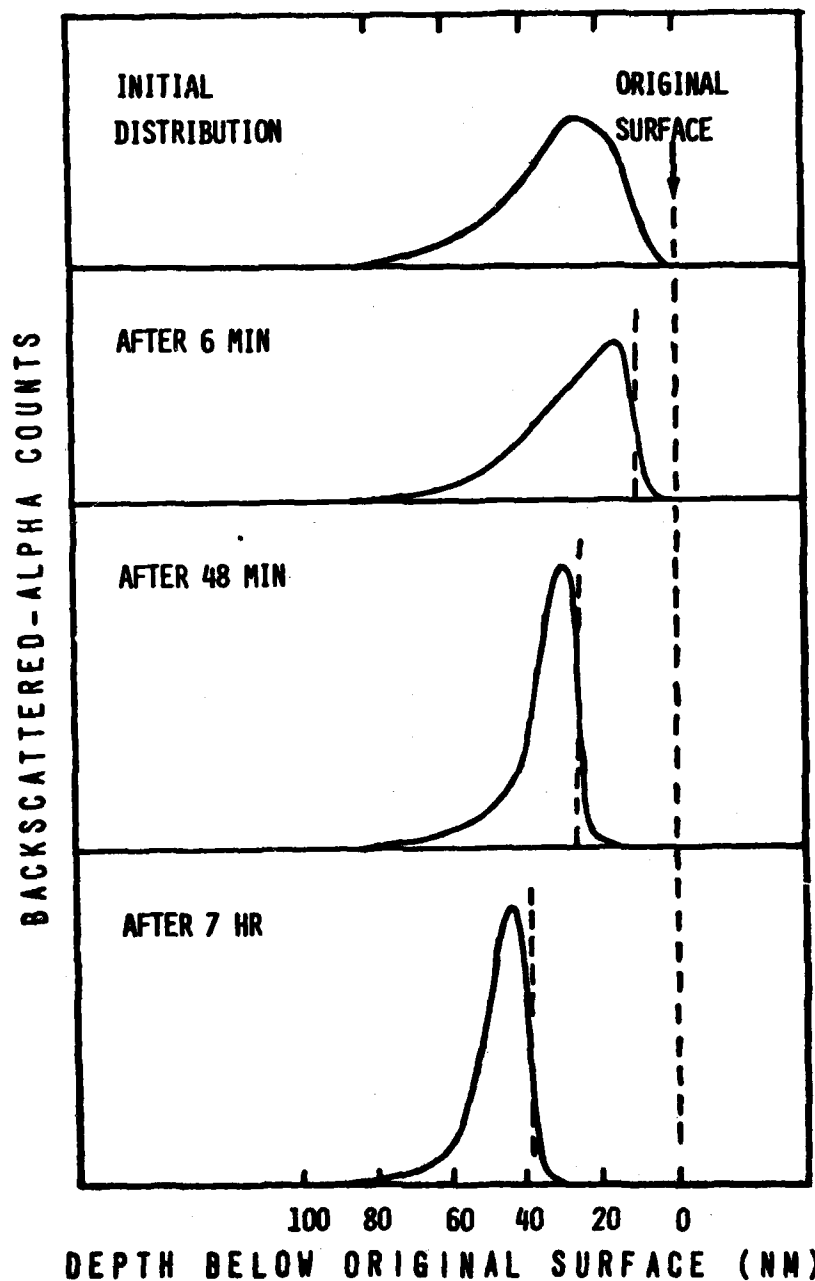


Figure 10. High-resolution helium-ion RBS spectra (2.5 MeV, 135°) of implanted Pd (1×10^{16} Pd/cm², 90 keV) in Ti as a function of time of immersion of the implanted sample in boiling 1M H₂SO₄. The spectra have been displaced on the abscissa to reflect the measured amount of Ti atoms dissolved from the surface during immersion in the boiling acid. (After Hubler and McCafferty, ref. 60).

to profiles obtained by the $^{52}\text{Cr}(p,\gamma)$ NRA method³⁴ and by RBS by means of a spectrum subtraction method described earlier.²⁹ The agreement between the profile measured by means of optical emission and the NRA is very good. The RBS profile is clearly not as precise as optical emission profile or NRA but is quite acceptable for many applications and is considerably more convenient to produce. The results of this study strongly support the idea that the optical emission of sputtered species parallels the surface atomic fractions during the sputter erosion of a binary alloy.

It is apparent that ion beam analysis is a major tool supporting the application of ion implantation to materials problems associated with wear, fatigue, oxidation, and corrosion of pure metals and engineering alloys. Moreover, it is hoped that from this discussion an appreciation is gained for the fact that the immense complexity of engineering alloys is the reason why it is generally true that a microscopic understanding of many mechanical properties and corrosion mechanisms is lacking. It appears certain that ion implantation coupled with ion beam surface layer analysis, TEM, and other surface analysis tools will provide new insights into many of the long-standing problems encountered in the theory of mechanical properties and corrosion behavior of metals.

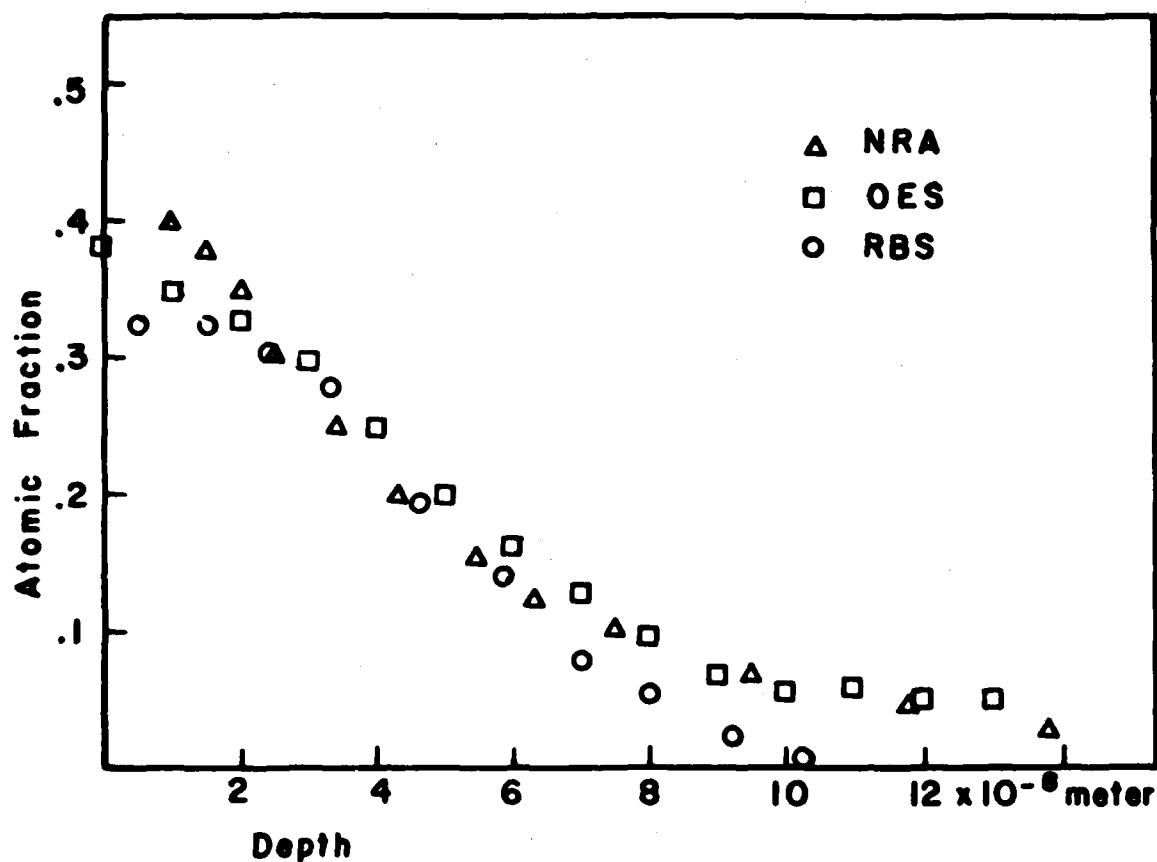


Figure 11. Depth concentration profiles of Cr implanted into Fe ($4.1 \times 10^{17}/\text{cm}^2$, 90 keV) by means of nuclear reaction analysis ($^{52}\text{Cr}(p,\gamma)^{53}\text{Mn}$), optical emission spectroscopy, and Rutherford backscattering techniques. (After Reynolds et al., ref. 90).

REFERENCES

1. J. K. Hirvonen, *J. Vac. Sci. Technol.* **15** (1978) 1662.
2. See Proceedings of International Conference on Metallurgical Coatings in Thin Solid Films **63** (1979).
3. H. E. Meyer, *Fortune*, Feb. 9 (1981) 68.
4. G. Dearnaley, J. H. Freeman, R. S. Nelson, and J. Stephan, "Ion Implantation" (North Holland, Amsterdam, 1973).
5. G. Dearnaley, "Ion Implantation Metallurgy," eds., C. M. Preece and J. K. Hirvonen (Am. Inst. of Mining, Metallurgical, and Petroleum Engineers, Inc., New York, 1980) p. 1.
6. G. K. Hubler, J. K. Hirvonen, C. R. Gossett, I. Singer, C. R. Clayton, Y. F. Wang, H. E. Munson, and G. Kuhlman, NRL Memorandum Report 4481, Jan. 1981.
7. "Ion Beam Handbook for Material Analysis," eds., J. W. Mayer and E. Rimini (Academic, NY, 1977).
8. J. R. Bird, *Nucl. Instrum. Methods* **168** (1980) 85.
9. "Application of Ion Beams to Metals," eds., S. T. Picraux, E. P. Eernisse, and F. L. Vook, (Plenum, New York, 1973).
10. Conference on Ion Implantation and Ion Beam Analysis Techniques in Corrosion, Univ. of Manchester, Manchester, UK, 28-30 June 1978, published in *Corros. Sci.* **20** Jan. (1980).
11. "Application of Ion Beams to Materials," eds., G. Carter, J. S. Colligen, and W. A. Grant, Conference Series 28 (Institute of Physics, London, 1976).
12. Conference on Ion Beam Modification of Materials, Budapest, Hungary, 4-8 Sept. 1978. Proceedings in *Radiat. Eff.* **47-49** (1980).
13. Ion Implantation Metallurgy Symposium at Annual Meeting of the Materials Research Society, Cambridge, MA, 30 Nov 1979. Proceedings in "Ion Implantation Metallurgy," eds., C. M. Preece and J. K. Hirvonen, (Am. Inst. of Mining, Metallurgical and Petroleum Engineers, Inc., New York, 1980).
14. Conference on Ion Beam Modification of Materials, Albany, New York, 14-18 July, 1980, to be published in *Nucl. Instrum. Methods*.
15. J. F. Ziegler et al., *Nucl. Instrum. Methods* **149** (1978) 9.
16. J. Bottiger, S. T. Picraux, and N. Rud, "Ion Beam Surface Layer Analysis," eds., O. Meyer, G. Linker, and F. Kappler (Plenum, NY, 1976) p. 811.
17. "Treatise on Materials Science and Technology," ed., H. S. Rosenbaum, Vol. 7 Microstructure of Irradiated Materials (Academic, NY 1975).

18. C. W. White and P. S. Peercy, eds., "Laser and Electron Beam Processing of Materials," (Academic, NY, 1980).
19. J. M. Poate, "Laser and Electron Beam Processing of Materials," eds., C. W. White and P. S. Peercy (Academic, NY, 1980) p. 691.
20. "Treatise on Materials Science and Technology," ed., J. K. Hirvonen, Vol. 18, Ion Implantation (Academic, NY, 1980).
21. G. Dearnaley, P. D. Goode, N. E. W. Hartley, G. W. Procter, J. F. Turner, and R. E. J. Watkins, "Ion Plating and Allied Techniques - 1979," ed., R. Hurley (CEP Consultants, Edinburgh, 1979) p. 243.
22. S. LoRusso, P. Mazzoldi, I. Scotoni, C. Tosello, and S. Tosto, Appl. Phys. Lett. **34** (1979) 627.
23. N. E. W. Hartley, TRIBOLOGY, Apr. (1975) p. 65.
24. I. J. R. Baumvol, R. E. J. Watkins, G. Longworth, and G. Dearnaley, to be published by Institute of Physics.
25. C. M. Preece, E. N. Kaufmann, A. Standings, and L. Buene, "Ion Implantation Metallurgy," eds., C. M. Preece and J. K. Hirvonen (Am. Institute of Mining, Metallurgical, and Petroleum Engineers, Inc., NY, 1980) p. 77.
26. N. E. W. Hartley, Thin Solid Films **64** (1979) 177.
27. H. Herman, presented at Conference on Ion Beam Modification of Materials, Albany, NY, 14-18 July, 1980, to be published in Nucl. Instrum. Methods.
28. R. A. Kant, J. K. Hirvonen, A. R. Knudson, and J. S. Wollam, Thin Solid Films **63** (1979) 27.
29. A. R. Knudson, private communication.
30. For an alternate subtraction method see Z. L. Liao, Appl. Phys. Lett. **36** (1980) 51.
31. J. F. Ziegler, R. F. Lever, and J. K. Hirvonen, "Ion Beam Surface Layer Analysis," eds., O. Meyer, G. Linker, and F. Kappler (Plenum, NY, 1976) p. 163.
32. C. A. Carosella, I. L. Singer, R. C. Bowers, and C. R. Gossett, "Ion Implantation Metallurgy," eds., C. M. Preece and J. K. Hirvonen (Am. Institute of Mining, Metallurgical and Petroleum Engineers, Inc., NY, 1980) p. 103.
33. I. L. Singer, R. N. Bolster, and C. A. Carosella, Thin Solid Films **73** (1980) 283.
34. C. R. Gossett, Nucl. Instrum. Methods **168** (1980) 217.
35. C. R. Gossett, this conference.
36. J. A. Knapp, D. M. Follstaedt, and S. T. Picraux, "Ion Implantation Metallurgy," eds., C. M. Preece and J. K. Hirvonen (Am. Institute of Mining, Metallurgical, and Petroleum Engineers, Inc., NY, 1980) p. 152.

37. I. L. Singer, C. A. Carosella, and J. R. Réed, presented at Conference on Ion Beam Modification of Materials, Albany, NY, 14-18 July, 1980, to be published in Nucl. Instrum. Methods.
38. N. E. W. Hartley, "Application of Ion Beams to Materials," eds., G. Carter, J. S. Colligan, and W. A. Grant, Conference Series 28, (Institute of Physics, London, 1976) p. 210.
39. R. G. Vardiman and C. R. Gossett, to be published.
40. W. W. Hu, H. Herman, C. R. Clayton, J. Kozubowski, R. A. Kant, J. K. Hirvonen, and R. K. MacCrone, "Ion Implantation Metallurgy," eds., C. M. Preece and J. K. Hirvonen (Am. Inst. Mining, Metallurgical, and Petroleum Engineers, NY, 1980) p. 92.
41. J. K. Hirvonen and W. H. Lucke, Nucl. Instrum. Methods **149** (1978) 295.
42. G. Dearnaley, "Ion Beam Surface Layer Analysis," eds., O Meyer, G. Linker, and F. Kappler (Plenum, NY, 1976) p. 885.
43. G. Dearnaley, "Application of Ion Beams to Metals," eds., S. T. Picraux, E. P. Eer Nisse, and F. L. Vook (Plenum, NY, 1974) p. 63.
44. G. Dearnaley, presented at Conference on Ion Beam Modification of Materials, Albany, NY 14-18 July, 1980, to be published in Nucl. Instrum. Methods.
45. C. R. Allen, G. Dearnaley, and N. E. W. Hartley, "Ion Beam Surface Layer Analysis," eds., O. Meyer, G. Linker, and F. Kappler (Plenum, NY, 1976) p. 901.
46. J. D. Benjamin and G. Dearnaley, "Application of Ion Beams to Materials," eds., G. Carter, J. S. Colligan, and W. A. Grant, Conference Series 28 (Institute of Physics, London, 1976) p. 141.
47. R. A. Collins, S. Muhl, and G. Dearnaley, J. Phys. F: Metal Phys. **9** (1979) 1245.
48. I. J. R. Baumvol, presented at Conference on Ion Beam Modification of Materials, Albany, NY, 14-18 July, 1980, to be published in Nucl. Instrum. Methods.
49. P. D. Goode, "Application of Ion Beams to Materials," eds., G. Carter, J. S. Colligan, and W. A. Grant, Conference Series 28 (Institute of Physics, London, 1976) p. 154.
50. J. Rickards and G. Dearnaley, "Application of Ion Beams to Metals," eds., S. T. Picraux, E. P. Eer Nisse, and F. L. Vook (Plenum, NY, 1974) p. 101.
51. L. G. Svendsen, Corros. Sci. **20** (1980) 63.
52. M. Berti, A. Carnera, A. V. Drigo, A. Armigliato, A. De Salvo, and R. Rosa, presented at Conference on Ion Beam Modification of Materials, Albany, NY, 14-18 July, 1980, to be published in Nucl. Instrum. Methods.
53. A. M. Pritchard, N. E. W. Hartley, J. F. Singleton, and A. E. Truswell, Corros. Sci. **20** (1980) 1.

54. J. W. McMillan and F. C. W. Pummery, *Corros. Sci.* **20** (1980) 41.
55. W. H. Lucke, J. A. Sprague, and J. K. Hirvonen, unpublished.
56. B. D. Sartwell, A. B. Campbell, and P. B. Needham, "Ion Implantation in Semiconductors and Other Materials," eds., F. Chernow, J. A. Borders, and D. Brice (Plenum, NY, 1977) p. 201.
57. V. Ashworth, D. Baxter, W. A. Grant, R. P. M. Procter, and T. C. Wellington, *Corros. Sci.* **16** (1976) 775.
58. V. Ashworth, D. Baxter, W. A. Grant, and R. P. M. Procter, *Corros. Sci.* **17** (1977) 947.
59. V. Ashworth, W. A. Grant, R. P. M. Procter, and E. J. Wright, *Corros. Sci.* **18** (1978) 681.
60. G. K. Hubler and E. McCafferty, *Corros. Sci.* **20** (1980) 103.
61. N. G. Thompson, B. D. Lichter, B. R. Appleton, E. J. Kelly, and C. W. White, "Ion Implantation Metallurgy," eds., C. M. Preece and J. K. Hirvonen (Am. Institute of Mining, Metallurgical, and Petroleum Engineers, NY, 1980) p. 181.
62. B. R. Appleton, E. J. Kelly, C. W. White, N. G. Thompson, and B. D. Lichter, presented at Conference on Ion Beam Modification of Materials, Albany, NY, 14-18 July, 1980, to be published in *Nucl. Instrum. Methods*.
63. W. D. Mackintosh and F. Brown, "Application of Ion Beams to Metals," eds., S. T. Picraux, E. P. Eernisse and F. L. Vook (Plenum, NY, 1974) p. 111.
64. A. H. Saffar, V. Ashworth, A. K. O. Bairamov, D. J. Chivers, W. A. Grant, and R. P. M. Procter, *Corros. Sci.* **20** (1980) 127.
65. C. Towler, R. A. Collins, and G. Dearnaley, *J. Vac. Sci. Technol.* **12** (1975) 520.
66. V. Ashworth, W. A. Grant, A. R. Mohammed, and R. P. M. Procter, "Ion Implantation Metallurgy," eds., C. M. Preece and J. K. Hirvonen (Am. Institute of Mining, Metallurgical, and Petroleum Engineers, NY, 1980) p. 47.
67. U. Akano, J. A. Davies, W. W. Smeltzer, I. S. Tashlykov, and D. A. Thompson, presented at Conference on Ion Beam Modification of Materials, Albany, NY, 14-18 July, 1980, to be published in *Nucl. Instrum. Methods*.
68. V. Ashworth, R. P. M. Procter, and W. A. Grant, "The Application of Ion Implantation to Aqueous Corrosion," in *Ion Implantation*, ed., J. K. Hirvonen (Academic, NY, 1980).
69. Y. F. Wang, C. R. Clayton, G. K. Hubler, W. H. Lucke, and J. K. Hirvonen, *Thin Solid Films* **63** (1979) 11.
70. C. R. Clayton, Y. F. Wang, J. K. Hirvonen, and G. K. Hubler, to be published.
71. M. Zamanzadeh, A. Allam, H. W. Pickering, and G. K. Hubler, *J. Electrochem. Soc.* **127** (1980) 1688.

72. M. Stern and H. Wissenberg, *J. Electrochem. Soc.* **106** (1960) 759.
73. W. Moller, Th. Pfeiffer, and M. C. Schluckebier, presented at Conference on Ion Beam Modification of Materials, Albany, NY, 14-18 July, 1980, to be published in *Nucl. Instrum. Methods*.
74. L. C. Feldman, E. N. Kaufmann, J. M. Poate, and W. M. Augustyniak, "Ion Implantation in Semiconductors and Other Materials," ed., B. L. Crowder (Plenum, NY, 1973) p. 491.
75. E. Johnson, U. Littmark, A. Johnson, and C. Christodavrides, presented at Conference on Ion Beam Modification of Materials, Albany, NY, 14-18 July 1980, to be published in *Nucl. Instrum. Methods*.
76. W. A. Grant, J. L. Whitton, and J. S. Williams, *Radiat. Eff.* **49** (1980) 65.
77. G. Foti, S. T. Picraux, S. U. Campisano, E. Rimini, and R. A. Kant, "Ion Implantation in Semiconductors," eds., F. Chernow, J. A. Borders, and D. K. Brice, (Plenum, NY, 1976) p. 247.
78. E. Rimini, S. U. Campisano, G. Foti, P. Baeri, and S. T. Picraux, "Ion Beam Surface Layer Analysis," eds., O. Meyer, G. Linker, and F. Kappler (Plenum, NY, 1976) p. 597.
79. S. T. Picraux, D. M. Follstaedt, P. Baeri, S. U. Campisano, G. Foti, and E. Rimini, *Radiat. Eff.* **49** (1980) 75.
80. J. M. Poate and A. G. Cullis, "Implantation Metallurgy—Metastable Alloy Formation" in *Ion Implantation*, ed., J. K. Hirvonen (Academic, NY, 1980).
81. J. S. Williams, R. Andrew, C. E. Christodoulides, W. A. Grant, P. J. Grundy, and G. A. Stephens, "Ion Implantation in Semiconductors," eds., F. Chernow, J. A. Borders, and D. K. Brice, (Plenum, NY, 1976) p. 247.
82. S. M. Myers, "Ion Implantation Metallurgy," eds., C. M. Preece and J. K. Hirvonen (Am. Inst. of Mining, Metallurgical, and Petroleum Engineers, NY, 1980) p. 21.
83. S. T. Picraux, presented at Conference on Ion Beam Modification of Materials, Albany, NY, 14-18 July, 1980, to be published in *Nucl. Instrum. Methods*.
84. J. W. Mayer, B. Y. Tsaur, S. S. Lau, and L. S. Hung, presented at Conference on Ion Beam Modification of Materials, Albany, NY, 14-18 July, 1980, to be published in *Nucl. Instrum. Methods*.
85. Z. L. Liao and J. W. Mayer, "Ion Bombardment Effects on Material Composition" in *Ion Implantation*, ed., J. K. Hirvonen (Academic, NY, 1980).
86. S. M. Myers, *Nucl. Instrum. Methods* **168** (1980) 265.
87. E. N. Kaufmann, presented at Conference on Ion Beam Modification of Materials, Albany, NY, 14-18 July, 1980, to be published in *Nucl. Instrum. Methods*.
88. S. M. Myers, *Radiat. Eff.* **49** (1980) 95.

89. S. M. Myers, "Implantation Metallurgy" in Ion Implantation, ed., J. K. Hirvonen (Academic, NY, 1980).
90. G. W. Reynolds, A. R. Knudson, and C. R. Gossett, presented at Conference on Ion Beam Modification of Materials, Albany, NY, 14-18 July, 1980, to be published in Nucl. Instrum. Methods.
91. C. W. White, Nucl. Instrum. Methods **149** (1978) 497.

Section I.B

SELF-ION SPUTTERING YIELDS FOR COPPER, NICKEL AND ALUMINUM

R. G. Alias and A. R. Knudson¹
J. M. Lambert and P. A.₃ Treado²
G. W. Reynolds

¹Materials Modification and Analysis Branch
Condensed Matter and Radiation Sciences Division
Naval Research Laboratory

²Georgetown University
Washington, D.C.
and
Naval Research Laboratory

³State University of New York at Albany
and
Naval Research Laboratory

This work was supported by the Office of Naval Research.

SELF-ION SPUTTERING YIELDS FOR COPPER, NICKEL, AND ALUMINUM

R. G. Allas and A. R. Knudson
Naval Research Laboratory, Washington, DC 20375 USA

J. M. Lambert and P. A. Treado
Georgetown University and NRL, Washington, DC 20375 USA

G. W. Reynolds
SUNY at Albany and NRL, Washington, DC 20375 USA

ABSTRACT

Self-ion sputtering yields were determined for copper, nickel, and aluminum at 60 keV, 90 keV, and 120 keV. The sputtering yields were determined by Rutherford backscattering measurements of the energy shifts of a deeply implanted xenon marker layer and by measuring the distribution and amount of sputtered material on a catcher foil using backscattering and particle induced x-ray emission. The effect of dose rate and net fluence on the yield were examined. Optical monitoring of the light intensity emitted by the sputtered particle confirmed no measurable change in the yield using self ion bombardment. The self-ion sputtering yields measured in this study are less than predicted by theory but are self consistent within experimental error independent of measurement technique. Additional measurement of self-ion sputtering yields in this energy range are needed for applications in materials modification.

1. INTRODUCTION

Among the most important parameters to be considered when modifying materials by ion implantation are the relevant sputtering yields. These yields control the surface behavior of the target during ion implantation and limit the maximum atomic fraction attainable at the surface through ion implantation (1). In an earlier investigation by Reynolds et.al. (2), it was noted that the self-ion sputtering yields for copper and chromium were significantly less than those previously published (3) and were significantly different from the values predicted by theory (4).

In this paper we describe the apparatus, experiments, and techniques used to measure the self-ion sputtering yields for aluminum, copper and nickel at 60 keV, 90 keV, and 120 keV and we report our findings and compare our results with the theoretical values calculated from the Sigmund theory (4).

The energy range selected for these measurements coincides with that range which we are using for studies in the modification of metallic surfaces by ion implantation. Our goal was to measure these self ion sputtering yields by several techniques to ascertain the reliability of the results and to provide yield values for more precise modeling of the surface behavior of metals during modification by ion implantation. During this study, the effects of dose rate and vacuum conditions on the self ion sputtering yield were examined.

2. EXPERIMENT

Various phases of the experiments were carried out at three laboratories: the Materials Modification and Analysis Branch of the Naval Research Laboratory (NRL); Physics Department, Georgetown University (GU); and the Institute for Particle-Solid Interactions at State University of New York at Albany (IPSI); using six accelerators. Table 1 shows the accelerators, location, and application during this investigation.

a. Sputtering Apparatus

The samples were 1 mm slices cut from high purity polycrystalline rods ranging from 12 mm to 20 mm diameter which were mechanically polished to a mirror finish at NRL and IPSI. The samples were implanted with xenon markers at either 1 MV or 1.5 MV to a fluence of 1×10^{16} ions/cm².

Figures 1 and 2 illustrate the two target assemblies used in these experiments at NRL and IPSI. The assembly in figure 1 was part of the ultra high vacuum (UHV) system attached to the low energy implanter (LEIM) at NRL. The base pressure of the UHV system was 2×10^{-9} torr and the dose rates were less than 2 microamperes scanned (approx. 10 microamperes peak). The target was placed at normal incidence to the ion beam with the catcher foil forming a portion of a 3 cm radius circle whose center was the center of the sputtering area on the target. The angular region covered by the catcher foil extended from 6 to 90 degrees with respect to the incident beam. The beam was raster scanned across a 3 mm x 5 mm aperture with electron suppression. The total charge was collected through a common connection of the catcher foil holder, the guard shield, and the target assembly. The assembly in figure 2 was connected to either the Extrion implanter at NRL or the Danphysik implanter at IPSI. The chamber, aperture, and cold can/target suppressor have been described (2). During some of the sputtering experiments the optical emission from the sputtered neutral atoms was monitored to confirm that the sputtering yield was not changing with increased fluence during implantation.

b. Analytic Apparatus

RBS measurements of the shift of the xenon marker position resulting from sputtering were obtained at NRL and IPSI. Data for each target examined were taken from both the sputtered region and the unsputtered regions. The data were then fitted with a peak position program and the marker shift was determined in channels. Repeated measurements of the sample gave agreement of the shift within 0.5 channels with the shift ranging from 3 to 5 channels depending on the sputtering beam fluence. The marker position after sputtering was determined by combining the measurement of the high energy edges associated with the various elements and the kinematic factors for scattering for these elements. The stopping powers for ⁴He as given by Ziegler (5) were used to convert the energy shift of the xenon peak to the number of atoms per cm² that had been removed from or added to the target.

The density of sputtered atoms adhering to the aluminum catcher foils was measured by both RBS and proton induced x-ray emission (PIXE). The PIXE measurements were performed using 2-MV and 1-MV proton beams.

Table 1 — Accelerators

<u>Machine</u>	<u>Location</u>	<u>Application</u>
1 MeV Van de Graaff	Georgetown University	PIXE analysis
4 MeV Dynamitron	IPSI, SUNY Albany	Xe implants, RBS
6 MeV Van de Graaff	Naval Research Lab	Xe implants, PIXE, RBS
150 keV Danfysik ion implanter	IPSI, SUNY Albany	low dose-rate 10^{-7} torr, 3 μ a
150 keV low-energy implanter (LEIM)	Naval Research Lab	UHV system 2×10^{-9} torr, 2 μ a
200 keV Extrion ion implanter	Naval Research Lab	high dose-rate 10^{-6} torr, 10 μ a

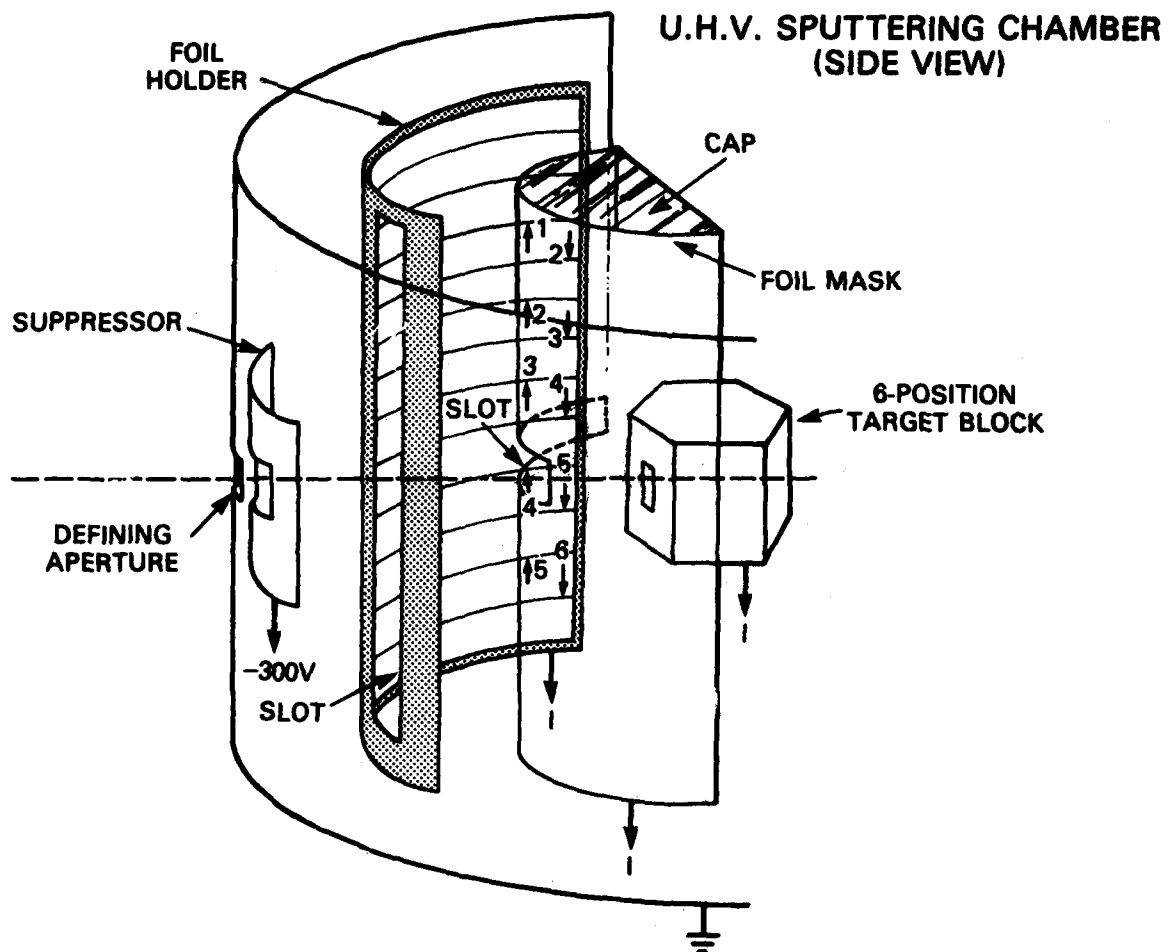


Fig. 1 — Target and catcher foil assembly for UHV system

HIGH-CURRENT SPUTTERING CHAMBER

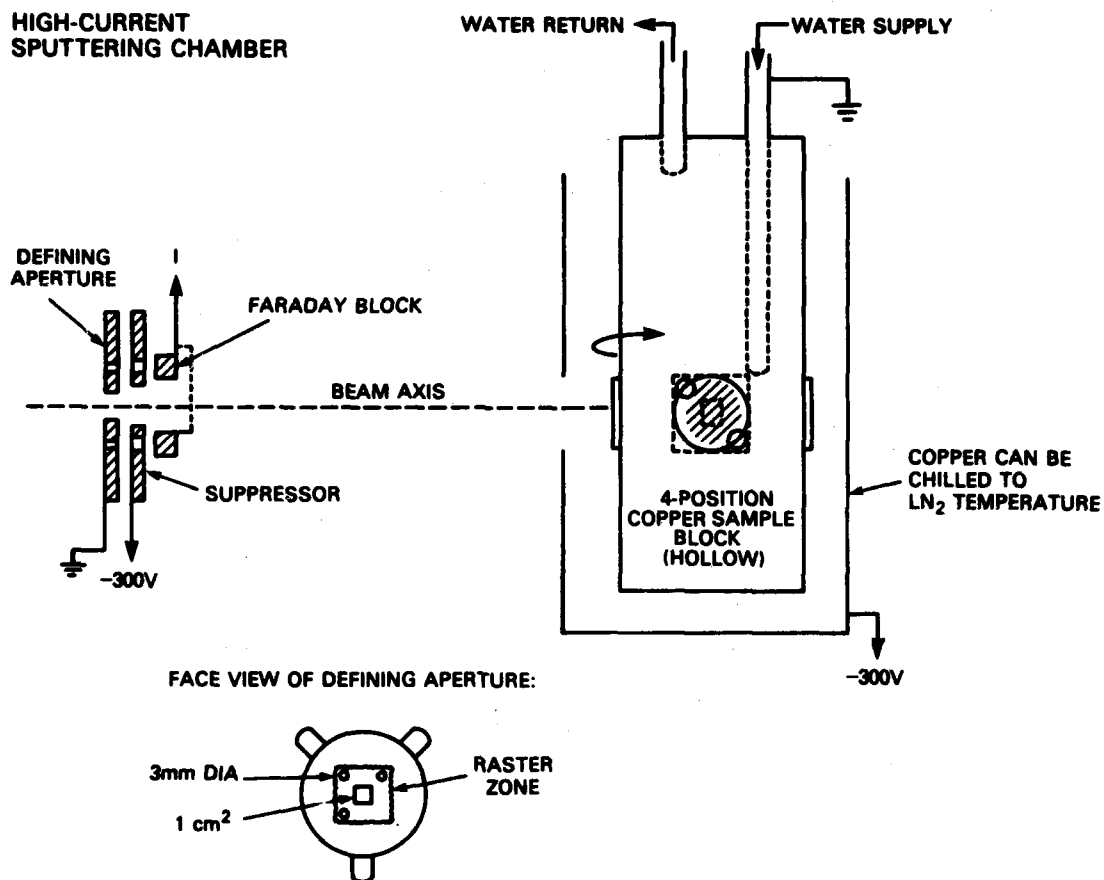


Fig. 2 — Target assembly for high current implanter studies

3. RESULTS

Table 2 summarizes the sputtering yields as determined in this investigation, and figures 3 and 4 depict the angular distribution of sputtered particles collected on the catcher foils. Figures 3a and b illustrate the distribution at the three selected energies for copper and nickel as measured by the PIXE technique. There was no significant difference in the normalized distributions for the foils analyzed at GU versus the foils analyzed at NRL, although the absolute counts per microcoulomb were different due to the differences in experimental parameters. Figures 4a and b show the results for a set of three foils at three different target fluences. In table 2 the values in the theoretical column were calculated using the Sigmund theory (4). The nuclear stopping power for each specific beam energy was obtained from computer calculation based on LSS theory and the sublimation energies for the elements were used for the surface binding energy.

Within experimental error, there was noted no difference in the yield as a function of dose rate, fluence, or vacuum condition.

4. ANALYSIS

The sputtering yield for a target material is experimentally determined by

$$Y = \frac{N_s}{N_i} \quad (1)$$

where N_s is the number of atoms removed from the surface, and N_i is the number of ions incident on the target.

The number of atoms removed from the surface by sputtering may be determined by measuring the change in the number of atoms between the xenon marker and the surface, or by the measuring the number of atoms emitted from the surface. In the first technique the major sources of possible error are in determining small changes in the position of a rather broad Xe peak and the uncertainties in the stopping power used to convert the energy shift to the change in the number of atoms per cm^2 present between the marker and the surface. In the second method the angular distribution of sputtered particles that has been determined from analysis of the catcher foil is used to determine the sputtering yield, by integrating the measured angular distribution over a hemisphere. Azimuthal symmetry is assumed in this integration, which should be a reasonable assumption for normal incidence of the beam on a polycrystalline target. It has been assumed that the sticking coefficient for the sputtered atoms on the catcher foil is unity. Thus the number of atoms sputtered from the target is given by:

$$N_s = 2\pi R^2 \int_0^{\pi/2} N_a(\theta) \sin\theta d\theta \quad (2)$$

where N_a is the number per unit area on the foil, R is the radius of curvature of the foil and θ is the angle with respect to the incident beam.

Table 2 — Self-sputtering results

Element	Beam Energy	Sputter Yield		Measurement Techniques and Sputtering Conditions
		Theory	Experiment	
Copper	60 KeV	8.51	4.2 \pm 0.8	RBS-Xe marker (IPSI), lo-I
			4.4 \pm 0.8	RBS-Xe marker (NRL), hi-I
			4.1 \pm 0.8	PIXE-catcher foil (GU), UHV
	90 KeV	8.44	4.3 \pm 0.9	RBS-Xe marker (NRL), hi-I
			4.0 \pm 0.8	RBS-Xe marker (NRL), UHV
			4.8 \pm 0.9	RBS/NUM-catcher foil (NRL), UHV
			4.0 \pm 0.8	RBS/COS-catcher foil (NRL), UHV
			4.2 \pm 0.8	PIXE/NUM-catcher foil (GU), UHV
	120 KeV	8.25	4.4 \pm 0.8	RBS-Xe marker (NRL), hi-I
			4.2 \pm 0.8	RBS-Xe marker (IPSI), lo-I
			4.4 \pm 0.8	PIXE-catcher foil (GU), UHV
Nickel	60 KeV	6.54	3.6 \pm 0.7	RBS-Xe marker (NRL), hi-I
	90 KeV	6.45	3.9 \pm 0.8	RBS-Xe marker (NRL), hi-I
			3.6 \pm 0.7	RBS-Xe marker (IPSI), lo-I
			2.8 \pm 0.6	PIXE-catcher foil (GU), UHV
	120 KeV	6.28	3.9 \pm 0.8	RBS-Xe marker (NRL), hi-I
			3.4 \pm 0.7	RBS-Xe marker (IPSI), lo-I
			3.2 \pm 0.7	PIXE-catcher foil (GU), UHV
			2.6 \pm 0.6	RBS-catcher foil (NRL), UHV
Aluminum	60 KeV	1.78	0.8 \pm 0.5	RBS-Xe marker (IPSI), lo-I
			0.7 \pm 0.2	RBS-Xe marker (NRL), hi-I
	90 KeV	1.54	0.9 \pm 0.5	RBS-Xe marker (IPSI), lo-I
			0.5 \pm 0.2	RBS-Xe marker (NRL), hi-I
	120 KeV	1.34	1.2 \pm 0.5	RBS-Xe marker (IPSI), lo-I
			0.4 \pm 0.1	RBS-Xe marker (NRL), hi-I

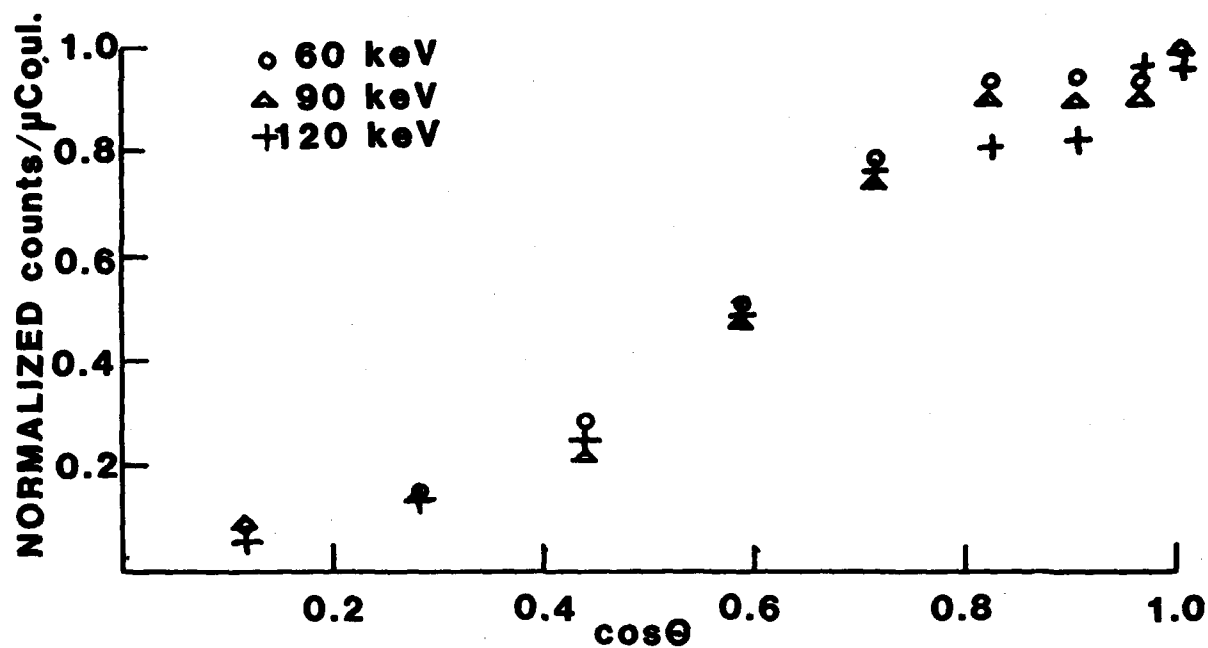


Fig. 3a - Angular distribution of sputtered product, copper beam incident on copper (PIXE)

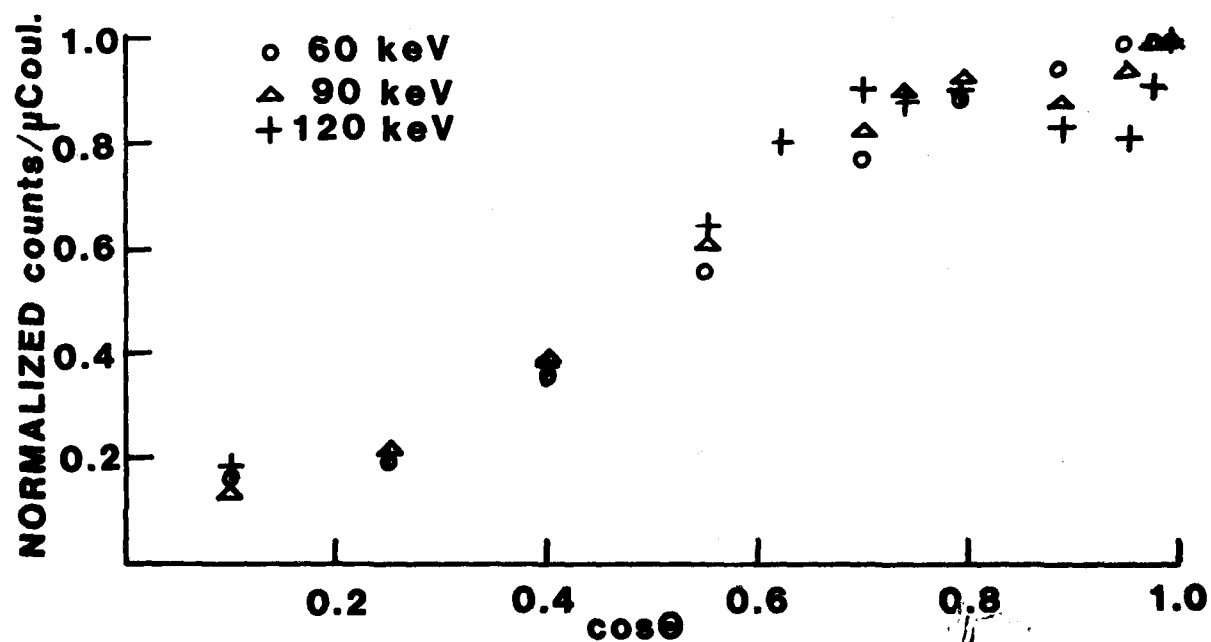


Fig. 3b - Angular distribution of sputtered product nickel beam incident on nickel (PIXE)

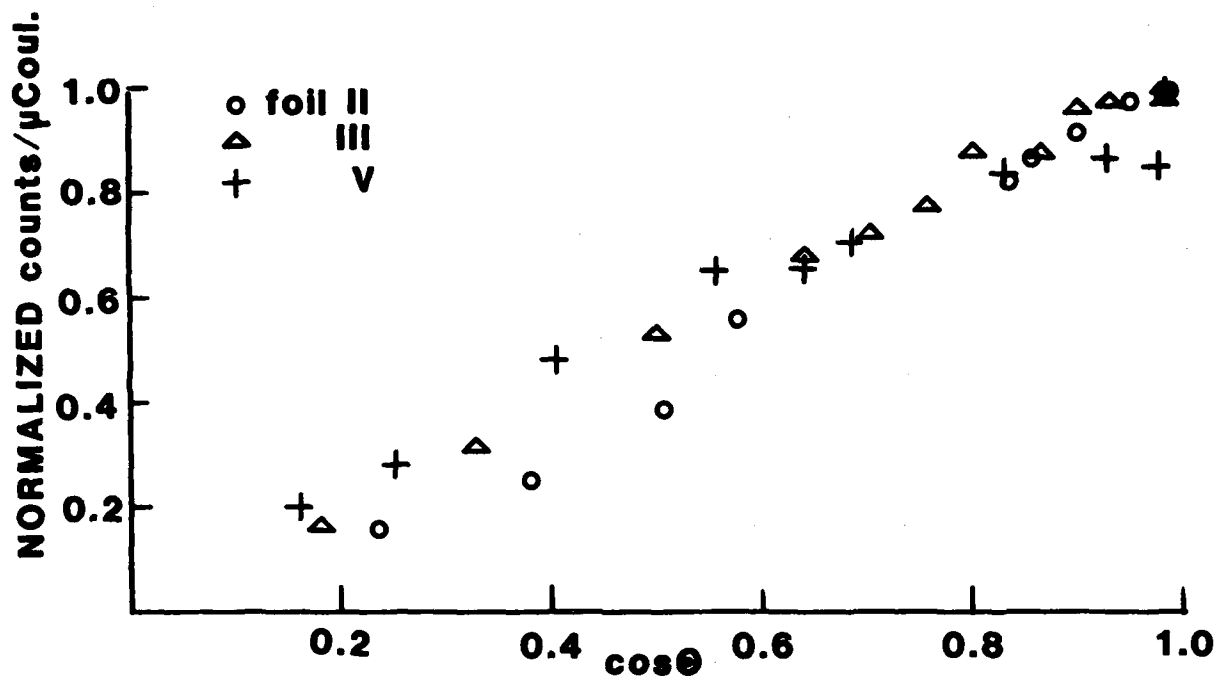


Fig. 4a — Angular distribution of copper sputtered by 90 keV copper ion beam measured by RBS. Foil V, target fluence 1.3×10^{17} Cu/cm². Foil III, 5.2×10^{17} Cu/cm². Foil II, 12×10^{17} Cu/cm².

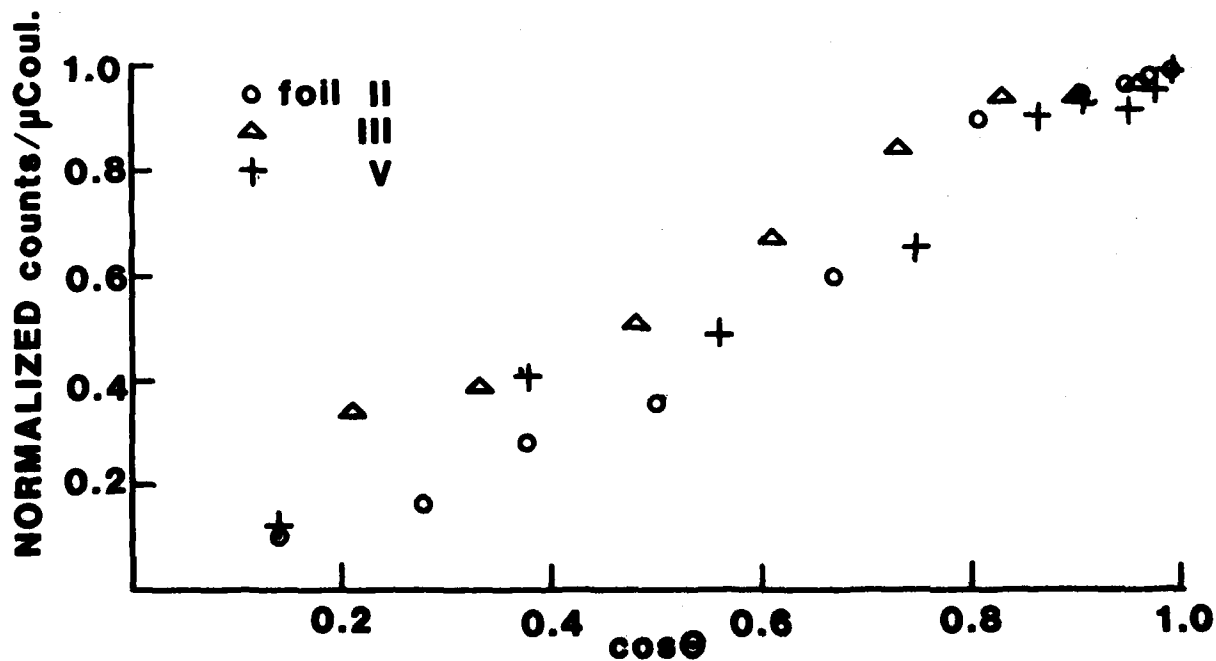


Fig. 4b — Angular distribution of copper sputtered by 90 keV copper ion beam measured by PIXE. Fluences as in figure 4a.

5. DISCUSSION

In examining the results, particularly those for 90 keV copper, one notes the internal consistency of the findings. The error bar placed on the yield as determined by the particular technique is conservative and represents a worst case condition for the particular technique. When comparison is made between these values and the appropriate value as predicted from the theory or the expected value extrapolated from literature (3), there is a discrepancy of a factor of two. Attempts to reconcile the experimental results as presented with the theory as suggested by Sigmund (4) have not been able to account for the discrepancy. A careful examination of the potential errors inherent in the experiments can offer no explanation for this discrepancy. Current experiments with the modification of metallic surfaces appear to follow predictions based on these measurements reinforcing our confidence in these self-ion sputtering yields. Although we have reported a value less than one for the self-ion sputtering yield for aluminum, we are not confident that the values reported for aluminum represent values usable for predictive calculations in the modification of metallic surfaces since there was observed a cerium contamination of the surface resulting from the sample preparation process. The values reported are larger than those reported in the literature (6,7) which were measured at slightly lower energy. The experiments for aluminum are scheduled for repetition following a modification of the sample preparation technique to prevent the contamination of the surface.

6. SUMMARY

In summary the following should be emphasized:

(1) The measurement of self-ion sputtering yields by different techniques gives the same results within experimental errors. The sputtering yields measured here are significantly lower than those interpolated from the literature (3). We measured the self-ion sputtering yields for copper, nickel, and aluminum by one or more techniques and found agreement within experimental error for the yields at 60 keV, 90 keV, and 120 keV using the energy shift of a deeply imbedded marker, and the determining of the amount of copper or nickel sputtered from the target onto catcher foils analyzed by PIXE and RBS.

(2) The optical monitoring of the light emitted by the sputtered neutral atoms from the target surface indicated no changes in the self-ion sputtering yield during self-ion bombardment and the measurements determined from the catcher foils as a function of fluence indicate no change with fluence within experimental errors.

We would like to acknowledge the assistance of P. Malmberg (NRL) and F. Vozzo (IPSI) for their assistance with the operation of the high energy accelerators.

REFERENCES

1. J. K. Hirvonen, ed., *Treatise on Materials Science and Technology*, Vol. 18; Ion Implantation Sputtering and their Applications, Academic Press (1976).
2. G. W. Reynolds, A. R. Knudson, and C. R. Gossett, "Sputtering Observations During Binary Alloy Production by Ion Implantation," *Nucl. Instrum. Methods* 181/183 (1981) 179.
3. H. H. Andersen and H. L. Bay, "Sputtering Yield Measurements," chapter 4 of: R. Behrisch, ed., *Sputtering by Ion Bombardment*, Springer (1980).
4. P. Sigmund, "Sputtering by Ion Bombardment: Theoretical Concepts," chapter 2 of: R. Behrisch, ed., *Sputtering by Ion Bombardment*, Springer (1980).
5. J. F. Ziegler, ed., *Helium: Stopping Powers and Ranges in All Elemental Matter*, Pergamon Press (1977).
6. O. Almen and G. Bruce, "Sputtering Experiments in the High Energy Region," *Nucl. Instrum. Methods* 11 (1961) 279.
7. H. Krautle, "Study of the Sputtering Process with Rutherford Backscattering," *Nucl. Instrum. Methods* 137 (1976) 553.

Section I.C

LASER IRRADIATION OF Ni:
DEFECT STRUCTURES AND SURFACE ALLOYS

L. Buene, D. C. Jacobson, S. Nakahara and J. M. Poate¹
C. W. Draper² and J. K. Hirvonen³

¹Bell Laboratories
Murray Hill, NJ 07974

²Western Electric Engineering Research Center
Princeton, NJ 08540

³Materials Modification and Analysis Branch
Condensed Matter and Radiation Sciences Division
Naval Research Laboratory

This work was supported by the Office of Naval Research,³
and Bell Laboratories.^{1,2}

LASER IRRADIATION OF NICKEL: DEFECT STRUCTURES AND SURFACE ALLOYING

L. BUENE, D.C. JACOBSON, S. NAKAHARA AND J.M. POATE⁺; C.W. DRAPER⁺⁺;
J.K. HIRVONEN⁺⁺⁺

⁺Bell Laboratories, Murray Hill, New Jersey 07974; ⁺⁺Western Electric Engineering Research Center, Princeton, New Jersey 08540; ⁺⁺⁺Naval Research Laboratory, Washington, DC 20375

ABSTRACT

Surface layers of Ni crystals have been melted with Q-switched Nd-YAG laser radiation. The epitaxially regrown surface layers show significant differences between $\langle 100 \rangle$ and $\langle 111 \rangle$ crystals cut from the same boule. The $\langle 100 \rangle$ crystals exhibit a dislocation cell structure with a dislocation density of $10^{11} - 10^{12} \text{ cm}^{-2}$. The $\langle 111 \rangle$ crystals contain a laterally uniform dislocation network resulting in a much higher dislocation density for the $\langle 111 \rangle$ surface. The elements Ag, Au, Pd, Sn and Ta have been implanted into Ni single crystals at surface concentrations of up to 20 at %. All the as-implanted systems demonstrate solid solubility. We have used these implanted systems to study the alloys formed by laser melting of Ni. In all systems, with the exception of Ag, 100% of the atoms are trapped on lattice sites.

INTRODUCTION

There is now an increasing interest in the modification of metal surfaces by means of ion, laser or electron beam irradiation. (1-3) The potential for improvements in surface behavior without affecting bulk properties and with a minimum consumption of noble or strategic elements has promoted much activity in this area. Also, the formation of new and metastable alloys by making use of the ultrarapid quenching inherent in these techniques is of great interest to material scientists.

We have previously (4,6) demonstrated that laser pulse melting in combination with ion implantation or vapour deposition can be used to make metastable alloys of high concentrations in the surface and near surface region. We have shown that the rapid solidification results in an epitaxially regrown surface layer where the alloying elements can be trapped on lattice sites. It has also been found (5) that the regrown layers contain a high density of extended defects (e.g., dislocations).

In the present paper we will examine in more detail the nature and structure of the defects introduced in Ni by laser irradiation. Furthermore, we will investigate Ni surface alloying by laser irradiation in combination with ion implantation. The elements Ag, Au, Pd, Sn and Ta have been implanted into Ni single crystals at concentrations of up to about 20 at %. These elements in equilibrium with Ni constitute (7) complete solid solution (Pd), miscibility gap in solid (Au), miscibility gap in liquid (Ag) and intermetallic compounds (Sn and Ta).

EXPERIMENTAL

The Ni single crystals were cut, lapped and electropolished to a mirror surface finish. The implantation was performed with the crystal mounted flat on the sample holder which was oriented approximately perpendicular to the ion beam. The implantation energy was 150 keV and the nominal fluences in the

10^{17} cm^{-2} range. The laser irradiation was performed with a Q-switched Nd:YAG laser which employed raster scanning for area coverage. Details of the scanning system appear elsewhere (8). The Q-switched pulse was of 130 nsec duration and optical spot sizes were about $35 \mu\text{m}$. The distributions of the implanted elements were measured by Rutherford backscattering before and after laser irradiation using MeV $^4\text{He}^+$ ions and an annular solid state detector positioned at a mean angle of 175° . The quality of the epitaxially regrown layers was determined by Rutherford backscattering and channeling as well as by transmission electron microscopy. Also, Normarski interference contrast microscopy was used to characterize the metal surfaces.

RESULTS

Figure 1 shows channeling and backscattering spectra from $\langle 100 \rangle$ and $\langle 111 \rangle$ Ni single crystals cut from the same boule and laser irradiated at power densities of 100 MW cm^{-2} . Normarski interference contrast microscopy reveals that the surfaces have been melted several times by overlapping melt puddles. It is evident from the high dechanneling rate in the near surface region that the laser irradiation introduces a high density of defects. Furthermore, the spectra clearly show that the epitaxial regrowth of the $\langle 111 \rangle$ crystal occurs with a much higher defect density than for the $\langle 100 \rangle$ crystal.

The difference in defect density between the $\langle 100 \rangle$ and $\langle 111 \rangle$ crystals is also observed by transmission electron microscopy which in addition reveals a difference in defect structure in the two cases. Figure 2 shows TEM micrographs of the laser irradiated $\langle 100 \rangle$ Ni crystal from Figure 1. The defects are predominantly in the form of dislocation cell structures, with two typical cell sizes and an estimated density of $10^{11} - 10^{12} \text{ cm}^{-2}$. The TEM observation of the $\langle 111 \rangle$ crystal shows a laterally uniform dislocation network with a much higher dislocation density than the $\langle 100 \rangle$ crystal.

Figures 3 and 4 show results of channeling and backscattering measurements on Ni $\langle 110 \rangle$ crystals implanted with Pd (Figs. 3 and 4) and Au (Fig. 4) before and after laser irradiation at 100 MW cm^{-2} . The peak concentrations are 24 and 16 % (Pd) and 9 and 4 at % (Au) before and after irradiation, respectively. The distribution of the impurities after irradiation is consistent with typical liquid phase diffusivities in metals. The Ni surface is highly damaged after implantation. However, the amount of channeling observed indicates that substitutional solid solutions are formed. The liquid phase epitaxial regrowth results in removal of the damage associated with implantation with the implanted species being incorporated on lattice sites (Fig. 4). However, the higher dechanneling rate in the surface region indicates the same high density of dislocations as found in virgin Ni crystals after laser pulse melting.

Rutherford backscattering and channeling measurements on $10^{17} \text{ Ag cm}^{-2}$ implants show that the peak concentration of Ag is 12 and 7 at % respectively, before and after laser irradiation. Ag is found to be highly substitutional in the as-implanted alloy, similar to Pd and Au. However, when the implanted layer is rapidly melted and resolidified by the Q-switched radiation, Ag is not trapped on lattice sites to the same extent as high dose Pd or Au. Close to the surface 50% of the Ag atoms reside on lattice sites, as measured by the channeling technique. The spectra also show that the distribution of Ag atoms is peaked toward the surface after melting and resolidification. Furthermore, it is observed that epitaxial regrowth occurs with greater lattice damage in the Ag case. The transmission electron diffraction pattern of this Ag implanted Ni single crystal is shown in Figure 5. The elongated Ni spots indicate a distorted Ni lattice. The rings are identified to originate from polycrystalline Ag, predominantly in the form of Ag dendrites on the surface. Figure 6 is a TEM bright field micrograph showing the Ag dendrites and high density of dislocations in the regrown layer.

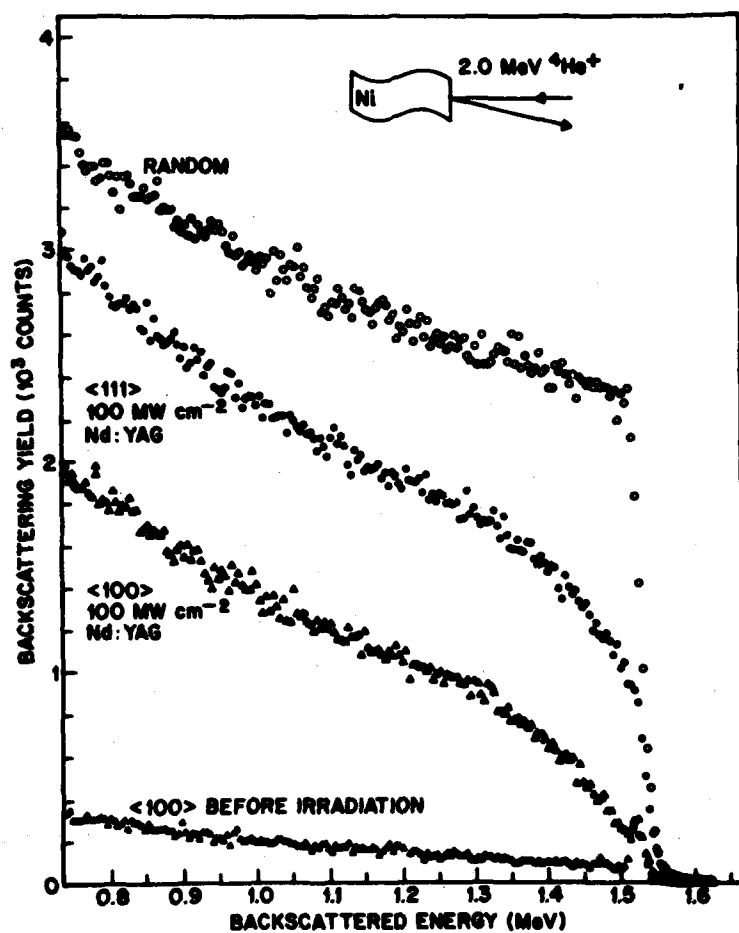


Fig. 1. RBS and channeling spectra for Ni<100> and Ni<111> crystal faces irradiated at 100 MW cm^{-2} with a Q-switched Nd-YAG laser. A higher density of defects is indicated for the <111> orientation.

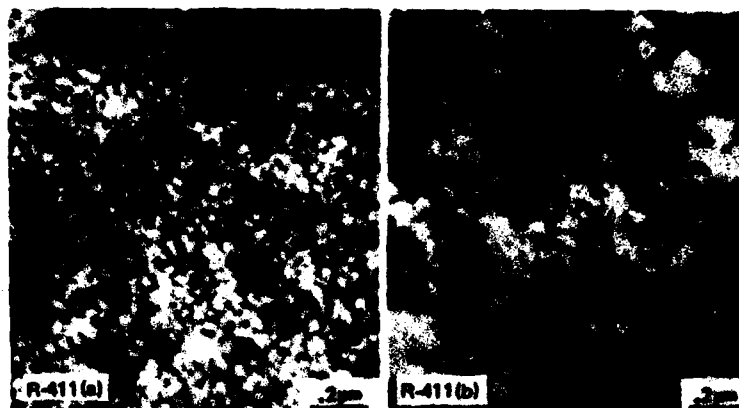


Fig. 2. TEM micrographs of laser irradiated $\langle 100 \rangle$ Ni crystal. Dislocation free cell structures of strikingly different dimensions are seen.

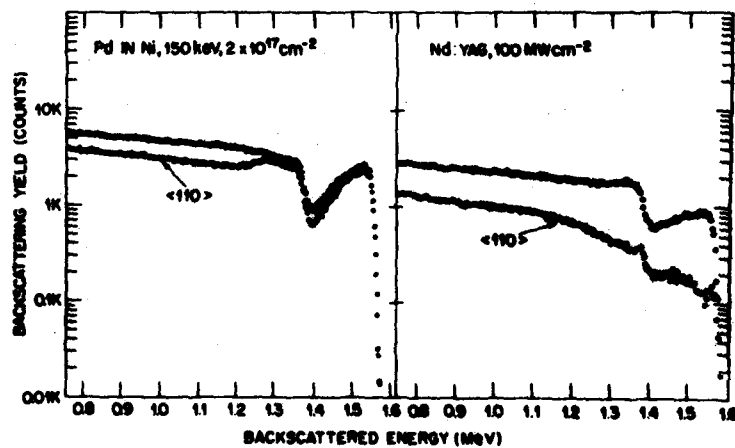


Fig. 3. RBS spectrum of 1.8-MeV He^+ ions from a high-dose-Pd-implanted $\langle 110 \rangle$ Ni single crystal before and after Nd-YAG laser irradiation.

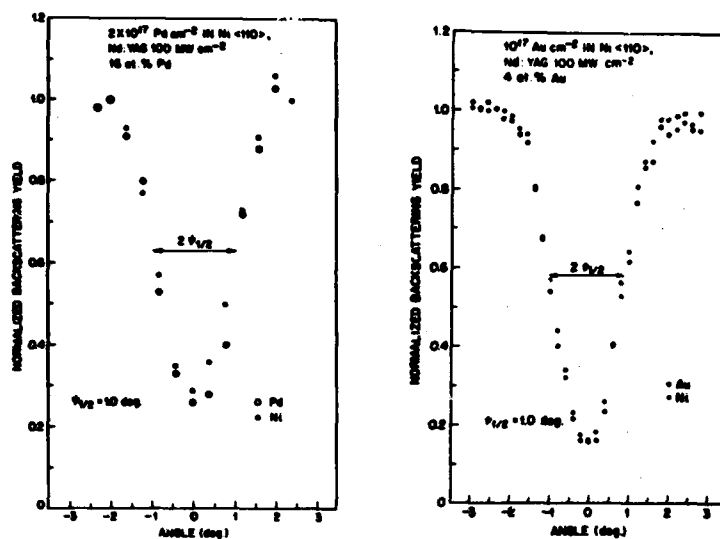


Fig. 4. Normalized channeling $\langle 110 \rangle$ angular scan for 10^{17} cm⁻² Pd and Au implanted in single crystal Ni and irradiated at 100 MW cm⁻² with a Q-switched Nd-YAG laser.



Fig. 5. Selected area electron diffraction pattern of high-dose-Ag-implanted $\langle 110 \rangle$ Ni single crystal following Nd-YAG laser irradiation.



Fig. 6. TEM bright field micrograph of the high-dose-Ag-implanted $\langle 110 \rangle$ Ni single crystal following Nd-YAG laser irradiation. Ag dendrites (white arrows)

The results for the Ni-Sn and Ni-Ta surface alloys formed by high fluence implantations in combinations with pulsed laser irradiation are summarized in Table 1 together with the other surface alloys. In all cases the as-implanted alloys are highly substitutional but with a high degree of lattice damage. The differences in defect densities following epitaxial regrowth are reflected in the different minimum normalized yields. With the exception of high dose Ag the alloys are highly substitutional after irradiation.

Table 1. Results for high dose ($\sim 10^{17} \text{ cm}^{-2}$) implantations in Ni $\langle 110 \rangle$ before (Bef.) and after (Aft.) laser pulse irradiation. The normalized channeling yield is given for both host and implant (host/implant).

Implant	Normalized Channeling Yield		Substitutional Fraction		Peak Concentration (At.%)		Peak Substitutional Concentration (At.%)	
	Bef.	Aft.	Bef.	Aft.	Bef.	Aft.	Bef.	Aft.
Pd	.8/.8	.27/.27	100	100	24	16	24	16
Au	.06/.17	.16/.16	90	100	9	4	8	4
Ag	.40/.52	.40/.70	80	50	12	7	10	3.5
Sn	.77/.77	.33/.33	100	100	19	5	19	5
Ta	.45/.45	.36/.36	100	100	8	4	8	4

DISCUSSION

The very high densities of dislocations observed in laser pulse melted Ni can be explained in terms of plastic deformation during the temperature cycling. The rapid heating and cooling process introduces extremely high thermal gradients. Heat flow calculations (9) indicate thermal gradients of up to 10^7 K/cm at the surface. These high gradients cause thermomechanical stresses which result in plastic deformation and movement and multiplication of dislocations. However, this mechanism does not require surface melting to produce dislocations. And indeed, laser irradiation with power densities lower than melting threshold is found (10,11) to produce dislocations of a lower density.

The reason for the orientation dependence of dislocation density and structure is not fully understood. However, it seems to lie in the fact that the $\langle 111 \rangle$ planes are the slip planes in the fcc crystal structure. Laser pulse melting of Mo $\langle 111 \rangle$ and $\langle 110 \rangle$ crystals cut from the same boule is also found (12) to give defect densities dependent on crystal orientation. Mo has a bcc crystal structure where $\langle 110 \rangle$ planes are main slip planes. Channeling and backscattering analysis show that the $\langle 110 \rangle$ crystal regrows epitaxially with a much higher defect density than the $\langle 111 \rangle$ crystal, consistent with the Ni results.

Even if the epitaxial regrowth after laser pulse melting occurs with a high density of extended defects, the crystallinity of the implanted Ni surfaces can be markedly improved with respect to point defects as evidenced by significant reduction in the channeling yield. It should be pointed out that the implantation of soluble elements (Pd) in Ni results in a highly damaged lattice. This is in contrast to high dose implantation in Cu (13) and is probably due to the greater susceptibility to damage of the Ni lattice, which possesses higher directionality in its bonding.

The channeling experiments indicate that all the as-implanted alloys are highly substitutional. The concentrations are higher than the equilibrium solubilities at room temperature (except for Pd which is completely soluble).

Consequently, these surface alloys may be characterized as metastable. After laser pulse melting Au, Pd-Sn and Ta remain on lattice sites whereas a large fraction of the Ag atoms do not remain on lattice sites and in fact precipitate to form polycrystalline Ag. This may be interpreted in terms of the phase diagrams (7). Au, Sn and Ta are soluble with Ni in the melt and have high solid solubilities at elevated temperatures. These elements can therefore be easily retained on lattice sites by the rapid quench. Ag has very limited solid solubility and limited liquid solubility in Ni and is therefore not so easily quenched onto lattice sites. Previously we assumed that no precipitation was occurring in the liquid phase (5) because we did not observe large scale redistribution of the Ag in the backscattering data. However the TEM micrograph of Figure 6 shows precipitated metallic Ag of dimensions that clearly require liquid state diffusion. Precipitation of liquid Ag in liquid Ni is therefore occurring in the concentrated liquid ahead of the resolidification interface.

In conclusion, it is found that when the surface region of Ni single crystals is melted by pulsed laser beam irradiation, good epitaxial regrowth occurs but with a high density of dislocations. The structure and density of these defects are dependent on crystal orientation. Such laser treatment can remove damage caused by high dose ion implantation and at the same time allow the redistributed implanted atoms to form metastable solid solutions.

ACKNOWLEDGEMENT

We wish to thank L.S. Meyer, P.P. Solan and W.L. Flood for their technical assistance. One of us (L.B.) also gratefully acknowledges the financial support of the Royal Norwegian Council for Scientific and Industrial Research.

REFERENCES

1. C.M. Preece and J.K. Hirvonen (eds.), Ion Implantation Metallurgy. (The Metallurgical Society of AIME, Warrendale, Pa., 1980).
2. S.D. Ferris, H.J. Leamy and J.M. Poate (eds.), Laser and Electron Beam Processing of Materials. (Academic Press, New York, 1980).
3. C.W. White and P.S. Peercy (eds.), Laser and Electron Beam Processing of Materials. (Academic Press, New York, 1980).
4. C.W. Draper, C.M. Preece, D.C. Jacobson, L. Buene and J.M. Poate, in Ref. 3 above, pp. 721-727.
5. L. Buene, J.M. Poate, D.C. Jacobson, C.W. Draper and J.K. Hirvonen, Appl. Phys. Lett. 37, 385 (1980).
6. C.W. Draper, L.S. Meyer, L. Buene, D.C. Jacobson and J.M. Poate, Appl. Surf. Sci., in press.
7. M. Hansen, Constitution of Binary Alloys, 2nd Ed. (McGraw-Hill, New York, 1958).
8. G.K. Celler, J.M. Poate and L.C. Kimerling, Appl. Phys. Lett. 32, 464 (1978).
9. A.L. Simons, Private Communication.

10. L. Buene, S. Nakahara, J.M. Poate, D.C. Jacobson, C.W. Draper and A.G. Cullis, submitted to Appl. Phys. Lett.
11. C.W. Draper, L. Buene, J.M. Poate, D.C. Jacobson and A.G. Cullis, submitted to Appl. Opt.
12. E.N. Kaufmann, L. Buene and C.W. Draper, this conference.
13. J.M. Poate, J.A. Borders, A.G. Cullis and J.K. Hirvonen, Appl. Phys. Lett. 30, 365 (1977).

Section I.D

**MIGRATION CURRENT AND IMPLANT DENSITIES IN
STEADY-STATE ION IMPLANTATION**

I. Manning

**Materials Modification and Analysis Branch
Condensed Matter and Radiation Sciences Division
Naval Research Laboratory**

This work was supported by the Office of Naval Research.

Migration Currents and Implant Densities in Steady-State Ion Implantation

Irwin Manning
Materials Modification and Analysis Branch
Condensed Matter and Radiation Sciences Division

ABSTRACT

The case first considered is that of A atoms bombarding a target of B and C atoms ($A \rightarrow BC$). Allowance is made for the possibility of atomic migration currents within the target of A, B, and C atoms, and expressions are obtained for these currents. The only major assumptions made in the analysis are that atoms are conserved and that the system is in steady state. Whenever preferential sputtering is large enough to substantially alter the surface concentrations of B and C atoms, there must also be substantial migration currents of these atoms. Migration currents may well be significant in other cases as well. The results are illustrated by considering Ar bombarding SiPt, where the Si and Pt migration currents turn out to be around one-half the bombarding flux. The analysis is also applied to rederiving expressions for the surface density of implanted ions, the energy deposited into target damage, and the density of PKA's at the surface. The analysis is easily extended to apply to implantation of a single-component target ($A \rightarrow B$) and to self-ion implantation of a two-component target ($A \rightarrow AB$).

I. INTRODUCTION

When a binary target is subjected to ion bombardment, its stoichiometric composition near the surface is often altered because the different atomic species have different probabilities for being sputtered [1]. In this work, we shall see that this preferential sputtering is accompanied by atomic migration currents in the target, which can become substantial. We restrict ourselves to examining only the steady state. The analysis is quite general: the only assumptions made are conservation of atoms, and that the target is in steady state. For the sake of completeness, the analysis is also applied in section IID to reobtaining expressions for implant density, damage energy density, and PKA's at the surface. The relation of atomic surface density to sputtering and migration fluxes is discussed in section IID2.

The analysis is developed in section II for implantation into a binary target, where atoms of species A bombard a target composed of B and C atoms ($A \rightarrow BC$). The modification of these results for other situations are discussed in section III, where implantation into a unary target ($A \rightarrow B$) and self-ion implantation into a binary target ($A \rightarrow AB$) are treated.

II. IMPLANTATION INTO A BINARY TARGET

A. Coordinate Frames

Referring to figure 1, consider a binary target composed of B and C atoms bombarded by an incident flux J_i of A atoms. Atoms of all these species will be sputtered off the surface, resulting in sputtering fluxes J_A , J_B , J_C , and in erosion of the surface. In the laboratory frame X_L , let Σ_0 denote the coordinate of the receding surface. Define the velocity U by the equation

$$d\Sigma_0 = U J_i dt = U d\tau \quad (1)$$

where τ is fluence. In the cgs system the units are

$$d\Sigma [\text{cm}] = U [\text{cm}^3/\text{atom}] \cdot J_i [\text{atoms}/\text{cm}^2\text{sec}] \cdot d\tau [\text{sec}].$$

Also define the target frame x_T as the coordinate system with origin fixed to the target surface.

Inside the target, the penetrating ion beam has flux $J_i'(x)$. We also allow for the possibility of atomic migration currents $J_A^M(x)$, $J_B^M(x)$, and $J_C^M(x)$ whose positive direction is defined in figure 1.

Throughout this work, we restrict ourselves to steady state, defined as follows: All macroscopic quantities, as viewed in the target frame, are constant in time.

The atomic currents $J_A^M(x)$, $J_B^M(x)$, $J_C^M(x)$ have the significance of migration currents only in the laboratory frame, while the steady state condition has significance only in the target frame. Thus, both coordinate frames must be considered. There is negligible difference in the penetrating ion beam $J_i(x)$ as seen in the two frames because, in transforming from one frame to the other, the change in this quantity is proportional to $U J_i / v_A$, where v_A is the velocity of the atoms of the penetrating beam. However, there is a significant change in the migration currents as seen in the two frames: One has

$$J_{BT}^M(x) = J_{BL}^M(x) + N_B(x) U J_i \quad (\text{ditto A,C}). \quad (2)$$

where $J_{BT}^M(x)$ and $J_{BL}^M(x)$ are, respectively, the atomic migration currents of B atoms as seen in the target and laboratory frames, and $N_B(x)$ is the density of target B atoms (atoms/cm^3). Let Σ_x be a surface perpendicular to the x -axis and fixed to the coordinate x in the target frame. The second term in the above equation is the number of target B atoms per unit area which Σ_x traverses in unit time interval. In the above equation, "ditto A,C" means that analogous equations apply for A and C atoms.

B. Global Steady State

The title of this section refers to the fact that here a finite volume element will be employed; in the remainder of this work the volume elements, while large enough to be considered macroscopic, will be small enough to be considered infinitesimal.

Referring to figure 1, we consider as volume element a cylinder bounded by surfaces Σ_0 and Σ_∞ : Σ_0 is the target surface and Σ_∞ is a parallel plane located at $x = x_\infty$, where x_∞ is deep enough into the target that the target there is undisturbed by ion

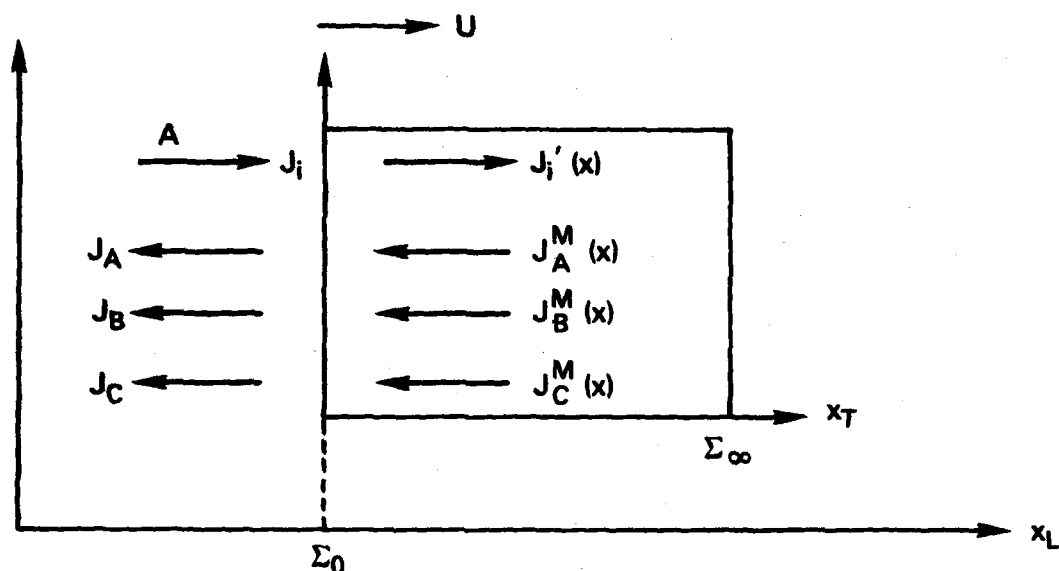


Figure 1. An incident beam J_i of A atoms bombards a target of B and C atoms, resulting in sputtering fluxes J_A , J_B , and J_C . The penetrating beam flux is J_i' and is a function of depth x into the target. J_A^M , J_B^M , and J_C^M are atomic migration currents within the target. Two coordinate frames play a role: laboratory and target frames. The target frame is fixed to the target surface Σ_0 and moves with velocity U relative to the laboratory frame.

implantation processes; that is, x_∞ is large compared to the ion beam range.

In steady state, and in the target frame, the total number of A, B, and C atoms contained in the volume element are constant in time. Correspondingly, the total atomic fluxes into the element must be zero. We have

$$J_A^* = J_i, \quad (3)$$

and

$$\begin{aligned} J_B^* &= J_{BT}^{M*}(\infty) \\ J_C^* &= J_{CT}^{M*}(\infty) \end{aligned} \quad (4)$$

where the asterisk signifies steady-state evaluations, and $J(\infty) \equiv J(x_\infty)$. In the laboratory frame there are no migration currents at x_∞ so, by equation (2), the above equations for J_B and J_C transform to

$$\begin{aligned} J_B^* &= N_B(\infty) U^* J_i \\ J_C^* &= N_C(\infty) U^* J_i. \end{aligned} \quad (5)$$

(Equation (3) reads, of course, the same in both target and laboratory frames.) The sputtering coefficients S_A , S_B , S_C , and S are defined as

$$J_A = S_A J_i \quad (\text{ditto } B, C), \quad (6)$$

and

$$S = S_A + S_B + S_C \quad (7)$$

Equations (3) and (5) give

$$S_A^* = 1 \quad (8)$$

and

$$S_B^* / S_C^* = N_B(x_\infty) / N_C(x_\infty) \quad (9)$$

Also, we have

$$J_B^* + J_C^* = (S^* - 1) J_i = [N_B(x_\infty) + N_C(x_\infty)] U^* J_i.$$

Defining

$$N(\infty) \equiv N_B(\infty) + N_C(\infty), \quad (10)$$

this gives

$$U^* = S^* - 1/N(\infty). \quad (11)$$

These results are all familiar [1]; they are rederived here for convenience and to establish notation.

We restrict ourselves to the case where S is greater than one so that the surface velocity in figure 1 is to the right, in the same direction as the incoming ion beam.

C. Migration currents

In the steady state, and in the target frame, the density of A, B, and C atoms are constant in time:

$$d/dt N_{AT}^*(x) = 0 \quad (\text{ditto B,C}) \quad (12)$$

Hence, by the particle conservation equation [3]

$$\text{div } J_A + d/dt N_A = 0 \quad (\text{ditto B,C})$$

we have

$$\partial / \partial x [J_i'^*(x) - J_{AT}^{M*}(x)] = 0$$

$$\partial / \partial x J_{BT}^{M*}(x) = 0 \quad (\text{ditto C}).$$

In integrating these equations, the constant of integration is determined by the function value at $x = x_\infty$, where

$$J_{AL}^M(\infty) = 0 \quad (\text{ditto B,C}).$$

One then has, using equation (2),

$$J_{AT}^{M*}(x) = J_i'^*(x)$$

$$J_{BT}^{M*}(x) = N_B(x_\infty) U^* J_i$$

$$J_{CT}^{M*}(x) = N_C(x_\infty) U^* J_i$$

These partial currents represent migration currents only in the laboratory frames, where they read

$$J_{AL}^{M*}(x) = J_i'^*(x) - N_A^*(x) U^* J_i \quad (13)$$

$$J_{BL}^{M*}(x) = [N_B(\infty) - N_B^*(x)] U^* J_i \quad (14)$$

$$J_{CL}^{M*}(x) = [N_C(\infty) - N_C^*(x)] U^* J_i$$

Let $f(x)$ be the range distribution for implanted ions. That is, in the target frame, $f(x) dx$ is the probability that an implanted ion will come to rest at target depth x about x . Then

$$\partial / \partial x J_i'(x) = -f(x) J_i$$

so that

$$J_i'(x) = J_i \int_x^\infty f(x) dx, \quad (15)$$

and equation (13) becomes

$$J_{AL}^{M*}(x) = \left[\int_x^\infty f(x) dx - N_A^*(x) U^* \right] J_i \quad (16)$$

The quantity

$$\alpha = \int_0^\infty f(x) dx \quad (17)$$

is the sticking probability, the fraction of ion beam particles which are not backscattered. In evaluating equation (16) at the target surface, we assume that one can take $x = x_0$, where x_0 is large enough as that all the ion-beam backscattering has taken place, yet small enough so that it can be considered macroscopically infinitesimally close to zero. We will denote this value as $x = x_0 = 0^+$.

Defining the quantities

$$C_B(x) = N_B(x)/N(\infty) \quad (18)$$

$$C_C(x) = N_C(x)/N(\infty)$$

$$C(x) = C_B(x) + C_C(x) \quad (19)$$

and using equation (11), one can write the target-atom migration currents (14) as

$$\begin{aligned} J_{BL}^{M*}(x) &= [C_B(\infty) - C_B(x)] (S^* - 1) J_i \\ J_{CL}^{M*}(x) &= [C_C(\infty) - C_C(x)] (S^* - 1) J_i \end{aligned} \quad (20)$$

Note that

$$J_{BL}^{M*}(x) + J_{CL}^{M*}(x) = [1 - c^*(x)] (S^* - 1) J_i, \quad (21)$$

so for $c=1$ the sum becomes zero.

1. Example

To illustrate the target atom migration, equation (20), consider the case A = argon, B = silicon, C = platinum, with $C_B(\infty) = C_C(\infty) = \frac{1}{2}$. For an 80 keV bombardment one has at steady state [2,4]

$$S^* = 4.0$$

$$N_B(0^+)/N_C(0^+) = 1/1.94.$$

Equations (20) become

$$J_{BL}^{M*}(0^+) = [1.5 - 1.02 C^*(0^+)] J_i$$

$$J_{CL}^{M*}(0^+) = [1.5 - 1.98 C^*(0^+)] J_i.$$

To get an idea of the magnitude of these currents, suppose that c is one; one then gets

$$J_{BL}^{M*}(0^+) = .48 J_i$$

$$J_{CL}^{M*}(o+) = .48 J_i,$$

$$\text{for } C^*(o+) = 1.$$

These migration currents are comparable to the sputtering currents (see equations (8) and (9))

$$J_B^* = J_C^* = 1.5 J_i$$

D. Implant densities

1. Implanted atom density

Following Liao and Mayer [2], define the ratios r_{BA} , r_{CA} via the equations

$$J_B/J_A = S_B/S_A = r_{BA} N_B(o+)/N_A(o+) \quad (\text{ditto } r_{CA}). \quad (22)$$

The usefulness of these ratios derives from the fact that there seems to be a tendency for these ratios to remain constant (independent of fluence) during the transient approach to steady state [2]. In terms of these ratios, one gets for the implant density

$$(N_B(o+) + N_C(o+))/(N_A(o+)) = 1/S_A (S_B/r_{BA} + S_C/r_{CA}).$$

Now define the ratio r by the equation

$$(S_B + S_C)/r = S_B/r_{BA} + S_C/r_{CA} \quad (23)$$

By using equation (9) one gets

$$1/r_{BA}^* + 1/r_{CA}^* N_B(\infty)/N_C(\infty) = 1/r^* [1 + N_B(\infty)/N_C(\infty)]. \quad (24)$$

On using equation (23), the above equation for the implant density yields

$$(N_A^*(o+))/(N_B^*(o+) + N_C^*(o+)) = r^*/(S^* - 1), \quad (25)$$

which is a generalization to a binary target of the unary target result of Liao and Mayer [2]. On using equation (11), this result can be restated as

$$N_A^*(o+) = C^*(o+) r^*/U^*. \quad (26)$$

If, and only if, there is no migration current of implanted atoms, equation (16) gives for the density of implanted atoms

$$N_A^*(x) = 1/U^* \int_x^\infty f(x) dx, \text{ all } x, \quad (27)$$

in agreement with Carter et al [5] and Schulz and Witmaack [6]. The expression (27) has been evaluated for Gaussian range distribution by Schulz and Witmaack [6] and by Manning [7]. For implantations where the range is greater than two or three times the range straggling, the gradient $(\partial/\partial x) N_A$ given by equation (27) will be effectively

zero, which makes more serious the possibility that the migration current J_{AL}^{M*} is in fact zero at $X = 0+$. In that case equations (26) and (27) would imply

$$C^* (0+) r^* = 1 \quad (28)$$

(The expression (17) gives $\alpha = 1$ in this case.)

2. Relation of atomic density to sputtering and migration fluxes

In the laboratory frame, the target surface recedes a distance $U J_i dt$ in time interval dt . By conservation of particles, the amount of A atoms sputtered off in that time interval must be

$$J_A dt = N_A (0+) U J_i dt + J_{AL}^M (0+) dt$$

so that

$$J_A = N_A (0+) U J_i + J_{AL}^M (0+) \quad (\text{ditto B,C}). \quad (29)$$

or

$$J_A = J_{AT}^M (0+) \quad (\text{ditto B,C}) \quad (30)$$

Corresponding equations apply to the other atomic constituents (B and C) and to any other conserved quantity, such as energy deposited into target damage.

3. Damage density

Now consider the energy deposited into elastic collisions in the target by the penetrating ion beam. Let $S_D(x)$ be the total of the damage energy per unit volume deposited into the target at the depth x . Following a line of reasoning similar to that of the section IID3 immediately above: In time dt the sputtered target material will carry with it $S_D(0+) U J_i dt$ of deposited energy per unit area. In that same time interval the target will be penetrated by $\alpha J_i dt$ atoms per unit area, each of which will deposit energy ηE_B into the target, where E_B is the bombarding beam energy and the partition factor $\eta(E_B)$ is the fraction of the particle energy E_B deposited into elastic collisions. In steady state, the damage energy deposited into the target must equal that carried off with sputtered target material:

$$\eta E_B \alpha J_i dt = S_D^*(x) U^* J_i dt$$

or

$$S_D^*(0+) = \alpha^* / U^* \eta(E_B) \quad (31)$$

This expression agrees with that of Manning [7] which was obtained by considering profile distortions due to sputtering. For a metal, the density of Frenkel defects created by the ion bombardment is given by [8]

$$\rho_d(x) = \eta S_D(x) / 2E_d, \quad (32)$$

where E_d is the target atom displacement energy (of the order of 25 e.v.), and the constant k can be taken as

$$\kappa = 0.8 . \quad (33)$$

The displacements per atom at the surface—the average number of displacements an atom suffers before it is finally sputtered off—is given by

$$\text{dpa} (o+) = \rho_d(o+)/N(o+),$$

where $N(O+)$ is the total atomic density at the surface. Equations (31), (32), and (11) give

$$\text{dpa} (o+) = \frac{1}{2} \alpha \kappa \eta \frac{E_B}{E_d} \frac{N(\infty)}{N(o+)} \frac{1}{S^* - 1} \quad (34)$$

The above analysis can be repeated almost unchanged to obtain the steady-state density of energy deposited into inelastic processes.

III. OTHER IMPLANTATION CASES

A. Implantation into a unary target

For the case of A atoms bombarding a target consisting entirely of B atoms, the above results apply with

$$N_C = S_C = J_C = J_C^M = 0 \quad (35)$$

$$C(x) = C_B(x) = N_B(x)/N_B(\infty) \quad (36)$$

$$N(x) = N_B(x) \quad (37)$$

and

$$r = r_{BA} \quad (38)$$

Equation (9) is inapplicable.

B. Self-ion implantation into a binary target.

For the case of A atoms implanted into a target consisting of A and B atoms, one has

$$N_C = S_C = J_C = J_C^M = 0 ,$$

$$N(x) = N_A(x) + N_B(x),$$

and

$$C_A(x) = N_A(x)/N_A(\infty) + N_B(\infty) \quad (\text{ditto B}) \quad (39)$$

Equations 3 and 5 are replaced by

$$\begin{aligned} J_A^* &= J_i + N_A(\infty) U^* J_i \\ J_B^* &= N_B(\infty) U^* J_i, \end{aligned} \quad (40)$$

and equations (8) and (9) are replaced by

$$\begin{aligned} S_A^* &= 1 + N_A(\infty) U^* \\ S_B^* &= N_B(\infty) U^* \end{aligned} \quad (41)$$

Equations (13) and (14) are replaced by

$$\begin{aligned} J_{AL}^{M*}(x) &= J_i^*(x) + [N_A(\infty) - N_A^*(x)] U^* J_i \\ J_{BL}^{M*}(x) &= [N_B(\infty) - N_B^*(x)] U^* J_i \end{aligned} \quad (42)$$

Equation (16) is replaced by

$$J_{AL}^{M*}(x) = \left\{ \int_x^\infty f^*(x) dx + [N_A(\infty) - N_A(x)] U^* \right\} J_i \quad (43)$$

Equations (20) are replaced by

$$J_{AL}^{M*}(x) = \left\{ \int_x^\infty f^*(x) dx + [C_A(\infty) - C_A^*(x)] (S^* - 1) \right\} J_i \quad (44)$$

$$J_{BL}^{M*}(x) = [C_B(\infty) - C_B^*(x)] (S^* - 1) J_i \quad (45)$$

Omit equation (21). The discussion of section IID1 should be repeated for this case according to the following sketch: In terms of the definition (22) of r_{BA} one has

$$N_A(o+)/N_B(o+) = r_{BA} S_B/S_A$$

Using equations (40) one then has

$$N_A^*(o+)/N_B^*(o+) = r_{BA}^* (1 + C_A(\infty) (S^* - 1)) / C_B(\infty) \quad (46)$$

This equation is a minor generalization of the result of Liau and Mayer [2].

IV. DISCUSSION

The possibility of there being substantial atomic migration currents during ion implantation is under intensive investigation for implantation into layered targets (ion-beam mixing) [2,9,10]. The above results on migration currents suggest that preferential sputtering experiments may be a fruitful area to investigate atomic migration phenomena.

ACKNOWLEDGEMENT

Thanks are due G. H. Herling and J. W. Butler for helpful conversations.

REFERENCES

1. See, for example, reference 2 below.
2. Z. L. Liao and J. W. Mayer, "Ion Bombardment Effects on Material Composition," Treatise on Mater. Sci. Tech., Vol. 18, p. 17 (1980).
3. See, for example, P. M. Morse and H. Feshbach, Methods of Theoretical Physics, (McGraw-Hill, 1953), p. 37.
4. Z. L. Liao and J. W. Mayer, "Limits of Composition Achievable by Ion Implantation," J. Vac. Sci. Techn. Vol. 15, p. 1629 (1978).
5. G. Carter, J. S. Colligon, and J. H. Lask, "Ion Sorption in the Presence of Sputtering," Proc. Phys. Soc. Vol. 79, p. 299 (1962).
6. F. Schulz and K. Wittmaack, "Model Calculation of Ion Collection in the Presence of Sputtering. I. Zero Order Approximation," Radiat. Eff. Vol. 29, p. 31 (1976).
7. I. Manning, "Sputter Distortion of Implantation Profiles," in Uses of Ion Implantation for Materials Processing. Program Report, F. A. Smidt, Ed., NRL Memo Rpt. 4527, 24 June 1981.
8. M. T. Robinson and I. M. Torrens, "Computer Simulation of Atomic Displacement Cascades in Solids in the Binary Collision Approximation, Phys. Rev.; Vol. B9, p. 5008 (1974).
9. S. M. Myers, "Ion-beam-induced Migration and its Effect on Concentration Profiles," Nucl. Instrum. Meth. Vol. 168, p. 265 (1980).
10. J. W. Mayer, B. Y. Tsaur, S. S. Liao, and L-S. Hang, "Ion-Beam Induced Reactions in Metal-Semiconductor and Metal-Metal Thin Film Structures, Nucl. Instrum. Meth., Vol. 182/183, p. 1 (1981), and the references cited there.

Section II.A

PRELIMINARY EVALUATION OF ION IMPLANTATION
AS A SURFACE TREATMENT TO REDUCE WEAR OF TOOL BITS

F. A. Smidt¹ and J. K. Hirvonen²
S. Ramalingam³

¹Thermostructural Materials Branch
Material Science and Technology Division
Naval Research Laboratory

²Materials Modification and Analysis Branch
Condensed Matter and Radiation Sciences Division
Naval Research Laboratory

³Formerly Georgia Institute of Technology
Atlanta, Georgia
Current address: University of Minnesota
Minneapolis, Minnesota

This work was supported by the Office of Naval Research
and the Naval Sea Systems Command

PRELIMINARY EVALUATION OF ION IMPLANTATION AS A SURFACE TREATMENT TO REDUCE WEAR OF TOOL BITS

I. INTRODUCTION

Material removal operations are a major cost factor in manufacturing operations. It has been estimated that \$60 billion per year is spent on such operations in the United States alone [1]. Machining costs are also a major factor in the manufacture of ordnance systems such as missile launchers where machining costs may reach 30 to 35 percent of the total production cost of the system. The present study was commissioned to evaluate ion implantation as a possible approach to reducing tooling costs in the manufacturing process and, in the longer term, reduction of life cycle costs and improvement of reliability in critical system components.

Ion implantation has been demonstrated to be a versatile technique for the modification of surfaces without changing the properties of the bulk material and with no change in physical dimensions of the component [2]. Improvements in wear life by a factor of 6 to 10 times have been observed for metal forming tools, injection molds for plastics, and slitting knives for rubber in commercial applications in industry in the United Kingdom [3]. These applications, however, represent relatively low wear situations at low temperatures. The wear of metal cutting tools represents a much more rigorous application of ion implantations which had not previously been evaluated. The sponsor suggested that machining of AISI 4340 steel with high speed steel tool bits was an area of interest and the bulk of the work was addressed to this application with a minor survey of improvements in the performance of TiC-coated carbide tool bits.

This report contains a brief description of ion implantation, a review of metal removal operations, rationale for ion implantation surface modification, initial test results, and recommendations.

II. ION IMPLANTATION BACKGROUND

A. Characteristics of Ion Implantation

Ion implantation is a process by which virtually any element can be injected into the near-surface region of any solid by means of a beam of high-velocity ions, usually tens to hundreds of KeV in energy, striking a target mounted in a vacuum chamber. The incident ions come to a stop at depths of tens to thousands of angstroms (i.e., 0.001 to 0.1 μm) in the host material as a result of losing energy during collisions with substrate atoms. The resulting depth concentration profile of implanted dopant atoms can be calculated for most projectile-target combinations from well established theoretical considerations. At low ion fluences (i.e., the number of ions per unit area), the depth concentration profiles are usually well characterized by a Gaussian distribution centered about an average range. An example of such a distribution is shown in Fig. 1. At higher fluences, other effects such as sputtering and ion beam induced migration of atoms can significantly alter or limit the ultimate depth concentrations attainable. During the slowing down process, the incident projectile

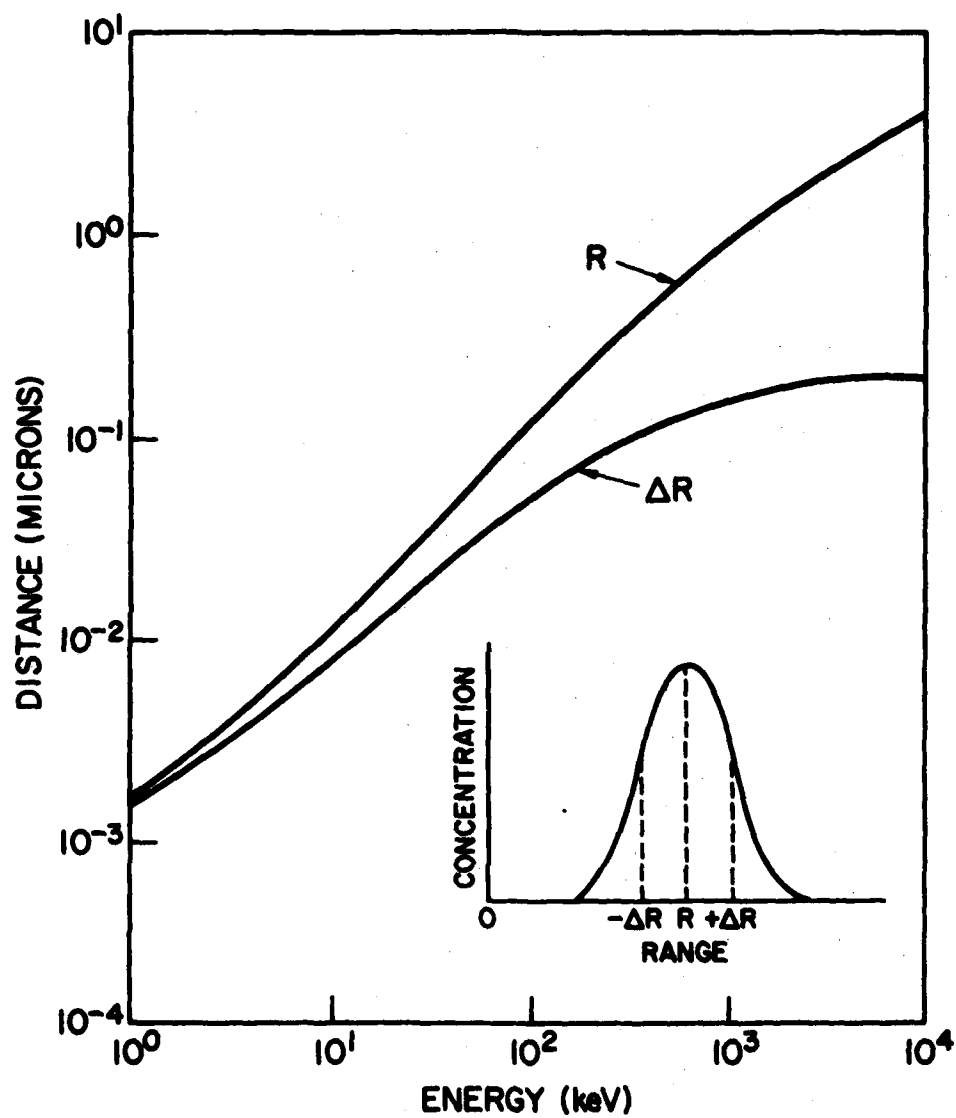


Fig. 1 — The projected range (R) and range straggling (ΔR) as a function of implantation energy for nitrogen in iron

ions transfer a significant amount of energy to the target atoms, resulting in the displacement of target atoms. There is a probability of atoms being ejected (sputtered) from the surface of the target as a result of such collisions, especially for heavier mass incident projectiles. Under these conditions, an equilibrium condition is eventually reached, where as many atoms are removed by sputtering as are replenished by implantation. The depth distribution of implanted atoms under this condition, has a maximum at the surface and falls off over a distance comparable to the initial range.

Because ion implantation is a process that modifies surface properties it is often compared with other conventional techniques, such as vacuum coating, chemical vapor deposition, and ion plating, which are all used for enhancing surface properties such as corrosion or wear resistance. It shares a number of advantages with these techniques but also has some basic limitation. These advantages and limitations are discussed in a later section. It is important to understand the differences between ion implantation and coating techniques especially ion plating. There are superficial similarities between the two techniques but they differ in many respects. The result of ion implantation into materials is the formation of a surface alloy of graded composition that possess no well defined interface with respect to the substrate, as does a deposited layer. The thickness of the implanted region is typically less than 1000 angstroms for implantation energies of 100 keV. In ion plating, however, the coating is typically much thicker, and its composition is independent of the nature of the substrate. Although ion plating is often carried out with the substrates electrically biased at several keV the mean energy of the particles reaching the surface is probably of the order of only 100 eV or so. In addition, only a small fraction (<10%) of the particles are ionized when they reach the substrate. Ion plating is carried out under a relatively high pressure that causes atomic collisions and scattering. This factor is responsible for the high "throwing power" of the ion plating technique versus the "line-of-sight" limitation of implantation.

B. Historical Perspective

Since the early 1970's, ion implantation has been extensively used by the semiconductor device industry as a method of introducing controlled amounts of dopants into the surface region of semiconductor substrates. Its principal advantages for this application include improved controllability and reproducibility for device fabrication, as compared to thermal diffusion. The absolute concentration of implanted atoms and the uniformity across the sample surface may be controlled to better than 5% and 1%, respectively. The volume concentrations of impurities required in semiconductors typically range from parts per million to as high as 0.1 at.%, whereas the concentrations required for many of the non-semiconductor applications, such as for tools, are typically several atomic percent.

C. Ion Implantation - Advantages and Limitations of Technique

Some of the advantages and limitations of ion implantation in comparison to other surface treatments (such as coatings) are listed in the table below. A basic limitation of ion implantation is that it is a line-of-sight process and therefore cannot be applied to samples having complicated reentrant surfaces. The shallow depth of penetration is also a limitation in applications where the surface is rapidly lost or removed. However, there are numerous situations involving both physical and chemical properties where the engineering properties are controlled by a very thin surface layer.

Advantages and Limitations of Technique as a Surface Modification Technique

Advantages	Limitations
(1) Solid solubility limit can be exceeded	(1) Line-of-sight process
(2) Alloy preparation independent of diffusion constants	(2) Shallow penetration
(3) Allows fast screening of the effects of changes in alloy composition	(3) Relatively expensive equipment and processing costs
(4) No sacrifice of bulk properties	
(5) Low temperature process	
(6) No significant dimensional changes	
(7) No adhesion problems since there is no sharp interface	
(8) Depth concentration distribution controllable	
(9) Clean vacuum process	
(10) Highly controllable and reproducible	

As for the advantages, the fact that ion implantation is a nonequilibrium technique permits the formation of surface alloys whose formation is independent of solubility limits and diffusivities governing conventional alloy formation.

Ion implantation often allows the convenient production and subsequent study of surface alloys with well defined compositions. In this manner the technique can be used as a powerful research tool to examine the physical state of alloys as a function of varying alloy composition.

Ion implantation has other potential advantages for treating limited area critical parts. The surface properties can be optimized independently of the bulk properties and implantation can be carried out at low temperatures without producing any significant dimensional changes. In addition the surface alloy produced by implantation should not suffer from adhesion problems since there is no sharp interface.

D. Ion Implantation Equipment and Costs

This section is not intended to be a comprehensive description of ion-implantation equipment and its operation but only to give a brief introduction. There already exist in the literature detailed articles concerning the production and manipulation of ion beams for implantation and articles discussing the various advantages and disadvantages of particular ion implantation system designs.

A typical research-type ion implanter is shown in Fig. 2. It consists of an ion source capable of producing low-intensity ion beams of practically any stable element. Ions are extracted from the ion source by an electrode held at high potential and subsequently accelerated through an evacuated acceleration column during their passage from the source (held at the high voltage) to ground potential. Since ion sources normally produce ions of many species other than those that are desired for implantation, it is ordinarily essential to mass-analyze the beam in order to allow only the species of interest to continue toward the target. After mass analysis, the beam is electrostatically focused and steered towards a target chamber as well as being

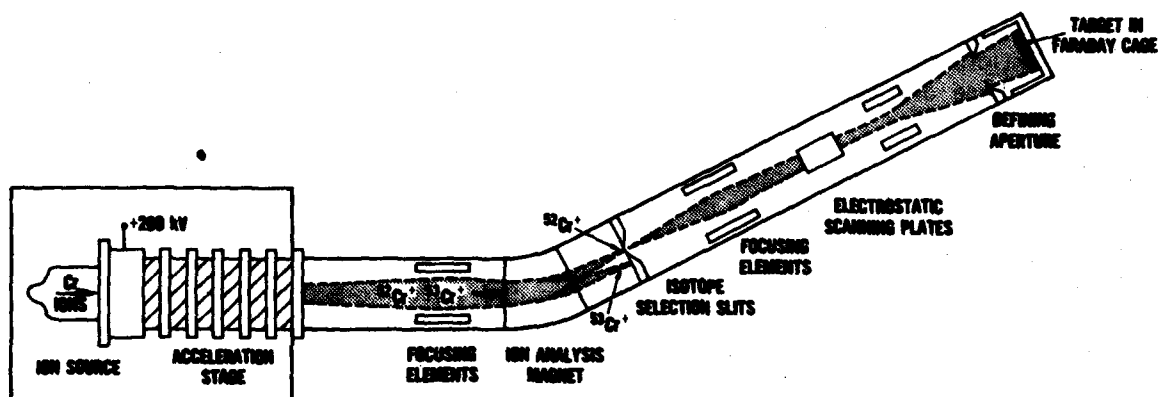


Fig. 2 — Schematic of a typical research-type ion implantation system

raster scanned over an aperture held in front of the target to ensure uniformity. The ion beam current passing through the defining aperture is then current integrated to obtain the impurity concentration (in dimensions of atoms per unit area) which in turn can be converted into a volume concentration by knowledge of the range-energy relationships for the projectile ion-host combination.

Before approximately 1970, the only machines available for implantation were either (i) modified research-type accelerators capable of producing microampere beams at energies up to several hundred keV or (ii) isotope separators capable of delivering milliampere beams at energies of tens of keV. These systems were quite satisfactory for semiconductor research applications but the desire to implement implantation for semiconductor device production provided a strong driving force for commercial companies to design production equipment to provide high-throughput and automated operation. The semiconductor applications have grown to the extent that there are now approximately 1400 production-type implanters throughout the world, with an estimated \$55 M worldwide sales in 1979. In addition to these production machines there are several hundred research-type machines in use throughout the world.

Figure 3 shows a schematic of a production-type ion implantation system used commercially for the processing of semiconductors. This type of implanter provides considerably higher beam currents than the system shown in Fig. 2. It is capable of processing approximately fifty three-inch wafers per hour with a doping uniformity less than 1% over the wafer and a day-to-day and wafer-to-wafer reproducibility of less than 0.5%. Present indications are that stringent dose and beam purity requirements can be significantly relaxed for many applications of implantation in metals (e.g., for improving wear or corrosion resistance). This should allow the machine designer more flexibility, possibly resulting in simpler machines. An important consideration for metals is the development of dedicated element ion sources and suitable target chambers that will allow the desired areas of the nonplanar targets (e.g., ball bearings) to be uniformly exposed to the ion beam. The estimated present cost for an implanter such as shown in Fig. 4 is \$400-500 K. High current machines built for non-semiconductor applications would probably cost about \$500-750 K.

For research application using limited areas, currently available machines will probably suffice. However any future engineering applications involving larger areas will necessarily require specialized systems involving either modification of existing design implantation systems, or development of entirely new design systems.

With currently available ion sources such as the one incorporated in the system shown in Fig. 4 it is possible to produce currents of up to approximately 1 mA for many of the ion species needed for non-semiconductor applications. This would correspond to a treatment time of approximately ten seconds per cm^2 to reach fluences that have been shown to improve corrosion or wear resistance (i.e., approximately 10^{17} atoms/ cm^2). If an operating cost of \$35/hr is assumed, these times correspond to costs of roughly \$0.15/ cm^2 . Further development of ion sources should significantly increase the attainable ion currents and hence lower costs. It should be noted that isotope separators (which are essentially low voltage ion implanters) were producing beam currents of tens to hundreds of milliamperes over 30 years ago. Given these currents and the significant improvements made in intervening years in ion beam technology the construction of high throughput implanters for metals processing should be quite feasible once the scientific merit and economic justification for each application is shown.

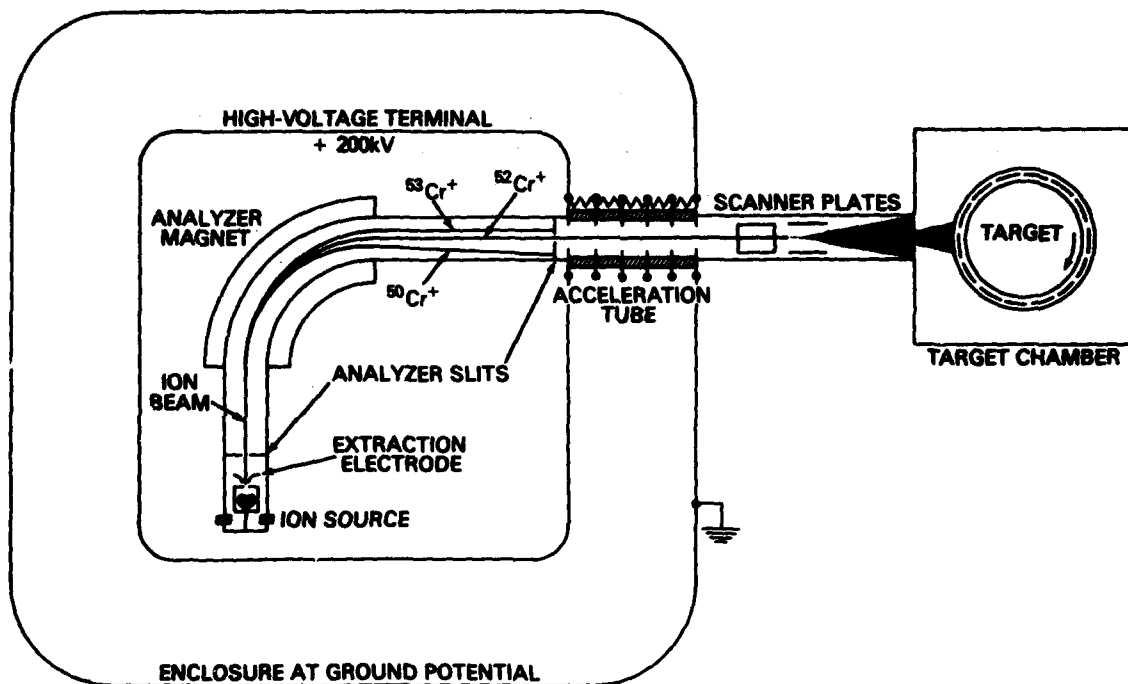


Fig. 3 — Schematic of a production-type ion implantation system for semiconductors

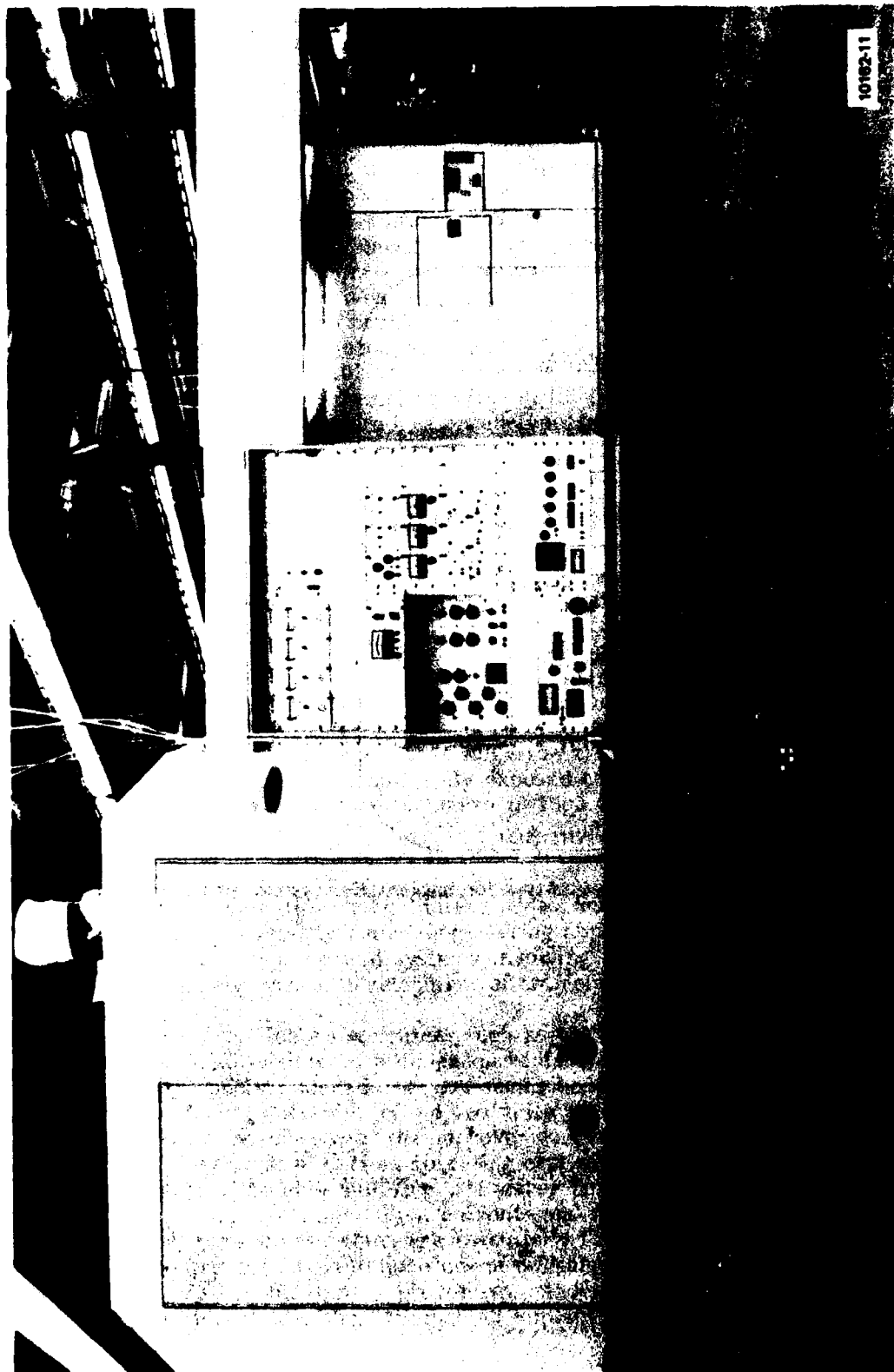


Fig. 4 — A 200-KeV high-current ion-implantation system used for semiconductor processing

III. MAJOR FACTORS IN METAL REMOVAL OPERATIONS

A brief examination of some of the major factors in metal removal operations is necessary to place the approach selected for this study in proper perspective. An exhaustive review of the literature is not intended and the reader is referred to several excellent reviews [1,4-6] for a more comprehensive treatment of the subject.

A. Factors Affecting Tool Wear and Failure

Metal removal operations such as drilling, boring, milling, and turning in a lathe differ in the geometrical relationship between the tool and work piece but all can be reduced to the same basic process illustrated in Fig. 5. A tool moves relative to a work piece so that a thin layer of material is removed from the surface to reduce the work piece in size and leave a suitable finish on the resulting surface. Highly localized shear takes place along the line OD, the shear plane. The chip then slides along the rake face and may assume various configurations such as continuous, discontinuous, or built-up edge depending on such factors as cutting speed, ductility and work hardening characteristics of the work piece material and the angle of the rake face.

In machining there is a finite length of contact (length BE in Fig. 6) between the tool and the chip. Over a part of this length (BD) the contact between the chip and the tool is plastic. The remainder of the contact is elastic. The applicable slip line field (determined with plasticity theory) consists of a region of plastic contact (BCD), a centered fan region (ACD) and an isolated slip line (OAB), as shown schematically in Fig. 6.

By ion implantation, it is expected that the frictional characteristics of the tool material can be altered to change the applicable boundary conditions (of the plasticity problem) which prevail during machining along BDE, the tool-chip contact length. A reduction in local friction coefficient leads to lowered frictional heat dissipation along BDE and lower power requirements for machining through a lowering of chip shear strain during machining. The net result, apart from improving the energy efficiency during machining, is a lowering of the tool temperature which results in a lowered wear severity encountered by the tool during machining.

Apart from changing the sliding friction coefficient, ion implantation is also known to improve the wear resistance. Improvement in wear resistance is ion-specific. It is a purpose of the present program to identify the appropriate ionic species and to document the relative improvement in wear resistance. The heat generated by the shear processes and the heat generated by the frictional forces between the tool face and the chip cause an increase in temperature of the chip. Much of this heat is carried away in the chip but substantial increases in temperature do occur on the rake face. Cutting fluids are used to cool the tool and provide lubrication to reduce cutting forces although lubrication is not a factor in high speed continuous removal processes where the cutting edge remains buried in the work piece for long periods of time.

Tool failure can occur as a result of wear of the tool, fracture or overheating. Fracture results from subjecting the tool to cutting forces which are too high or using a tool which is too brittle for the work piece material. Overheating of the tool results from operating at a cutting speed too high for the tool material and may result in loss of strength of the tool material with resultant blunting of the tool edge and a catastrophic rise in temperature. The loss of strength may result from a metallurgical change such as overaging of martensitic tool steels or simply from a decrease in flow

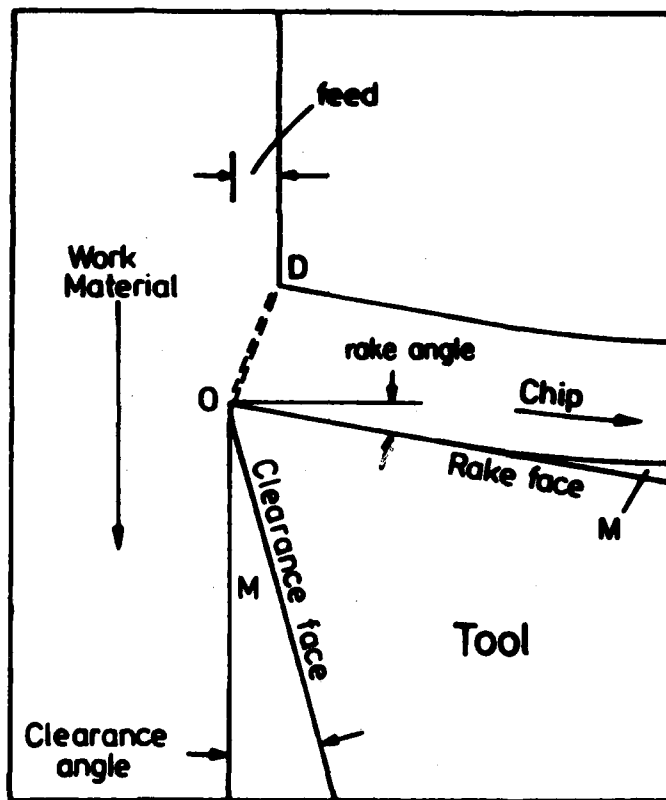


Fig. 5 — Schematic of the principle features of the tool and work material interaction during metal cutting operations

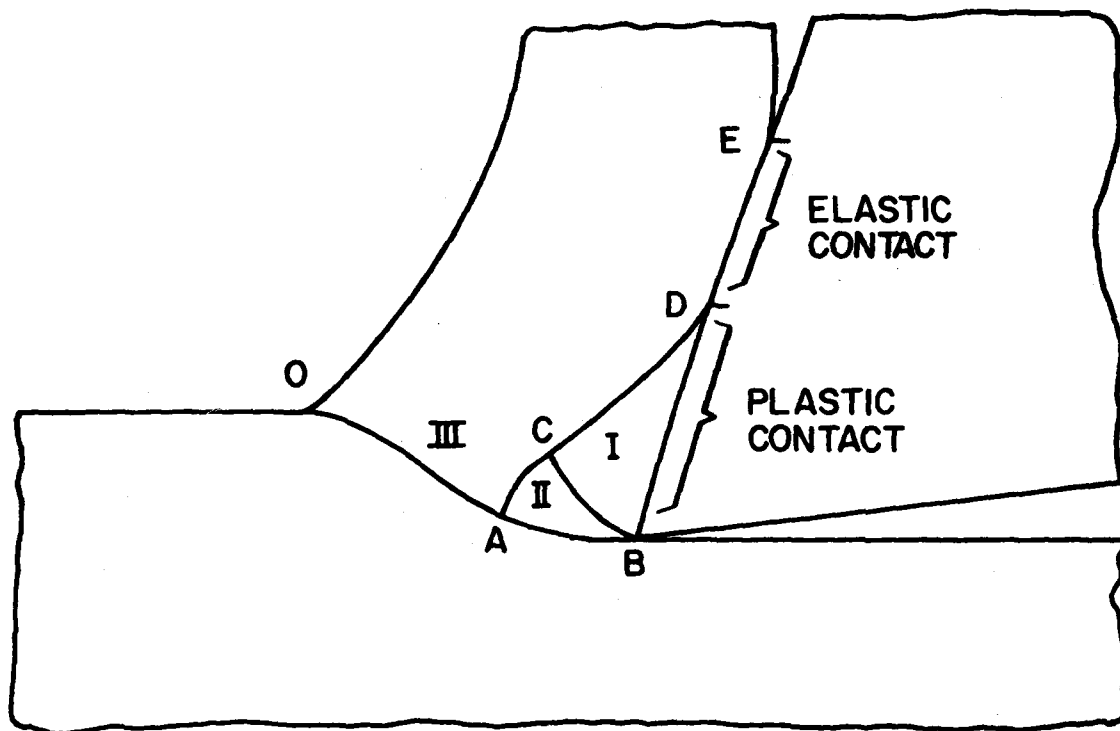


Fig. 6 — Slip line field applicable to chip formation during orthogonal machining

stress with temperature. The major cause of tool failure, for tools used under the normal range of operating conditions, are crater wear on the rake face and the development of wear lands on the clearance face. The location of these wear regions are illustrated in Fig. 7. Wear in these locations leads to a degradation in surface finish and loss of tolerance on the part. Crater wear is related to the temperature of the rake face and the location of the crater correlates directly with the distribution of temperature on the rake face. Trent [4] has shown some graphic examples of this relationship. Cratering may also be accelerated if a chemical reaction occurs as in the case of the machining of low carbon steels with cemented tungsten carbide tools where the WC decomposes during the machining and the iron reacts with the carbon.

The wear of cutting tools is a complex phenomena and it seems unlikely that a single mechanism is responsible for all forms of wear observed in practice. Abrasive wear, surface fatigue or delamination, and oxidative or corrosive wear are recognized by most workers in the field as being the principal contributors to tool wear

Abrasive wear is visualized as a process in which a small hard particle ploughs a track in a softer material serving as a miniature cutting tool to remove material from the softer surface. Empirical correlations between hardness and abrasive resistance such as those illustrated in Fig. 8 are well known. Oxide inclusions have been shown to be the primary source of abrasive wear particles in the machining of steels [7]. Alumina and silica in particular have high hardness. The situation is exacerbated because the tool hardness decreases faster as it heats up during the machining operation while the oxide inclusions impact the tool face at near ambient temperature. Table 1 shows the change in hardness for various phases present in steel [5]. Suh quotes a figure of 4.5 as the necessary hardness ratio between tool and work piece to eliminate abrasive wear [5]. No such materials currently exist. Abrasive wear can also be ameliorated by inclusions in the steel such as MnS or Lead which provide a low friction surface film at the tool face-chip interface [7].

The delamination theory of wear developed by Suh postulates that repeated contact with a sliding surface results in cyclical plastic deformation of the surface layers. As the plastic strain increases, cracks nucleate around inclusions or in dislocation cell walls. The cracks first propagate and link up below the surface and subsequently shear to the surface so that the surface flakes or delaminates in sheets. Suh predicts that delamination wear will occur for tool wear under hard abrasive particles when hard abrasive particles have a ratio of width of penetration to tip radius less than 0.2 [5].

Chemical instability as a factor in wear was mentioned in the previous discussion of crater wear and its correlation with temperature profiles on the rake surface. Older literature sometimes mentions a diffusional wear process in which solutes were hypothesized to diffuse across the chip-tool interface to degrade the properties of the tool material and accelerate wear rate. A more thorough analysis of the chip motion relative to the tool makes a diffusional process appear less likely. Dissociation of the cutting tool material with subsequent dissolution of the constituents provides a more viable alternative. Suh and co-workers have shown good correlation between high heats of formation of refractory compounds and wear resistance [5]. Reaction of the tool material with the atmosphere or the cutting fluid can also contribute to oxidative or corrosive wear.

B. Materials Selection and Processing for Wear Reduction

The major classes of materials with high usage for cutting tools include the high

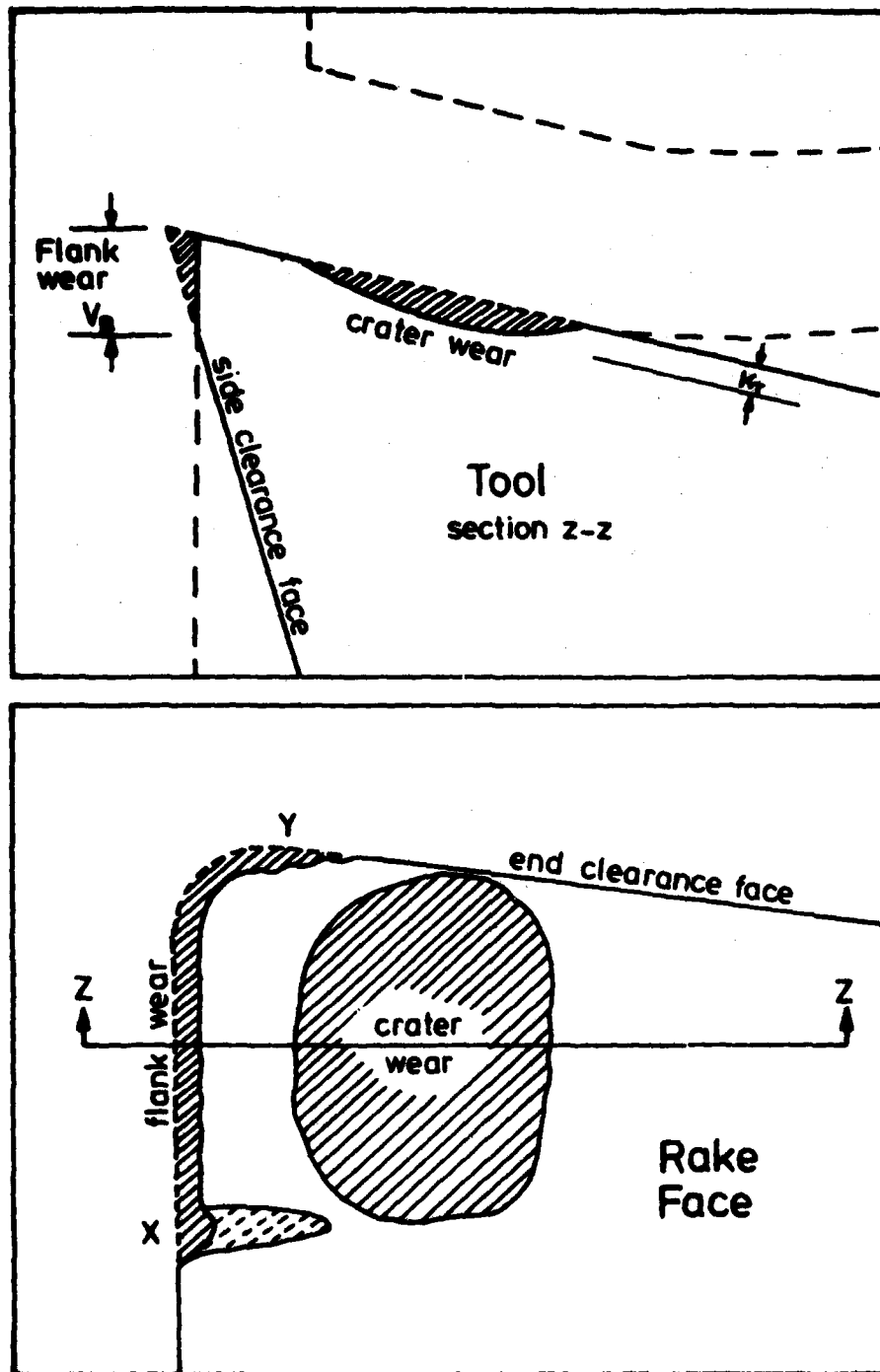


Fig. 7 — Schematic illustration of the characteristic wear features that develop on a lathe tool bit during machining operations

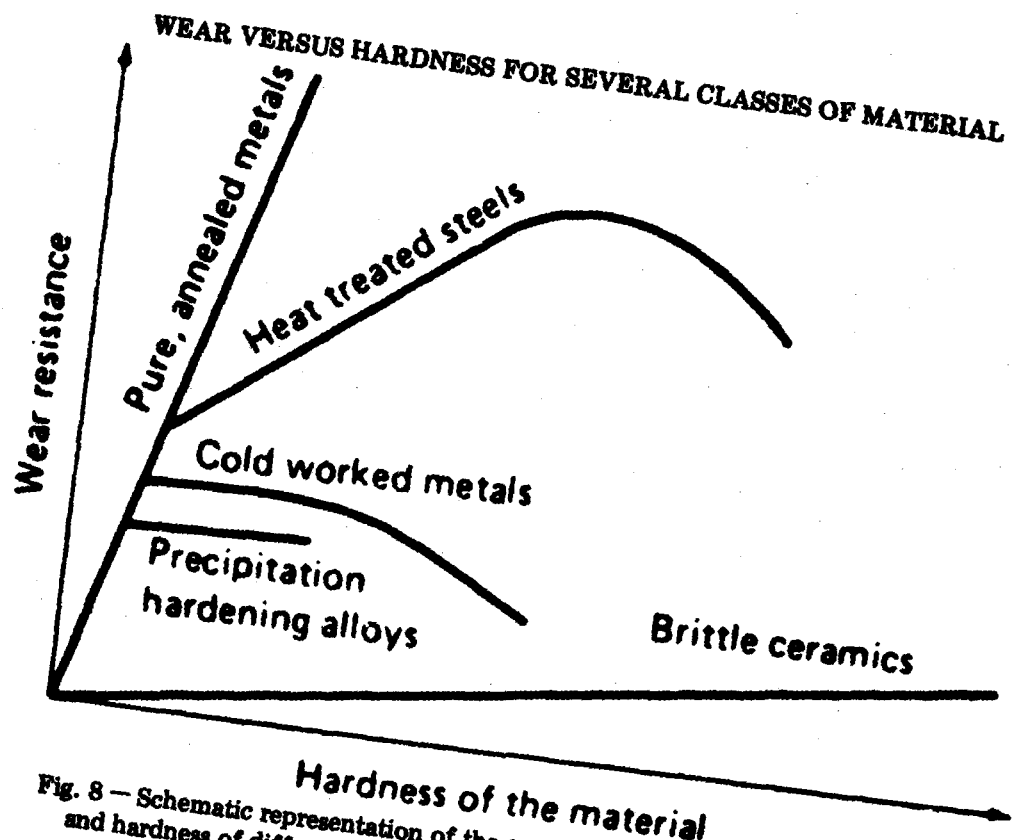


Fig. 8 — Schematic representation of the correlation between wear resistance and hardness of different materials in various microstructural conditions

TABLE 1

**Hardness at Specified Temperatures of the Phases
that May Be Present in a Steel**

Phase	Hardness H_V (kgf mm^{-2})		
	400°C	600°C	800°C
Iron	45	27	10
Iron and Interstitials	90	27	10
TiO	1300	1000	650
FeO	350	210	50
MgO	320	220	130
NiO	200	140	100
MnO	120	60	45
Al_2O_3	1300	1000	650
SiO_2	700	500	300
ZrO_2	650	400	350
TiO_2	380	250	160
MgAlO_4	1250	1200	1050
ZrSiO_4	400	290	140

speed steels, cemented tungsten carbides in cobalt binders, cemented tungsten carbides plus titanium and tantalum carbides in cobalt binder, aluminum oxide ceramics, diamond and titanium carbide coated cemented carbide tools. More detailed information on each material and its performance characteristics can be found in the Metals Handbook [6] and a more general review of wear resisting materials and surface treatment is given by Eyre [9]. Suh [5] discusses conventional materials as well as new concepts in tool materials.

The selection of tool material for a particular machining application depends on a number of factors such as hardness of the work piece, cutting speed and the accompanying rise in temperature, reactivity with work piece material, fabricability of tool material and intricacy of the cutting tool geometry, cost, available power for the machine, rigidity of the machine, and surface finish required. In general, one would like to select a material to operate at the highest cutting speed possible with the power and rigidity of the machine available. The upper limit is established by excessive failure rates for the tool by fracture, overheating, excessive wear, or an unacceptable surface finish. In general, the wear resistance and thermal stability increase in the series of high speed steel - cemented tungsten carbide - cemented tungsten carbide with additions of titanium and tantalum carbide - ceramics. The shock resistance decreases as the wear resistance increases so compromises must be made to select an acceptable failure rate. This choice is usually on the basis of economic considerations.

Surface treatment is an attractive approach to achieve the compromise between adequate shock resistance in the bulk material and a favorable hardness or friction coefficient on the surface. Surface hardening treatments such as carburizing and nitriding of steel have been in commercial practice for a long time. Their principal disadvantage is that many of these treatments require temperatures in the range where tempering and annealing of the steel take place. Chemical vapor deposition (CVD) of the titanium carbide to provide a thin (.0002-.0003 in.) coating over cemented tungsten carbide tools produces a substantial increase in performance of the tool. Figure 9 shows a comparison of machining speeds attainable with coated tools and other common tool materials. This increase in performance is attributed to the decrease in friction with TiC and attendant lowering of temperature as well as the excellent high temperature stability and high hardness. In the CVD process the substrate is heated and exposed to a mixture of gases which react at the substrate surface to form a solid deposit. The technique is a batch process in which many small parts are exposed at one time. A limitation of the process is the high temperature required (near 1000°C) so that only refractory tool materials can be used for the substrate. Another disadvantage is that such tools cannot be sharpened without recoating of the tool. Adherence of the coating is also a problem. Ion plating and ion implantation offer some attractive features as surface treatment techniques because of the flexibility in elemental species which can be added to the surface, the absence of adherence problems, and the ability to modify the surface without exposing the bulk material to excessive temperatures.

C. Cost Factors in Machining Operations

The ultimate driving factor in machining operations is the economy of the operation. A qualitative analysis of the principal cost factors is provided in Fig. 10. The major parameters are the cost per unit produced and the cutting speed. Material costs and facility costs are fixed. Machining cost per part decreases with cutting speed; tool cost including reconditioning eventually increases rapidly at high cutting speeds. Tool changing costs also increase with the high failure rate. A linear

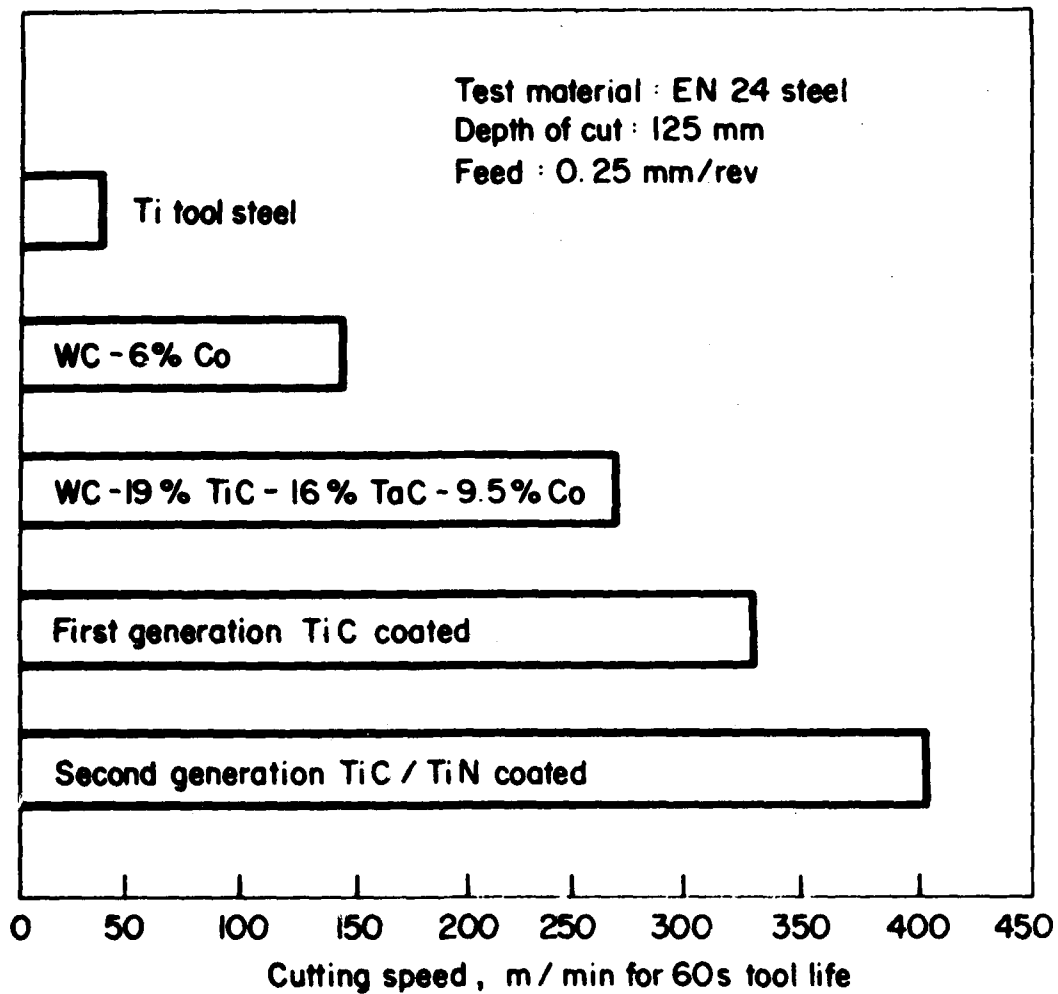


Fig. 9 — Improvements in the cutting speed which have been achieved by advances in cutting tool materials

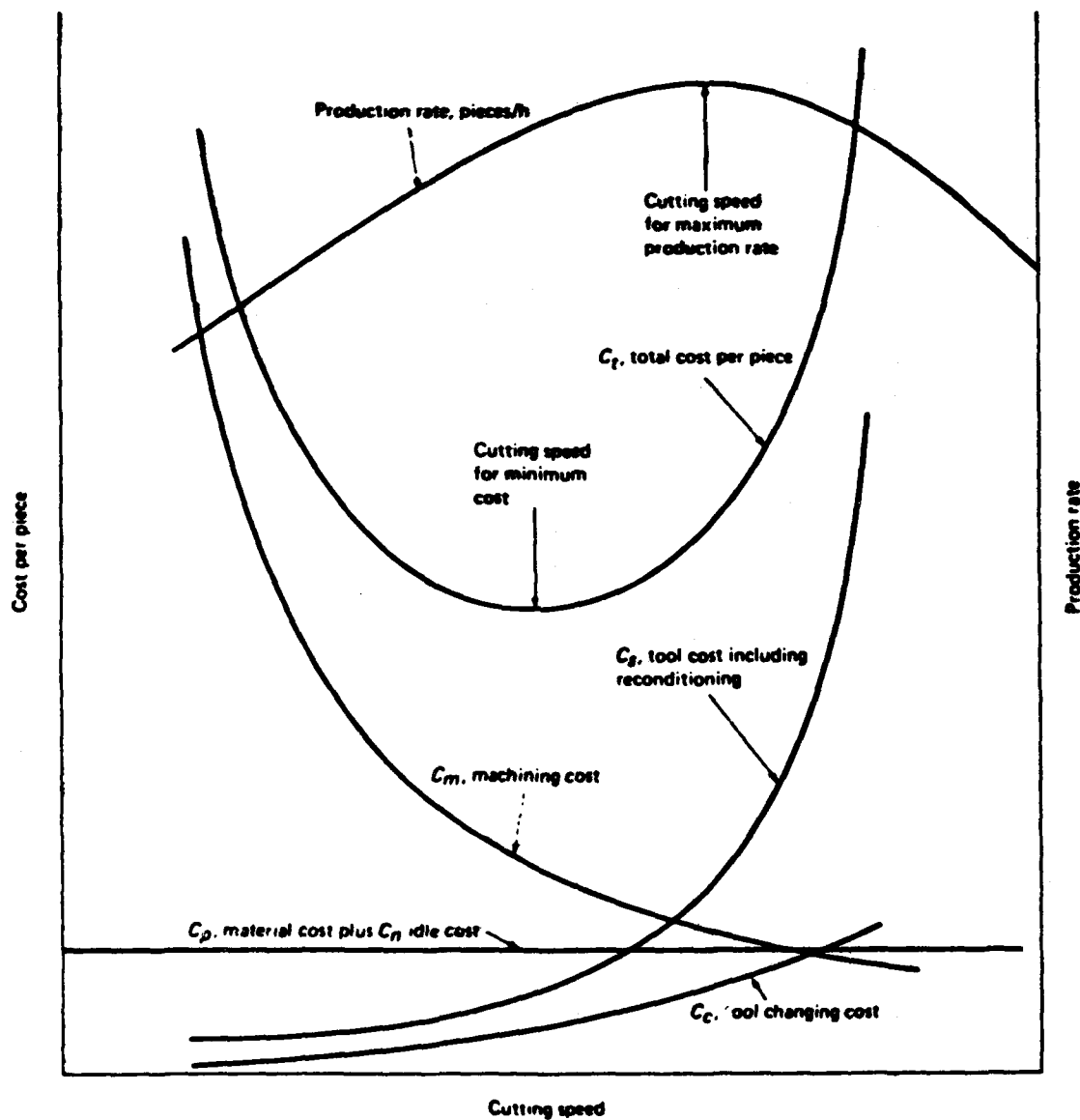


Fig. 10 — Schematic representation of the major cost factors in machining operations and the dependence of cost and production rate on cutting speed

superposition of the above factors leads to total cost per part curves with a minimum that represents the most economical cutting speed. The production rate curve shows a maximum which is somewhat above the most economical cutting speed. Shaw [1] gives the analytical form of the above equation for optimum cost per part and provides some sample calculations. More sophisticated analytical methods using operations research have also been applied to the problem [10] but yield qualitatively similar results. The most important point to recognize is the impact of cutting speed on the economics of the process.

Another important perspective on the economics of machining is provided in Fig. 11 which shows the contribution of various costs to the total cost of slotting cutters and face mills for three types of material and three sizes. Costs considered are tool material, cost to make the tool, cost to grind the tool and other costs such as heat treating. It is important to note that the actual cost of the tool material is a small fraction of the total cost. Surface treatments such as ion implantation that extend the life of tools with intricate shapes and therefore high manufacturing costs are easily justified on a cost basis.

IV. SELECTION OF MATERIAL SYSTEM FOR EXPERIMENTAL EVALUATION OF WEAR REDUCTION IN MACHINE TOOLS

The previous section described briefly the major classes of materials used in metal cutting tools. The most widely used material for severe metal cutting conditions are the cemented tungsten carbides while the high speed steels are the highest tonnage material because of superior fabricability and lower cost. High speed steels are still used in metal cutting applications where power and rigidity limitations of older equipment do not permit the effective use of carbide inserts and where the complexity of the tool design dictates the use of more easily fabricated materials. Preliminary discussions with the sponsor established a strong interest in the high speed steel class of tool materials so the experimental evaluations were centered on those materials. Metal cutting operations where high speed steel would find extensive use include forming, parting, grooving, planing, shaping, broaching, milling, hobbing, drilling, reaming, tapping and sawing.

The high speed steels are high carbon, hardenable, alloy steels produced to close quality control for reproducible properties. Carbon contents typically range from 0.75 to 1.25 wt%. Alloy contents are 3 to 4% Cr plus W, Mo, V and sometimes Co. Typical compositions for the high tonnage alloys M2, M50, M7, T1, and T15 are given in Table 2 along with AISI 52100, an alloy which will be mentioned in the following discussion. Steels of this composition can be deep hardened to Rockwell C-65 when quenched from the austenitizing temperature of 1230°C. An oil quench is used for sections over 3 in. in diameter while a hot salt quench and air cool is used for thinner sections. This heat treatment produces a hard martensitic structure with alloy carbides. In the "as-quenched" condition these steels contain 0.5 percent carbon in the matrix with the balance in alloy carbides of the M₆C and MC type Fe₄(Mo,W)₃C and VC. Figure 12 shows the softening characteristics of several classes of tool material including T1 and M2 high speed steels. And it can be seen that substantial softening occurs above 1050°F (565°C). Improvements in wear resistance of high speed steel tools should then be sought in surface treatments yielding a higher surface hardness than Rockwell C-65 (or Knoop microhardness of 846) and better retention of hardness at temperatures above 565°C.

Research on wear improvement of AISI 52100 bearing steel conducted at NRL [12,13] offered some promising directions for the initial experiments on high speed

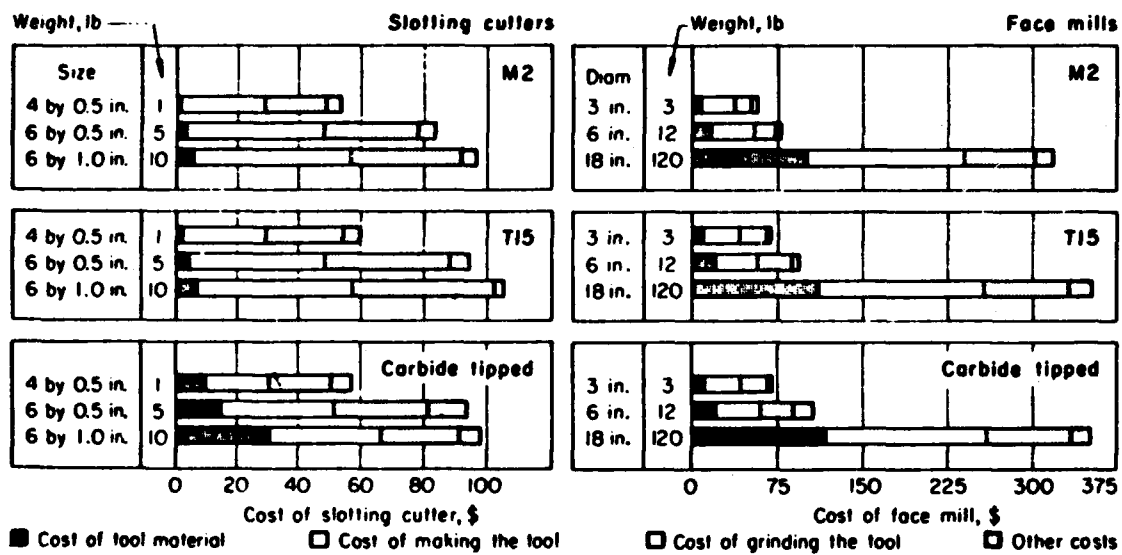


Fig. 11 — Effect of tool size and weight on material cost, processing cost and total cost of slotting cutters and face mills

UNCLASSIFIED

23

NRL-MR-4821

NL

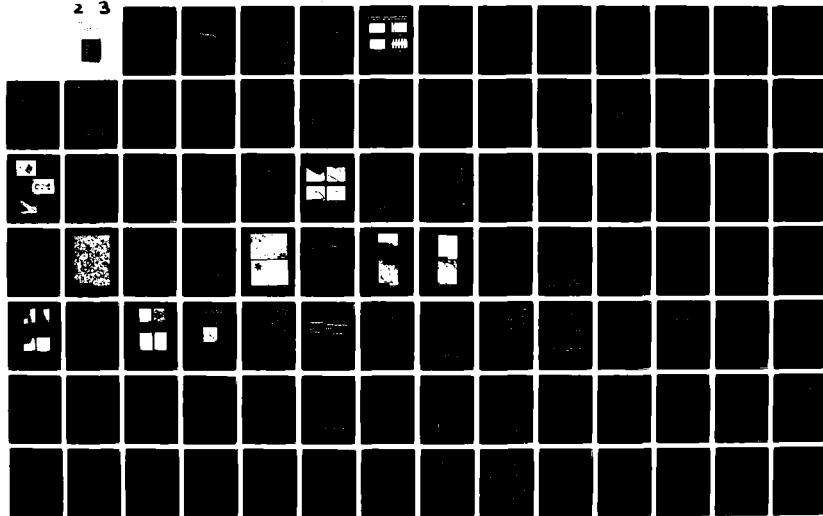


TABLE 2

Nominal Composition of High Speed Steels (Wt-%)

Steel	C	Cr	V	W	Mo	Co
<u>Molybdenum High Speed Steels</u>						
M2, Class 1	0.85	4.00	2.00	6.25	5.00	
M7	1.02	3.75	2.00	1.75	8.75	
M50	0.80	4.00	1.00	-	4.25	
<u>Tungsten High Speed Steels</u>						
T1	0.73	4.00	1.00	18.00		
T15	1.55	4.50	5.00	12.50	0.60	5.00
<u>Bearing Steel</u>						
52100	1.05	1.45				

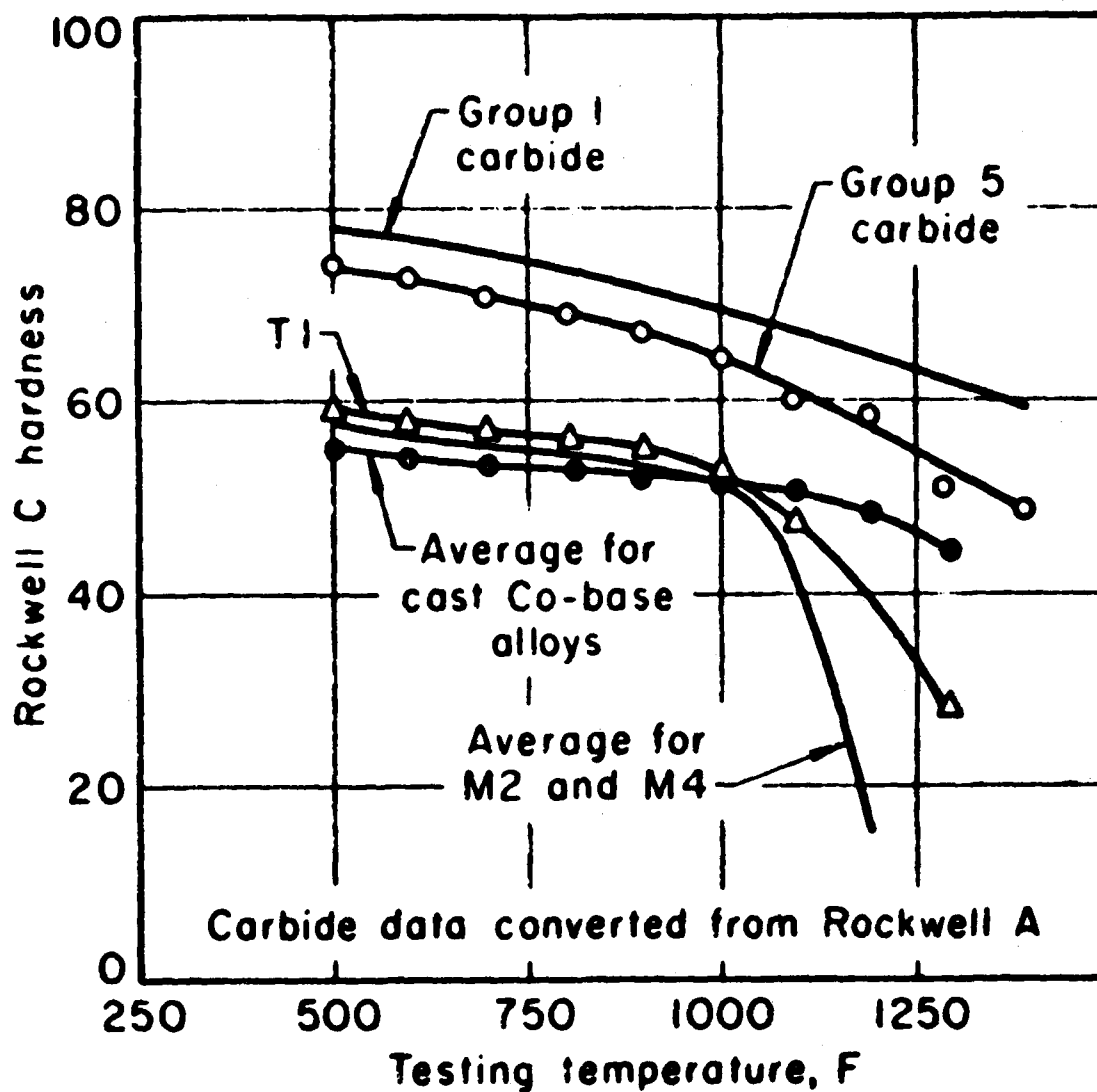


Fig. 12 — Effect of testing temperature on the hardness of high speed steels, cast cobalt-base alloys and sintered carbides

steels. AISI 52100 is also a high carbon steel used in high wear applications such as bearings but the alloy content is less than the high speed steels with no Mo, W, or V as shown in Table 2. The experiments on AISI 52100 consisted of surface modification of the steel by implantation of titanium, several types of wear experiments to compare the wear properties with unimplanted material, and surface analysis to determine the structure and composition of the implanted surface. Figure 13 shows the experimental arrangement for the determination of coefficient of friction. A 52100 ball with a one kg load imposed bears on a platen implanted with titanium. The platen is then moved with respect to the ball. The coefficient of friction was found to vary with the number of passes and with the implantation dose. Wear scars viewed with an interference microscope are shown in Fig. 14 for the corresponding conditions in the friction experiment. A full explanation of these results requires additional information on the analysis of the surface layers. It should be noted however that the 50×10^{16} Ti/cm² fluence results in a persistent reduction of the coefficient of friction from 0.61 to 0.35 and that the surface is so hard that it is not scarred by the wear test with 1 kg load (Hertzian pressure of 400 MPa [58 ksi]).

Two types of wear tests were also conducted and show the benefits of ion implantation. Figure 15 shows a pin-on disk test where wear volume is measured by the change in diameter of a tapered pin and the profile of the wear scar. Hexadecane Z, a poor boundary lubricant, was used to adjust the wear life for periods that could be reasonably measured. A load of 1 kg was used in the test. The major effect of the titanium implant was to delay the onset of severe wear. This initiation point was somewhat variable but in all cases extended the threshold for onset of severe wear by a factor of ten. Lubricated wear tests were also conducted for a 52100 ball sliding against a 52100 race implanted with 2×10^{17} Ti/cm² under a load of 2 kg (Hertzian pressure of 810 MPa, [117 ksi]). The lubricant was a synthetic polyester lubricant used for turbojet engine bearings. As can be seen in Fig. 16 the wear rate after running-in is a factor of 7 lower for the Ti implanted bearing race under lubricated wear conditions.

The friction and wear results for AISI 52100 can be rationalized when information on the surface chemistry is available. Figure 17 shows composition profiles for oxygen, carbon, titanium and iron obtained from Auger electron spectroscopy peak height measurements on the implanted region in a 5×10^{17} Ti/cm² specimen which has been ion milled to give a depth profile. The vertical line at 7 minutes indicates a change in milling speed. Information on the chemical state of the elements can also be determined from the Auger electron line shapes and characteristic lineshapes are noted on the figure. The composition changes from the outer surface into the metal interior show a hydrocarbon overlayer, a thin iron oxide layer, a titanium oxide layer, titanium carbide, and finally, metallic titanium, iron and carbon in solid solution. Auger analyses of lower fluence specimens show proportionally more titanium and less carbon than in the high fluence specimen. The higher proportion of titanium produces a high coefficient of friction because it prevents the formation of the normal air-formed iron oxide which provides some lubrication of the sliding surface. In the high fluence specimen the titanium carbide provides a hard surface with excellent tribological properties. This information on composition of the surface layer provides a suitable explanation of the change in frictional properties with Ti implant fluence shown in Fig. 13. The most desirable properties are those of the hard TiC layer.

Transmission electron microscopy observation of the surface [13] shows the surface layer to be amorphous. It is hypothesized that carbon from hydrocarbon vapors in the vacuum chamber reacts with the exposed titanium in the surface of the specimen under ion bombardment and reacts to form the Ti-C-Fe amorphous layer. Research is still in progress to determine the relative importance of the TiC bonding

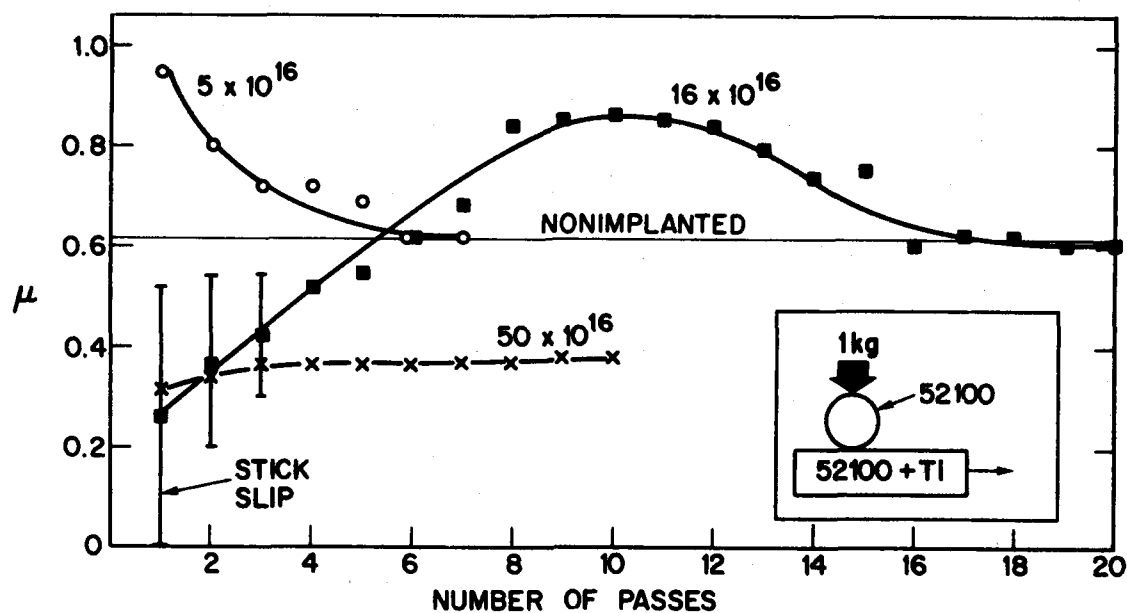
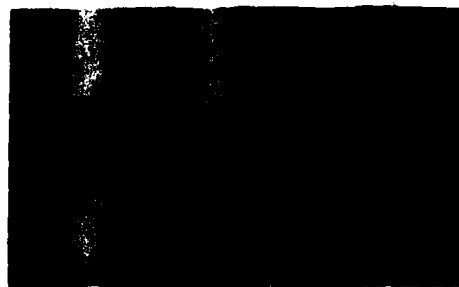


Fig. 13 — Experimental arrangement (lower right hand corner), and data for the coefficient of friction between an AISI-52100 steel ball and a 52100 flat surface implanted with Ti. Three distinct types of behavior are observed which are dependent on the fluence of Ti ions implanted onto the surface.

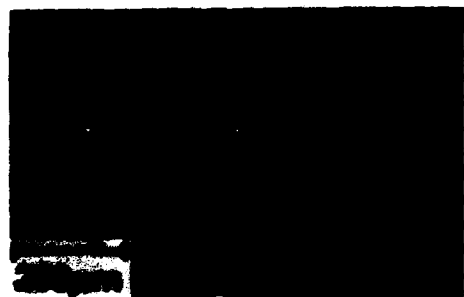
INTERFERENCE MICROGRAPH OF WEAR SCARS ON TI-IMPLANTED 52100 STEEL



$16 \times 10^{16} \text{ Ti/cm}^2$
10 PASSES



$16 \times 10^{16} \text{ Ti/cm}^2$
20 PASSES



$50 \times 10^{16} \text{ Ti/cm}^2$
10 PASSES



$5 \times 10^{16} \text{ Ti/cm}^2$
7 PASSES

R-144

Fig. 14 — Wear scars produced on AISI-52100 steel polished flats implanted with various fluences of Ti ions as viewed by interferrometry. Experimental conditions are as follows: (a) $50 \times 10^{16} \text{ ions/cm}^2$ after 10 passes of loaded ball (b) $16 \times 10^{16} \text{ ions/cm}^2$ after 10 passes (c) $16 \times 10^{16} \text{ ions/cm}^2$ after 20 passes (d) $5 \times 10^{16} \text{ ions/cm}^2$ after 7 passes (similar in appearance to unimplanted surface).

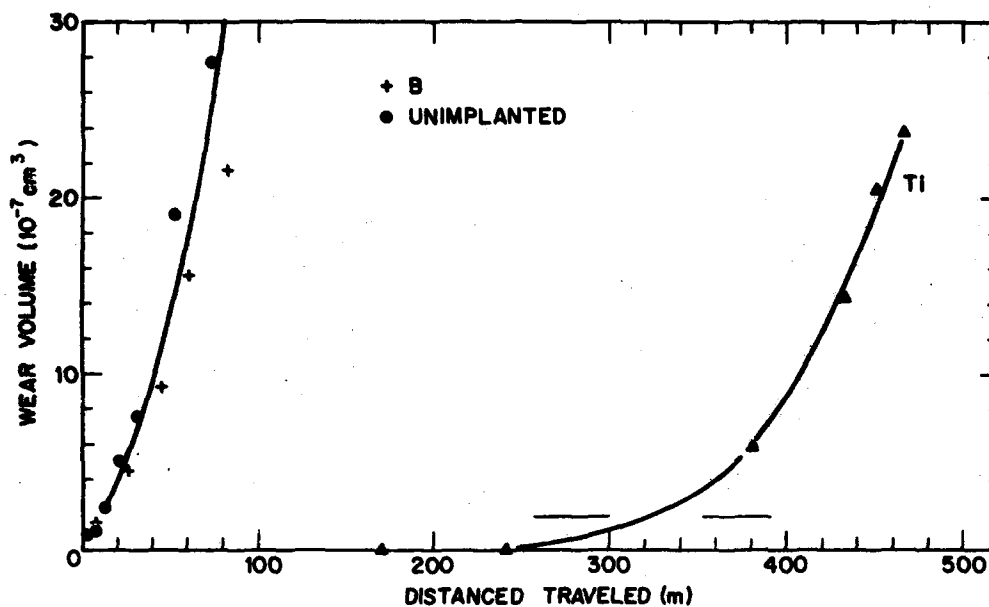


Fig. 15 — Wear volume for AISE-52100 ball on 52100 disk surfaces unimplanted, implanted with B, and implanted with 5×10^{17} Ti ions/cm². The arrows beside the Ti curve indicate that the onset of severe wear is variable but begins at substantially larger distances than in the unimplanted specimen.

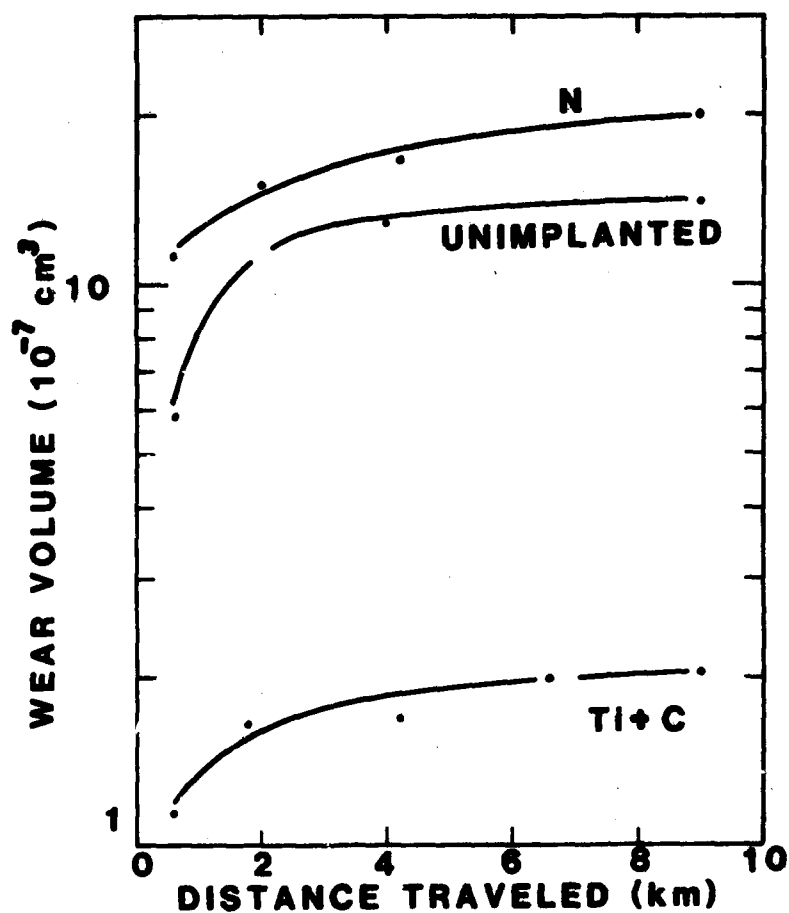


Fig. 16 — Wear experiments using a ball on cylinder configuration to investigate the "running-in" portion of the wear regime. Ti implants of 2×10^{17} ions/cm² show substantially better performance than unimplanted and nitrogen implanted specimens.

and the amorphous layer in imparting the remarkable improvements in wear observed in this material. A similar approach is proposed to improve the wear resistance of high speed steel in wear applications.

While high speed steel is the largest tonnage material for machine tool bits, it does not have the wear resistance of either cemented tungsten carbides or the titanium carbide coated tools. A minor effort was undertaken to evaluate the possibility of improving the wear resistance of these latter materials by ion implantation. A carbide tool insert of Carbolloy Grade 895, 94WC-6Co, was implanted with carbon ions to surface harden the cobalt binder. A titanium carbide coated Carbolloy 895 tool insert was also implanted with carbon, nitrogen and boron ions to evaluate the benefits of surface modification of the TiC. The addition of nitrogen to TiC to form Ti(CN) is known to strengthen the material while the implantation of boron was done to strengthen the material with TiB_2 [14].

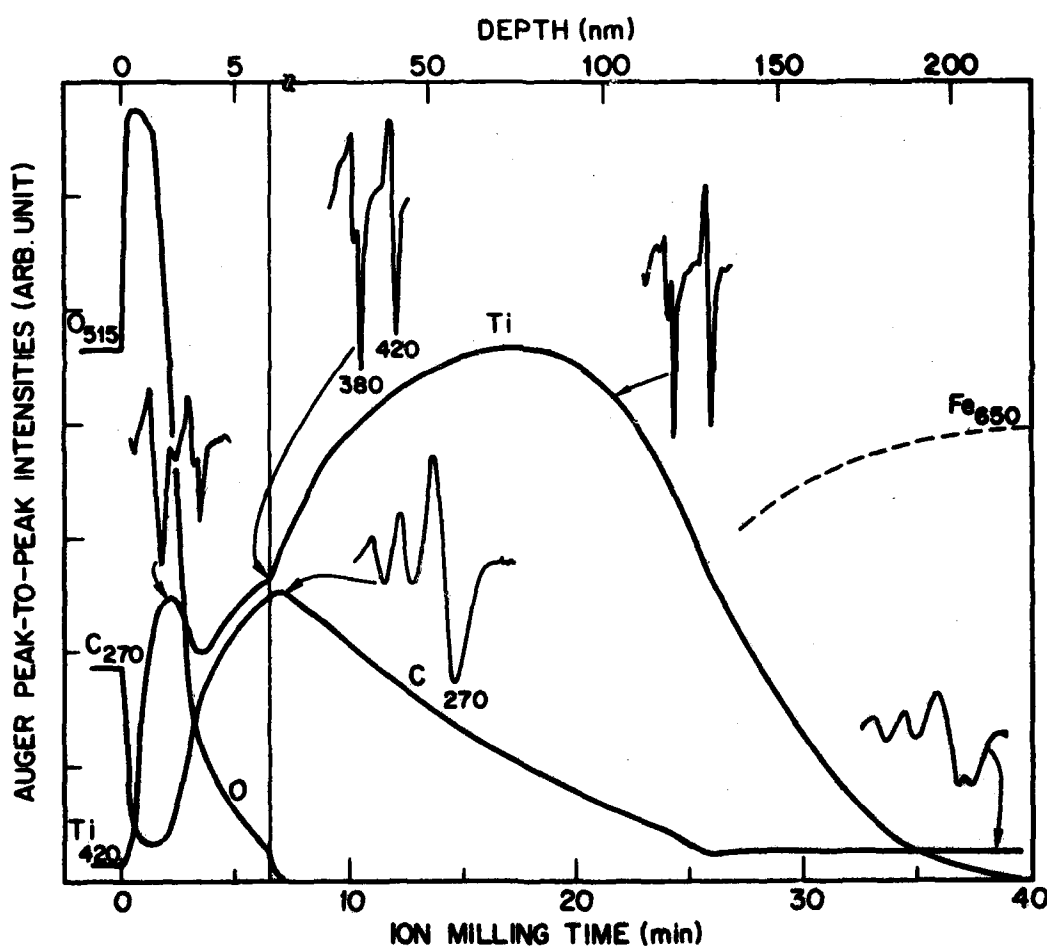


Fig. 17 — Concentration profiles for carbon, oxygen, titanium and iron for an AISI-52100 specimen implanted with 5×10^{17} Ti ions/cm². The profiles were determined from Auger electron spectroscopy measurements taken periodically during ion milling of the implanted surface. The vertical line at 7 minutes indicates a change in milling rate. Characteristic Auger peak shapes at various locations in the specimen are shown to illustrate changes in atomic bonding as a function of depth in the specimen.

V. EXPERIMENTAL RESULTS

The experimental program conducted as part of this evaluation was designed to provide a quick screening of the materials system concepts described in Section IV so as to provide guidance for the most promising system for application of ion implantation. Experimental tests for wear behavior are numerous because of the difficulty in correlating the different types of wear and the complexity of the conditions controlling wear. The wear of cutting tools is one of the most severe forms of wear with unlubricated metal-to-metal contact under stresses approaching the yield stress. Several tests were selected to evaluate the ion implanted cutting tools: a pin-on disk test commonly used to evaluate sliding wear, an instrumented lathe test used to measure cutting forces and flank wear under carefully controlled conditions, and some actual machining tests with several diameters of end mills and drills. The results of each of these tests in which ion implanted specimens are compared with unimplanted specimens is given in the following sections. The conditions of ion implantation are also described.

A. Ion Implantation

The implantations were performed on a Varian/Extrion medium current semiconductor implanter adapted by NRL for metals implantations. Titanium was chosen to be implanted into the M2 tool steel on the basis of previous NRL wear studies which showed that Ti-implanted AISI 52100 bearing alloy has an abrasive wear resistance approaching that of refractory carbides. A minor effort was also devoted to implanting N and B into the surface of TiC coated Carbolloy 895 tools.

The samples were implanted on all faces experiencing wear. The M2 samples were thermally attached to the water cooled target holder so as to limit their temperature rise to less than 150°C during implantation. One group of TiC on WC inserts was implanted at low temperature and another group was intentionally thermally isolated so as to induce the diffusion and subsequent interaction of the implanted species with the TiC matrix. These samples reached a maximum temperature of 600°C for a period of about 1 hour during implantation.

The Ti implantation into the M2 cutting tool inserts was done at an energy (150 keV) and dose (5×10^{17} Ti ions/cm²) to produce an implanted region about 80 nm in depth. The N, B, and C implants into TiC were all done at two energies (75 and 150 keV) at a dose of 2.5×10^{17} ions/cm² at each energy. The dual energy implants were done in order to spread the implanted species (i.e., initially from about .1 μ m to .2 μ m).

Selected machine tools have been implanted and tested at FMC Corporation. The tools implanted and the quantity are as follows:

<u>Tool</u>	<u>Size</u>	<u>No.</u>	<u>NRL Code</u>
End Mills, 2 flute	1" diam	2 ea	1A, 1B
End Mill, 4 flute	7/16" diam	2 ea	2A, 2B
End Mill, 2 flute	3/16" diam	1 ea	3A
End Mill, 2 flute	1/4" diam	1 ea	3B
Drills	1 1/8" diam x 8" length	2 ea	4A, 4B

All tools were previously identified as M7 high speed steel by FMC.

The tools have all received an implant of 4×10^{17} Titanium ions/cm² with an implantation energy of 100 kV. The objective of this treatment is to form a thin layer of hard TiC at the surface. All tools except the 7/16", 4 flute end mill were implanted from the side while rotating the tool. The 7/16" end mill used for facing cuts was also implanted on the end to assure coverage of the cutting surfaces. The bright surface shows the area of implant. This mode of implantation would permit regrinding of the tool without removing the implanted layer on the inner surface of the flute and cutting edge.

In addition, eight M7 experimental wear discs have been implanted at the same energy and fluences as above for the purpose of conducting laboratory pin-on disc wear measurements.

B. Instrumented Lathe Tests

The instrumented lathe tests were the primary vehicle for evaluation of the effect of ion implantation on the machining parameters and tool life. The tests were conducted by Professor S. Ramalingam of Georgia Institute of Technology in his laboratory. This test provides a quantitative evaluation of the cutting forces on a lathe tool as a function of cutting speed and a measurement of wear rate from the flank wear of a tool under carefully controlled conditions.

Test Conditions. Two series of tests are in progress to evaluate the possible benefits of ion implanting cutting tools for machining applications. The first series of tests are cutting force measurement studies to assess the effect of ion implantation on the tool-chip interface friction and on the specific power consumption during machining. The second series of studies are concerned with the effect of ion implantation on tool wear.

Fully hardened unimplanted and ion implanted M2 high speed steel inserts were used in these studies. Unimplanted cutting tool edges were compared with those implanted with titanium ions (150 keV ions; 5×10^{17} ions/cm² fluence).

An annealed carbon steel (4140) was machined in a 7.5 kW (10 hp) lathe equipped with a continuously variable speed drive. The lathe is instrumented with a Kistler 3-component dynamometer, charge amplifiers, recorders and digital speed indicators. The Kistler 3-component dynamometer measures the principal cutting forces exerted on a lathe tool bit as illustrated in Fig. 18. F_c - the cutting force is the major force component on the tool and is parallel to the direction of movement of the metal being removed prior to shearing by the cutting edge. The force, F_f , is the feed force normal to the surface of the work piece while the force F_R is the radial force which is zero in orthogonal cutting. Figure 19 shows a schematic diagram of the piezoelectric cutting force instrument in the form of a tool holder and the signal processing and readout system used for the measurements. Full details of the measurement system are provided in ref [15].

For all tests, the cutting tool inserts were held in a standard square insert tool holder with a 6° rake position during machining. To simulate semi-orthogonal cutting, an approach angle of 5° was used in the force measurement tests. In tool wear tests (flank wear studies), the normal 15° approach angle was used. Figure 20 illustrates the tool geometry used during machining for the cases described above.

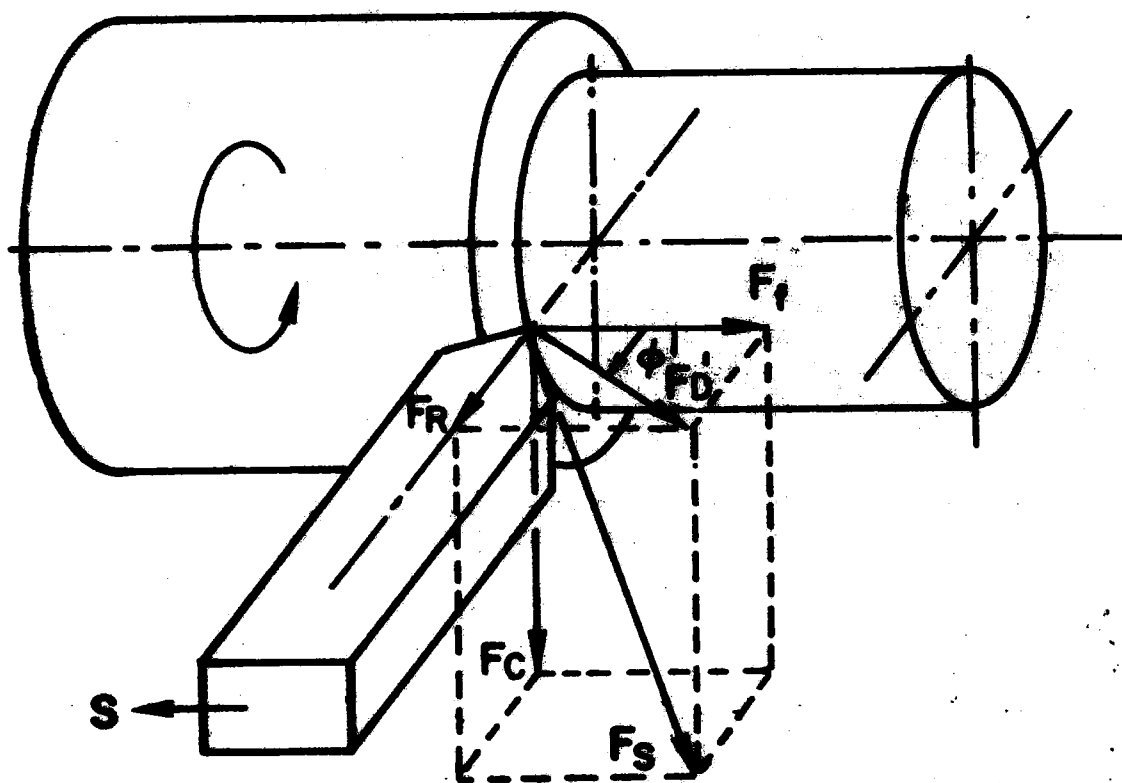


Fig. 18 — Geometry and cutting forces for a lathe tool. F_c is the cutting force, F_f is the feed force, and F_r is the radial force.

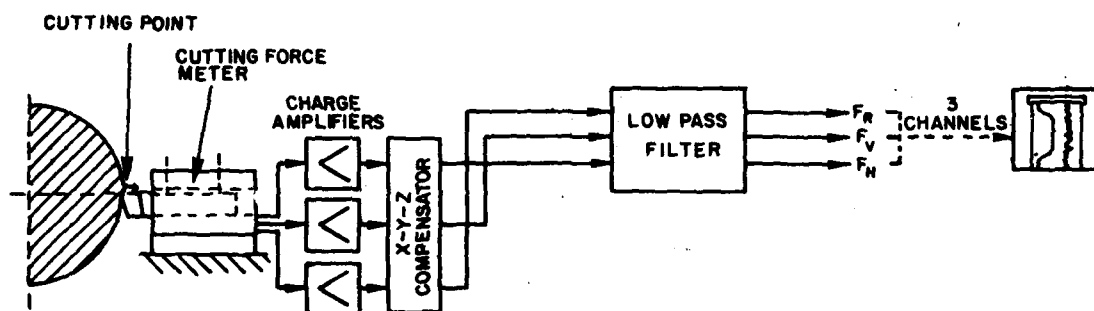
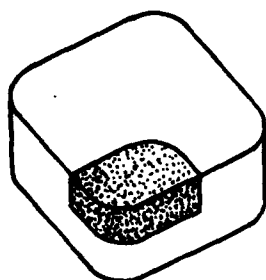
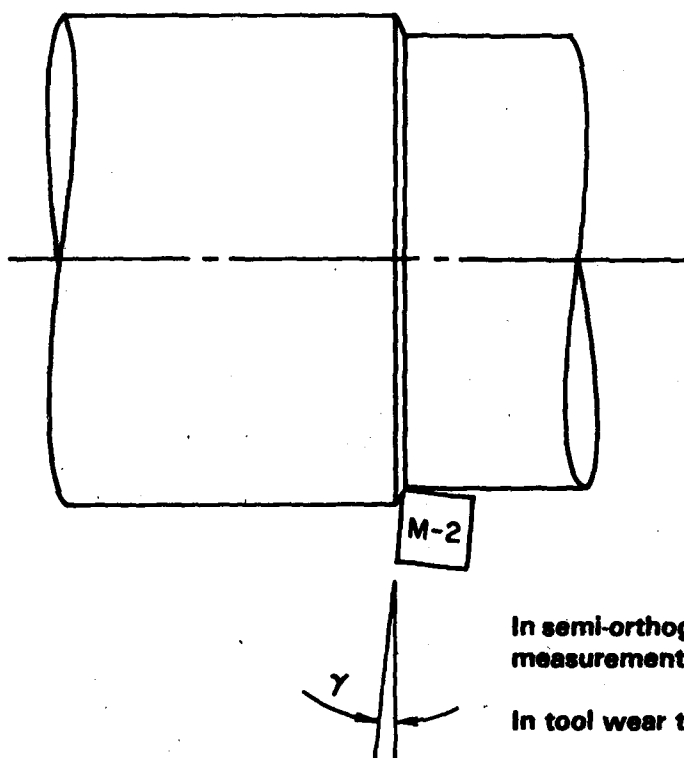


Fig. 19 — Block diagram showing the principal components of the system used to measure cutting forces on the lathe tool bit



Schematic illustration of ion implanted, $1/2" \times 1/2"$ high speed steel tool inserts. Crater face and flank faces were implanted with 150 keV titanium ions. Implanted region is shaded.



In semi-orthogonal cutting tests for force measurements, $\gamma = 5^\circ$ was used.

In tool wear tests $\gamma = 15^\circ$ was used.

Fig. 20 — Geometry used for semi-orthogonal cutting tests

Test Results. Ion implanted M2 high speed steel inserts (6° positive rake) and TiC-coated cemented carbide inserts (6° negative rake) have been used to machine a medium carbon steel in an instrumented lathe. Measured force components have been used to determine the effective friction coefficient at the tool-chip interface during machining. An orthogonal cutting mode (simulation of two-dimensional cutting) was used for the high speed steel inserts and a semi-orthogonal cutting mode (oblique cutting) was used for the TiC-coated carbide inserts.

The test results obtained are summarized in Tables 3 through 5. They show the data from the orthogonal cutting tests for triple replication on the same bar of material. All three tests show a reduction in the cutting force for the ion implanted tools which is reflected in the lower power measurements for the tests. No consistent or discernable trends can be detected in the tool-chip interface effecting friction coefficients calculated for the tests.

Flank wear tests were carried out on the same lot of steel. The tests were carried out at a cutting speed of 33.5 m/min., with a depth of cut of 1.5 mm and a feed rate of 0.125 mm/revolution. The speed and feed were chosen to obtain a flank wear of the order of 0.2 mm in some 20 minutes of cutting tests (actual cutting time). The results obtained are shown in Fig. 21. While the unimplanted tool yielded a flank wear of approximately 0.25 mm in 10 minutes of cutting, the implanted tools did not produce a wear land of 0.20 mm in 20 minutes of cutting. The tests were run without lubrication.

Tool wear tests under controlled laboratory conditions unambiguously show that titanium ion implantation leads to a lowering of flank wear rate in M2 high speed steel tools.

Data for the TiC-coated carbide inserts is shown in Tables 6 and 7 and Fig. 22. The nitrogen, boron, and carbon implants were all done at two energies (75 and 150 keV) to broaden the implant profile. A dose of 2.5×10^{17} ions/cm² was implanted at each energy for all three ion species. The force measurement results show lower cutting forces for the carbon implanted tools at all cutting speeds and somewhat higher cutting forces for the nitrogen and boron implanted tools. The measured friction coefficients as shown in Table 6 are higher than the unimplanted tools at low cutting speeds but decrease to a value below the unimplanted tool at the upper end of the useful cutting speed range for TiC-coated carbide inserts (approximately 200 meters per minute). The specific power also appears to be lowered by ion implantation especially for the carbon implant. Further experiments are in progress to evaluate the effect of a higher temperature implant which should assist the formation of the refractory nitrides and borides.

Additional data of relevance to the current investigation but as yet unpublished were obtained by Carosella and Ramalingam. It is reproduced here with their kind permission. The material-implant systems were of two types, a straight 94WC-6Co grade implanted with carbon to harden the Co binder and a 94WC-6Co grade with a TiC coating which was a preliminary study of the effects of carbon, nitrogen, and boron on wear performance of TiC. The uncoated 94WC-6Co type is a "cast iron cutting grade" (CI) while the TiC coated type is typically used for the machining of steels. The CI cutting grade tool inserts, Carboloy Grade 895, were implanted with C⁺ at 25 and 50 keV. The TiC-coated tools were implanted with carbon, boron and nitrogen ions.

Unreplicated machining tests carried out on hot-rolled steel bars of AISI

Table 3 - Orthogonal cutting (two dimensional cuttings) test data. Comparison of implanted and unimplanted M-2 high speed steel tools. Width of cut = 2.54 mm and feed rate = 0.125 mm/rev. at indicated cutting speed.

Cutting Speed	F_c	F_t	μ	ΔP
m/min	Newtons	Newtons		%
<u>Datum: Unimplanted tool</u>				
20	859	368	0.56	
25	827	364	0.57	
30	788	355	0.58	
35	772	337	0.57	
40	756	328	0.56	
45	725	326	0.58	
50	693	309	0.58	
<u>Implanted Tool</u>				
20	789	355	0.59	- 8.14
25	749	337	0.58	- 9.43
30	725	327	0.58	- 7.99
35	693	319	0.59	- 10.23
40	678	314	0.60	- 10.31
45	662	309	0.60	- 8.68
50	638	305	0.61	- 7.93

Preliminary data indicates (column 5) that specific power consumption for metal removal is lowered by ion implantation.

Significant effect on 'friction' is not noted

Table 4 - Orthogonal cutting (two dimensional cuttings) test data. Comparison of implanted and unimplanted M-2 high speed steel tools. Width of cut = 2.54 mm and feed rate = 0.125 mm/rev. at indicated cutting speed.

Cutting Speed	F_c	F_t	μ	ΔP
m/min	Newtons	Newtons		%
<u>Datum: Unimplanted tool</u>				
20	847	405	0.61	
25	792	378	0.61	
30	764	369	0.62	
35	749	365	0.62	
40	733	360	0.63	
45	717	352	0.63	
50	693	338	0.62	
<u>Implanted Tool</u>				
20	804	352	0.57	- 5.07
25	768	343	0.58	- 3.03
30	744	334	0.58	- 2.61
35	725	325	0.58	- 3.20
40	697	312	0.58	- 4.91
45	678	307	0.59	- 5.43
50	662	303	0.59	- 4.47

Preliminary data indicates (column 5) that specific power consumption for metal removal is lowered by ion implantation.

Significant effect on 'friction' is not noted

Table 5 - Orthogonal cutting (two dimensional cuttings) test data. Comparison of implanted and unimplanted M-2 high speed steel tools. Width of cut = 2.54 mm and feed rate = 0.125 mm/rev. at indicated cutting speed.

Cutting Speed	F_c	F_t	μ	ΔP
m/min	Newtons	Newtons		%
<u>Datum: Unimplanted tool</u>				
20	851	409	0.62	
25	843	405	0.62	
30	804	378	0.61	
35	784	369	0.61	
40	756	365	0.59	
45	737	358	0.62	
50	721	356	0.63	
<u>Implanted Tool</u>				
20	717	334	0.60	- 15.74
25	693	332	0.61	- 17.79
30	662	320	0.62	- 17.66
35	646	318	0.63	- 17.60
40	642	316	0.63	- 15.07
45	640	307	0.60	- 13.16
50	634	303	0.61	- 12.06

Preliminary data indicates (column 5) that specific power consumption for metal removal is lowered by ion implantation.

Significant effect on 'friction' is not noted

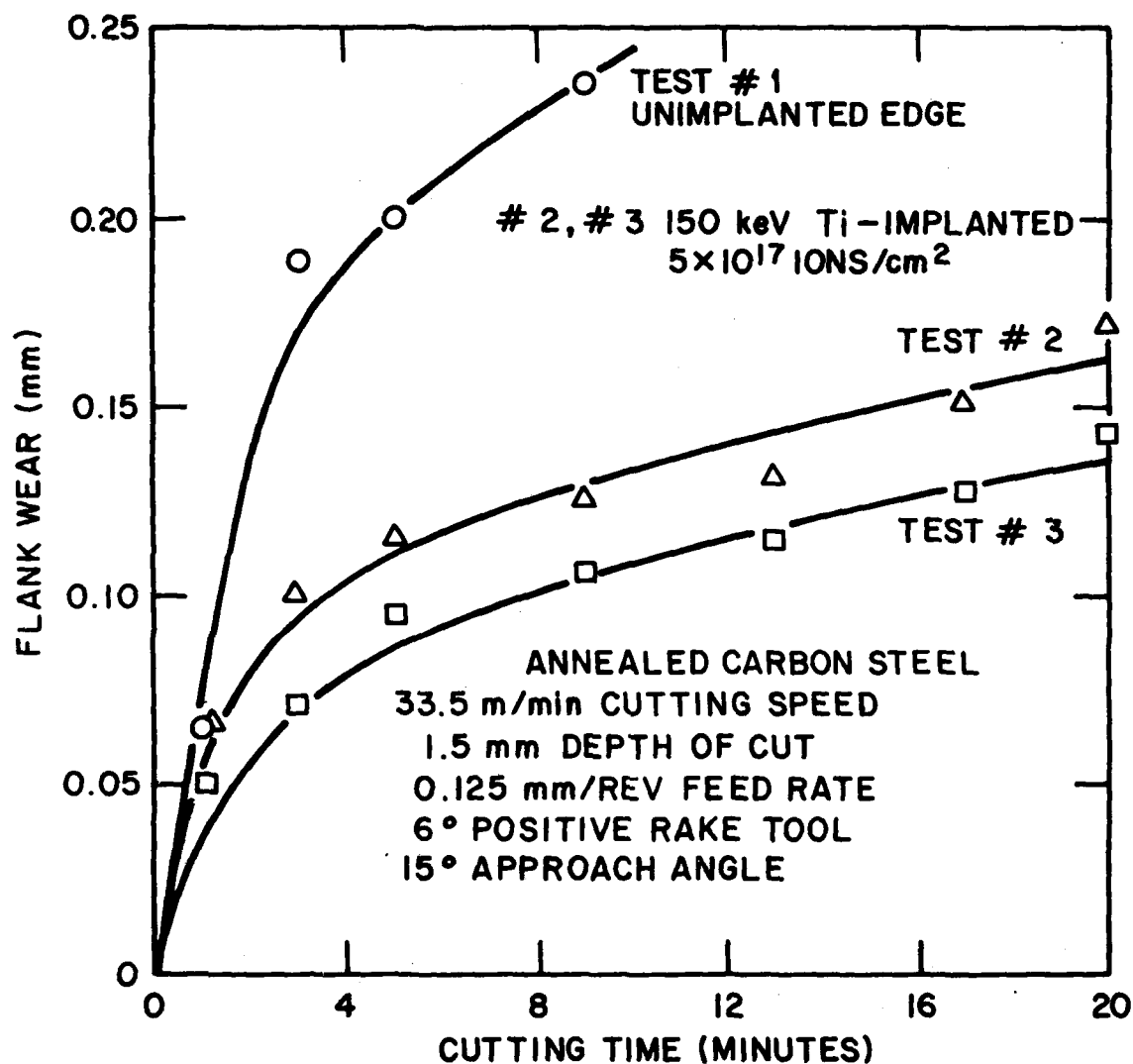


Fig. 21 — Comparison of tool wear characteristics of unimplanted and titanium implanted M2 high speed steel tool inserts

Table 6 - Effect of ion implantation on the tool-chip 'friction' during machining as a function of cutting speed. A medium carbon steel was machined with TiC coated WC tool inserts.

Cutting Speed meters/min	Measured friction coef. in semi-orthogonal cutting		
	Unimplanted	<u>Carbon implanted</u>	<u>Boron implanted</u>
100	.660	.725	.741
130	.709	.704	.712
160	.704	.695	.699
190	.700	.686	.681
220	.698	.664	.625
			<u>Nitrogen implanted</u>
			.734
			.728
			.713
			.693
			.685

Preliminary test data when machining a medium carbon steel.

Measured test data are shown in Figure 22 attached.

Table 7 - Effect of ion implantation on the specific power consumption* in machining. Percent change is tabulated with the unimplanted tool as the datum.

Cutting speed m/min.	Implanted Species		
	Carbon	Boron	Nitrogen
100	- 11.4	+ 2.3	+ 5.7
130	- 1.9	+ 4.6	+ 1.9
160	- 2.0	- 4.6	- 1.0
190	- 6.2	- 0.1	- 4.5
220	- 7.7	0	- 4.7

*Specific power
consumption

=

Power dissipated per unit
volume of metal removed.
Includes the deformation
and frictional component.

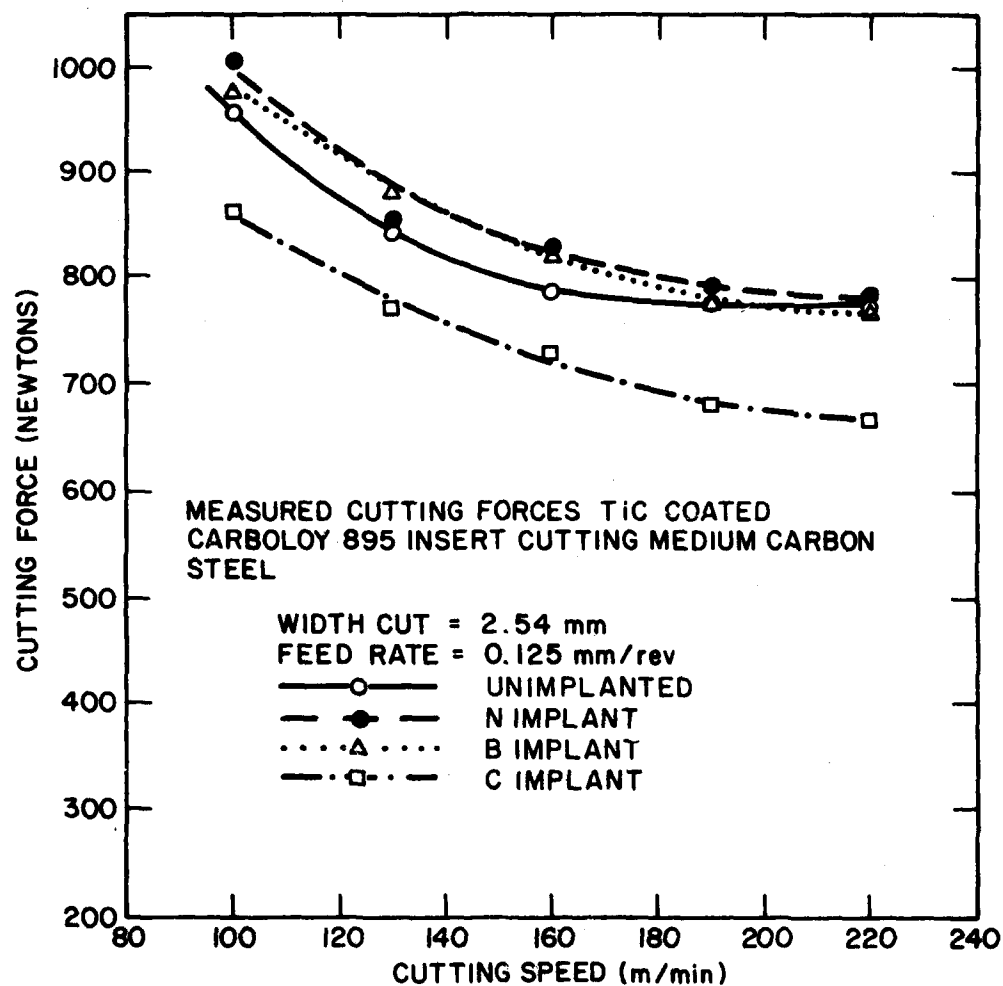


Fig. 22 — Comparison of the cutting force, F_c , measured on unimplanted and C implanted TiC coated tool bits of carboly grade 895 cemented tungsten carbide during machining of a medium carbon steel

1045 chemistry with implanted CI-grade tool inserts showed that carbon implantation had no significant effect either on the flank wear or on the crater wear (see Fig. 23). Typically, the wear tests were carried out at a cutting speed of the order of 100 m min⁻¹ with a depth of cut of 1.5 mm and a feed rate of 0.125 mm Rev⁻¹. The carbon-implanted tools were found to lower the cutting forces by some 10 to 20 percent while machining cast iron as shown in Fig. 24.

The TiC-coated tools were tested by machining the same steel as in the case of uncoated tools. In this instance, the measured cutting forces are the same with and without implantation (Fig. 25). The 30-minute tool life tests (1.5 mm depth of cut; 0.125 mm Rev⁻¹ feed rate) show that while boron and nitrogen lower the flank wear rate, the carbon-implanted tool exhibits a higher wear rate (Fig. 26).

The above results from the instrumented lathe tests show some definite modifications in tool performance can be achieved by ion implantation. The M2 high speed implants with titanium lowered the cutting force and specific power requirements and reduced the rate of tool wear by a factor of two in the machining of annealed 4140 steel. Implants of TiC-coated cutting tools showed a less pronounced effect but may not have received the optimum heat treatment to produce a fully hardened coating. Previous experiments on C, N and B implants of TiC coatings had shown a 20 percent reduction in flank wear for the B and N implants when machining a hot rolled AISI 1045 steel.

C. Service Tests of Ion Implanted Tools

The final test of ion implantation as a means to improve wear resistance of metal cutting tools was the service testing of a selection of end mills and drills at FMC Corporation, Northern Ordnance Division, Minneapolis, MN. The tools selected for testing are shown in Fig. 27 following implantation with 4×10^{17} Ti ions/cm². All the tools except the 7/16 in. diameter end mills were implanted from the side while rotating the tool. The 7/16 in. diameter mill was also implanted from the end.

The end mills were evaluated in typical service operations by noting the performance of implanted and unimplanted tools on identical machining operations with identical operating parameters. The machining applications are summarized in Table 8. Materials used in the tests were hot rolled AISI 4140 and cold forged AISI 4340 steels. A water soluble oil lubricant, "Trimsol," manufactured by Master Chemical Corporation of Perrysburg, OH, was used in all tests. The tool materials used in the service tests were designed to provide a limited comparison between an implanted tool and an unimplanted tool from the same manufacturer and the same lot of materials. In the case of the 7/16 in. diameter end mills both unimplanted controls broke under atypical conditions so no direct comparison is possible. The current stock tool, a Japanese product with a proprietary composition, was substituted. In the case of the 1/4 in. and 1 in. diameter end mills, Japanese products known to contain cobalt in some cases, were also added to the test for comparison purposes.

Observations of the wear performance are compared in Table 9. The tests were of two types. One performed with numerically controlled machines used the criteria that the tool bit was removed from service when the machine could no longer compensate for tool wear. Measures of wear in those tests were number of parts machined and the change in diameter of the tip of the tool. The other test involved machining under the observation of a machinist with the unimplanted tools pulled from service when the surface finish or chip formation characteristics indicated the tool cutting edge had deteriorated. The implanted tools were run for the same length of

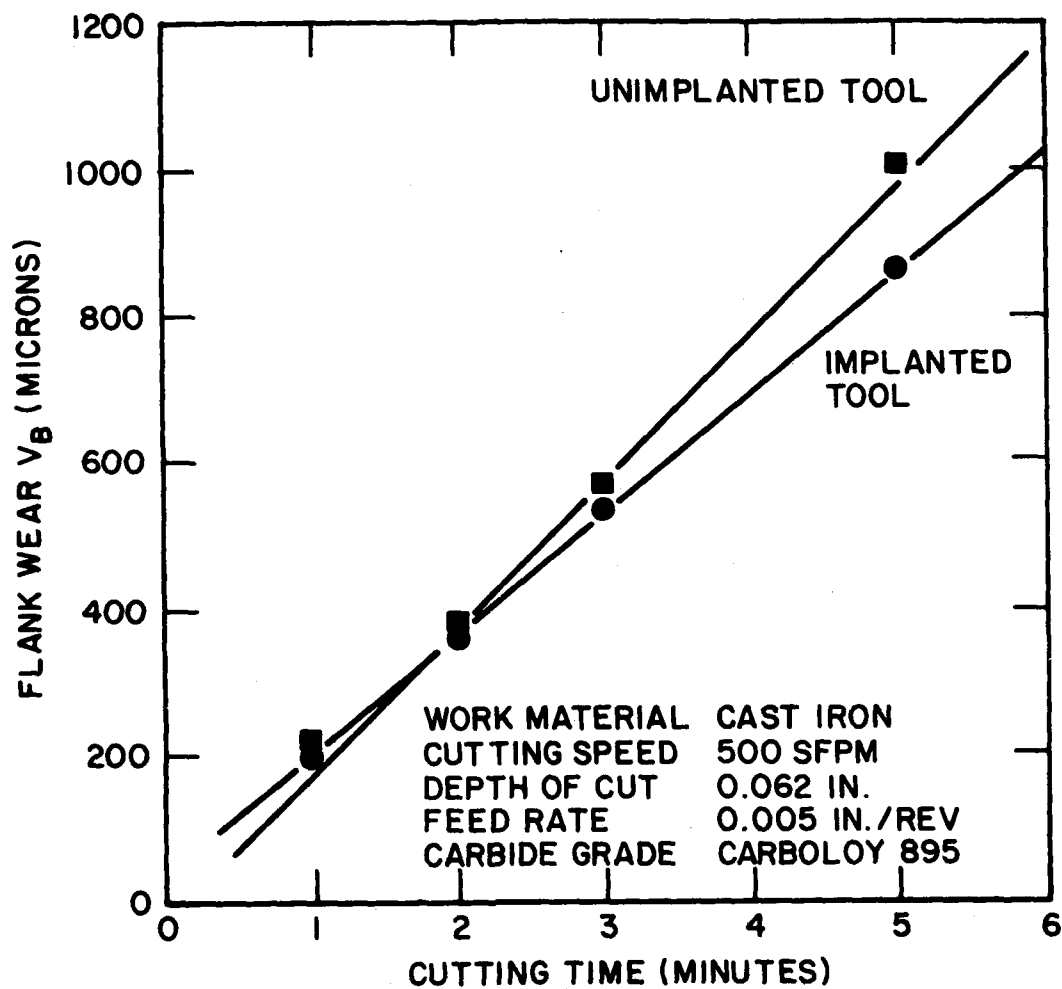


Fig. 23 — Effect of carbon implantation on flank wear while machining cast iron with 94WC-6 Co cutting tool

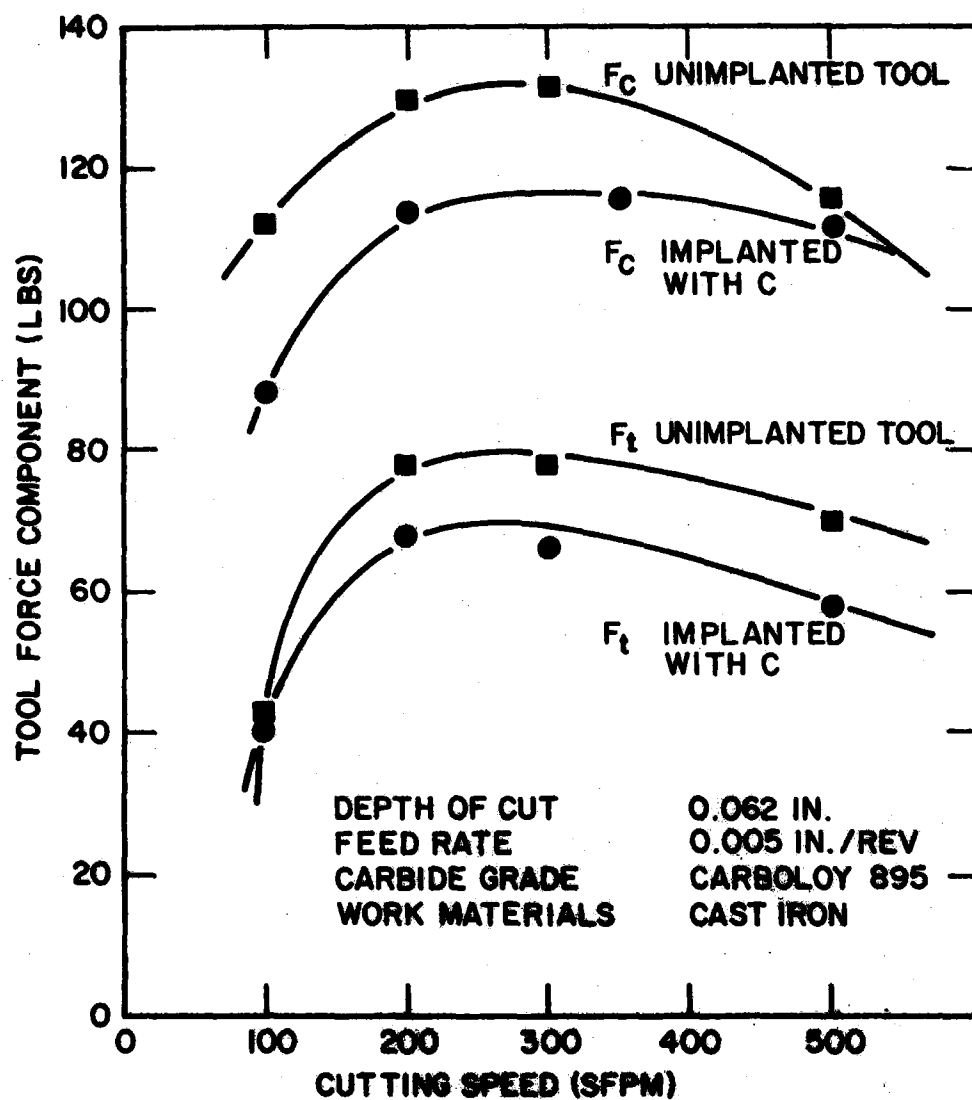


Fig. 24 — Cutting forces measured while machining cast iron with carbon implanted and unimplanted 94WC-6 Co cutting tool

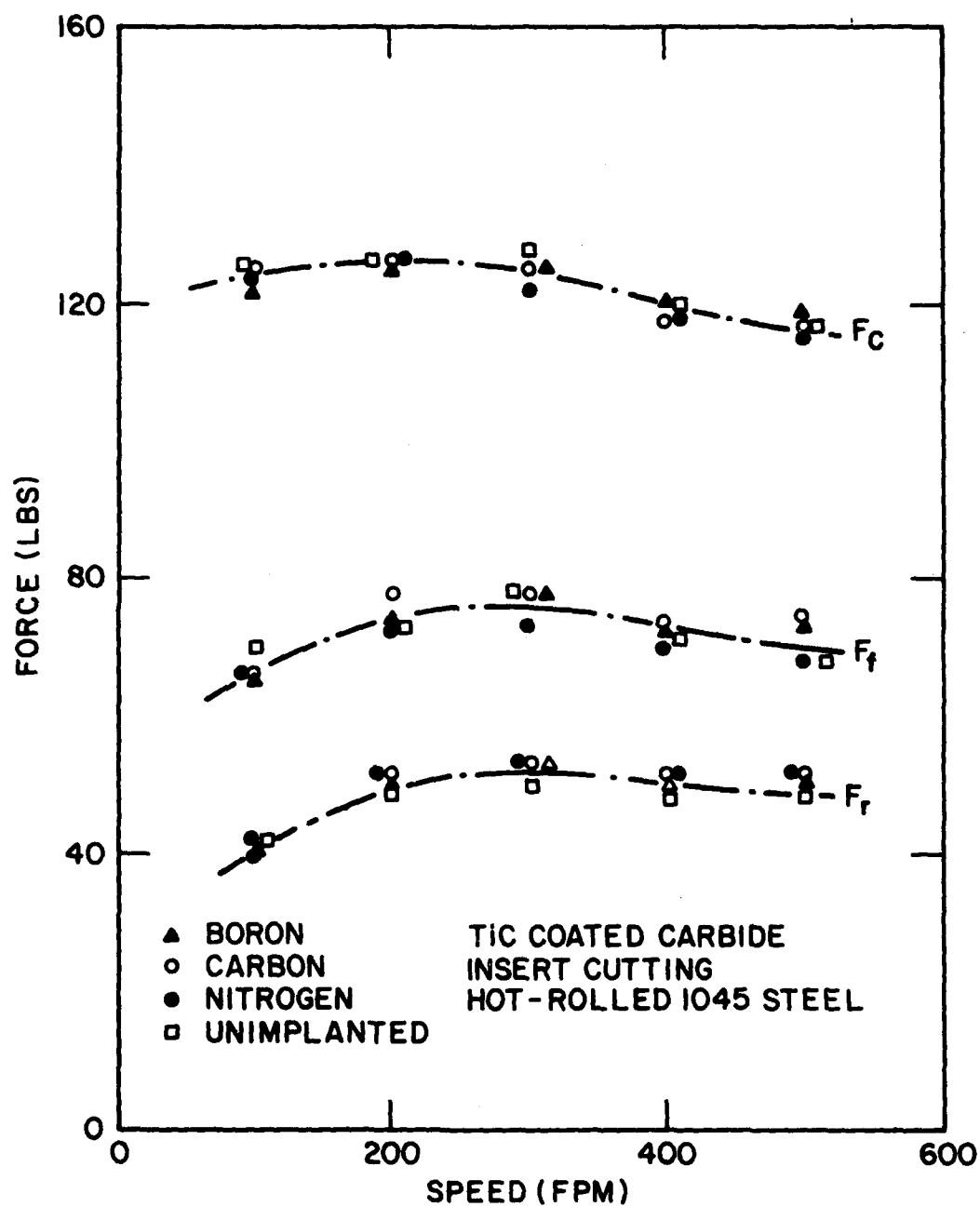


Fig. 25 — Cutting forces measured while machining hot-rolled 1045 steel with implanted and unimplanted TiC coated cemented tungsten carbide tool inserts

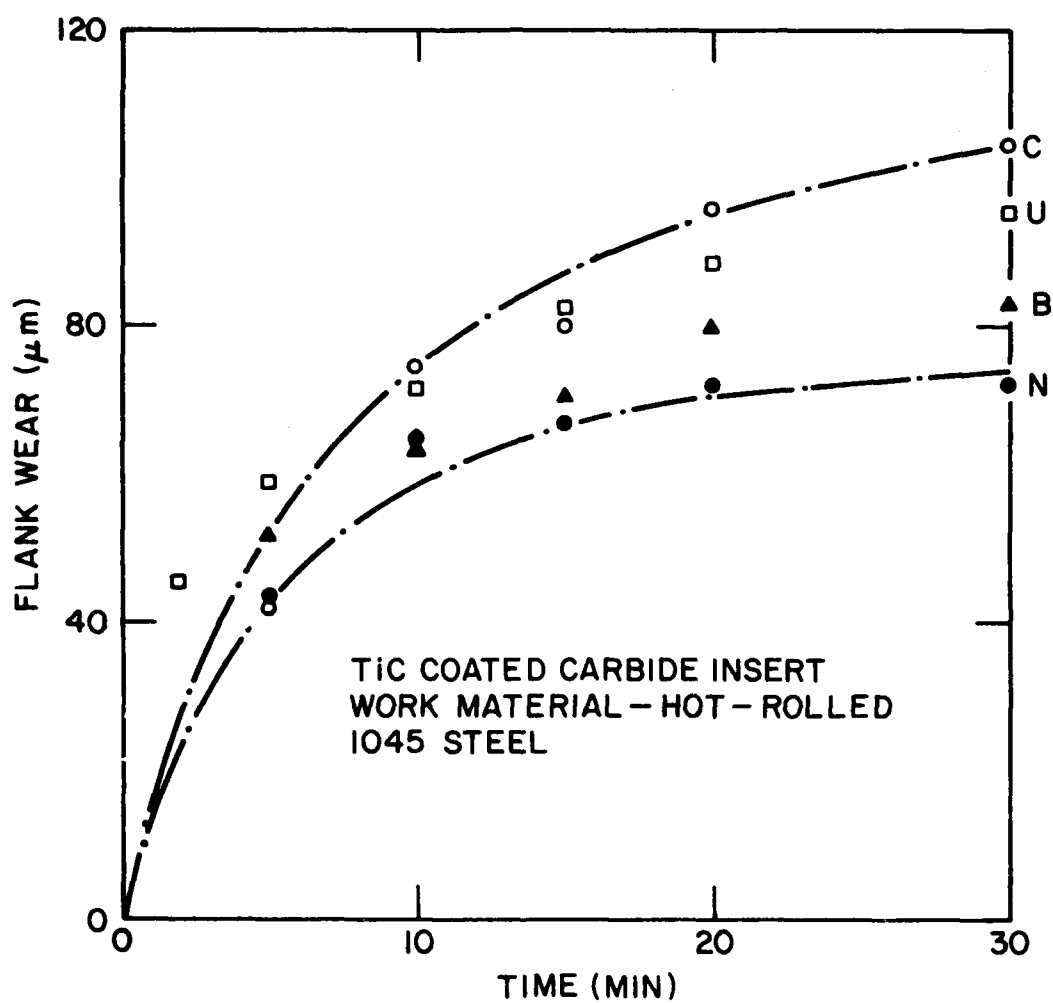
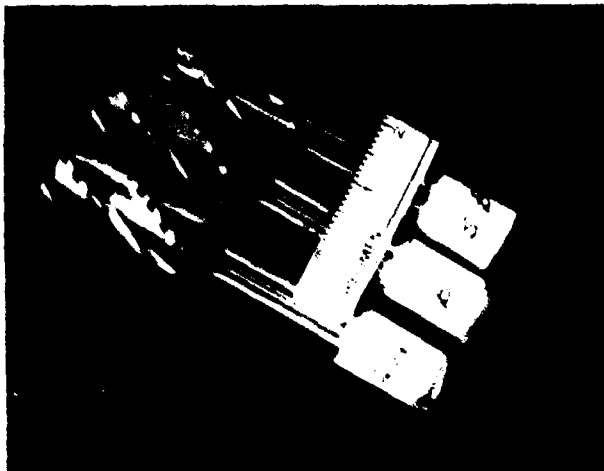


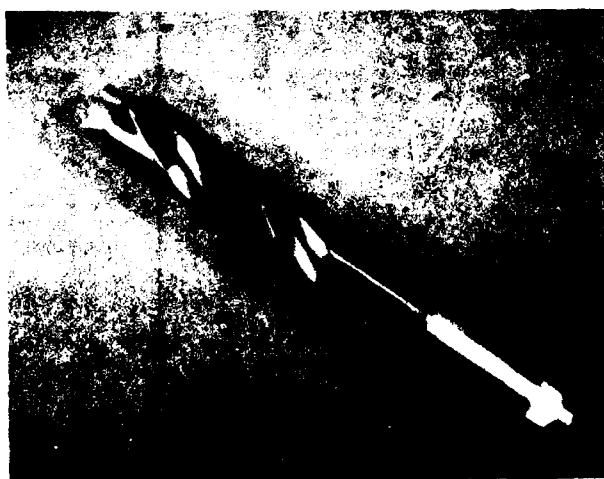
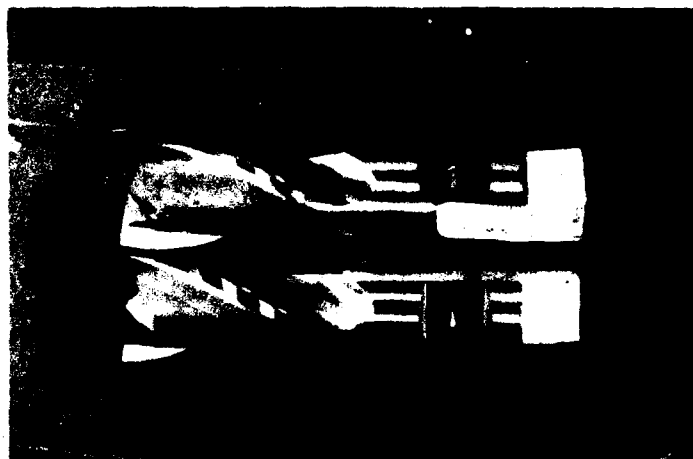
Fig. 26 — Effect of implantation on flank wear while machining a hot-rolled 1045 steel with TiC coated cemented tungsten carbide tool inserts



**7/16" DIAM. END MILLS
AND 1/4" DIAM. END MILL
IMPLANTED WITH
TITANIUM IONS.**

1 × PHOTO

**1" DIAM. END MILLS
IMPLANTED WITH
TITANIUM IONS
0.7 × PHOTO**



**1 1/8" DIAM. × 8" DRILL
IMPLANTED WITH TITANIUM
IONS**

0.36 × PHOTO

Fig. 27 — End mills and drills implanted with Ti for service tests of tools

R-142

TABLE 8

Machining Applications

Tool	Description of Machining Operation	Operating Parameters	Material
End Mill 7/16" - 4 flute	Face and Mill Slot Cut Parameters W = .438" d = .219 L = 40 - 65"	62 Surface ft/min Machining Speed 1.1 and 1.5 in./min Feed Rate	4140 HR Plate BHN 205-212 Trimsol Lubricant
End Mill 1/4" - 2 flute	Finish Mill Sides Ramp Cut Parameters d = .062" W = .125" L = 10"	58.9 Surface ft/min Machining Speed 2.3 in./min Feed Rate	E4340 CF Plate BHN 245 Trimsol Lubricant
End Mill 1" - 2 flute	Finish Mill and Face Cut Parameters W = .750: d = .125" L = 20"	65.5 Surface ft/min. Machining Speed 1-5 in./min Feed Rate	E4340 CF Plate BHN 245 Trimsol Lubricant
Drill 1-1/8" diam. x 8" long	Results not yet available.		

TABLE 9
Service Performance Tests

Tool Code Number	Condition ^a (I or U)	Hardness Rc	Tool Life	Diameter Change	Comments
<u>7/16" Diameter End Mill</u>					
1E	U (1.1 in./min) (Kobe Steel)	66.2	59 min	.004"	Poor finish-2 of 4 flutes chipped.
1F	U (1.5 in./min (Kobe Steel)	66.2	26.7 min	.0015	Tool Failure-3 of 4 flutes chipped, shaft broke.
2A	I (1.1 in./min)	64.5	59 min.	.003	No failure.
2B	I (1.5 in./min)	64.8	26.7 min.	.0025	No failure.
			+30.0 ^b	.0000	No failure.
<u>1/4" Diameter End Mill</u>					
3D ₁	U	65.1	14 parts	.003	Tests terminated. When numerical Control Machines could no longer compensate for tool wear.
3D ₂	U	63.3	13 parts	.003	
3C	U (Nipon Steel)	66.0	20 parts	.003	
3B	I	65.7	14 parts	.003	
<u>1" Diameter End Mill</u>					
1C	U (Kobe Steel 8%)	48.1	19 parts	.002	Tests terminated. When numerical Control Machines could no long compensate for tool wear
1D	U	66.9	17 parts	.001	
1A	I	64.8	14 parts	.001	
1B	I	65.8	14 parts	.003	

^aI - Implanted
^bTotal time = 56.7 Min.
U - Unimplanted

time (although they had not failed) and the tip diameter change measured.

The service tests showed mixed results. The most promising were those on the 7/16 in. diameter end mill where both unimplanted control specimens broke under atypical conditions (mill hit the case hardened section of the part). The two replacement tools, 1E and 1F, which had a slightly higher R_c hardness also failed because of chipping of the cutting edge. Tool 1F actually fractured in the shaft although this was undoubtedly induced by loss of the cutting edge. The implanted tools showed no indication of micro-chipping and one was run to twice the life of the unimplanted tool without a loss in quality of the finished product. The flute edges were examined in an SEM to determine if there were any apparent differences in the wear mode. Figure 28 shows a schematic of the region of the tool examined. The regions in the schematic diagram are most easily seen in the 100 x SEM photograph of the implanted tool in Fig. 29. The upper portion of the photograph with the deep grinding marks is on the section of the flute tapered for clearance and experiences no wear during the machining operation. The land is the 0.015 in. wide darker region from the cutting edge at the bottom of the photograph to the tapered section in the upper portion. Wear starts on the cutting edge and progressively extends across the land.

The most severe wear was on the cutting edge which in all cases was blunted. The unimplanted tool showed regions where the surface had cracked and spalled in sheets leaving rough craters behind as can be seen in the upper portion of Fig. 29. Surface cracks are also visible. This wear mode appears to be a form of surface fatigue failure. Tool 1E, which had a lower feed rate than 1F, did not show cratering but had a heavily worked surface at the cutting edge. The implanted tools, 2A and 2B, by contrast show no surface cracking or spalling but rather have more of a smeared metal appearance as can be seen in Fig. 29.

A comparison of the M7 1/4 in. diameter end mills, (Codes 3D₁, 3D₂, and 3B) showed the same performance for all three. A Nipon Steel product with proprietary composition showed substantially better performance. An optical examination of the cutting edge revealed no significant differences between the implanted and unimplanted M7 tools. Preliminary SEM examinations of the cutting edge on 3D₁ and 3B show the most severe wear is in a band 0.0034 in. wide along the cutting edge on the side of the flute. Heavy abrasive wear tracks are observed in this band with some evidence that carbides or other constituents of the microstructure have been gouged from the surface. The implanted tool 3B is very similar in appearance. The Japanese tool, 3C, has not yet been examined.

The 1 in. diameter M7 tools (1D, 1A and 1B) would tend to indicate the implanted tools had poorer performance with 14 parts produced as compared with 17 parts for the unimplanted tool. SEM examination of the worn cutting edges, however shows the wear rate as measured by the (width of worn region/No. of parts) to be the same for both implanted and unimplanted tools. Tool 1C, an 8 percent Co modification of M2 produced by Kobe Steel Company of Japan, showed substantially better performance than the non-cobalt containing materials as would be expected. The material is also unique in having a low hardness of only R_c 48 compared to the R_c 65-66 values expected for a quenched martensitic tool steel.

The observations from the service tests of the tools and SEM examinations of the cutting edges would indicate that implantation of M7 tool steel was not successful in producing a wear resistant surface layer. Abrasive wear erosion of the cutting edge was judged to be essentially the same for both implanted and unimplanted M7 end

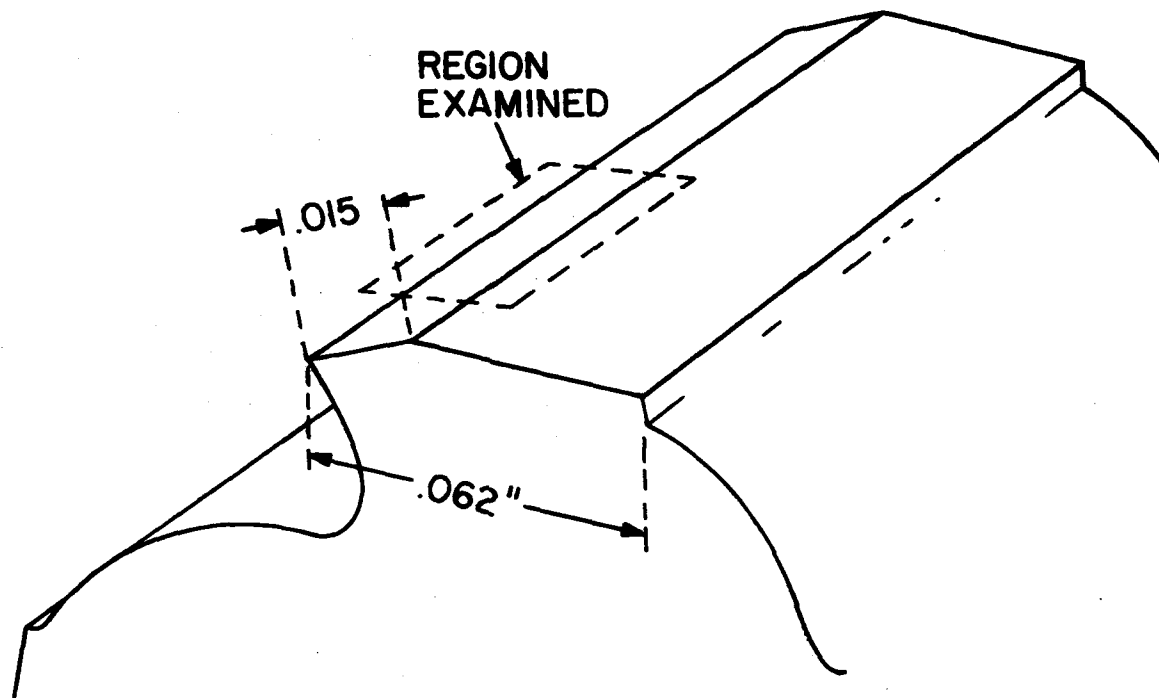
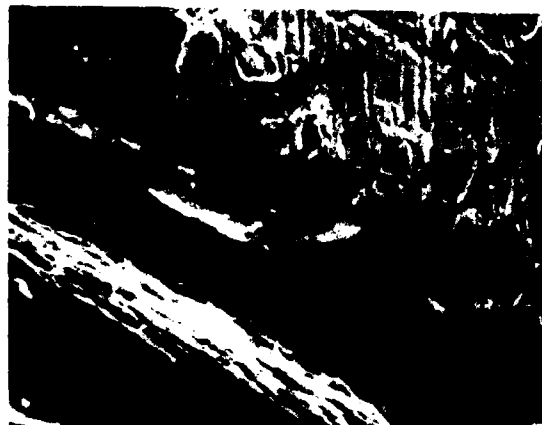


Fig. 28 — Schematic of region of flute examined in SEM photographs of Fig. 29. Wear occurs along the cutting edge and extends across the 0.015 in. wide land

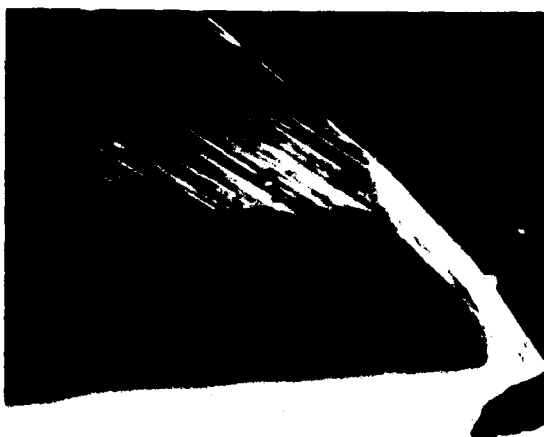


100 ×



500 ×

UNIMPLANTED TOOL



100 ×



500 ×

IMPLANTED TOOL

Fig. 29 — SEM micrographs of worn flutes on specimens 1F and 2B of the 7/16 in. diam. end mill. The lower left hand photograph shows the principal regions starting from the cutting edge at the bottom, land with wear region extending up from the cutting edge, and lighter region on back of flute with grinding marks readily visible. The unimplanted tool (top) has cracked and chipped in the worn region while the implanted tool shows abrasive wear and plastic flow along the worn surface.

R-143

mills. Some benefit may have been achieved for the 7/16 in. end mill application in which unimplanted tools fractured under the same conditions for which the implanted tools did not fail although the difference in material may also be a factor. The above results for the end mills were somewhat at variance with the observations from the lathe tests so a check was made of one of the surfaces exposed to the ion beam to ascertain if a TiC surface layer had in fact been obtained. The preliminary results showed that a thin layer of TiC had formed but the Ti concentration and the thickness of the TiC layer were less than those which produced the beneficial effects in the AISI 52100 steel. Additional details of the analysis will be provided in a future progress report. The present service tests of tools are therefore inconclusive and must be repeated at higher Ti implant levels.

CONCLUSIONS AND RECOMMENDATIONS

Ion implantation as a surface treatment technique to improve the wear resistance of materials was severely tested in this evaluation of metal cutting applications. A concept of implantation with Ti ions and subsequent reaction to produce TiC had been shown to give significant improvements in the wear performance of AISI 52100 in both unlubricated and lubricated conditions for pin-on disk tests where the normal stress was approximately one half the yield stress of the material. In the instrumented lathe tests, stresses were estimated to approach to within 10 to 20 percent of the yield stress while SEM observations of the end mill cutting surfaces showed localized regions of plastic flow. Such high surface stresses cause severe wear and abrasion of the surface layer in relatively short times. In spite of the severe conditions, ion implantation did produce measurable and consistent improvements in instrumented lathe tests where the power consumption was approximately 10 percent less than for unimplanted tools, the cutting forces were consistently lower than unimplanted tools, and the flank wear rate was roughly one half that of the unimplanted tools. The 7/16 in. diameter end mill implanted on all surfaces also showed improved performance by virtue of preventing failure of the tools by chipping and microcracking. The above effects suggest that ion implantation is modifying the surface layers involved in sliding wear. Other implant species which provide surface lubrication or are conducive to the formation of lubricating surface oxides should be explored as well as additional characterization of the wear mode and improvements in the post-implant reaction process to form TiC in alloy tool steels.

The fact that some beneficial effects of ion implantation were observed under these severe unlubricated wear conditions helps establish the efficacy of ion implantation as a surface wear treatment for lighter load, lubricated conditions such as rolling contact bearings, electrical contacts, and slip rings. The inconclusive end mill service tests need to be repeated with a higher Ti implant level to determine if the implanted cutting edge can withstand wear when conditions are optimum for formation of a thicker layer of TiC.

ACKNOWLEDGMENTS

This evaluation was performed with funding provided by Naval Sea Systems Command, Surface Warfare Systems Division. The authors wish to thank Mr. G. Brown/NAVSEA062 for his assistance and encouragement, Mr. E. Wigand and Mr. D. Brazys of FMC Corporation, Northern Ordnance Division, for providing the service tests of the implanted tools, and Mr. J. Reed, NRL, for performing the SEM examination of the tools.

REFERENCES

1. M. C. Shaw, "Principles of Material Removal," Vol. 1, ICM-3, Cambridge, England, pp. 227-253, August 1979.
2. "Ion Implantation as a New Surface Treatment Technology," National Materials Advisory Board Report, NMAB-349, Washington, DC (1979).
3. G. Dearnailey, "Practical Applications of Ion Implantation" in Ion Implantation Metallurgy, D. M. Preece and J. K. Hirvonen (Eds.), Metallurgical Society of AIME, Warrendale, PA, pp. 1-20, 1980.
4. E. M. Trent, "Wear of Metal-Cutting Tools," in Wear, Vol. 13, Treatise on Materials Science and Technology, D. Scott (Ed.), Academic Press, New York, pp. 443-488, 1979.
5. N. P. Suh, "New Theories of Wear and Their Implications for Tool Materials," Wear, Vol. 62, pp. 1-20, 1980.
6. ASM Handbook Committee, "Materials for Cutting Tools," Vol. 3, Machining, 8th Edition, Metals Handbook, American Society for Metals, Metals Park, OH, pp. 311-332, 1967; "Wear Resistance" in Vol. 1, Properties and Selection: Iron and Steels, 9th Edition, Metals Handbook, American Society for Metals, Metals Park, OH, pp. 597-638, 1978.
7. S. Ramalingam and J. D. Watson, "Inclusion Chemistry Control for Machinability Enhancement in Steels," Materials Science and Engineering, Vol. 43, pp. 101-108, 1980.
8. S. Ramalingam and G. Faulring, "An Experimental Validation of the Abrasive Tool Wear Theory and the Conceptual Design of Ferrous Alloys for Machinability," Proceedings of the 6th North American Metal Working Research Conference, Gainesville, FL, 1978, Soc. Manuf. Engrs., Detroit, MI, pp. 290-297, 1978.
9. T. S. Eyre, "Wear Resistance of Metals," in Wear, Vol. 13, Treatise on Materials Science and Technology, D. Scott (Ed.), Academic Press, New York, pp. 363-441, 1979.
10. R. H. Philipson and A. Ravindran, "Application of Mathematical Programming to Metal Cutting," Mathematical Programming Study 11, pp. 116-134, 1979, North Holland Publishing Co., The Netherlands.
11. C. A. Carosella, I. L. Singer, R. C. Bowers and C. R. Gossett, "Frictional Wear Reduction of Bearing Steel via Ion Implantation" in Ion Implantation Metallurgy, C. M. Preece and J. K. Hirvonen (Eds.), Metallurgical Society of AIME, Warrendale, PA, pp. 103-115, 1980.
12. I. L. Singer, C. A. Carosella, and J. R. Reed, "Friction Behavior of 52100 Steel Modified by Ion Implanted Ti," Proceedings, Ion Beam Modification of Materials Conference, Albany, NY, July 1980.
13. J. A. Sprague, Naval Research Laboratory, private communication, 1980 (see also Ref. 12).

14. S. Ramalingam, Georgia Inst. of Tech., private communication on Strengthening Concepts for TiC, October 1980.
15. K. Langhammer, "Cutting Forces as Parameters for Determining Wear on Carbide Lathe Tools and as Machinability Criterion for Steel," The Carbide Journal, May-June 1976.

Section II.B

THE EFFECT OF ION IMPLANTATION ON FRETTING FATIGUE IN T1-6Al-4V

R. G. Vardiman,¹ D. Creighton,² G. Saliver²
A. Effatian,² and B. B. Rath¹

¹Physical Metallurgy Branch
Material Science and Technology Division
Naval Research Laboratory

²Department of Mechanical and Aerospace Engineering
University of Missouri-Columbia
Columbia, Missouri 65201

This work was sponsored by the Office of Naval Research.

The Effect of Ion Implantation on Fretting Fatigue in Ti-6Al-4V

R. G. Vardiman⁽¹⁾, D. Greighton⁽²⁾, G. Salivar⁽²⁾,
A. Effatian⁽²⁾, and B. B. Rath⁽¹⁾

ABSTRACT

The effect of fretting on the fatigue life of titanium alloys is known to be severely deleterious. A preliminary study shows ion implantation to hold great promise for improving fretting fatigue life in Ti-6Al-4V.

Carbon implanted at 75 keV to a dose of 2×10^{17} at/cm² gives a peak concentration of 30 atomic percent at approximately 1700 Å depth. Incoherent particles of TiC averaging 100 Å in size were found by TEM. Fatigue samples were subjected to fretting on one surface at a normal stress of 20.7 MPa. Significant improvement in lifetime was found. No difference in the mode of failure was observed between implanted and unimplanted specimens.

INTRODUCTION

The reduction of fatigue life due to fretting has been identified as a serious problem in a wide variety of structural alloys and components (1). Particularly in the case of titanium alloys, the reduction in lifetime and endurance limit has been shown to be severe (2). Although various methods have been proposed to reduce the effect of fretting (1), none has proven satisfactory in all respects.

Ion implantation has been shown to improve the resistance of metals and alloys to surface sensitive phenomena such as wear, fatigue, and corrosion (3). Since all three of these phenomena occur concurrently during fretting fatigue, implantation of suitable ions would appear an excellent prospect for improvement of material lifetime under these conditions.

Ion implantation begins with the formation of an ionized plasma from either a sputtered source or a dissociated gas. The ions are passed through a magnet and the isotope of interest is selected and then accelerated to energies typically in the range of 25 to 200 keV. Fig. 1 illustrates this procedure for implantation of chromium in any target using the NRL implanter. Following a series of successive collisions with the lattice atoms, the ions imbed in the target forming roughly a gaussian distribution of the implanted species at depths ranging from hundreds to several thousand angstroms. The incident ions also knock target atoms out of their lattice positions creating a damage layer consisting of interstitials, vacancies, and dislocation loops. This damage can become extremely heavy at ion doses of 10^{16} at./cm² or greater, which are typically used for mechanical property improvements.

(1) Material Science and Technology Division, Naval Research Laboratory, Washington, D. C. 20375

(2) Dept of Mechanical and Aerospace Engineering, University of Missouri-Columbia, Columbia, Mo. 65201

For implants of light atoms such as carbon or nitrogen sputtering of the target surface is negligible, and peak concentrations of 40 atomic percent or greater can be obtained, most of which is retained in solution. Such metastable surface alloys are unique, and have exhibited effects on surface sensitive properties quite out of proportion to the thickness of the layer directly affected by the implantation.

At the present time, no implanted species is known to give substantial improvement in both oxidation and wear resistance of structural alloys. The oxidation of titanium at 600°C was improved by implantation of alkaline earths and divalent lanthanides [4]. Among these, barium was reported to improve fretting fatigue in Ti-6Al-4V [5]. No wear studies on ion implanted titanium have been published, but carbon implantation has been shown to give considerable improvement in abrasive wear resistance [6]. Carbon also gives a strong increase in fatigue life in Ti-6Al-4V [7].

In the present study, carbon was selected as the implanted species. Fretting fatigue life was measured on both implanted and unimplanted specimens. A substantial improvement in lifetime was found for the implanted specimens.

EXPERIMENTAL METHODS

The alloy Ti-6Al-4V was used for both the fretting pads and the fatigue specimens. The microstructure of the fatigue specimens is shown in Fig. 2. The yield strength of this material was measured as 993 MPa. Each specimen was polished to 600 grit paper lengthwise on each side. The fretted side was further polished to less than 0.1 μm rms. with 1 μ alumina, as was the surface of the fretting pad.

Since only one side of the fatigue sample was fretted, only this side was implanted, in the necked region. Carbon ions were implanted at an energy of 75 keV to a dose of 2×10^{17} at/cm². Temperature was estimated not to exceed 100°C during implantation. These conditions produce a concentration profile of carbon shown in Fig. 3, as determined by nuclear reaction analysis [8]. The fretting pads were not implanted.

The microstructure developed in the implanted layer was characterized by transmission electron microscopy. Three millimeter discs about 100 μ thick were partially thinned on one side, implanted on this electropolished side, and then thinned through from the opposite side. A 200 keV transmission electron microscope was used.

The fretting fatigue apparatus used in this study has been described elsewhere [9,10]. Briefly, it is a closed loop electrohydraulic servo controlled system, with the fatigue stress applied axially on the sample as a sine wave of frequency 10 Hz and $R=+0.1$. A normal stress of 20.7 MPa measured through a load cell, was applied to the fretting pad for all tests. Changing the level of the normal stress to 41.4 MPa has been found to have negligible effect on lifetime for Ti-6Al-4V [11]. The fatigue specimen and fretting pad dimensions are shown in Fig. 4.

After fracture, both the fretted surface and the fracture surface of the fatigue specimens were examined by scanning electron microscopy.

RESULTS

The damaged layer due to implantation appears in transmission microscopy as a very dense, unresolvable array, as seen in Fig. 5(a). Electron diffraction patterns show rings superimposed on the spot pattern of the titanium grains (insert of Fig. 5(b)). These rings correspond to a face centered cubic phase with a lattice parameter of 4.24Å. This may be compared with the lattice parameter of face centered cubic TiC which is 4.33Å [12]. Dark field imaging using segments of the two innermost rings shows a fine dispersion of precipitates with a maximum size of about 200Å (Fig. 5b). Although the total volume of precipitate is difficult to quantify, it would appear that a large portion of the implanted carbon remains in solution.

The results of the fretting fatigue tests are shown in Fig. 6. Baseline fatigue data are from reference 2 and are shown for comparison purposes. The relatively high tensile strength of our fatigue specimens may be reflected in a higher fatigue strength. The unimplanted fretting curve in fact lies slightly higher than that found in reference 2. The main point, however, is that significant improvement in fretting fatigue lifetime is found with carbon implantation.

Examination of the fretted and fractured surfaces in the SEM showed no differences between the implanted and unimplanted specimens. The general aspect is typical of fretting fatigue in this material (2). In Fig. 7(a), score marks on the polished surface lead to a fretting pit. In Fig. 7(b), debris and small cracks are found at the edge of a fretting pit. Fig. 8(a) shows the intersection of the wear and fracture surfaces, again with debris and secondary cracking. A view of the fracture surface near the wear surface in Fig. 8(b) shows secondary cracks and some fatigue striations. Failure seems to be definitely associated with the surface damage.

DISCUSSION

Although it does not appear that the mechanism of failure is affected by implantation, there is an obvious increase in lifetime. It is unlikely that this is due simply to an increase in fatigue strength, as only one side of the fatigue specimen was implanted. Increases in fatigue strength would be expected only when the entire potential fracture originating surface was implanted. The increase in lifetime could reasonably be ascribed to a slowing of debris formation and damage on the hardened, implanted surface. Eventually the implanted layer is breached, and a fracture develops in the normal manner.

We have chosen carbon as an implant species in this initial study basically for its hardening properties. It would be very interesting to compare the effects of oxidation inhibiting implants, as we hope to do in future work. Also there are a number of parameters, such as dose, energy, and post-implant heat treatment which could be explored to optimize the lifetime increase. Increased understanding of fretting fatigue mechanisms should help point the way to improved implantations. We may conclude that ion implantation is an extremely promising technique for alleviating the problem of fretting fatigue.

ACKNOWLEDGMENT

Dr. R. A. Kant was very helpful in obtaining the implantations. The nuclear reaction analysis was performed by C. R. Gossett.

REFERENCES

1. "Control of Fretting Fatigue," report of the Committee on Control of Fretting-Initiated Fatigue, National Materials Advisory Board, publication NMAB-333, 1977.
2. Goss, G. L., and Hoepfner, D. W., Wear, Vol. 24, 1973, p. 77.
3. Hirvonen, J. K., Jour. Vac. Sci. and Tech., Vol. 15, 1978, p. 1662.
4. Benjamin, J. D., and Dearnaley, G., Inst. of Physics Conf. Series, Vol. 28, 1976, p. 141.
5. Dearnaley, G., IEEE Trans. on Nuclear Sci., Vol. NS-28, 1981, p. 1808.
6. Bolster, R. N., private communication
7. Vardiman, R. G., and Kant, R. A., Journal of Applied Physics, to be published.
8. Gossett, C. R., Proc. of the Fifth Int. Conf. on Ion Beam Analysis, to be published
9. Reeves, R. K., and Hoepfner, D. W., Wear, Vol. 45, 1977, p. 127.
10. Reeves, R. K., Ph.D. Thesis, University of Missouri-Columbia, 1977.
11. Hoepfner, D. W., and Goss, G. L., Wear, Vol. 27, 1974, p. 61.
12. Krikorian, N. H., Wallace, T. C., and Anderson, J. L., Jour. Electrochem Soc., Vol. 110, 1963, p. 587

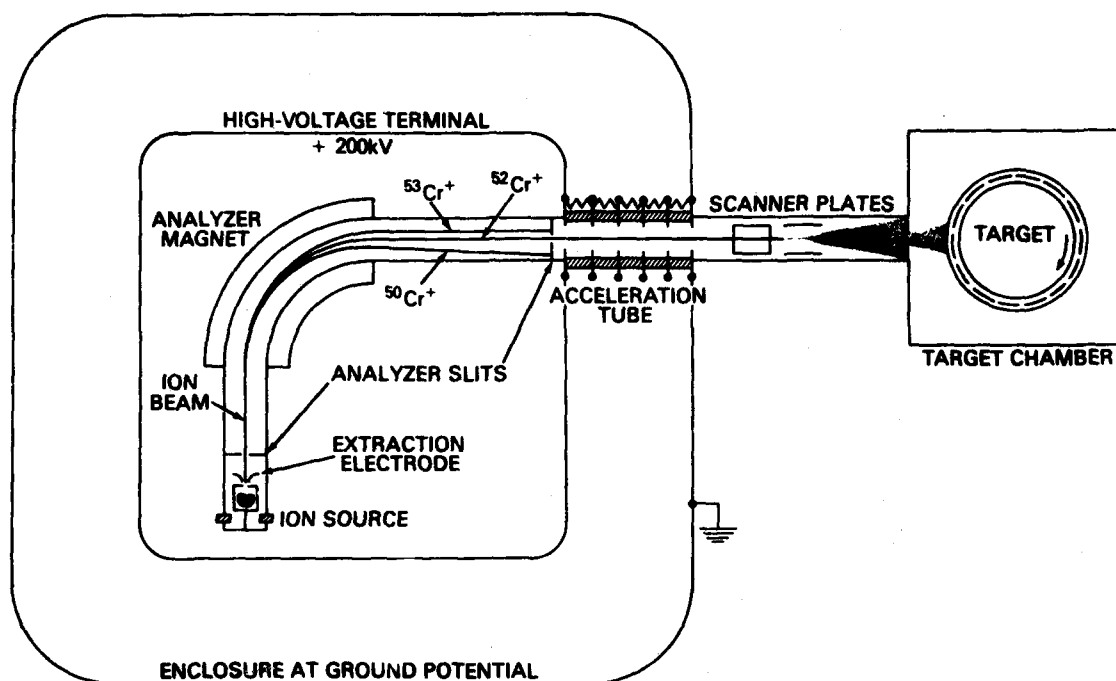


Fig. 1 — Schematic of the Naval Research Laboratory ion implanter, illustrating isotope selection using a chromium beam

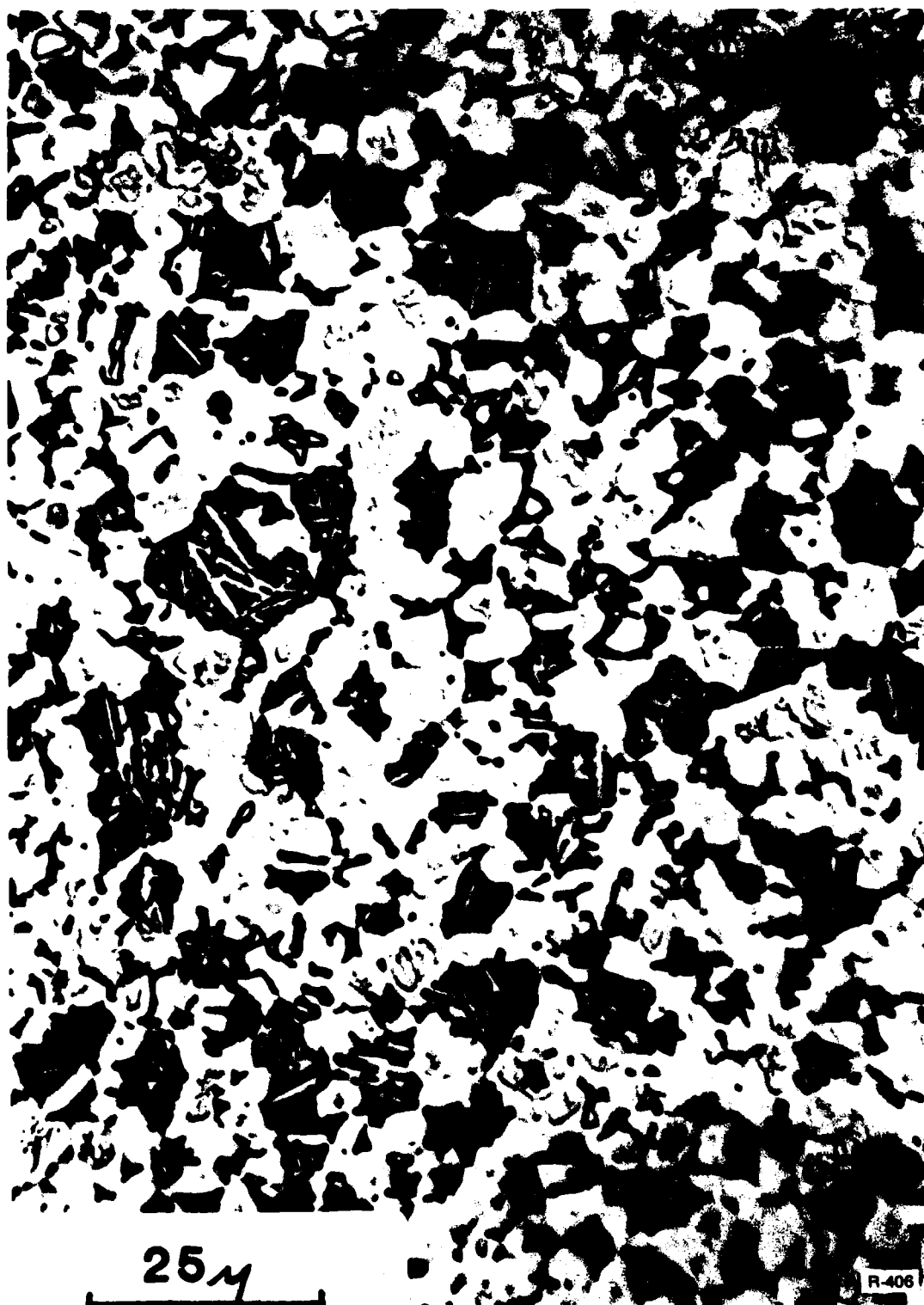


Fig. 2 — Microstructure of the fatigue specimens

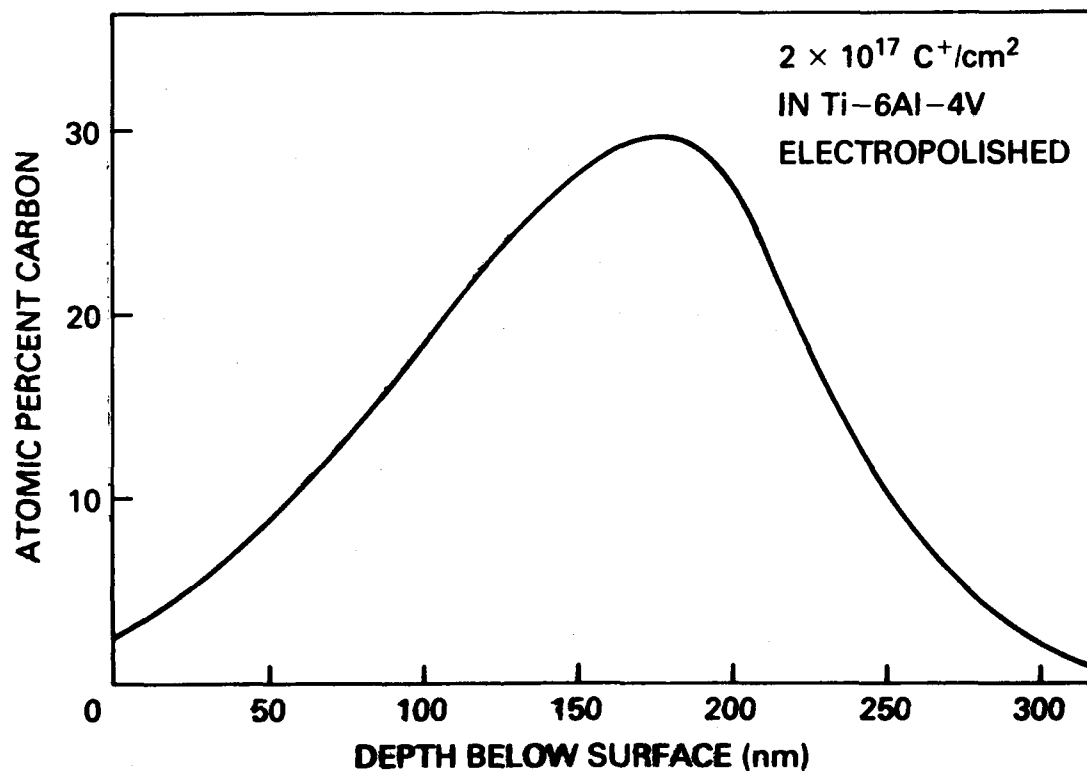


Fig. 3 — Concentration of carbon near the electropolished surface of a Ti-6Al-4V sample for a dose of 2×10^{17} at./cm² at 75 keV. Obtained by nuclear reaction analysis using $^{12}\text{C}(^3\text{He}, \alpha_0)^{11}\text{C}$.

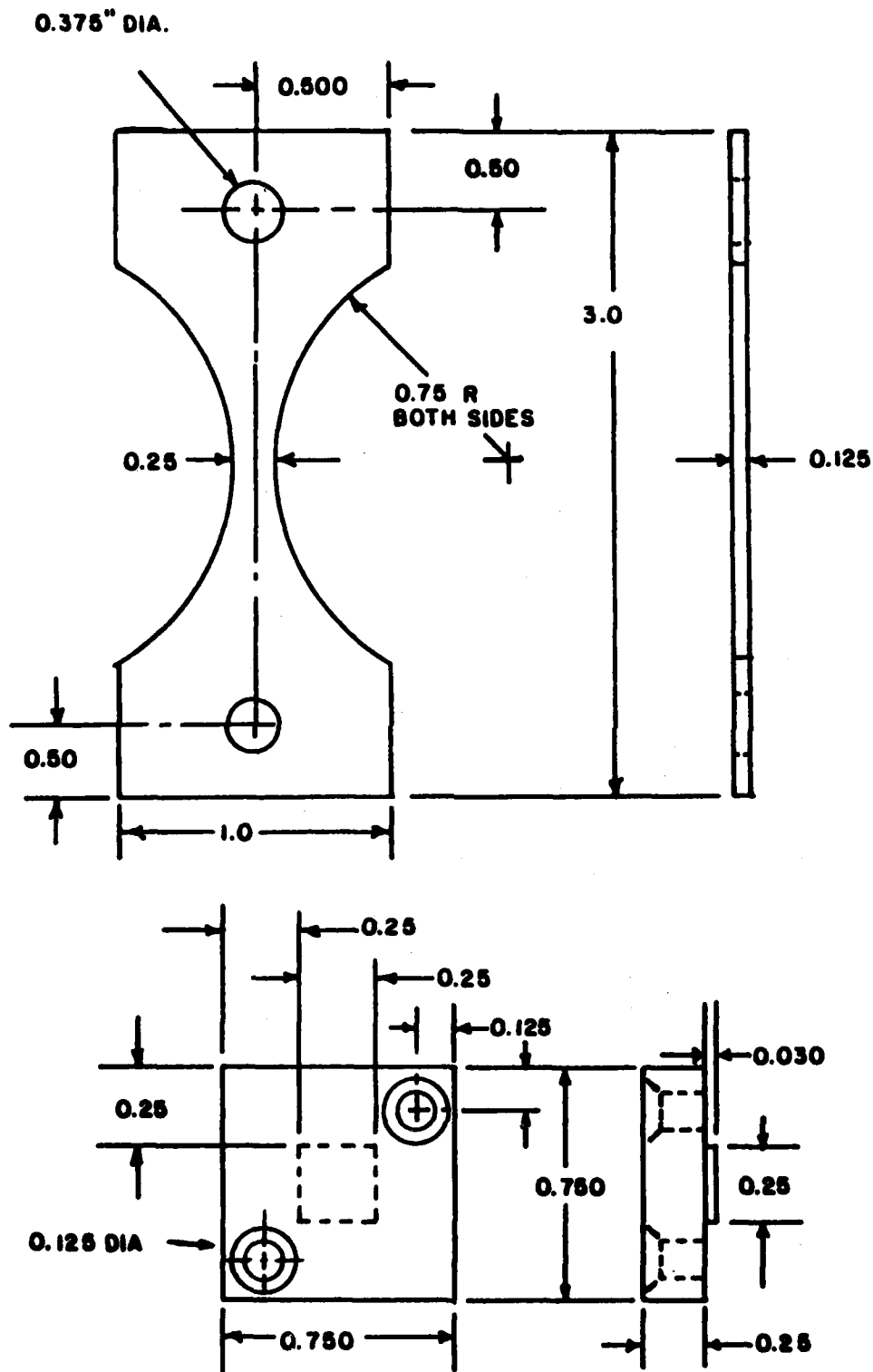


Fig. 4 — Size and configuration of fatigue specimens and fretting pad

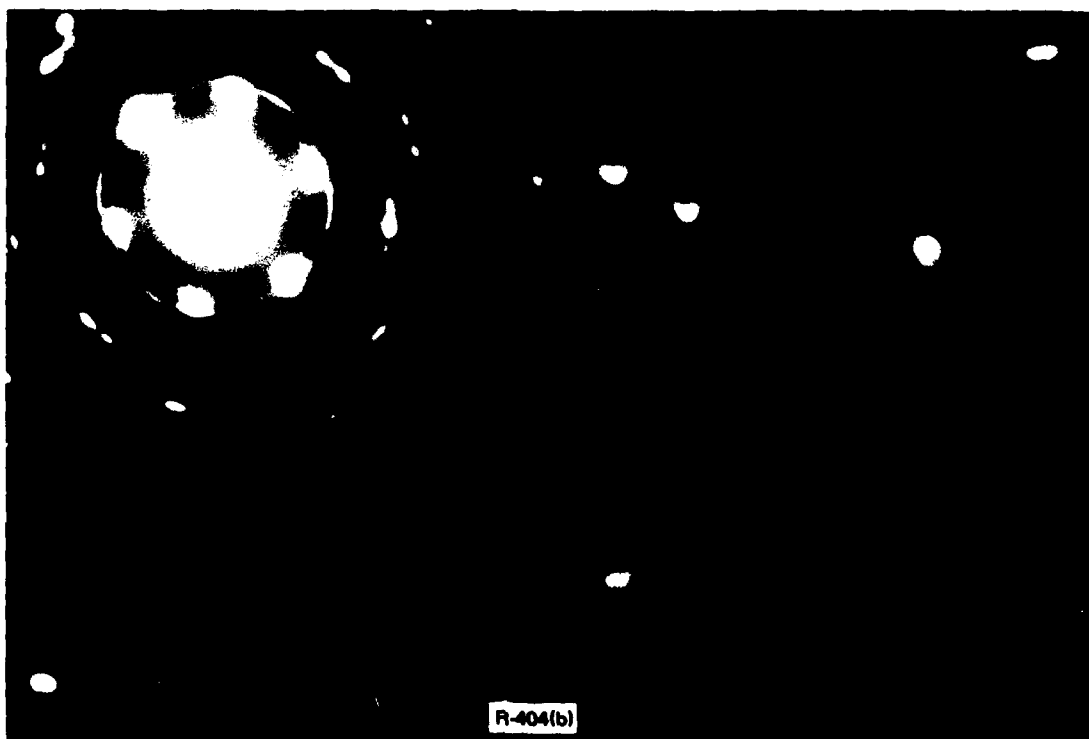
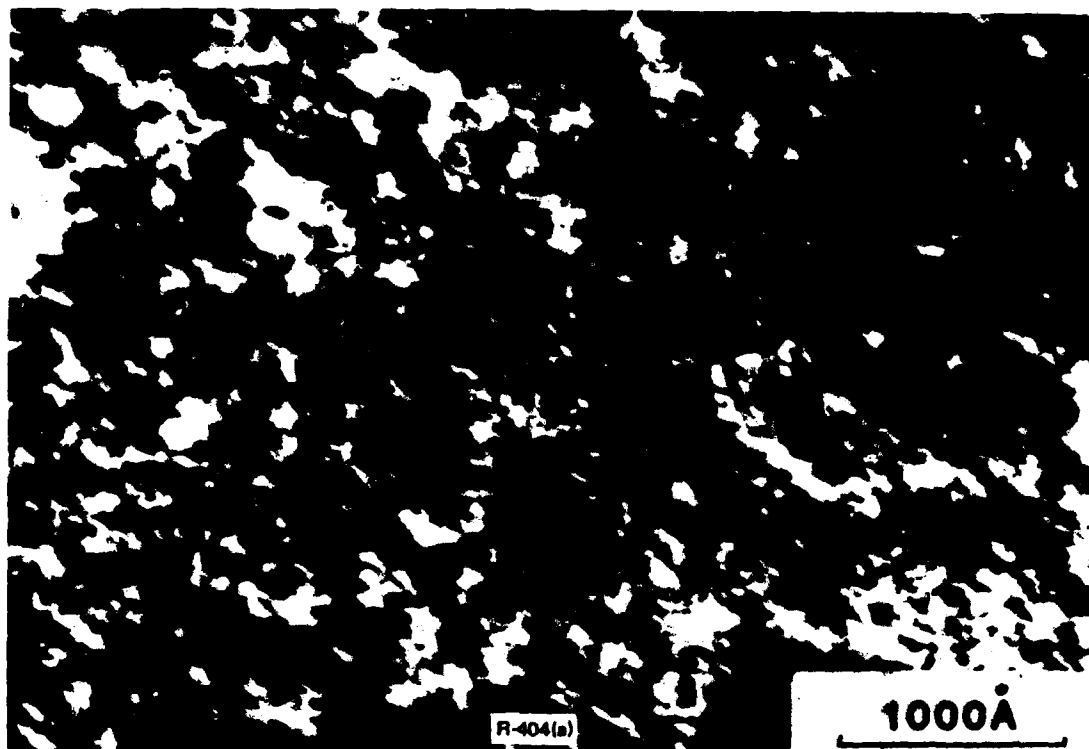


Fig. 5 — TEM micrographs of carbon implanted Ti-6Al-4V: (a) dark field using -Ti reflection; (b) insert, electron diffraction pattern; micrograph is dark field using a segment of the two innermost diffracted rings.

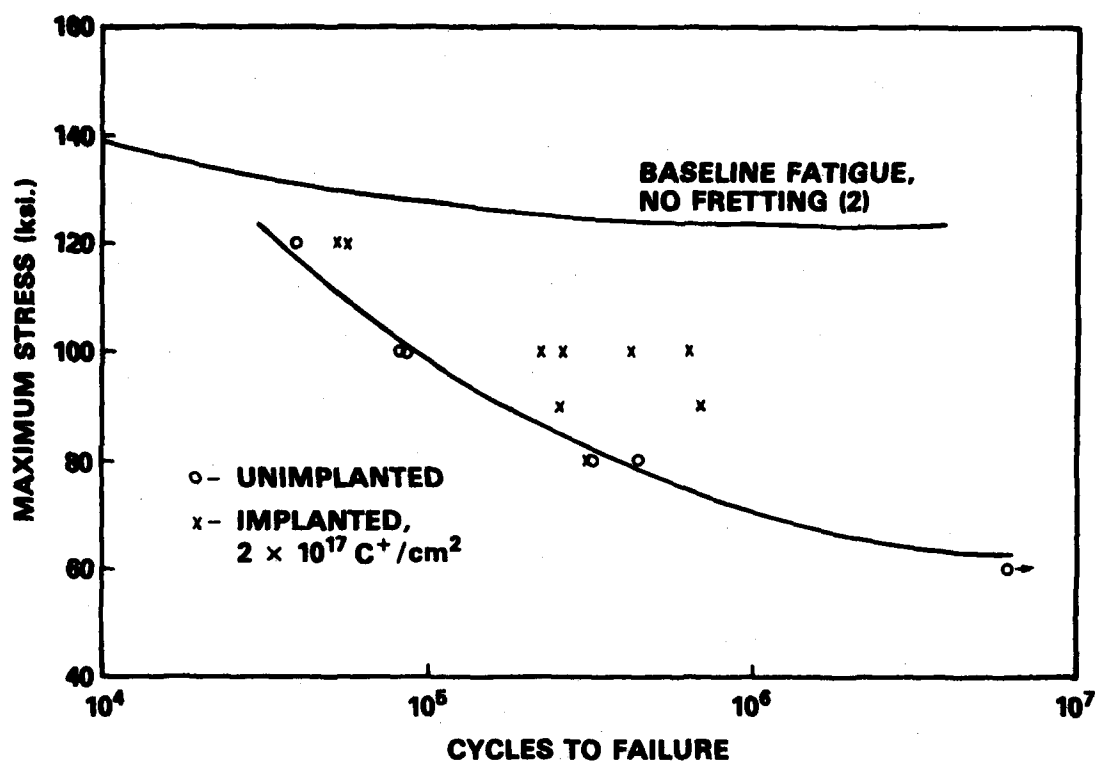


Fig. 6 — Cycles to failure vs maximum fatigue stress for carbon implanted and unimplanted Ti-6Al-4V. 100 ksi = 689 MPa. Normal stress, 20.7 MPa. Baseline fatigue taken from ref (2).



Fig. 7 — SEM micrographs of the fretted surface, showing debris, fretting pits, and secondary cracking

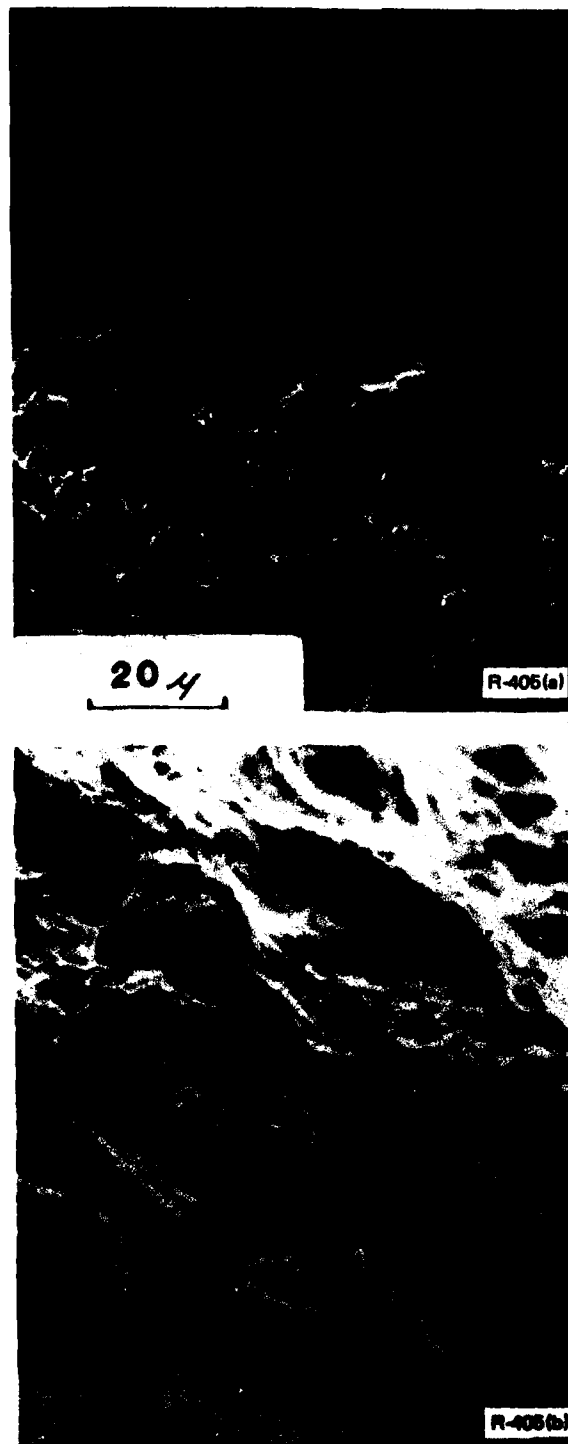


Fig. 8 — SEM micrographs of the fracture surface: (a) intersection of the wear and fracture surfaces in the vicinity of crack initiation; (b) fracture surface showing secondary cracks and fatigue striations.

Section III.A

ELECTROCHEMICAL BEHAVIOR OF AN AMORPHOUS Fe-Ti-C
SURFACE IN TITANIUM-IMPLANTED STEEL

G. K. Hubler,¹ P. Trzaskoma,² E. McCafferty²
and I. L. Singer³

¹Materials Modification and Analysis Branch
Condensed Matter and Radiation Sciences Division
Naval Research Laboratory

²Environmental Effects Branch
Material Science and Technology Division
Naval Research Laboratory

³Surface Chemistry Branch
Chemistry Division
Naval Research Laboratory

This work was supported by the Office of Naval Research.

ELECTROCHEMICAL BEHAVIOR OF AN AMORPHOUS Fe-Ti-C SURFACE IN TITANIUM-IMPLANTED STEEL

G. K. Hubler, P. Trzaskoma, E. McCafferty, and I. L. Singer
U. S. Naval Research Laboratory
Washington, DC 20375

ABSTRACT

Implantation of Ti at high fluences into 52100 steel produces an amorphous surface containing Ti, Fe, and C. This amorphous surface provides modest improvements in corrosion resistance in 1N H₂SO₄ and 0.1 N NaCl, as indicated by potentiodynamic polarization scans. In both solutions the anodic current density is about 10% that of unimplanted 52100 steel up to anodic overpotentials of about 800 mV. Pitting corrosion, which is initiated at lower overpotentials, leads to undermining and peeling of the implanted layer at higher overpotentials. Detailed optical and microstructural studies of pit initiation in a nital/pical/methanol etch suggest that pitting begins at surface flaws, which are either carbides or impurity inclusions.

KEYWORDS

Ion implantation; pitting corrosion; amorphous metals; Auger Electron Spectroscopy; ion and chemical etching; metallography.

INTRODUCTION

Previous work by Singer, Carosella, and Reed (1981) has shown that a thin amorphous layer 30 nm to 50 nm in thickness is formed on AISI 52100 steel upon implantation with greater than 4×10^{17} Ti ions/cm² at an energy of 190 keV. Furthermore it was demonstrated that the amorphous layer was formed only at high fluences when sputter erosion of the surface caused implanted Ti atoms to emerge. The gettering of hydrocarbons in the ambient vacuum by the surface concentration of Ti caused appreciable in-diffusion of C which in turn stabilized an amorphous Fe-Ti-C layer (Singer, Carosella, and Reed, 1981; Knapp, Follstaedt, and Picraux, 1980).

Additional work by these authors showed that the amorphous layer was a factor of 6 harder than the already hardened bearing steel (Singer, Bolster, and Carosella, 1980), that the coefficient of friction under poorly lubricated sliding conditions was reduced by a factor of two, and that the lubricated sliding wear rate was greatly improved (Singer, Carosella, and Reed, 1981; Carosella and co-workers, 1980). Because of the improved mechanical properties in this widely used bearing steel, it was of interest to investigate the corrosion behavior of this novel surface alloy. One of the major causes of bearing failure is fatigue spalling which is thought to be initiated by corrosion pitting (Wang and co-workers, 1979).

In this paper the behavior of Ti-implanted 52100 steel is investigated in 1 N H₂SO₄, 0.1 N NaCl, and in a nital/pical/methanol etch. The techniques employed were potentiodynamic electrochemical polarization, metallographic etching in conjunction with optical microscopy, Auger electron spectroscopy and ion milling, scanning electron microscopy, and electron microprobe analysis. These studies are intended to provide

general information on the electrochemical behavior of the amorphous surface, rather than testing its performance in specific service conditions. A possible application involves improving the corrosion resistance of steel bearings used in jet engines. The problem arises when salt-spray condensates accumulate in the engine lubricants of aircraft not in regular use (Wang and co-workers, 1979). Such environments, however, consisting of a lubricating oil contaminated with about 3 ppm NaCl are quite different than the electrolytes used in the present study.

EXPERIMENTAL METHODS

Samples of AISI 52100 steel (1.1% Cr, 1% C, 0.25% Si, 0.35% Mn, by wt %) were polished to a mirror finish with #6 diamond paste and unless otherwise noted, were ion implanted with 4.6×10^{17} Ti/cm² at 190 keV. The samples were cooled during implantation by intimate contact with a water cooled aluminum block such that surface temperatures never exceeded about 50°C.

Auger spectroscopy in conjunction with Ar⁺ ion milling was used to obtain compositions vs depth profiles of the implanted layer. Chemical states of detected elements were identified by Auger lineshape analysis. The ion beam, operated at 2 keV and near normal incidence left a crater in the surface which was later examined by standard metallographical techniques. The crater depth was measured by Michelson interferometry by which depth scales for composition vs depth profiles were established.

Optical microscopy and scanning electron microscopy were used to study pit initiation and growth, which was the major cause of the breakdown of passivity in these films. Implanted and unimplanted samples were etched for various times in a solution of 1 part 1% nital, 2 parts 4% picral, and 3 parts methanol. A Knoop microhardness testor was used to place a series of indents at a 100 gm load in the surface which provided "markers" to enable micrographs to be taken of precisely the same area of the surface after each successive etch time (measured Knoop hardness = 750 for 100 gm load for implanted and unimplanted samples). At a magnification of 925x, thirteen different areas 123 μ m by 96 μ m in dimension were monitored and any changes which resulted from etching were noted. Sample etching was performed by flooding the surface with etchant and lightly rubbing the surface with a cotton swab.

Electrochemical polarization measurements were done potentiodynamically (10 mV/min) in room temperature deaerated solutions of either 1 N H₂SO₄ or 0.1 N NaCl. All samples were allowed to reach their equilibrium open circuit potential for between 2 to 4 h prior to polarization.

RESULTS

The composition versus depth of C, Ti, and Fe obtained by Auger electron spectroscopy in conjunction with Ar-ion milling are shown in Fig. 1 for an implanted but unetched sample. This data is repeated from Singer, Carosella, and Reed (1981) primarily to illustrate the chemical character of this surface. After sputtering about 4 nm of oxide and carbonaceous material, the carbon concentration at the metal surface is measured to be about 20 at.%. The carbon concentration decreases monotonically as the depth increases and reaches the bulk value at about 120 nm. The titanium concentration increases from the surface (i.e., 4 nm) to a peak concentration near 40 at.% at 75 nm and then decreases to zero between 150 and 200 nm. The Auger

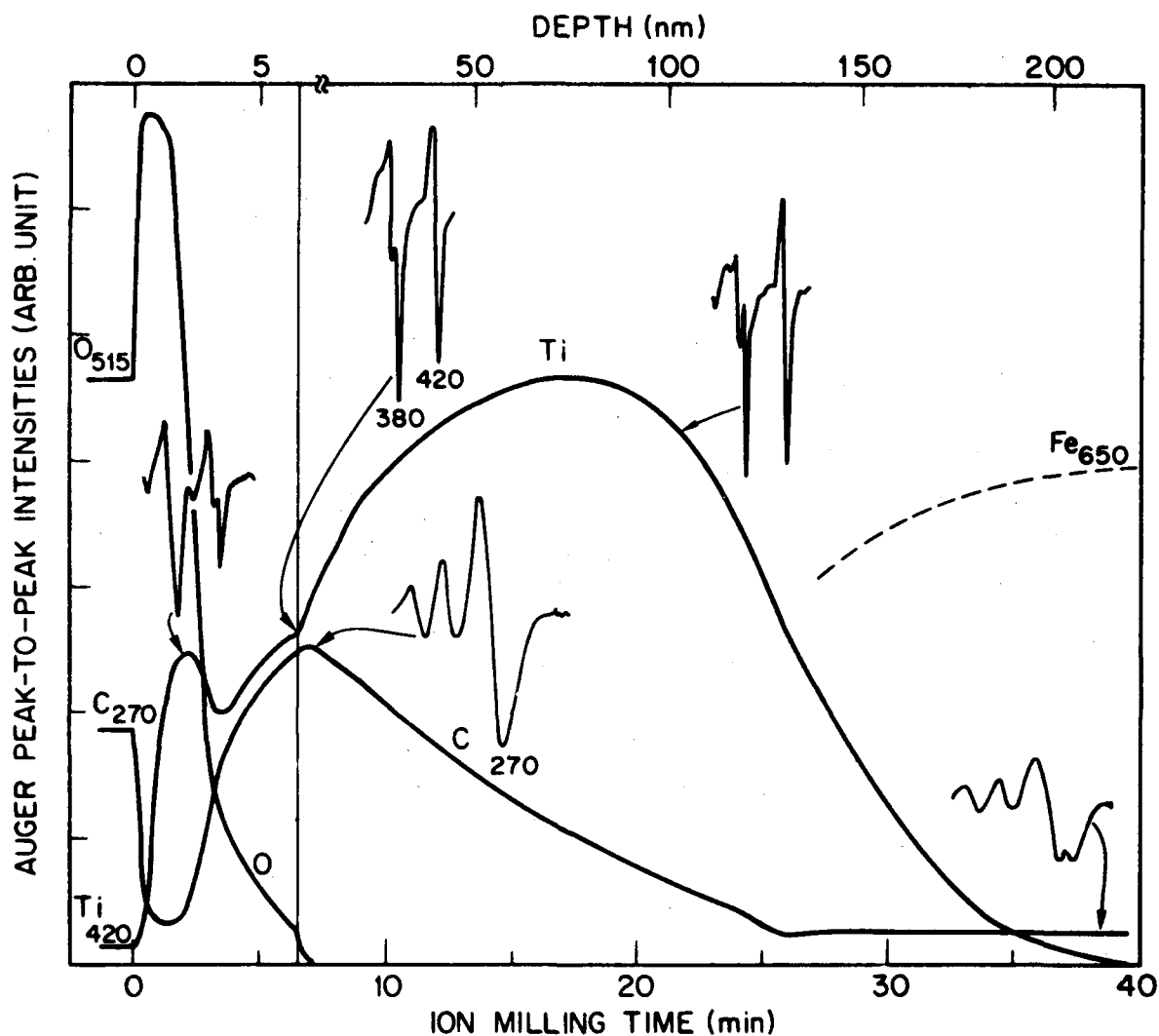


Fig. 1 — Auger depth profile of Ti-implanted 52100 steel ($50 \times 10^{16} \text{Ti/cm}^2$ at 190 keV). Portions of the Ti and C Auger electron spectra are shown at several depths and the energies of the Auger peaks are indicated in eV.

lineshape for carbon at the surface has been identified as that for TiC, while the lineshape of carbon near 200 nm is associated with the normal carbide in 52100 steel. At its maximum in the oxide layer, the Ti lineshape is that for TiO₂. After 6 nm sputtering, however, the Ti lineshape is nearly identical to that of TiC and becomes more metallic like by a depth of 100 nm. It has been established by transmission electron microscopy (Singer, Carosella, and Reed, 1981) that the near surface region (about 50 nm) of this alloy is amorphous to the extent that no second phases are observed down to a resolution of 0.5 nm. Therefore, the TiC observed chemically by Auger lineshape analysis must be in precipitates no greater than 0.5 nm diameter. It has been suggested (Singer, Carosella, and Reed, 1981) that the TiC Auger signal is associated with the amorphous layer; and that at depths where the carbon concentration is small and where a metallic Ti Auger lineshape is observed, the material is no longer amorphous. The picture that emerges is that at depths < 100 nm the surface is amorphous (where the C concentration is high) and at depths > 100 nm, the material is crystalline and contains some metallic Ti.

Figure 2 shows typical potentiodynamic anodic polarization scans for unimplanted 52100 steel, Ti-implanted 52100, and pure Ti in 1 N H₂SO₄. Unimplanted 52100 shows active-passive behavior typical of low Cr content ferrous alloys. Up to about +0.5 V vs. N.H.E., the anodic current density of the Ti-implanted 52100 is about one-tenth that of the unimplanted sample. During this scan, however, there is some pitting and undermining of the implanted layer. Beyond +0.5 V, there is noticeable flaking of the surface; and further polarization results in an increase in anodic current density.

Similar behavior is observed in 0.1 N NaCl. As shown in Fig. 3, the anodic current density for Ti-implanted 52100 is again about one-tenth that for the 52100 steel for anodic potentials up to about +0.8 V vs. N.H.E. Beyond +0.8 V, however, there is considerable peeling of the implanted surface, and the anodic behavior approaches that of the unimplanted sample.

Several methods of surface analysis were performed to elucidate the mechanism responsible for initiating the corrosion failure of the surface alloy as observed in the electrochemical measurements.

The microstructure of high-dose Ti-implanted 52100 can be revealed indirectly by a metallographic analysis of ion-eroded surfaces (Paulis, 1975). Nomarski micrographs (475x) are shown in Fig. 4 of craters eroded to a depth of 150 nm. In Figures 4a and 4b, the area on the left of the photographs was masked so that only the area on the right has been sputtered. The crater bottom in the sample implanted to 5×10^{17} Ti/cm² (Fig. 4a) is as regular as the implanted surface (i.e., has the same texture). However, the crater bottom of a sample implanted to 5×10^{16} Ti/cm² (Fig. 4b) is heavily etched. This texture, typical of nonimplanted surfaces as well, results from anisotropic sputtering, common to multiphased, polycrystalline solids (Paulis, 1975). Since the eroded surface retained its original finish on the high dose implanted sample, (Fig. 4a) the sputtering was isotropic and the implanted surface was in fact amorphous. Continued sputtering of this surface eventually revealed the relief observed in Fig. 4b.

Nomarsky photomicrographs of the as-polished surface and the implanted but unetched surface of 52100 are shown in Fig. 5a and 5b, respectively. The only notable feature of the as-polished surface is the numerous scratches that are approximately 30 nm in average depth (Singer, Bolster, and Carosella, 1980). The implanted but unetched surface shows a texture produced by the sputtering of surface atoms during the high fluence implantation of Ti. Most of the polishing scratches have been removed, and the

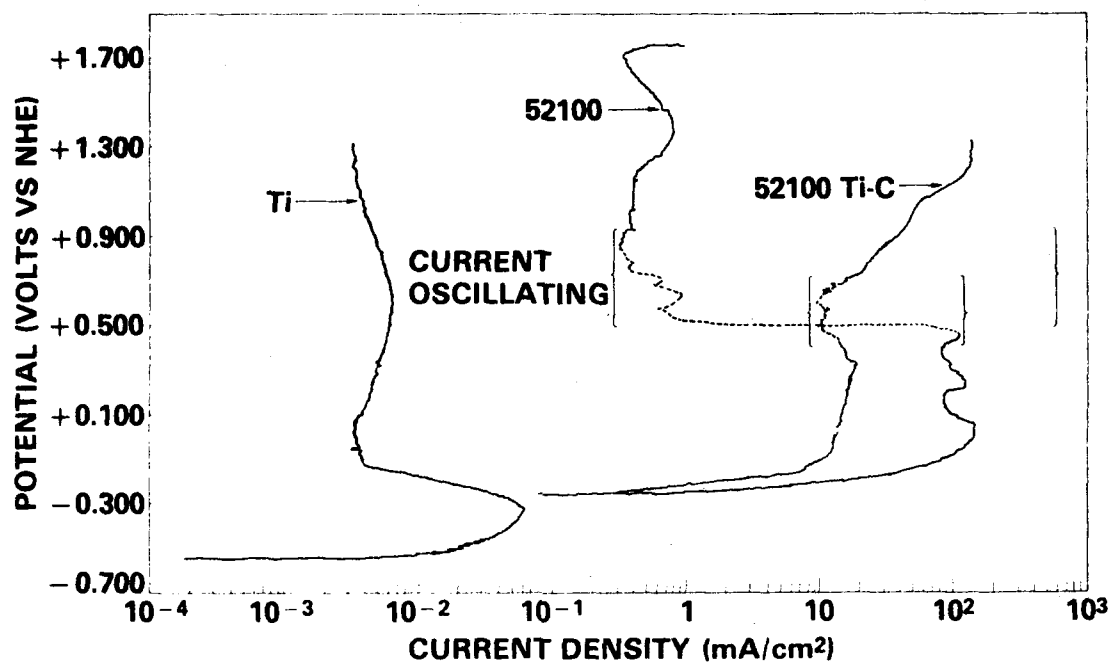


Fig. 2 — Anodic potentiodynamic polarization curves (10 mV/min) for pure Ti, 52100 steel, and Ti-implanted 52100 steel ($4.6 \times 10^{17}/\text{cm}^2$, 190 keV) in deaerated 1 N H_2SO_4

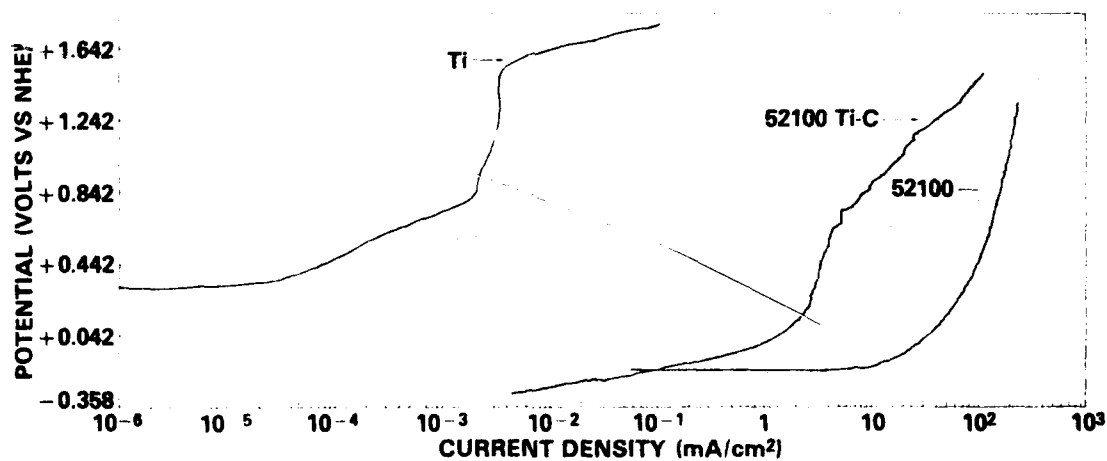


Fig. 3 — Anodic potentiodynamic polarization curves for unimplanted 52100 steel and Ti-implanted 52100 steel ($4.6 \times 10^{17}\text{Ti}/\text{cm}^2$ at 190 keV) in 0.1 M NaCl solution.

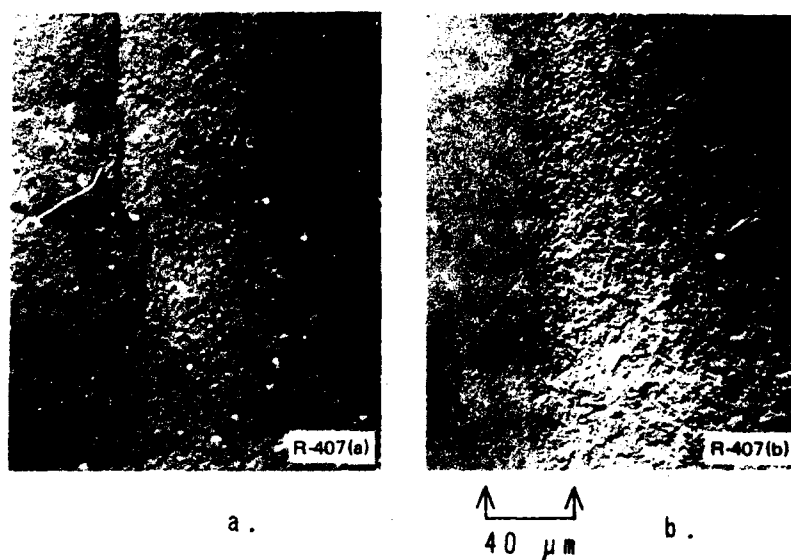


Fig. 4. Nomarsky photomicrographs (475x) of 52100 steel. (a) Implanted with $5 \times 10^{17} \text{ Ti/cm}^2$ at 190 keV and ion milled to a depth of 150 nm. (b) Implanted with $5 \times 10^{16} \text{ Ti/cm}^2$ at 190 keV and ion milled to a depth of 150 nm. The left hand portion of each micrograph is as-implanted material that was masked to prevent ion milling.

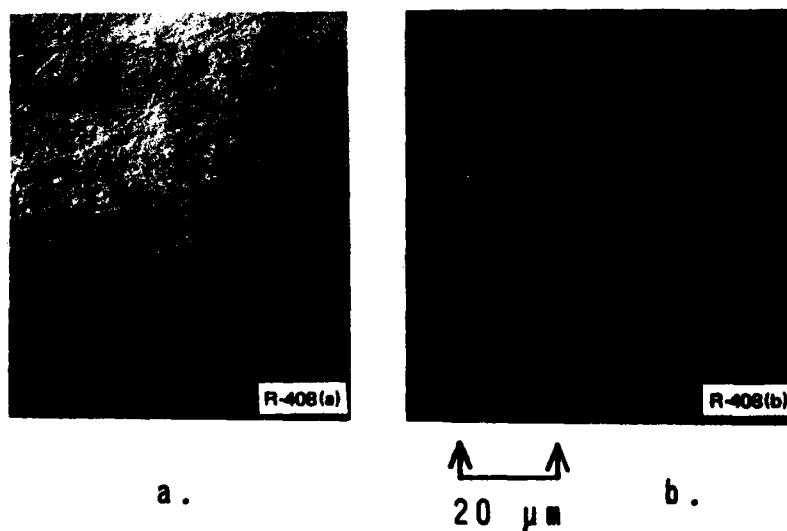


Fig. 5. Nomarsky micrographs (925x) of 52100 steel surface, (a) as-polished and, (b) as-implanted with $4.6 \times 10^{17} \text{ Ti/cm}^2$ at 190 keV.

surface is characterized by a uniform rough texture punctuated by occasional flaws which are usually circular and about $1\text{ }\mu\text{m}$ in diameter (i.e., flaw in lower left corner of Fig. 5b).

The effects of chemical etching on unimplanted surfaces are shown in Fig. 6. A Nomarsky micrograph of unimplanted 52100 etched for 5 s in Figure 6a shows that the polishing scratches are removed and the surface is characterized by a rough texture caused by unequal etch rates for carbides and the very fine grain martensite matrix (Metals Handbook, 1972). The chemically etched surface resembles the ion milled surface in Figure 4b. Figure 6b is a bright field micrograph of the same unimplanted etched surface. The numerous "white" circular spots about $1\text{ }\mu\text{m}$ diameter are carbides. The size and frequency of carbide particles in Figure 6b correspond closely to the size and frequency of the dimples and bumps randomly distributed in the surface of the implanted but etched sample in Figure 5b. This correspondence suggests that the dimples and bumps are implantation modified carbide particles protruding out from the surface. After chemically etching the implanted sample for up to 500 s, there is virtually no discernible change observed in the surface topography shown in Figure 5b.

For etch times greater than about 500 s, a low density of deep pits began to form. Over the entire field of view (thirteen $123\text{ }\mu\text{m} \times 96\text{ }\mu\text{m}$ areas) monitored at a magnification of 925x with optical micrographs, 3 pits were initiated. All three pits were initiated at the approximately $1\text{ }\mu\text{m}$ diameter flaws described previously. The surface coverage of these flaws was about 0.3% of the total area and a pit initiated at about 1 flaw in 200.

The pits were quite circular in shape, gradually grew in diameter with etch time, and initially would appear as a blister with a hole in the center or as a crater with a hole in the center. At later times the blister would collapse into a crater. Figures 7a and 7b show Nomarsky micrographs of the development of several pits for two different etch times. Note the blister or depression appearance in Fig. 7a. Focusing into the bottom of the hole in the center of the pit in bright field revealed a microstructure very similar to an unimplanted, etched surface as in Fig. 6b. The topography of the blistered or cratered material overlying the pits was identical to the surrounding amorphous material. These observations indicate that the thin amorphous layer was being undermined by corrosion within the pit and that the pit was deeper than the thickness of the amorphous layer.

Scanning electron microscopy (SEM) and x-ray analysis (EDAX) were employed to ascertain the nature of the surface flaws and the pit initiation process. It was immediately apparent that it was not possible to analyze the surface flaw pit initiation sites because there was no secondary electron contrast from any feature on these surfaces other than from the Knoop indents and the corrosion pits already present. This held true for all etch times up to the maximum of 1300 s. Figure 8 is an SEM micrograph (2000x) of a region which contained an abnormally large number of pits. It appears that several pits have coalesced into a large irregular pit. Again, it appears that there is a cover layer of material partially overlying the pit cavity for the pit at the upper right in the micrograph. The bright spots within the cavities are Cr-rich carbide particles as determined by x-ray analysis. Analysis by x-rays within the pit opening showed Cr/Fe ratios typical of bulk material and also no Ti. On the other hand, x-ray analysis on the cover layers over the pit cavities consistently revealed the presence of more than 75% of the implanted Ti atoms compared to the x-ray signal for material adjacent to a pit. In addition, no loss of Ti could be measured by x-ray analysis on unpitted material for etch times up to 1300 s.

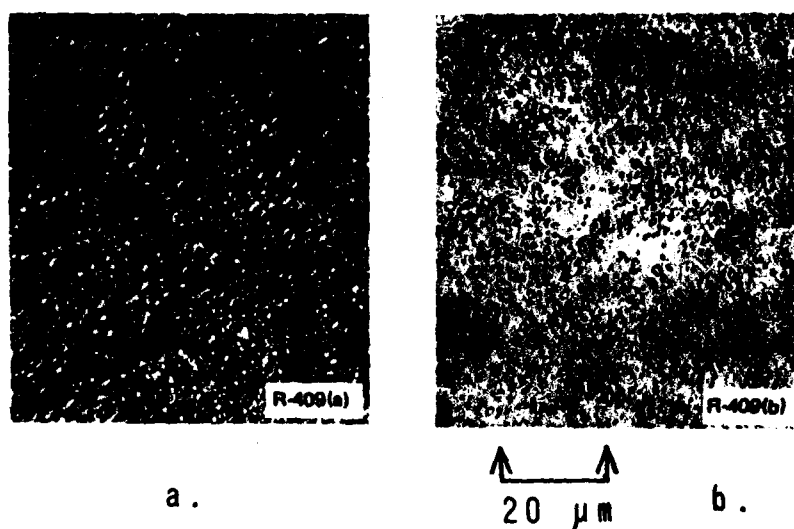


Fig. 6. (a) Nomarsky micrograph (925x) of unimplanted 52100 steel after a 5 s chemical etch. (b) Bright field micrograph (925x) of same surface as in (a).

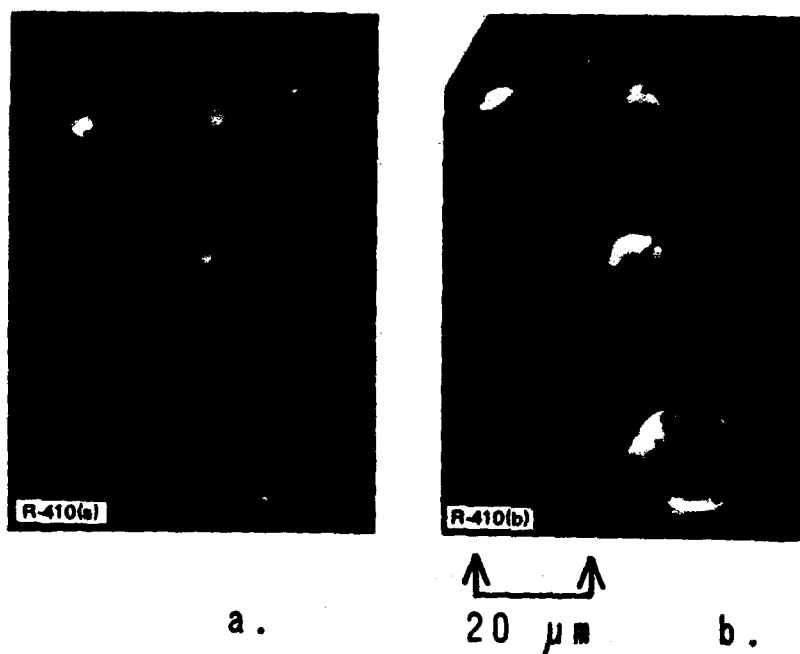


Fig. 7. Nomarsky micrographs (925x) of pits on 52100 steel surface implanted with $4.6 \times 10^{17} \text{ Ti/cm}^2$ at 190 keV after chemical etching for (a) 885 s, and (b) same spot as (a) after etching for 1250 s.

Another interesting feature of these surfaces was that the diamond shape knoop stylus indents placed on the surface for area location purposes did not corrode or act as pit initiation sites which strongly implies that the amorphous layer plastically flowed beneath the indenter. From the maximum penetration depth of the indenter ($1.4 \mu\text{m}$) and the width of the small dimension of the diamond shaped indent ($6.5 \mu\text{m}$), we calculate that the maximum elongation of the amorphous layer required for this to occur is about 10%—a reasonable number for ductile amorphous metals (Masumoto and Maddin, 1975).

DISCUSSION

Returning to Fig. 2, we note that the open circuit potential of Ti in $1 \text{ N H}_2\text{SO}_4$ is more than 300 mV below that of 52100 steel. If it were not for the formation of an amorphous layer, Ti and Fe would form a galvanic couple which would dissolve the implanted titanium. In 0.1 M NaCl the relative electrode potentials of Ti and 52100 steel are reversed (see Fig. 3) so that the steel would dissolve if there were a galvanic couple rather than an amorphous surface layer.

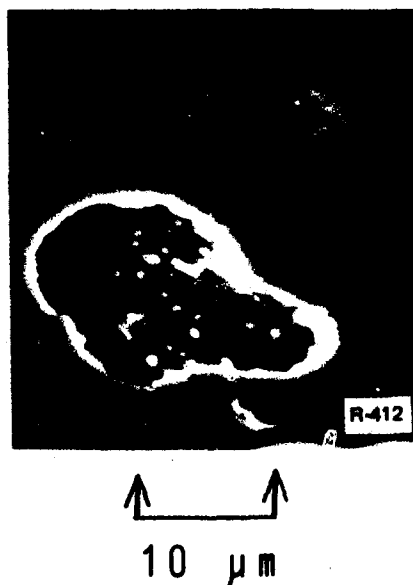


Fig. 8. Scanning electron micrograph (2000x) of pits on 52100 steel surface implanted with Ti ions. Pits were produced by chemically etching for 1300 s.

The polarization behavior indicates that there are modest improvements in corrosion resistance. In both solutions, the anodic dissolution rate is one-tenth that of the unimplanted 52100 steel, for potentials up to about 800 mV anodic to the open-circuit potentials. The problem is that pitting corrosion, which initiates at low overpotentials, becomes increasingly severe leading to undermining and eventual loss of the implanted layer at high anodic overpotentials. Once the local attack is initiated, it is accelerated by galvanic action between free Ti beneath the amorphous film and Fe in the bulk material. Dissolution of either free Ti or Fe would lead to undermining of the amorphous surface layer.

The surface flaws seen in the optical photographs of Fig. 5b are weak points in the surface alloy. Comparison of the texture of the implanted surface with the appearance of the etched, unimplanted surface (Figs. 5b with 6) has suggested that the flaws might be surface carbides. The carbides are about 1 μm in diameter, the topmost surface of which is implanted with Ti atoms. Another possibility is that the surface flaws are impurity inclusions of Al_2O_3 , SiO_2 , etc., which, although less numerous, are known to exist in these materials, and which are also implanted with high dose Ti. In either case, the composition and structure of these second phases has been modified by implantation to be similar to Ti-implanted 52100 because there is no contrast in secondary electron emission and because they do not readily corrode in the nital/picral/methanol etch. Whether the weak points are carbides or impurity inclusions, it is clear that after a time, material of somewhat different composition from the amorphous film dissolves from around the flaw, or the inclusion itself dissolves, exposing the underlying material. At this pit, the galvanic couple is activated between the free Ti beneath the amorphous film and the underlying Fe, and the film is undermined. This is consistent with the morphology of the initial pit formation seen in the optical micrographs and with the flaking observed during extensive anodic polarization. The film can be undermined by anodic dissolution of either implanted free Ti (1N H_2SO_4) or of the steel base (0.1 N NaCl). The SEM and EDAX observations clearly show that corrosion pits formed in the etching solution extend through the implanted layer into the bulk steel.

The present study indicates the important influence that non-metallic second phases can have on the corrosion behavior of ion implanted systems. Although repair of localized corrosion damage did not occur in the present system, it should not be inferred that implanted surfaces are generally susceptible to such continued attack. With Pd-implanted titanium in hot sulfuric acid, for example, the more active metal (Ti) was dissolved initially, but the noble metal component polarized the composite surface into the passive range (Hubler and McCafferty, 1980).

The present experiments were intended to provide preliminary information on the electrochemical behavior of the novel surface alloy produced by Ti implantation into 52100 steel. The actual service conditions are very much different for possible applications involving bearing surfaces in jet engines. There the service environment is less severe, i.e., about 3 ppm chloride in a lubricating oil.

It is anticipated that improvements in the amorphous layer could be made by altering the implantation conditions. By consuming all of the Ti in the amorphous layer so that the galvanic couple is eliminated and/or by making the film thicker, improved resistance to pitting corrosion should be obtained.

SUMMARY

1. The amorphous Ti-Fe-C surface (produced with high fluences of implanted Ti) provides modest improvements in corrosion resistance in 1 N H_2SO_4 and 0.1 N NaCl.
2. The anodic current density in both solutions is about 10% that of unimplanted 52100 steel, up to an anodic overpotential of about 800 mV.
3. Pitting, which is initiated at low overpotentials, leads to undermining of the implanted layer and its eventual peeling off at higher overpotentials.
4. Detailed optical and surface analytical studies show that pitting of the amorphous surface in a nital/picral/methanol etchant initiates at surface flaws, which are most likely surface carbides or oxide inclusions.

5. Galvanic action between free Ti beneath the pitted amorphous film and Fe in the bulk steel leads to undermining of the amorphous layer.

ACKNOWLEDGEMENTS

The authors are indebted to Russ Jeffries for the SEM micrographs and several of the Nomarsky optical micrographs.

REFERENCES

- Carosella, C. A., I. L. Singer, R. C. Bowers, and C. R. Gossett, (1980). Ion Implantation Metallurgy. American Institute of Mining, Metallurgical, and Petroleum Engineers, New York. p. 103.
- Hubler, G. K., and E. McCafferty, (1980). Corrosion Sci., 20, 103.
- Knapp, J. A., D. M. Follstaedt, and S. T. Pieraux, (1980). Ion Implantation Metallurgy. American Institute of Mining, Metallurgical, and Petroleum Engineers, Inc., New York. p. 152.
- Masumoto, T., and R. Maddin, (1975). Mat. Sci. Eng., 19, 1.
- Metals Handbook, Vol. 7, (1972). American Society for Metals, Metals Park, Ohio. p. 51.
- Paulis, M., (1975). In P. M. French, R. J. Gray, and J. L. McCall (Eds.), Microstructural Science, Vol. 3, American Elsevier, New York. p. 453.
- Singer, I. L., R. N. Bolster, and C. A. Carosella, (1980). Thin Solid Films, 73, 283.
- Singer, I. L., C. A. Carosella, and J. R. Reed, (1981). Nucl. Instrum. Methods, 182/183, 923.
- Wang, Y. F., C. R. Clayton, G. K. Hubler, W. H. Lucke, and J. K. Hirvonen, (1979). Thin Solid Films, 63, 11.

Section IV.A

ELECTRICAL AND STRUCTURAL CHARACTERIZATION OF
IMPLANTATION DOPED SILICON BY INFRARED REFLECTION

G. K. Hubler and P. R. Malmberg¹
C. N. Waddell and W. G. Spitzer²
J. E. Fredrickson³

¹Materials Modification and Analysis Branch
Condensed Matter and Radiation Sciences Division
Naval Research Laboratory

²Department of Physics
University of Southern California
Los Angeles, CA 90007

³Department of Physics
California State University at Long Beach
Long Beach, CA 90801

This work was supported by the Naval Material Command and the
Air Force Office of Scientific Research.

Electrical and Structural Characterization of Implantation Doped Silicon by Infrared Reflection

G. K. Hubler and P. R. Malmberg
Naval Research Laboratory
Washington DC 20375

C. N. Waddell and W. G. Spitzer
Department of Physics, University of Southern California
Los Angeles, CA 90007

J. E. Fredrickson
Department of Physics, California State University at Long Beach
Long Beach, CA 90801

ABSTRACT

A physical model is presented for calculating infrared reflection interference spectra from ion implanted and annealed crystalline materials. The utility of the method is illustrated by presenting best fit spectra for a $\langle 111 \rangle$ silicon sample implanted with 2.7 MeV phosphorous to a fluence of 1.74×10^{16} ions/cm² and isothermally annealed at 500°C. Non-linear least-squares fitting of reflection data yields structural and electrical information about the implanted region with reasonable precision. The physical quantities determined are (i) the depth of the amorphous layer produced by implantation both before and during isothermal annealing, the thickness of the recrystallized material, and the widths of any transition regions, (ii) the dielectric properties of the amorphous and recrystallized material, and (iii) the characteristics of the free carrier plasma which yield the carrier density profile, the mobility near the carrier density maximum, and the carrier activation efficiency. Up to nine fitting parameters are necessary to describe these physical quantities. A critical discussion of the sensitivity of data fit to variation in the parameter is given to establish the uniqueness of fitted parameters. The infrared method is non-destructive, is applicable to other dopants and semiconductors, and provides information complementary to both ion channeling and resistivity profiling techniques.

INTRODUCTION

In recent years there have been a number of studies employing optical techniques to characterize materials which have been ion implanted.^{1-4,6-18} These materials include a number of semiconductor and insulator crystals which are transparent in some portion of the visible-infrared part of the spectrum. One of the techniques frequently employed uses interference effects observed in reflection or transmission of a crystalline sample on which a heavily disordered or amorphous layer is produced by the implantation process.^{1-4,6-18} In the present work, physical models are constructed which can be used for least-squares computer fitting of the measured reflection for heavily implanted silicon both in the as-implanted condition and after isothermal annealing, and for both electrically active and electrically inactive implanted impurities. As a result of this fitting procedure a number of special features have been incorporated into the models and a general model has evolved. This model is quite

satisfactory for implanted and annealed Si samples and will presumably also apply to other implanted materials with perhaps some slight modification. This model is conceptually quite simple and will be discussed. The fitting process will be illustrated here by the application of the model to a high fluence, high energy, P^+ ion-implanted Si sample in the as-implanted state and in several stages of thermal annealing. The intent of this paper is to give a detailed description of the optical characterization of ion implanted semiconductors technique so that discussion of new physical insights deriving from the data analyses are deferred to future publications.

Examples of the type of data which one would like to reproduce are shown in Figures 1a and 1b. These data are the measured reflection at normal incidence from a $\langle 111 \rangle$ oriented Si sample implanted with 2.7 MeV ions of P^+ with a fluence of 1.74×10^{16} ions/cm². The measurements of Figure 1a are reproduced from Ref. 1 for the sample in the as-implanted condition (these fringes were first observed by Crowder et al., ref-9) while the other set is for the same sample after annealing at 500°C for 70 h. The reflection is measured from the implanted surface with the rear surface coarse-ground to eliminate multiple reflections. The interference effects are a result of the dielectric changes produced by the implantation.^{6,9} Interference fringes, observed as a periodic modulation of the reflected or transmitted light as a function of frequency, are produced by the interference of light which is multiply reflected between the front surface and (i) the amorphous/crystalline material interface where there is an approximately 15% change in the refractive index⁹ (Fig. 1a) or, (ii) the free carrier plasma in cases where an electrical dopant is implanted and when the light frequency is near or below the free carrier plasma frequency^{4,5,8,12} (Fig. 1b). Previous work has centered on measuring only the refractive index and the thickness of the amorphous layer,^{9-11,13-17} or has used oversimplified models of dopant distributions to describe free carrier effects.^{4,18} The work is an extension of the previous work cited and also builds upon previous work by these authors.^{1-4,8,10-12} Although the use of an interference formulation to predict the general features of the data is common in the literature,^{1-4,6-13,16-18} it will be shown that careful, detailed fitting for high fluence implants, i.e., approximately 10^{15} ions/cm² or greater, can yield meaningful information concerning not only the change in dielectric constant due to the creation of an amorphous layer and thickness of the amorphous layer, but in addition the width of the transition region, the refractive index in the recrystallized region, and the annealing-induced change in the refractive index of the amorphous layer. In those cases where the implanted ion is a donor or acceptor we also now obtain results determining the carrier density and its distribution in the recrystallized material, the carrier mobility in the high carrier density portion of the implanted region, and the carrier activation efficiency. A critical discussion of the sensitivity of data fit to variation in the parameters is given which establishes the uniqueness of the fitted parameters.

DESCRIPTION OF MODEL

Elements of a general model that has been developed for the calculation of reflection spectra are illustrated in Figure 2. The upper portions (2a and 2b) represent the refractive index n and extinction coefficient k profiles for frequencies well above the free carrier plasma frequency where the free carrier electric susceptibility is negligible. The three regions shown are the damaged region near the surface of the sample (D), an intermediate region in which the material has recrystallized by epitaxial regrowth (R), and the substrate material (S). The substrate is taken to be of infinite extent because the back surface is roughened to scatter the reflected light, thus eliminating multiple reflections. It is assumed that the frequency is far removed from any strong characteristic absorption of the host lattice so that the substrate material is

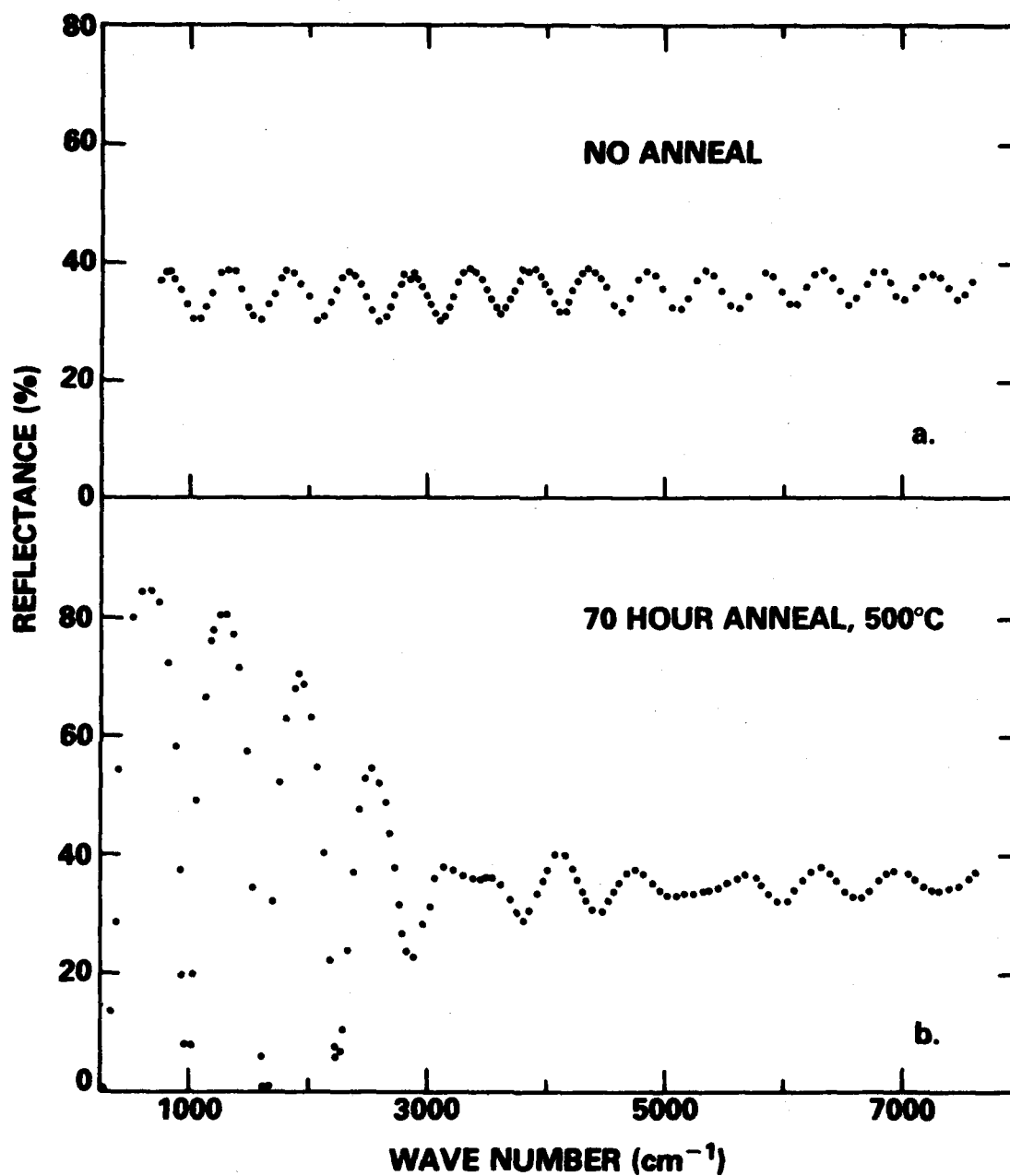


Figure 1. Infrared reflection data for a $\langle 111 \rangle$ oriented silicon sample implanted with 2.7 MeV phosphorus to a fluence of 1.74×10^{16} ions/cm². (a) Non-annealed. (b) After a 70h, 500°C anneal.

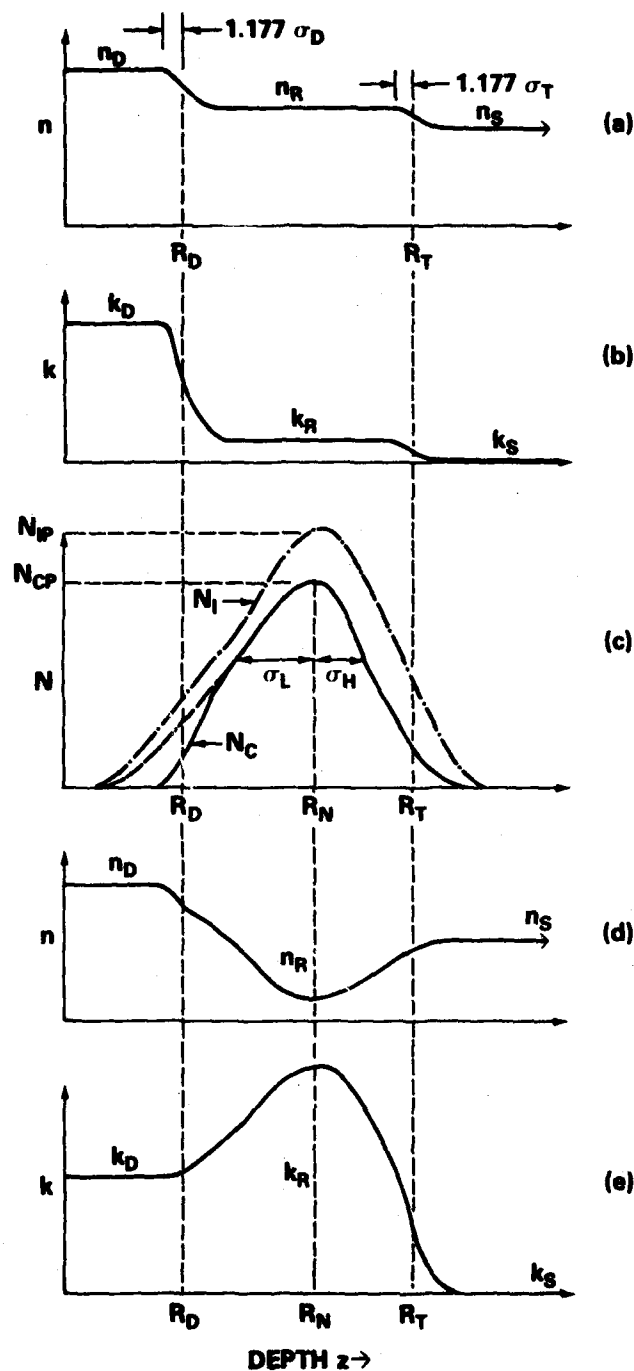


Figure 2. A schematic representation of the model used to calculate infrared reflection spectra. (a,b) show the depth profiles for the high frequency refractive index and extinction coefficient in the damaged surface layer (n_D , k_D), the recrystallized region (n_R , k_R), and the crystalline substrate (n_S , $k_S = 0$). (c) illustrates the impurity distribution (dash-dot) and carrier distribution (solid line) in the recrystallized region represented by a truncated skewed Gaussian. (d,e) illustrate the depth profiles of the refractive index and extinction coefficient due to the free carrier plasma in the recrystallized region for a frequency near the plasma frequency.

transparent, i.e., $k_s = 0$. The index of refraction of the substrate is kept constant during all analyses and in the present work is set equal to that of crystalline Si.¹⁹

It is assumed that the fluence of ions is sufficiently large that the damage in the front layer is saturated so that the disordered region has uniform dielectric properties (n_D, k_D).^{16,17} (For smaller fluences it is necessary to introduce a spatial variation of n_D and k_D .) The depth of the damaged region produced during implantation is R_T . It is assumed that during annealing the position of the amorphous to crystalline transition moves via epitaxial regrowth to R_D . It is known that epitaxial regrowth is the dominant recrystallization process during thermal annealing of ion implanted Si crystals.^{20,21} The refractive index and extinction coefficient (n_R, k_R) of the regrown material are not necessarily equal to those of the substrate. The transitions between the three regions are characterized by half-Gaussians of width σ_D and σ_T (see Figure 2a). The effect of the finite width of these transition regions is to reduce the amplitude of the interference fringes at high frequencies as illustrated in Figure 1a for an as-implanted Si sample. It is convenient to define R_D and R_T as the refractive index half-heights of the transitions as shown in Figure 2a.

If the implanted ions are normally donors (or acceptors) there will be a distribution of free carriers within the recrystallized region.² Because, in general, the implanted ion distributions are assymmetric,²² two half Gaussians with different standard deviations σ_N are used to represent the carrier distributions. The model description of the free carriers is illustrated in Figure 2c, 2d, and 2e. The centroid position is R_N , the carrier width σ_N on the implanted side is σ_L , and the width on the back side is σ_H ; i.e., $\sigma_N = \sigma_L$ for $z < R_N$ and $\sigma_N = \sigma_H$ for $z > R_N$. The free carrier concentration is represented by the solid curve in Figure 2c and has a peak carrier concentration N_{CP} . The carriers reside in the regrown material but have a tail into the substrate region. If it is assumed that the carrier activation efficiency E is independent of the implanted ion concentration N_I (dash-dot curve in Figure 2c), the carrier distribution would be the same as the impurity ion distribution. In general the activation efficiency is significantly less than one so the peak carrier density N_{CP} is less than the peak impurity concentration N_{IP} . The position of the transition from the damaged to the plasma region is taken to be R_D and the width of the transition region to be σ_D , the same parameters used for the high frequency refractive index and extinction coefficient (Figures 2a, 2b). The dashed portion of N_C in Figure 2c represents the carrier density that results when R_D goes to 0.

The optical constants n_R and k_R at the lower frequencies are dominated by the free carrier plasma which is characterized by a plasma frequency $\omega_p(N)$ and damping constant γ . These quantities are determined by the type and density of the free carriers, and consequently n_R and k_R vary with position in the regrown material. This is illustrated in Figures 2d and 2e and is discussed later. A list of parameter symbols and definitions appear in the appendix for convenient reference.

In order to describe the model presented in Figure 2 which includes the effect of an inhomogeneous but smoothly varying free carrier density profile, a computer code was written which calculates the reflection R for normal incidence from the thin-film equations of Heavens.²³ This code computes R for an arbitrary number of layers having indices n_j , extinction coefficient k_j , and layer thicknesses Δz_j . The substrate was taken to be infinitely thick of index n_s , and extinction coefficient $k_s = 0$.

A somewhat simpler version of this code was initially used to characterize non-annealed, implanted Si.¹ Since there was no recrystallized material, there was no n_R or

$k_R, R_D = R_T$, and $N_C = 0$ for all z . The tail of implanted ions into the substrate region did not produce any discernible effects due to free carrier plasma in the unannealed samples. For the fluences studied the disordered layer refractive index was shown to be uniform from the surface to the amorphous-crystalline interface. The damping of the interference fringes at high frequencies illustrated in Figure 1a was the same for 300 keV and 2.7 MeV implants. If this damping were due to the extinction coefficient k , the damping would be very different for these two cases because of the widely different thicknesses of the amorphous layers. The damping was reproduced only by introducing a finite width transition region σ_T between the amorphous and crystalline regions. The average width σ_T was 35 nm and there was no discernible variation with ion species or energy. It was also found that the measured values of k_D were small and had little effect on the analysis for the frequency range $250 \lesssim \nu \lesssim 7600 \text{ cm}^{-1}$, where $\nu = 1/\lambda$ is the wave number in cm^{-1} . Excellent fits were obtained for $k_D = 0$.

One of the first changes that occurs when the samples are thermally annealed is an increase in the amplitude of the high frequency interference fringes due to a sharp reduction in the width of the transition region σ_T to less than our fitting sensitivity of about 20 nm. Therefore, for the annealed samples a large reduction in computer time was gained by setting $\sigma_R = \sigma_D = 0$ with essentially no change in the quality of the fits. All calculations presented are for $k_D = k_S = 0$ and $\sigma_R = \sigma_D = 0$ for the annealed samples.

DISCUSSION AND APPLICATION OF MODEL

To illustrate the changes in the reflection spectra that are predicted by the model for a sample which is being thermally annealed the curves in Figure 3 were generated by allowing only R_D , the depth of the damaged region, to vary. The parameters used are typical of those obtained in the fitting of Si reflection spectra. As R_D decreases from R_T to 0 corresponding to increased annealing times at an elevated temperature, the thickness of the regrown layer becomes progressively larger. It is clear that the calculated curves closely resemble those of the Si data presented in Figure 1 (and in Figure 7 which will be discussed later).

In generating these curves the process is similar to that presented in Ref. 1 except that the effects of regrowth and free carriers have been included. The parameters for the example in Figure 3 are as follows:

- (1) R_T and R_D : The depth of the amorphous layer in the as-implanted case is $R_T = 2.52 \text{ } \mu\text{m}$ which is the value for a 2.7 MeV P^+ implant in Si. The depth of the amorphous-crystalline interface R_D was the only parameter changed in Figure 3 and the values used are $R_D = 2.52, 2.31, 1.80$, and $0 \text{ } \mu\text{m}$.
- (2) n_S, n_R, n_D : In the absence of free carrier effects, i.e., at high frequencies, the refractive indices are fitted to a Sellmeier equation of the form

$$n_{S,R,D} = \left(A_{S,R,D} + \frac{B_{S,R,D}}{\Omega_{S,R,D}^2 - \nu^2} \right)^{\frac{1}{2}}, \quad (1)$$

where ν is the wave number in cm^{-1} .

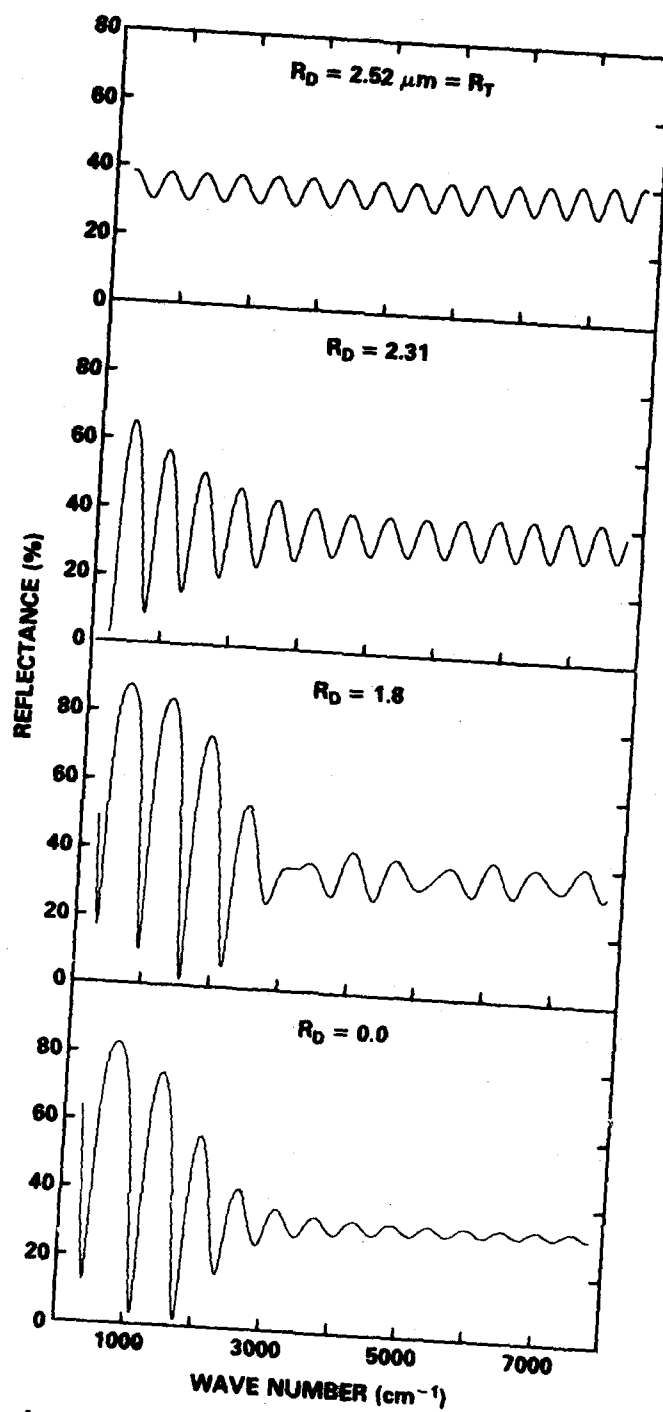


Figure 3. Calculated curves for four different values of the amorphous layer depth R_D with all other parameters fixed at values given in text.

For the calculations of Figure 3 the values of the constants A, B, and Ω for the substrate refractive index n_S were taken to be those for crystalline Si determined in Ref. 1 and these values are listed in Table I.

The high frequency refractive index n_R was set equal to $1.03 n_S$. The values of the constants A, B, and Ω for the damaged layer refractive index n_D were taken to be those for amorphous Si determined in Ref. 1 and these values are also listed in Table I.

TABLE I
Crystalline and Amorphous Si Constants

$A_S = 4.1476$	$A_a = 7.03$
$B_S = 5.8876 \times 10^9 \text{ cm}^{-2}$	$B_a = 2.64 \times 10^9 \text{ cm}^{-2}$
$\Omega_S = 27,973 \text{ cm}^{-1}$	$\Omega_a = 18,860 \text{ cm}^{-1}$

- (3) σ_D and σ_T : These widths were set equal to zero for all curves in Figure 3. Therefore Figure 3a does not represent a non-annealed sample but one that has had a short anneal.
- (4) k_D and k_S : For the frequency range studied both k_D and k_S were set equal to zero. As previously discussed, these conditions apply to Si.
- (5) N_C and γ : If the implanted ions become electrically active as donors or acceptors in the recrystallized region, the low frequency behavior is dominated by a free-carrier plasma. The calculations of n_R and k_R must include the dispersion effects produced by the plasma. In the recrystallized region, n_R and k_R are functions of $N_C(z)$, $\gamma(z)$, and ν . Following the procedures of Refs. 1 and 3, the carrier profile was partitioned into layers of equal thickness Δz_N with the carrier concentration N_{Cj} in each region given by:

$$N_{Cj} = N_{CP} \exp \{ -(z_j - R_N)^2 / 2\sigma_N^2 \}, \quad (2a)$$

$$\text{where} \quad z_j = R_N - 4\sigma_N + (j - 1) \Delta z_N \quad (2b)$$

$$\Delta z_N = \sigma_N / 10 \quad (2c)$$

$$\text{and} \quad \sigma_N = \sigma_L \text{ for } R < R_N, \sigma_N = \sigma_H \text{ for } R > R_N. \quad (2d)$$

N_{CP} was equal to $1 \times 10^{20} \text{ cm}^{-3}$, $R_N = 2.23 \text{ } \mu\text{m}$, $\sigma_L = 0.35 \text{ } \mu\text{m}$, and $\sigma_H = 0.14 \text{ } \mu\text{m}$ for the calculations shown in Figure 3.

Given the depth dependence of $N_C(z)$ the optical constants n_j and k_j can be computed. The complex dielectric function $\epsilon = \epsilon' + i\epsilon''$ for layer j may be written

$$\epsilon_j = (n_j - ik_j)^2 = A_R + \frac{B_R}{\Omega_R^2 - \nu^2} - \frac{\omega_{pj}^2}{\omega^2 - i\gamma_j\omega} \quad (3)$$

The first two terms are the normal dispersion terms already discussed. The third term is the dielectric response for free carriers where $\omega = 2\pi c\nu$, γ_j is the damping constant, and ω_{pj} is the plasma frequency defined by

$$\omega_{pj}^2 = \frac{4\pi N_{Cj} e^2}{m^*} \quad (4)$$

where m^* is taken here as the conductivity effective mass for electrons in Si, $m^* \approx 0.2 m_e$. For the calculation of the spectra in Figure 3, γ was kept constant in depth and set equal to $7 \times 10^{13} \text{ sec}^{-1}$. With γ taken as a constant the depth dependence of the dielectric constant enters through the carrier density dependence of the plasma frequency.

Factoring equation 3 for ϵ_j into its real and imaginary parts gives

$$\epsilon_j' = n_j^2 - k_j^2 = A_R + \frac{B_R}{\Omega_R^2 - \nu^2} - \frac{\omega_{pj}^2}{\omega^2 + \gamma_j^2} \quad (5)$$

$$\epsilon_j'' = 2n_j k_j = \frac{\gamma \omega_{pj}^2}{\omega(\omega^2 + \gamma_j^2)} \quad (6)$$

Solving equations 5 and 6 for the refractive index n_j and extinction coefficients k_j gives

$$n_j = \left\{ \frac{1}{2} \epsilon_j' + \frac{1}{2} (\epsilon_j'^2 + \epsilon_j''^2)^{\frac{1}{2}} \right\}^{\frac{1}{2}} \quad (7)$$

and

$$k_j = \left\{ -\frac{1}{2} \epsilon_j' + \frac{1}{2} (\epsilon_j'^2 + \epsilon_j''^2)^{\frac{1}{2}} \right\}^{\frac{1}{2}} \quad (8)$$

Inserting the optical parameters n_j , k_j , and the layer width Δz_N into the thin film equations of Heavens²³ permits the computation of the reflection R at any frequency.

As a practical matter, testing of the computer code has shown that the calculations converge to better than 0.1% R if the distribution for N_C is computed to 4 standard deviations (σ_L , σ_H) on both sides of R_N (as explicitly described by equation 2b) and if $\Delta z_N < \sigma_N/10$ (equation 2c).

SIGNIFICANCE AND SENSITIVITY OF MODEL PARAMETERS

The model described above characterizes physical changes taking place during implantation and subsequent annealing. The model incorporates a number of parameters representing positions (R_D , R_N , R_T), widths (σ_D , σ_T , σ_L , σ_H), indices of refraction (n_D , n_R , n_S), absorption (k_D , k_R), and properties of the plasma region (N_C , γ). The large number of parameters to be determined from the fitting of interference spectra might cause one to question the significance and uniqueness of the parameters obtained. In this

section this question is discussed by presenting calculated curves that demonstrate the particular features of the interference spectra governed by each parameter.

This separation of features has already been implicitly made in the presentation of the model in Figure 2. Figures 2a and 2b are representative of the system at high frequencies where $\omega \gg \omega_{pj}$ and Figures 2d and 2e determine the response at lower frequencies where $\omega \approx \omega_{pj}$. This division occurs because the influence of the plasma is significant at frequencies near the plasma frequency, and for the cases of interest here ω_{pj} ranges over values corresponding to frequencies from zero to about 1500 cm^{-1} . Thus, for data similar to the curves presented in Figure 3, the spectra above about 3500 cm^{-1} are not affected by the plasma parameters (R_N , σ_L , σ_H , N_{CP} , and γ) but are sensitive to the remaining parameters (n_D , n_R , k_D , k_R , R_D , R_T , σ_D , and σ_T). In the case of Si, the extinction coefficients (k_D , k_R) can be set equal to zero for the frequency range under consideration. Our experience also indicates that for the annealed samples the widths σ_D and σ_T are small ($\lesssim 20 \text{ nm}$) and may be set equal to zero with negligible effect on the quality of the fits obtained. This leaves only the parameters n_D , n_R , R_D , and R_T to describe the high frequency spectra. The curves calculated in Figure 3 incorporate these simplifications.

The calculation in Figure 3a is for $R_D = R_T$ and would therefore represent a non-annealed sample except for the fact that $\sigma_D = \sigma_T = 0$. N_{CP} is set equal to zero because there is no plasma effect observed in the as-implanted samples. The index of refraction of the damaged layer can be obtained from the average value of the reflection R using

$$\bar{R} = \left(\frac{n_D - 1}{n_D + 1} \right)^2. \quad (9)$$

Neglecting the frequency dependence of n_D , the depth of the damaged region ($R_D = R_T$) is determined from the frequency interval $\Delta\nu$ of the high frequency fringes from the simple thin film relation

$$R_T = \frac{1}{2n_D \Delta\nu}, \quad (10)$$

where $\Delta\nu$ is the difference in frequency between two successive maxima or minima in the reflection spectra in the units of wave numbers. If the interface between the damaged and crystalline region is sharp ($\sigma_D = \sigma_T = 0$) the peak to peak amplitude of the oscillation is given by

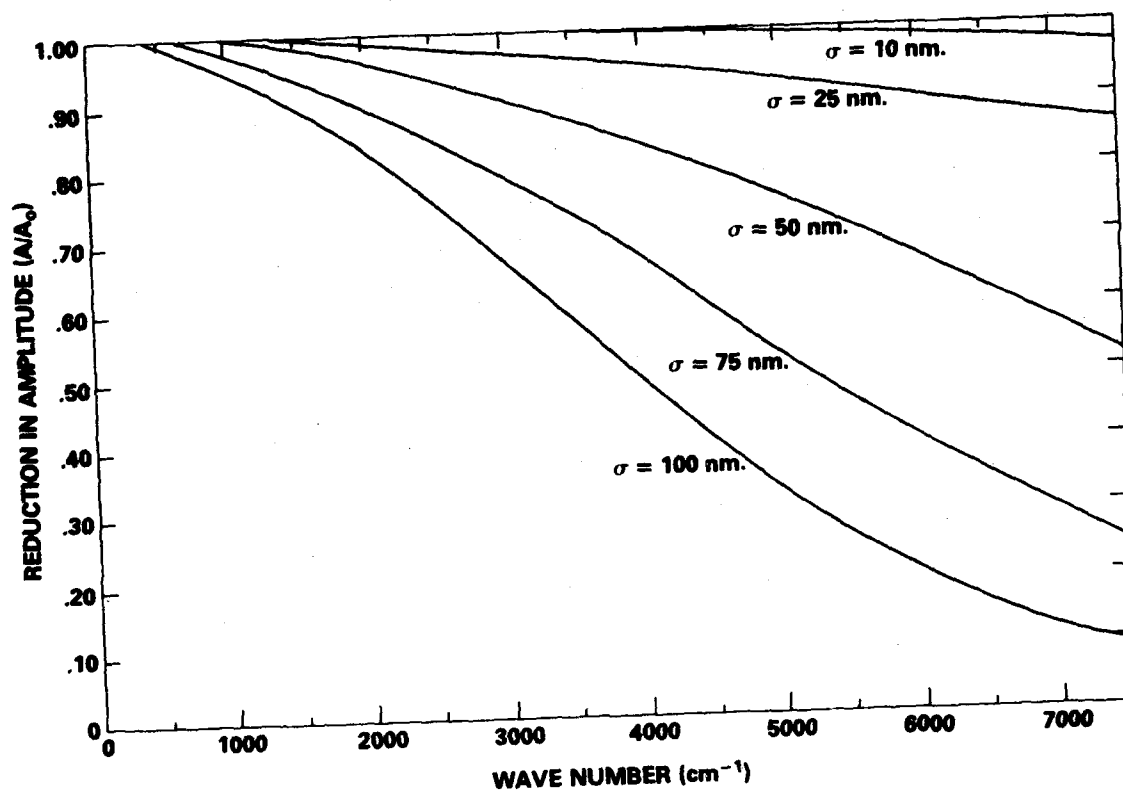


Figure 4. The reduction in the amplitude of high frequency fringes due to a transition region of width σ_D between the damaged and crystalline regions.

$$A_0 = 2 \left[\left(\frac{n_D - 1}{n_D + 1} \right)^2 - \left(\frac{n_S - 1}{n_S + 1} \right)^2 \right]. \quad (11)$$

If the interface is not sharp, the width of the transition region can be obtained by comparing the measured amplitude of oscillations to A_0 and using Figure 4 which shows the calculated frequency dependence of the oscillation amplitude. Thus, the measured reflection spectrum from a non-annealed sample in which the amorphous layer extends to the surface yields n_D , R_T , and σ_T directly.

The computer program performs a non-linear least-squares fit to R for the parameters n_D , R_T , and σ_T . However, we note that n_D is frequency dependent and therefore from Equation 1 requires 3 parameters, i.e., A_D , B_D , and Ω_D . The parameters given in the second column of Table I are the average values obtained for a large number of amorphized, non-annealed, Si samples. The parameters A_a , B_a , and Ω_a can be taken directly from the table and then only R_T and σ_T are variables. But, a better fit to individual samples can be obtained if n_D is permitted to vary slightly from the average value. This can be accomplished by defining

$$n_D = f_D n_a = f_D \left(A_a + \frac{B_a}{\Omega_a^2 - \nu^2} \right)^{\frac{1}{2}}, \quad (12)$$

where A_a , B_a , and Ω_a are the average values from Table I and f_D is a fitting parameter. For 15 Si samples analyzed in Ref. 1, $f_D = 1.00 \pm 0.01$.

In Figure 3b, the lower frequency region shows the effect of the plasma in the recrystallized region between R_D and R_T . The frequency interval $\Delta\nu$ of the high frequency fringes increases as R_D decreases in depth, i.e. $\Delta\nu = 1/(2 n_D R_D)$.

There will also be a reflected wave from the interface at R_T if $n_R \neq n_S$. The effect of this reflection is seen in the high frequency fringes in Figures 3c and 3d. The curve in Figure 3c demonstrates the beating that occurs from the interference of these two waves. Figure 5a shows the same calculation except that $n_R = n_S$ and we see that the high frequency beating pattern disappears. Figure 3d is for a completely recrystallized sample in which $R_D = 0$ and $n_R > n_S$. That the high frequency fringes are due to the reflection at R_T is demonstrated by the calculation of Figure 5b for which $n_R = n_S$ and the high frequency fringes disappear. The frequency interval of the high frequency oscillations in Figure 3d is given by $\Delta\nu = 1/(2 n_R R_T)$.

Fitting high frequency measurements of the type illustrated in Figure 3c requires simultaneous adjustment of n_D , R_D , n_R , and R_T . But, because of dispersion, 3 parameters are required to specify each n . Since n_R is only slightly greater than n_S , it is convenient to reduce the number of parameters by using

$$n_R = f_R n_S = f_R \left(A_S + \frac{B_S}{\Omega_S^2 - \nu^2} \right)^{\frac{1}{2}}, \quad (13)$$

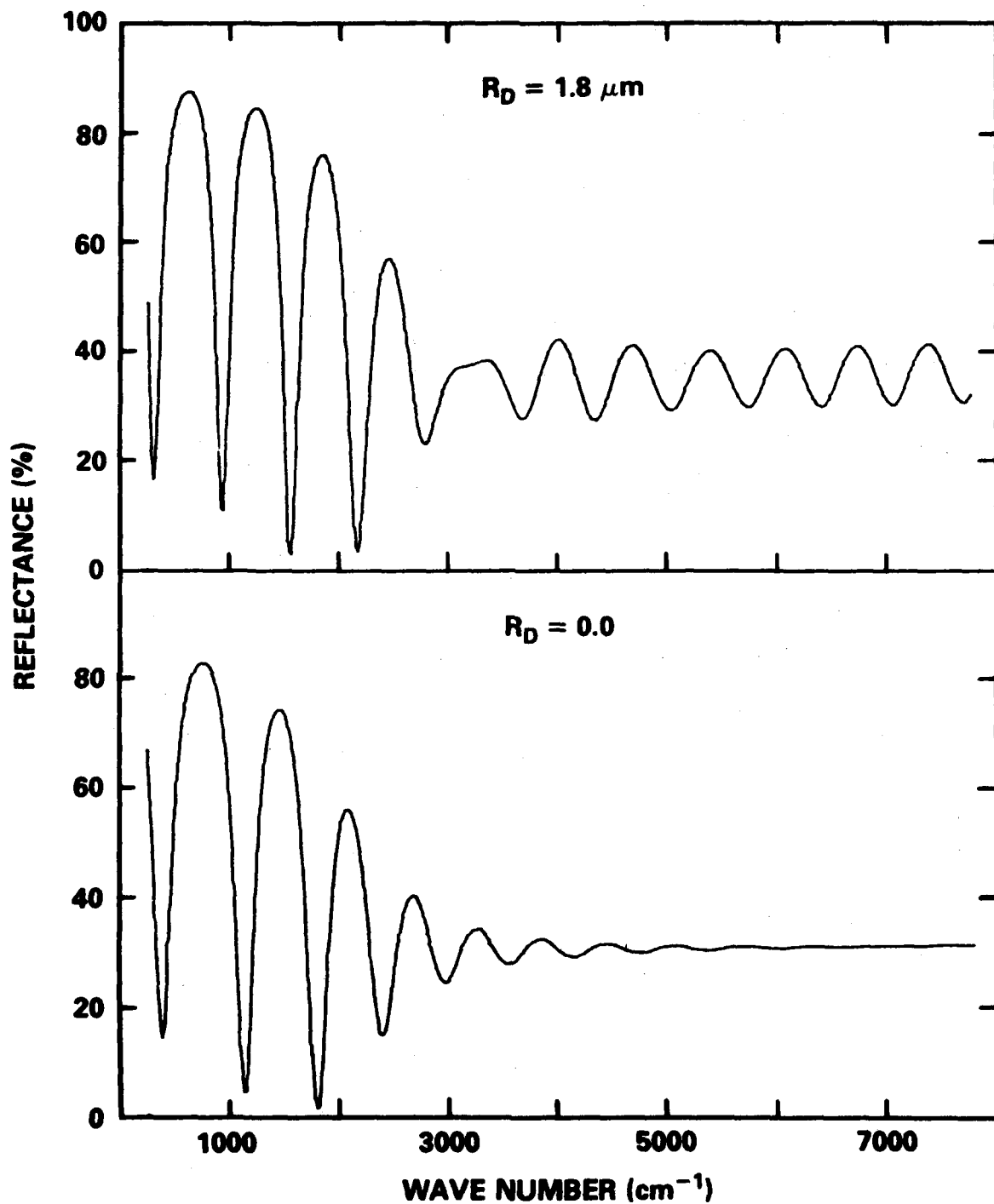


Figure 5. Calculated curves demonstrating the results of setting $n_R = n_S$. All other parameters are the same as those for Figure 3. (a) is for $R_D = 1.8 \mu\text{m}$ and is to be compared to Figure 3c. (b) is for $R_D = 0$ and is to be compared to Figure 3d.

where A_S , B_S , and Ω_S are the substrate constants from Table I and f_R is a fitting parameter. Fitting of these interference measurements puts close tolerances on f_D , R_D , f_R , and R_T .

We now turn to the parameters in the model which give information concerning the carrier density changes occurring during the regrowth process and which determine the low frequency portion of the interference spectra, i.e. $\nu < 3500 \text{ cm}^{-1}$. These parameters are N_{CP} , R_N , σ_L , σ_H , and γ . For the curves presented in Figures 3 and 5 the values of these parameters are: $N_{CP} = 10^{20} \text{ cm}^{-3}$, $R_N = 2.23 \mu\text{m}$, $\sigma_L = 0.35 \mu\text{m}$, $\sigma_H = 0.14 \mu\text{m}$ and $\gamma = 7 \times 10^{13} \text{ s}^{-1}$. These figures illustrate the growth of the plasma as the damaged region recrystallizes.

The curves in Figure 6 were generated to illustrate the changes produced as each of these parameters is independently varied. To reduce possible confusion due to the high frequency region, R_D was set equal to zero and $n_R = n_S$. Because of difficulties of presentation only one change for each parameter is shown but families of such curves have been generated. The discussion which follows is based on these calculations.

The variations in R_N (Figure 6a) change the spacing and phase of the fringes, but the envelope of maximum and minimum amplitudes is maintained. On the other hand, the variations in N_{CP} (Figure 6b) maintain the same fringe spacing but move the envelope along the frequency axis. In both cases the shape of the envelope is unchanged. For variations in γ (Figure 6c) the spacing and phase are unchanged but the shape of the envelope is altered. Thus, the effects of small variations of R_N , N_{CP} , and γ are nominally independent.

The two curves in Figure 6d illustrate the effect of introducing asymmetry in the carrier distribution. These curves were calculated for the same total number of carriers. The sharpening of one of the edges accompanying the introduction of an asymmetric distribution increases the amplitude of the fringes at the higher frequency end of the plasma reflection spectra ($> 3500 \text{ cm}^{-1}$). This effect is more significant when $R_D \neq 0$ or $n_R \neq n_S$ because these fringes contribute strongly to the beating pattern observed in this frequency region.

COMPARISON TO Si MEASUREMENTS

In this section we illustrate the use of the model to fit the reflection spectra for a series of anneal times at 500°C for the 2.7 MeV P-implanted $\langle 111 \rangle$ oriented Si sample used to provide the illustrative data in Figure 1. Figure 7 shows the reflection data for the sample in the as-implanted state and in three different anneal stages. The curves are best fit computer calculations where the best fit was determined by a reduced chi-squared criterion. The experimental points actually used in the fitting procedure are shown although many additional points were measured. The anneal stages and best fit parameters are listed in Table II. One can see that the "typical" parameter values used to generate the model curves of Figures 3 and 5 were chosen to be close to those of Table II.

DISCUSSION

- (a) The fit to the non-annealed samples is from Ref. 1 and is for $\sigma_D = 53 \text{ nm}$, and $R_D = R_T$. For all other calculations σ_D and σ_T were set equal to zero to reduce computer time.

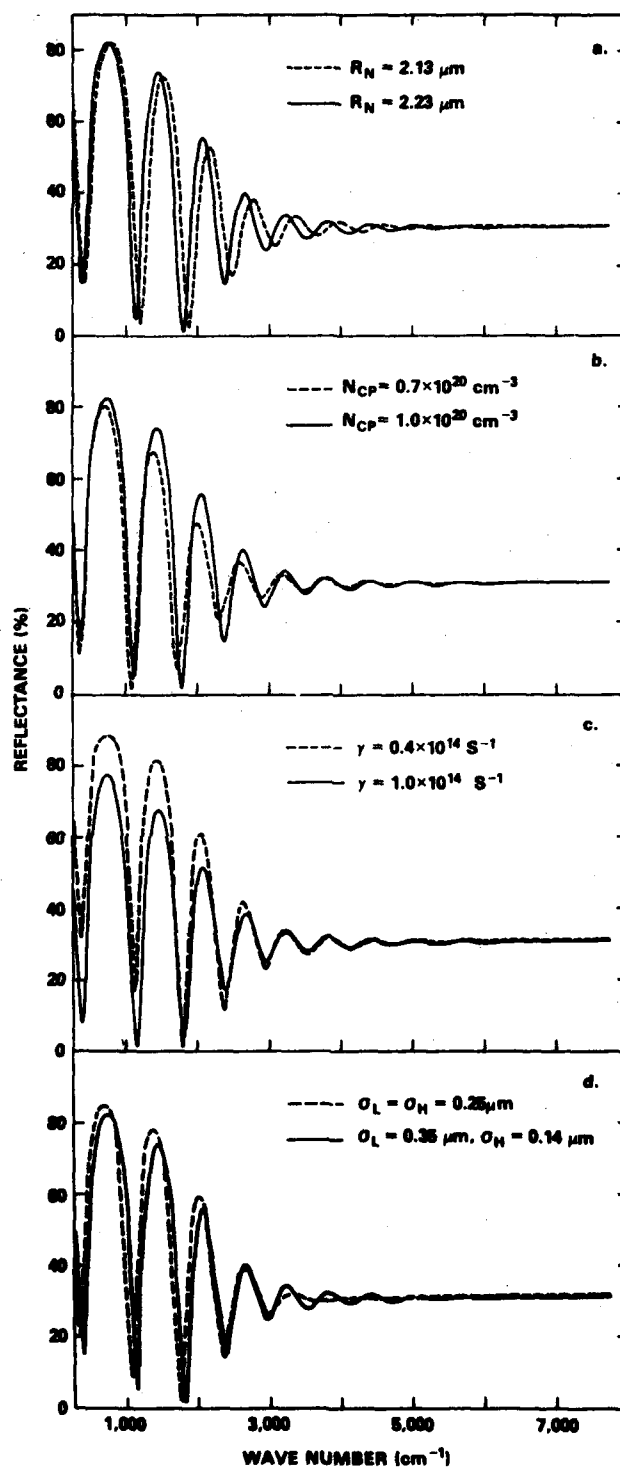


Figure 6. Calculated curves demonstrating the sensitivity of the low frequency portion of the reflection spectra to changes in individual plasma parameters. $R_D = 0$ and $n_R = n_S$ for all curves.

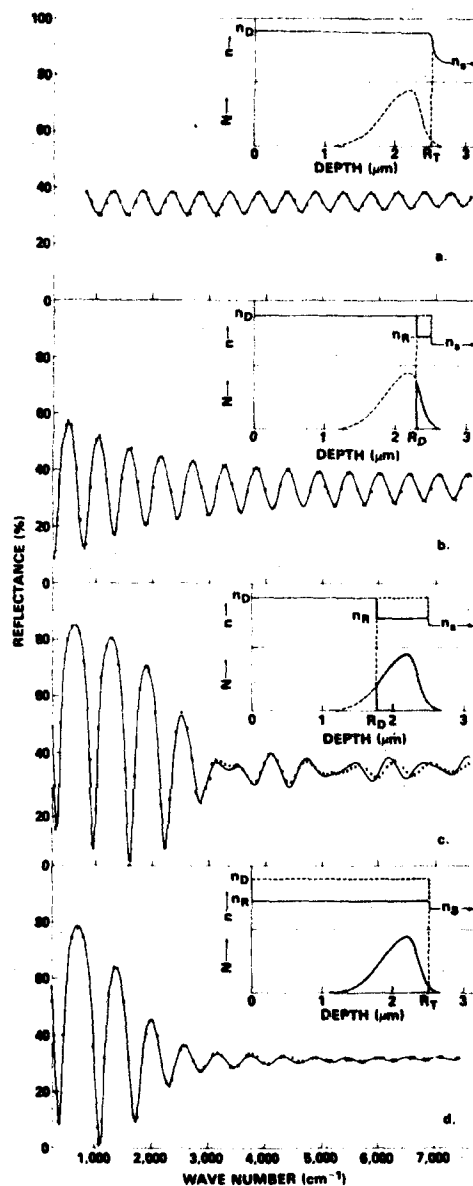


Figure 7. Comparison of measurements (x) to the best fit calculations for a $\langle 111 \rangle$ oriented Si sample implanted with 2.7 MeV P^+ to a fluence of $1.74 \times 10^{16}/\text{cm}^2$. (a) As-implanted at 200°K and no annealing other than at room temperature. (b) Annealed for 30h at 500°C. (c) Annealed for 70h at 500°C. (d) Annealed for 750h at 500°C. The inserts are schematic representations for the high frequency refractive index n and carrier concentration N_C used to fit the data. The cross-hatched areas for n indicate the change in refractive index caused by recrystallization and also the thickness of material that has recrystallized. The cross-hatched areas for N_C indicate electrically active carriers in recrystallized material. The dashed portion of the curve for N_C is the carrier concentration that will eventually result from the recrystallization process.

- (b) The depths R_N and R_T were not kept fixed during the fitting procedure so the constancy of these quantities is a measure of the validity of the model and the reliability of these parameters.
- (c) It was found that the quality of fit to the data could be significantly improved by making the carrier distribution assymmetric. As in the case of R_N and R_T above, σ_L and σ_H were permitted to vary and their constancy in Table II is a measure of their accuracy. The structure in the interference pattern near 3400 cm^{-1} in Figure 7c was reproduced when the assymmetric distribution was introduced.
- (d) The amorphous material was found to anneal at 500°C prior to recrystallization. This is shown by the reduction in f_D in Table II.
- (e) Two methods were used to describe the damping constant γ . In the first, experimental values of the conductivity σ as a function of carrier density were incorporated into the code by means of the analytical expression of Irvin.²⁴ From the depth dependence of N_{Cj} the depth dependent conductivity σ_j was computed. The damping constant γ_j was then taken as

$$\gamma_j = \frac{N_{Cj} e^2}{m^* \sigma_j F_\gamma} \quad (14)$$

A fitting parameter F_γ was introduced to allow adjustments of γ_j while maintaining the same functional dependence. F_γ was determined in the fitting process and the mobility for any slab was computed by the usual expression

$$\mu_j = \frac{e}{m^* \gamma_j} \quad (15)$$

The second method is that used in generating the illustrative curves and simply assumed that γ in Equations 3, 5, and 6 is a single adjustable parameter for all values of N_{Cj} . Then an effective average mobility for the carriers in the conducting layer is obtained from

$$\mu_{\text{eff}} = \frac{e}{m^* \gamma} \quad (16)$$

The two methods used for obtaining γ were applied to the data in Figure 7d for the fully annealed sample. The resultant values of the damping constant as a function of the Gaussian carrier distribution are plotted in Figure 8 with the number of standard deviations from the centroid R_N on the abscissa and the carrier concentration and damping constant γ as the ordinates. The points are the carrier density, the smooth curve is the damping constant for γ chosen from experimental conductivity values according to Irvin²⁴ and the fitted parameter F_γ and the dashed line is the value of γ from the best fit for the constant γ calculation. The fitted curves for the two different cases were indistinguishable and both give the curve shown in Figure 7d. Note the excellent agreement between experiment and calculation. Therefore either method seems appropriate to describe the data.

Table II — Parameter values for best fit curves of Figure 7

<u>Parameter</u>	<u>Figure 7a</u>	<u>Figure 7b</u>	<u>Figure 7c</u>	<u>Figure 7d</u>	<u>Uncertainty</u>
R_T/σ_T (μm)	2.52/0.053	2.59/—	2.51/—	2.52/—	$\pm 0.06/0.02$
R_D/σ_D (μm)	2.52/0.053	2.32/—	1.80/—	0	± 0.02
R_N (μm)	—	2.26	2.20	2.22	± 0.04
σ_L (μm)	—	—	0.33	0.36	± 0.06
σ_H (μm)	—	0.11	0.14	0.14	± 0.04
N_{CP} ($\times 10^{20}/\text{cm}^3$)	—	1.15	1.16	0.68	± 0.08
f_D	1.0	0.97	0.97	—	± 0.01
f_R	—	1.01	1.04	1.02	± 0.02
F_Y	—	1.07	0.77	0.78	± 0.09
E (%)	—	—	—	24	

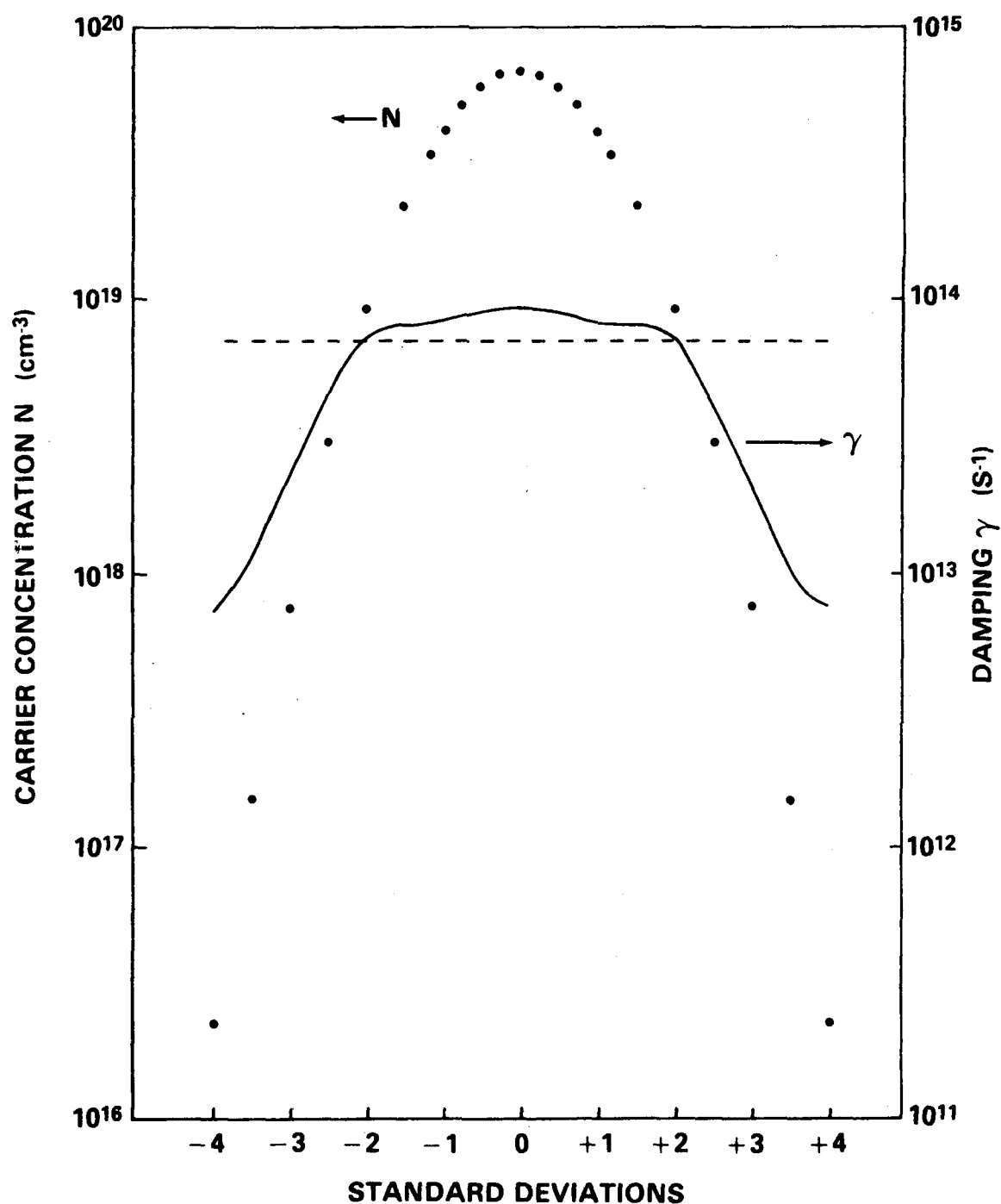


Figure 8. Comparison of the carrier density profile $N_C(z)$ to the depth dependence of the damping constant $\gamma(z)$. The dots are the best fit carrier density for the sample annealed for 750h in Figure 7d as a function of the number of standard deviations from the centroid. The solid curve is the best fit damping constant γ using a carrier density dependent γ and the dashed line is the best fit damping factor assuming γ is independent of N_C (see text). The best fits to the data using both methods are indistinguishable.

The empirical fact that the calculation is insensitive to the depth dependence of γ may be qualitatively understood by noting that in Figure 8, γ is constant to within 20% from -2 to +2 standard deviations while the corresponding change in carrier density is a factor of seven. Therefore, the damping constant γ is nearly constant in the region where 95% of the carriers are concentrated.

Having determined values of γ , the calculated mobility at the peak carrier density for the variable γ method is $\mu = 100 \text{ cm}^2/\text{V-s}$ and the mobility for the constant γ method is $\mu = 120 \text{ cm}^2/\text{V-s}$. These values agree reasonably well with the data in the literature^{24,25} which give $\mu = 70 \text{ cm}^2/\text{V-s}$ for $N_C = 10^{20} \text{ cm}^{-3}$. From the discussion of the calculation of γ we conclude that the mobility measured by fitting with the constant γ method is representative of the mobility for carrier densities in the vicinity of the peak carrier density.

- (f) An estimate of the carrier activation efficiency can be determined from the ratio of the integral of the fitted carrier profile to the implant fluence Φ . for a skewed Gaussian distribution $E = \sqrt{\pi}/2 N_{CP} (\sigma_L + \sigma_H)/\Phi$. This gives a value of 24% for the fully annealed sample.
- (g) An estimate of the uncertainty of each parameter was obtained by determining the change in one parameter that doubles χ^2 with all other parameters fixed. The reduced χ^2 for the four fits in Table II vary from about 10^{-5} to about 10^{-4} and this corresponds to an average deviation per point of 0.4% and 0.8%, respectively. The experimental error in R is $\pm 0.5\%$ so that the agreement in either case is quite satisfactory. The uncertainties included in Table II are for the data in Figure 7c because in this case all parameters are involved in the fitting. This represents a "worst-case" situation because χ^2 is largest for this fit and, in this method of determining uncertainties, the estimated uncertainties decrease as χ^2 decreases. The uncertainty in particular parameters depends upon the position of R_D with respect to R_N . For example, if $R_D > R_N$ there is no sensitivity to σ_L , and the sensitivity to R_N is reduced. However, in these cases where the number of significant parameters is reduced, significant reductions in uncertainty are obtained.

SUMMARY

The success of the model presented here in predicting infrared reflection data shows that this technique can be used to determine physical characteristics of ion-implanted semiconductor materials with reasonable precision. Although the infrared (ir) method has only been applied to phosphorus implanted silicon, it is general and applies to other dopants in silicon as well as other semiconductor materials. Minor modifications of the dielectric function to include lattice absorption (reststrahl) are required for most semiconductors and insulators and these modifications have been treated elsewhere.^{10,11} As already noted the method is chiefly useful at high carrier densities ($> 10^{18}/\text{cm}^3$ in silicon). Within this limit the information obtained is complementary to the methods of ion channeling and resistivity profiling. It is evident that the ir method can determine whether the implanted material is in an amorphous or crystalline state, and also measures the depth of the amorphous material. The ir method is unable to distinguish between single crystal and polycrystalline phases. On the other hand, the ion channeling technique can determine whether the material is in a single crystal or disordered state, and measures the depth of the disordered phase. Channeling cannot distinguish between polycrystalline and amorphous phases. Both the

ir method and ion channeling can determine regrowth kinetics from isothermal annealing data.

The ir method cannot directly determine the activated carrier density profile but requires a priori knowledge about the shape of the impurity distribution. However, it is possible to distinguish between several different distributions by determining which one gives minimum χ^2 . Therefore it is possible, for example, to follow simple redistribution effects by determining variations in parameters (e.g., N_{CP} , σ_L , σ_H) with annealing condition. However, characterization of anomalous redistributions such as seen in the annealing of Al implanted Si would presumably be difficult to do.²⁶ The measured activated carrier density profile can be converted to a resistivity profile for most semiconductors by means of well established resistivity versus carrier density relationships.²⁷ Resistivity profiling of high carrier densities is usually performed by sheet resistivity measurements combined with stripping and thus measures the resistivity directly. With the ir method, carrier density profile, the carrier mobility near the peak carrier density, and carrier conversion efficiency are obtained nondestructively.

Higher energy implants provide ir reflection spectra with many features in the 250 cm^{-1} - 7600 cm^{-1} range and thus give a good test for the model. However, most implantations of practical importance are performed at energies below about 300 keV and the interference spectra contain few oscillations in this frequency range. Our work on the thermal annealing of 200 keV to 300 KeV implanted Si samples indicates that the desired physical quantities can also be determined for lower energy implants. This work will be published soon.

ACKNOWLEDGEMENTS

The work of these authors was supported in part by the Navy Material Command (GKH, PRM) and in part by the Joint Services Electronics Program monitored by the Air Force Office of Scientific Research under Contract No. F44670-76C-0061 (CNW, WGS).

REFERENCES

1. G. K. Hubler, C. N. Waddell, W. G. Spitzer, J. E. Fredrickson, S. Prussin, and R. G. Wilson, J. Appl. Phys. **50**, 3294 (1979).
2. W. G. Spitzer, J. S. Ko, C. N. Waddell, G. K. Hubler, and J. E. Fredrickson, J. Appl. Phys. **50**, 3775 (1979).
3. G. K. Hubler, P. R. Malmberg, and T. P. Smith, III, J. Appl. Phys. **50**, 7147 (1979).
4. S. -L. Kwun, W. G. Spitzer, C. L. Anderson, H. L. Dunlap, and K. V. Vaidyanathan, J. Appl. Phys. **50**, 6873 (1979).
5. G. Horowitz, Phys. Status Solidi A **39**, 533 (1977).
6. T. E. Seidel, G. A. Pasteur, and J. C. C. Tsai, Appl. Phys. Lett. **29**, 648 (1976).

7. B. L. Crowder and R. S. Title, Ion Implantation, edited by F. Eisen and L. Chadderton (Gordon & Breach, New York, 1971), p. 87.
8. G. K. Hubler, P. R. Malmberg, C. A. Carosella, T. P. Smith, III, W. G. Spitzer, C. N. Waddell, and C. N. Phillippi, *Radiat. Eff.* **48**, 81 (1980).
9. B. L. Crowder, R. S. Title, M. H. Brodsky, and G. D. Pettit, *Appl. Phys. Lett.* **16**, 205 (1970).
10. A. H. Kachare, W. G. Spitzer, and J. E. Fredrickson, *J. Appl. Phys.* **47**, 4209 (1976).
11. A. H. Kachare, W. G. Spitzer, J. E. Fredrickson, and F. K. Euler, *J. Appl. Phys.* **47**, 5374 (1976).
12. W. G. Spitzer, C. N. Waddell, G. H. Narayanan, J. E. Fredrickson, and S. Prussin, *Appl. Phys. Lett.* **30**, 623 (1977).
13. W. Primak, *Phys. Rev. B* **14**, 4679 (1976).
14. V. M. Gusev, L. N. Strelatsov, and I. B. Khaibulin, *Sov. Phys. Semicond.* **5**, 737 (1971).
15. H. J. Stein, Ion Implantation in Semiconductors, edited by I. Ruge and J. Graul (Springer-Verlag, New York, 1971), p. 2.
16. W. Wesch and G. Gotz, *Radiat. Eff.* **49**, 137 (1980).
17. K. Hehl and W. Wesch, to be published in *Phys. Status Solidi B*.
18. H. H. Wagner and R. R. Schaefer, *J. Appl. Phys.* **50**, 2697 (1979).
19. C. D. Salzberg and J. J. Villa, *J. Opt. Soc.* **47**, 244 (1957).
20. L. Cspregi, J. W. Mayer, and T. W. Sigmon, *Phys. Lett.* **54A**, 157 (1975).
21. L. Cspregi, J. W. Mayer, and T. W. Sigmon, *Appl. Phys. Lett.* **29**, 92 (1976).
22. J. F. Gibbons and S. Mylroie, *Appl. Phys. Lett.* **22**, 568 (1973).
23. O. S. Heavens, Optical Properties of Thin Solid Films (Academic, New York, 1955).
24. J. C. Irvin, *Bell Sys. Tech. J.* **41**, 387 (1962).
25. J. L. Moll, Physics of Semiconductors (McGraw-Hill, New York, 1964), p. 192.
26. H. B. Dietrich, W. H. Weisenberger, and J. Comas, *Appl. Phys. Lett.* **28**, 182 (1976).
27. S. S. Li and W. R. Thurber, *Solid State Electron.* **20**, 609 (1977).

APPENDIX: SYMBOLS

$n (n_D, n_R, n_S)$	Index of Refraction (Damaged, Recrystallized, Substrate Regions)
$k (k_D, k_R, k_S)$	Extinction Coefficient (Damaged, Recrystallized, Substrate Regions)
$\epsilon = \epsilon' + i\epsilon''$	Complex Dielectric Constant
ν	Wave Number ($1/\lambda$) in cm^{-1}
$\Delta \nu$	Frequency Interval of Oscillation in Reflection Spectra
ω_p	Plasma frequency
γ	Plasma damping constant
μ	Carrier mobility
σ	Conductivity
A, B, Ω	Sellmeir parameters
R_D	Depth of Damaged Region
R_T	Total depth of damaged region in as-implanted condition
R_N	Depth of peak carrier concentration
σ_D	Width of transition from damaged to recrystallized regions
σ_T	Width of transition from recrystallized to substrate regions
σ_N	Width of carrier distribution
σ_L, σ_H	Assymetric carrier distribution widths - L towards surface, H towards substrate
N_C/N_I	Density of carriers/implanted ions
N_{CP}/N_{IP}	Peak density of carriers/implanted ions
Φ	Fluence (ions/cm^2)

Section IV.B

EFFECTS OF THERMAL ANNEALING ON THE REFRACTIVE INDEX
OF AMORPHOUS SILICON PRODUCED BY ION IMPLANTATION

J. E. Fredrickson¹
C. N. Waddell and W. G. Spitzer²
G. K. Hubler³

¹Department of Physics
California State University at Long Beach
Long Beach, CA 90801

²Departments of Physics and Materials Science
University of Southern California
Los Angeles, CA 90007

³Materials Modification and Analysis Branch
Condensed Matters and Radiation Sciences Division
Naval Research Laboratory

This work was supported by the Air Force Office of Scientific Research
and the Naval Material Command.

**Effects of Thermal Annealing on the Refractive Index
of Amorphous Silicon Produced by Ion Implantation**

J. E. Fredrickson
Department of Physics, California State University at Long Beach
Long Beach, CA 90801

C. N. Waddell and W. G. Spitzer
Departments of Physics and Materials Science
University of Southern California
Los Angeles, CA 90007

G. K. Hubler
Naval Research Laboratory
Washington, DC 20375

ABSTRACT

Precise infrared reflection measurements of the refractive index of silicon show that there are two well-defined optical states of amorphous silicon produced by ion implantation. One is the as-implanted amorphous state which is the high refractive index state produced by high fluence implantation of Si or P ions into Si samples. The other state, which has a refractive index intermediate between the as-implanted and crystalline values, is induced by thermal annealing and is thermally stable until epitaxial recrystallization occurs. A comparison is made to the optical properties of amorphous Si produced by other means.

Wide variations in the optical properties of amorphous Si (a-Si) films are reported in the literature.⁽¹⁻²⁰⁾ For example, the presence of hydrogen, incorporated during production of the a-Si films, is known to produce large changes in the refractive index and optical absorption.^(15,17) Even for methods of preparation in which hydrogen is not present there are substantial differences in reported values which are generally thought to be related to variations in the density and electronic band structure.

Some recent infrared interference studies demonstrated that reflection measurements of heavily implanted samples can provide the depth dependence of the dielectric constant, $\epsilon(\nu)$.⁽¹⁸⁻²²⁾ These measurements give information which is complementary to that obtained from Rutherford backscattering data⁽²³⁾ and in some cases also yield information that could not be extracted from Rutherford backscattering experiments.^(21,22) The present letter reports infrared reflection measurements of ion implanted Si which indicate that there are two well-defined optical states for the implantation-induced a-Si. One is the as-implanted state produced by a high fluence implantation of Si samples that are maintained at a temperature between 200 and 300°K during implantation. The second is an annealing-induced, thermally stabilized state. This state is reached after annealing the implanted sample for about 20 min at 550°C or about 2h at 500°C and is stable until the amorphous layer recrystallizes via epitaxial regrowth (measured up to 150h at 500°C). This work differs from previous investigations in that isothermal annealing is used in

conjunction with precision measurements of the depth dependence of the refractive index to study a-Si films. Our measurements reveal features of the temperature dependence of the refractive index which are difficult to observe in the isochronal anneals of most previous investigations.

A number of $\langle 100 \rangle$ and $\langle 111 \rangle$ oriented Si samples were implanted 8° off axis with Si or P ions having energies of 300 keV, 380 keV, and 2.7 MeV (P ions only). The sample temperature during implantation was 200°K in some cases and 300°K in others. In all cases the fluences were sufficient to produce a continuous amorphous layer on the surface. Some of the implantation details are given in Table I, where R_D is the depth of the amorphous-crystalline interface determined from the room temperature infrared reflection measurements. The analysis of the measurements has been described previously.^(20,21,24)

The indices of refraction $n_D(\nu)$ of all the as-implanted samples were the same within the errors expected from the reproducibility of the reflection measurements (about 1%R). Within the range of implantation parameters employed here $n_D(\nu)$ is independent of whether Si or P ions are used, ion energy, fluence, orientation, or sample temperature during implantation. The $n_D(\nu)$ is the same as that given in a previous work,⁽²⁰⁾ and the values are repeated here in Table II.

The samples of Table I were annealed at 500°C except for A' which was annealed at 550°C . The values for the refractive index and thickness regrown (reduction in amorphous layer thickness) are deduced from a complete computer fitting of reflection curves like those of Fig. 1 for sample A by using a dielectric layer model described previously.⁽²⁴⁾ The decrease in both the mean reflection and the fringe amplitude between curves 1a and 1b indicates that the index of refraction has decreased during the 2h, 500°C , anneal. The constancy of this new value, $n_D(\nu)$, during further annealing and regrowth is demonstrated by the comparison of the mean reflection and amplitudes of curves 1b and 1c. Some of the parameter values including annealing times are given in the figure caption.

To determine the variation of the index of refraction during annealing, the reflection spectra were least-squares fitted using $n_D(\nu) = f_D n_D(\nu)$ where $n_D(\nu)$ is the index of refraction of non-annealed a-Si and f_D is a parameter. The results are shown in Fig. 2 where f_D is plotted as a function of time for isothermal anneals at 500 and 550°C for $\langle 100 \rangle$ and $\langle 111 \rangle$ Si samples implanted with Si or P ions. In all cases the value of f_D decreases from near 1.00 prior to any anneal to near 0.96 during the early part of the anneal—about 2h at 500°C and about 0.3 h for sample A annealed at 550°C . The average value of f_D for Si implanted samples is 0.961 ± 0.004 and for P implanted samples it is 0.963 ± 0.009 . If the implanted ions are electrical dopants (e.g., P) there will also be a buildup of large reflection oscillations at lower frequencies, $\nu < 3000 \text{ cm}^{-1}$, due to a plasma within the recrystallized material.⁽²²⁾ In these cases, only the spectral region above about 3500 cm^{-1} was used to determine the value of $n_D(\nu)$.

The thickness of the amorphous region decreases during the anneal cycle due to epitaxial recrystallization at the interface.⁽²³⁾ During the early part of the anneal when f_D is changing from 1.0 to 0.96, the thickness of the amorphous layer decreases about 0.05–0.1 μm for all samples. It should be noted that this decrease in thickness can be the result of regrowth, densification of the amorphous layer, or a combination of both. However, the fact that the change in thickness is independent of the thickness of the amorphous layer indicates that epitaxial regrowth is the dominant mechanism, although a change in density of <3% cannot be ruled out from our data.

Table 1 — Implanted Si samples

<u>Orientation</u>	<u>Sample #</u>	<u>Ion Implanted</u>	<u>R_D</u> (prior to annealing) (μm)	<u>Ion Energy</u> (keV)	<u>Fluence</u> (ions/cm ²)
<100>	A	Si ^(a)	0.71	380	0.5 x 10 ¹⁶
	A ^(b)	Si	0.70	380	0.5
	B	Si	0.75	380	0.5
	B'	Si	0.72	380	0.5
	B''	Si	0.72	380	0.5
<111>	76-2	Si	0.57	300	1.0
	76-3	P	0.51	300	1.0
	76-4	P	0.51	300	1.0
	77-3	Si	0.61	300	3.0
	78-6	P	2.52	2700	1.7
	78-8	P	2.61	2700	10.0

(a) All <100> samples were implanted with Si⁺⁺ at 190 kV

(b) This sample was annealed at 550°C, all others were annealed at 500°C

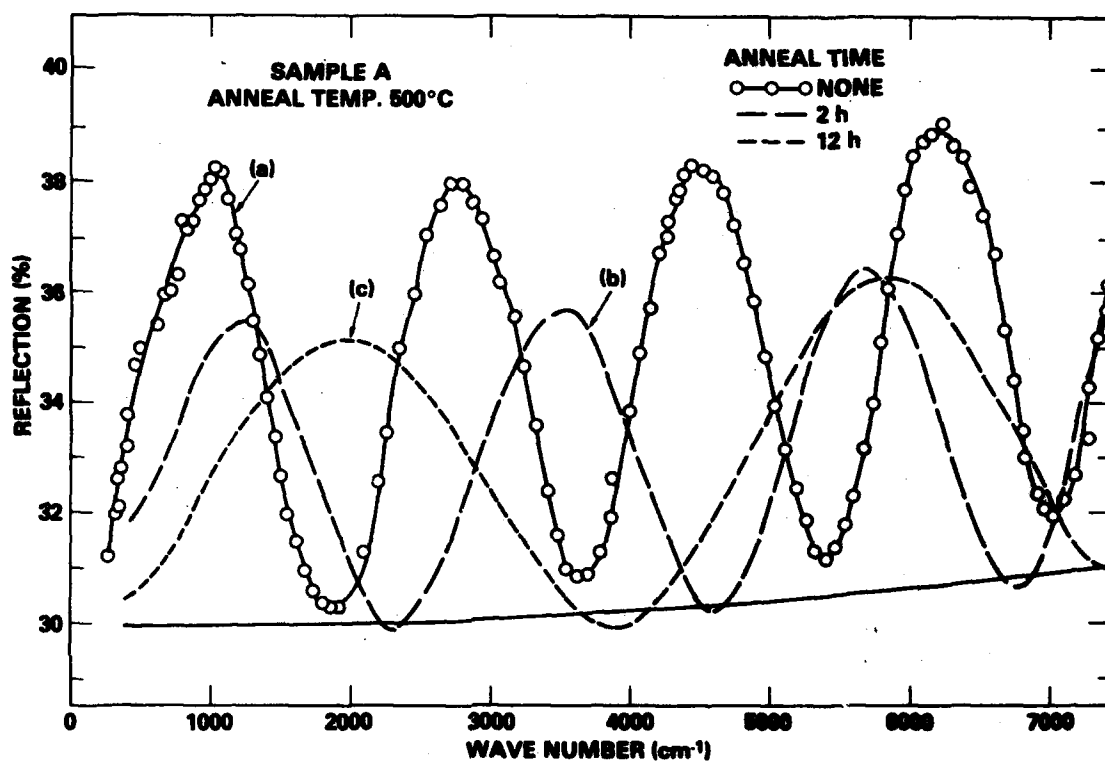


Fig. 1. Measured ir reflection spectra of implanted Si sample A which was annealed at 500°C. Measurements are made with the back surface heavily lapped. The conditions for the 3 interference curves are:

- (a) as-implanted, $n = 0.997 n_D$, $R_D = 0.707 \mu m$
- (b) 500°C-2h, $n = 0.961 n_D$, $R_D = 0.577 \mu m$
- (c) 500°C-12h, $n = 0.958 n_D$, $R_D = 0.343 \mu m$

The solid curve at the base of the others is the single-surface reflectivity of crystalline Si. For clarity the data points have been shown for only one case. The curves are drawn smoothly through the data points.

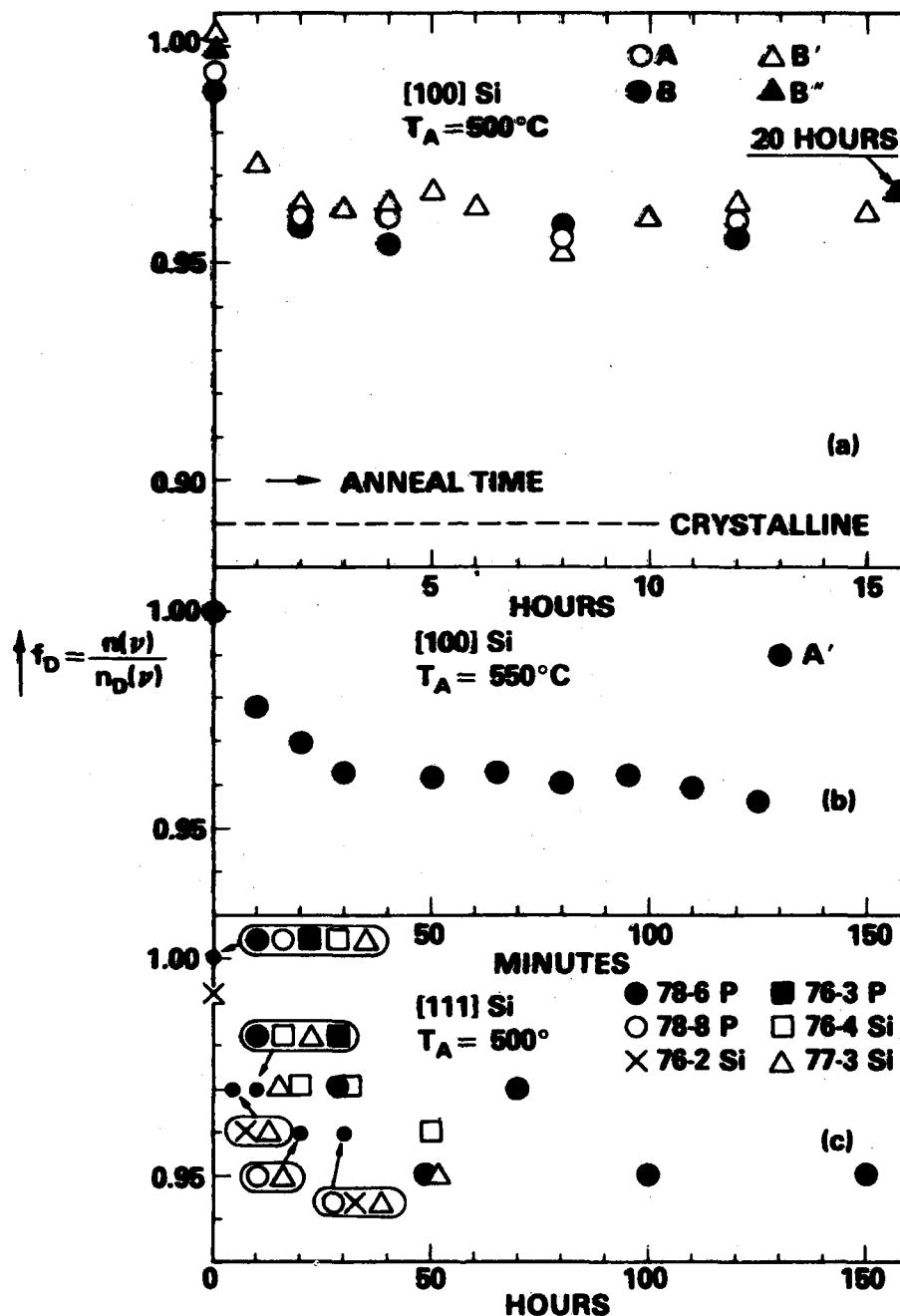


Fig. 2. $f_D = n/n_D$ of a-Si as a function of annealing time for:
 (a) $\langle 100 \rangle$ Si implanted samples annealed at 500°C ,
 (b) $\langle 100 \rangle$ Si implanted samples annealed at 550°C , and
 (c) $\langle 111 \rangle$ Si and P implanted samples annealed at 500°C .
 n_D is the refractive index of as-implanted Si given in Table 2. The dashed line at $f_D = 0.89$ corresponds to crystalline Si.

Since the amorphous-crystalline interface moves towards the sample surface with increasing annealing time and since $n_D(\nu)$ is obtained largely from the change in n across this interface, the measurements also indicate the uniformity of $n_D(\nu)$ within the annealed amorphous layer.

In Fig. 2a the average value $f_D = 0.89$ for crystalline Si is indicated by the dashed line. We note that the change in index due to annealing is about 1/3 the amorphous-crystalline difference. The analysis presented above assumes that the dispersion of the annealed a-Si is the same as that of the as-implanted a-Si, but the dispersion of crystalline Si is less than that of as-implanted a-Si. Therefore the reflection spectra from the five $\langle 100 \rangle$ Si⁺ implanted samples were reanalyzed using a Sellmeier equation of the form $n_D(\nu) = (A + B/(\Omega^2 - \nu^2))^{1/2}$ to represent the index of refraction. The parameters A, B, and Ω were adjusted for best fits by using a least-squares criterion.⁽²⁴⁾ Better fits were obtained for an $n_D(\nu)$ having intermediate dispersion. The average values of $n_D(\nu)$ and their standard deviations are given in Table II and compared in Fig. 3 to $n_D(\nu)$ and the crystalline refractive index, $n_c(\nu)$. The solid curves are generated by Sellmeier equations fitted to the average values, and the parameters are presented in the figure caption.

These experimental results show that as-implanted a-Si samples have the same index of refraction $n_D(\nu)$ for a rather broad range of implantation conditions, and suggest that the a-Si is initially in a defect-saturated state.⁽²⁰⁾ Annealing at 500° or 550° C changes the defect structure so that all samples have the same index $n_D(\nu)$ given in Table II and shown in Fig. 3. The fact that the index does not change again until the material is recrystallized indicates that this state should correspond to "thermally-stabilized" a-Si.⁽¹³⁾

Despite the widespread in the published values of $n(\nu)$ alluded to earlier there is a suggestion in the data that the larger $n(\nu)$ values may be associated with the low temperature production of amorphous films⁽¹⁵⁾ which may correspond to the state of our as-implanted layers. When the substrate temperature is elevated during formation of the film, the a-Si may be formed in the thermally-stabilized state. Some refractive index data for a-Si were recently reported⁽¹³⁾ for material produced by pyrolytic decomposition of silane onto fused silica substrates maintained at temperatures between 550° and 650° C. The crosses on Fig. 3 are values taken from a curve given in this work for a sample deposited at a temperature of 590° C—there is good agreement with the thermally-stable $n_D(\nu)$. Secondary ion mass spectroscopy measurements give a hydrogen concentration $C_H = 0.3$ atomic % at this temperature.⁽¹⁴⁾ It is difficult to compare our data with those produced with high concentrations of hydrogen since the refractive index of such films is dependent upon their method of fabrication and in most cases the refractive index after high temperature annealing does not return to that of crystalline Si.

The nature of the physical change occurring when the index changes from $n_D(\nu)$ to $n_D(\nu)$ is not evident. Possible mechanisms for refractive index changes in a-Si films include hydrogen evolution in hydrogenated films,^(18,25) changes in void structure and network reorganization.^(17,26) Since our films are hydrogen free, we expect no contribution from hydrogen evolution. While small voids have been observed in P-implanted but still crystalline Si which change with annealing,⁽²⁷⁾ there is scant evidence in the literature of void formation in a-Si films produced by ion implantation. In a study of Si films formed by evaporation and by thermal decomposition of silane onto substrates of thermally oxidized Si it was found⁽²⁸⁾ that the change in refractive index appeared to be related to the presence of dangling bonds with a polarizing ability considerably enhanced over that for covalent bonds. This study could indicate that the

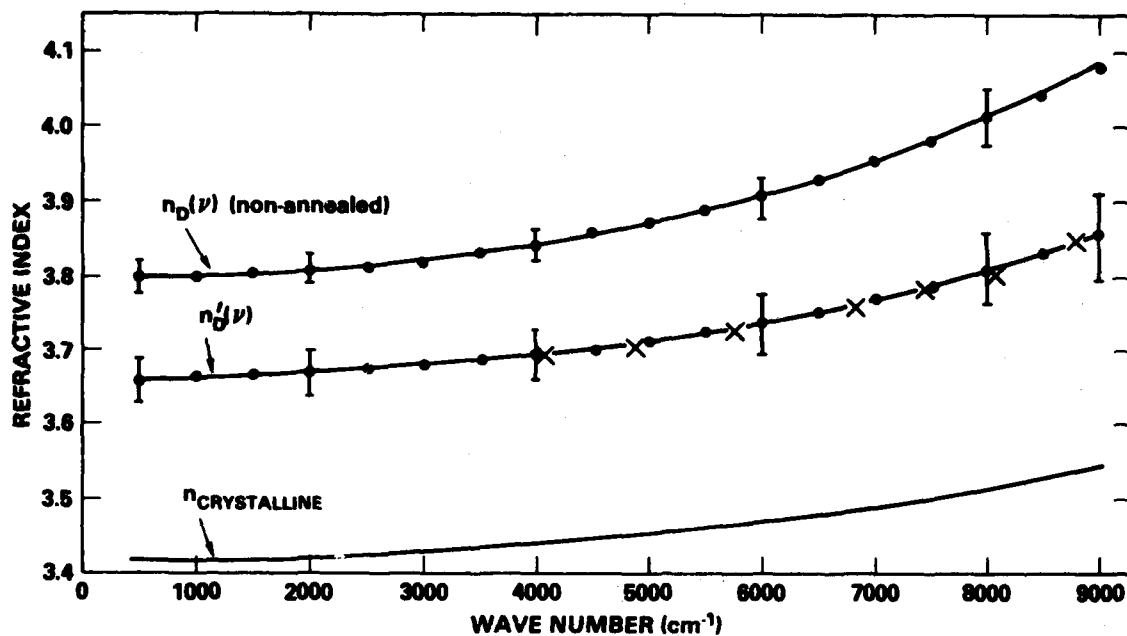


Fig. 3. Measured refractive indices vs frequency. Representative errors are shown. The curves are fits to $n^2 = A + B/(\Omega^2 - \nu^2)$ with the following values:

	A	B	$\Omega(\text{cm}^{-1})$
Crystalline Si	4.1476	5.8876×10^9	27,973
As-implanted amorphous Si	7.03	2.64	18,860
Implanted-annealed amorphous Si	7.17	2.67	20,700

The x's are from ref. 13 for $T_s = 590^\circ\text{C}$, $C_H = 0.3$ at.-%.

Table II — Indices of refraction for the two optical states of amorphous Si

$\nu(\text{cm}^{-1})$	n_D	n'_D
600	3.798 ± 0.019	3.662 ± 0.031
1000	3.800 ± 0.019	3.663 ± 0.031
1500	3.803 ± 0.020	3.666 ± 0.032
2000	3.808 ± 0.020	3.669 ± 0.032
2500	3.814 ± 0.020	3.674 ± 0.033
3000	3.821 ± 0.021	3.679 ± 0.034
3500	3.830 ± 0.022	3.686 ± 0.034
4000	3.841 ± 0.022	3.695 ± 0.035
4500	3.854 ± 0.023	3.703 ± 0.036
5000	3.869 ± 0.024	3.713 ± 0.038
5500	3.886 ± 0.025	3.725 ± 0.039
6000	3.905 ± 0.027	3.738 ± 0.041
6500	3.926 ± 0.030	3.753 ± 0.043
7000	3.952 ± 0.032	3.769 ± 0.045
7500	3.980 ± 0.034	3.787 ± 0.048
8000	4.013 ± 0.038	3.807 ± 0.051
8500		3.829 ± 0.055
9000		3.854 ± 0.060

present results could be related to dangling bond concentration changes during network reorganization. However, clearly further work is required to adequately characterize these two states of a-Si and the transition between them.

The work of authors J.E.F., C.N.W., and W.G.S., was partially supported by the Joint Services Electronics Program under contract #F44620-76C-0061 monitored by the Air Force Office of Scientific Research. The authors wish to acknowledge the high-energy P implantations carefully performed by P. R. Malmberg.

REFERENCES

1. R. Grigorovici and A. Vancu, *Thin Solid Films* **2**, 105 (1968).
2. D. Beaglehole and M. Zaveata, *J. Non-Cryst. Solids* **4**, 270 (1970).
3. M. H. Brodsky, R. S. Title, K. Weiser, and G. D. Pettit, *Phys. Rev. B* **1**, 2632 (1970).
4. R. C. Chittick, *J. Non-Cryst. Solids* **3**, 255 (1970).
5. B. L. Crowder, R. S. Title, M. H. Brodsky, and G. D. Pettit, *Appl. Phys. Lett.* **16**, 205 (1970).
6. J. E. Fischer and T. M. Donovan, *J. Non-Cryst. Solids* **8**, 202 (1972).
7. E. C. Baranova, V. M. Gusev, Yu. V. Martyneuko, C. V. Stainin, and I. B. Haibullin, *Radiat. Eff.* **18**, 21 (1973).
8. E. C. Baranova, V. M. Gusev, Yu. V. Martyneuko, and I. B. Haibullin, *Radiat. Eff.* **25**, 157 (1975).
9. S. K. Bahl and S. M. Bhagat, *J. Non-Cryst. Solids* **17**, 409 (1975).
10. G. K. M. Thutupalli and S. G. Tomlin, *J. Phys. C* **10**, 467 (1977).
11. P. J. Zanzucchi, C. R. Wronski, and D. E. Carlson, *J. Appl. Phys.* **48**, 5227 (1977).
12. C. C. Tsai, H. Fritzsche, M. H. Tanelian, P. J. Gaczi, P. D. Persans, and M. A. Vesaghi, p. 339; M. Hirose, M. Taniguchi, and Y. Osaka, p. 352, *Proceedings of the Seventh International Conference on Amorphous and Liquid Semiconductors*, Edinburgh (edited by W. E. Spear) 1977.
13. M. Janai, D. D. Allred, D. C. Booth, and B. O. Seraphin, *Solar Energy Mat.* **1**, 11 (1979).
14. D. C. Booth, D. D. Allred, and B. O. Seraphin, *Solar Energy Mat.* **2**, 107 (1979).
15. E. C. Freeman and W. Paul, *Phys. Rev. B* **20**, 716 (1979).
16. C. C. Tsai and H. Fritzsche, *Solar Energy Mat.* **1**, 29 (1979).
17. G. A. N. Connell, "Optical Properties of Amorphous Semiconductors" in *Amorphous Semiconductors*, edited M. H. Brodsky, Springer-Verlag (1979).

18. W. Wesch and G. Gotz, *Radiat. Eff.* **49**, 137 (1980).
19. K. Hehl and W. Wesch, to be published, *Phys. Status Solidi B*.
20. G. K. Hubler, C. N. Waddell, W. G. Spitzer, J. E. Fredrickson, S. Prussin, and R. G. Wilson, *J. Appl. Phys.* **50**, 3294 (1979).
21. G. K. Hubler, P. R. Malmberg, and T. P. Smith, *J. Appl. Phys.* **50**, 7149 (1979).
22. W. G. Spitzer, J. S. Ko, C. N. Waddell, G. K. Hubler, and J. E. Fredrickson, *J. Appl. Phys.* **50**, 3775 (1979).
23. L. Caspary, E. F. Kennedy, J. W. Mayer, and T. W. Sigmon, *J. Appl. Phys.* **49**, 3906 (1978).
24. G. K. Hubler, P. R. Malmberg, C. N. Waddell, W. G. Spitzer, and J. E. Fredrickson, to be published, *Radiat. Eff.*
25. D. I. Jones, R. A. Gibson, P. G. Le Comber, and W. E. Spear, *Solar Energy Mat.* **2**, 93 (1979).
26. E. A. Davis, "States in the Gap and Defects in Amorphous Semiconductors," in *Amorphous Semiconductors*, edited by M. H. Brodsky, Springer-Verlag (1979).
27. S. I. Romanov and L. S. Smirnov, *Radiat. Eff.* **37**, 121 (1978).
28. F. Schwidetsky, *Thin Solid Films* **18**, 45 (1973).

Section IV.C

DEFECT PROCESSES IN THIN FILMS OF METAL OXIDES

R. H. Bassel and I. Manning

Materials Modification and Analysis Branch
Condensed Matter and Radiation Sciences Division
Naval Research Laboratory

This work was supported by the Office of Naval Research.

AD-A119 719

NAVAL RESEARCH LAB WASHINGTON DC

F/G 20/8

THE USE OF ION IMPLANTATION FOR MATERIALS PROCESSING.(U)

JUL 82 F A SMIDT

UNCLASSIFIED

NRL-MR-4821

NL

33



END
1001
1002
11 82
PTD

Defect Processes in Thin Films of Metal Oxides
R. H. Bassel and Irwin Manning
Materials Modification and Analysis Branch

Recent experiments indicate that thin films of certain perovskites may play a significant role in inhibiting thermal oxidation in ion-implanted metals. Work is underway to employ the realistic ionic crystal computer simulation codes CERES and HADES to study the properties of these films.

More generally, defect processes in thin films of metal oxides are of interest. Frequently, important parameters are not experimentally accessible.

CERES takes as input the interatomic potentials and the parameters for the Dick-Overhauser shell model of ionic crystals; the output are the crystal macroscopic properties. It has a capability for varying input parameters to fit these properties. HADES computes excitation, activation, and creation energies for point defects in ionic crystals. Lattice relaxation effects (that is, the shifting in position of lattice atoms in the vicinity of the defect) are included. (Both of these codes model the crystal as being infinitely large; we assume that this will be an acceptable model for the thin films of actual interest.)

These codes have been converted to run on the NRL computer, and an NRL capability to employ these codes has been developed. There were discrepancies seen between runs on the NRL and Harwell (England) computers which seemed too small to be due to systematic error, yet too large to be attributed to ordinary roundoff error. Our analysis of those discrepancies is nearly completed; they involve the interaction of roundoff error and branching decisions in the two machines.

The perovskite BaTiO_3 is of particular interest for ion implantation. Our results with CERES indicates that the interatomic potential of the Buckingham type, usually used in realistic calculations of ionic crystals, is inadequate for the Ba-O and Ti-O interactions in this case: the best-fit Buckingham parameters give excessively large lattice strains, implying that the corresponding HADES results will be unreliable. The Kim-Gordon model of interatomic potentials is being considered as the basis for improved Ba-O and Ti-O interatomic potentials.

The perovskite SrTiO_3 is also of interest. The elastic and dielectric constants are known experimentally, and the activation energy for oxygen diffusion has been experimentally determined. We are calculating this activation energy to compare with experiment. The calculation is expected to give an indication of the applicability to perovskites of our approach in employing CERES and HADES.

Section IV.D

**A THEORETICAL STUDY OF THE DEFECT STRUCTURE
OF PRASEODYMIUM CHRONITE**

J. H. Harding¹ and R. H. Bassel²

¹Theoretical Physics Division
AERE Harwell
Oxfordshire, United Kingdom

²Materials Modification and Analysis Branch
Condensed Matter and Radiation Sciences Division
Naval Research Laboratory

**This work was conducted during R. H. Bassel's extended advanced
study at the Atomic Energy Research Agency, Harwell.**

A THEORETICAL STUDY OF THE DEFECT STRUCTURE
OF PRASEODYMIUM CHROMITE

J. H. Harding
Theoretical Physics Branch
AERE, Harwell
Oxfordshire, United Kingdom

R. H. Bassel*
Materials Modification and Analysis Branch
Condensed Matter and Radiation Sciences Division
Naval Research Laboratory

ABSTRACT

We present some theoretical calculations of the compound PrCrO_3 using the Harwell HADES code. The results show that all simple diffusion mechanisms involve high activation energies. Also we predict that the most important defect is electronic disorder in the chromium sublattice.

INTRODUCTION

Praseodymium chromite is one of a group of compounds that has been of considerable interest because of its high conductivity and refractory properties as a candidate on electrode material in MHD generators. These materials crystallise in the perovskite structure or slightly distorted modifications of it. At high temperatures they all are found in the simple cubic form. There is no available experimental data on this compound so the results presented here are theoretical only. It is hoped that our results will stimulate some experimental work. Some results, however, are available for the closely-related compound lanthanum chromite and we shall consider these where appropriate.

Calculations have been performed using the Harwell HADES routine (Lidiard and Norgett, 1972) incorporating extensions due to Catlow and James (1980). The HADES III code can handle crystals which do not have all their ions in sites of cubic symmetry.

*This work was conducted during R.H. Bassel's extended advanced study at AERE, Harwell.

POTENTIALS

The HADES program calculates defect energies using the shell model. We thus require short-range potentials to represent the non-Coulombic part of the ion-ion interactions (i.e., Pauli repulsions between the shells, Van der Waals interactions and so on) and also shell charges and spring constants to model the ionic polarisabilities.

We assume that the short-range cation-cation interaction may be represented by a Born-Mayer-type expression

$$\phi_{+-} = A_{+-} \exp \left(-\frac{r}{\rho_{+-}} \right) \quad (1)$$

but use the more general Buckingham form to model the anion-anion interaction

$$\phi_{--} = A_{--} \exp \left(-\frac{r}{\rho_{--}} \right) - \frac{C_{--}}{r^6} \quad (2)$$

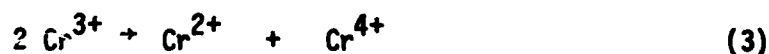
We ignore all short-range cation-cation interactions. Since the cation-cation distances are significantly greater than the sum of the Goldschmidt radii, this is reasonable. This limitation is necessary since there are very little data available to fit the empirical parameters in these potentials. We can now attempt to construct a set of empirical potentials for this compound from other compounds where more data are available. We therefore use the set of potentials set out in Table 1. These potentials give a lattice strain of under 0.1% (calculated by the Harwell PLUTO program) which gives some confidence that they are a reasonable set to use. We also give the calculated elastic constants (Table 2). The constants C_{44} and C_{66} are found to be markedly insensitive to the ionic polarisability.

We model the ionic polarisability by assuming that the Pr^{3+} ion is unpolarisable and by taking shell charges and spring constants from the empirical Cr_2O_3 potential of Catlow (1980). This gives dielectric constants $\epsilon_0 = 11.6$ and $\epsilon_\infty = 2.7$. The value for ϵ_0 seems rather low for this compound (values for the LnAlO_3 compounds for example are typically of the order of 20) and so we derive a second potential in which we refit the spring constants to give an ϵ_0 value of about 20. These two cases are referred to respectively as model I and model II in Table 3 and throughout the paper.

CALCULATIONS

We first attempt to see which will be the most important defects in this compound. From considerations of the perfect lattice (Fig. 1), it is clear that there are two possible sites for the interstitials; in the face-centering position or in the tetrahedral site. In all cases the face-centering site is much more favourable and the Frenkel energies quoted are for this position of the interstitial.

Since the Cr^{3+} ion can ionise fairly readily we also consider the energetics of the charge-transfer reaction.



which produces electronic disorder. The energy of formation of these electronic defects may be written as

$$\Delta E = \Delta E_{11} - I(\text{Cr}^{2+}) + I(\text{Cr}^{3+}) + \Delta_{\text{CF}} \quad (4)$$

where ΔE_{11} is the defect energy calculated by the HADES code (i.e., the changes in coulombic energy, polarisation terms and so forth), $I(X^{n+})$ is the ionisation energy of the X^{n+} ion and Δ_{CF} is the contribution of any crystal field terms. If we consider the strong field limit we may write this as

$$\Delta_{\text{CF}} \approx -\frac{12}{5} \Delta(\text{Cr}^{3+}) + \frac{4}{5} \Delta(\text{Cr}^{2+}) + \frac{3}{5} \Delta(\text{Cr}^{4+}) \quad (5)$$

where $\Delta(X^{n+})$ is the crystal field splitting for the X^{n+} ion.

The values of $\Delta(\text{Cr}^{2+})$, $\Delta(\text{Cr}^{3+})$, $\Delta(\text{Cr}^{4+})$ are, of course, different and, as a rough guide they increase by a factor of two for each increment of charge on the central ion. This gives a value of $\Delta_{\text{CF}} \sim \Delta(\text{Cr}^{3+})$, i.e., of the order of 1 to 2 eV. From the results of Table 4 and 5 it is clear that the major defect populations result from electronic disorder and Schottky defects. This result of considerable electronic disorder is supported by work on LaCrO_3 and the doped compound $\text{La}_{1-x}\text{Sr}_x\text{CrO}_3$ (Karim and Aldred, 1979). Pr^{3+} and La^{3+} are chemically very similar and so the corresponding Pr compounds should be similar. We hope to consider this type of disorder in the lanthanide chromites, in particular the calculation of migration energies and entropies in a later paper.

To obtain the ionic migration energies we consider two simple mechanisms, the vacancy mechanism and the interstitial mechanism. The results for the vacancy mechanism are shown in Table 6. In this case the ionic transport mode with lowest energy is that of the O^{2-} ion ($E_A = 5.3$ eV) with cation migration rendered very improbable for Cr^{3+} because of the high migration energy. However, the migration of Pr^{3+} is much more favourable because E_M , the migration energy, is low.

The interstitialcy mechanism is much less favourable than the vacancy mechanism in general. E_M for the O^{2-} interstitialcy is 15.3 eV. In the case of Pr^{3+} there is a possibility of the formation of an interstitial dumbbell. Model I predicts that this will be stable against the simple interstitial by about 3.5 eV. However, this is not obtained using Model II with the higher dielectric constant. No such effect is observed with either model for Cr^{3+} .

CONCLUSIONS

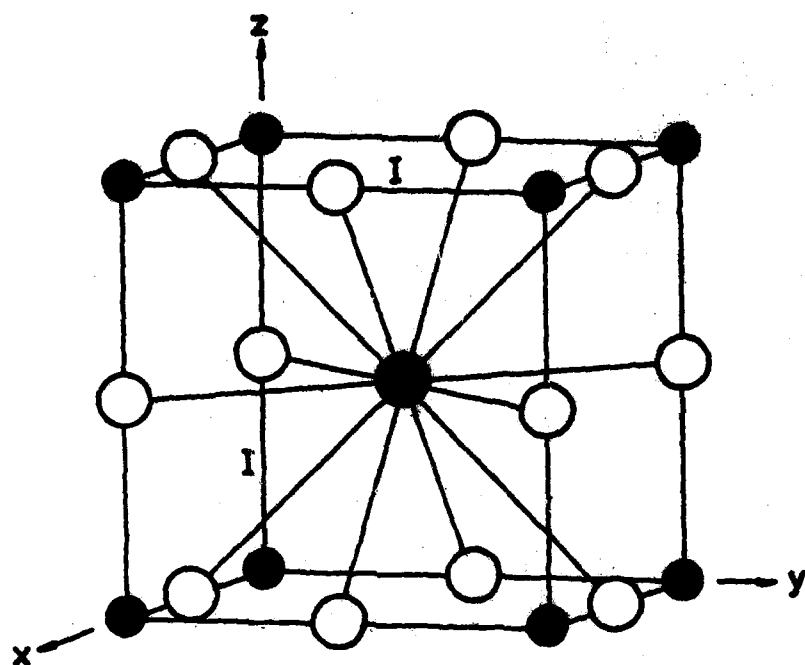
We have performed a series of calculations on this chromite and have identified the most important defects and migration pathways. It seems clear that the cation migration is very difficult unless extrinsic defects are present, but oxygen migration is much more favourable, however even here the activation energy is 5.3 eV. These calculations also predict that electronic disorder is important. It would be interesting to see the results of some experimental work on this compound.

ACKNOWLEDGMENT

This report has been published as Harwell Report AERE-TP.682, November 1980.

REFERENCES

- C.R.A. Catlow, 1980, private communication.
- A.B. Lidiard, M.J. Norgett, 1972. Computational Solid State Physics, eds. F. Herman, N.W. Dalton, T.R. Koehler (New York, Plenum), p. 385.
- R. James, 1980. Ph.D. Thesis, University College, London. Available as Harwell Report AERE-TP.814.
- D.P. Karim, A. T. Aldred, 1979, Phys. Rev. **820**, p.2255.



● Pr³⁺ Ion

● Cr³⁺ Ion

○ O²⁻ Ion

I Interstitial Site

Fig. 1 — Praseodymium chromite structure

Table 1: Potentials

Interaction	A.	ρ .	C.	Reference
Pr. 0.	5302.8	0.3	0.0	Kilner and Brooks
Cr. 0.	3306.6	0.2795	45.94	Catlow
O. 0.	22764.3	0.149	27.88	Catlow

Table 2: Elastic Constants (Calculated)

C_{11}	53.13×10^{11}	dynes cm^{-2}
C_{33}	53.09×10^{11}	dynes cm^{-2}
C_{12}	18.08×10^{11}	dynes cm^{-2}
C_{44}	18.11×10^{11}	dynes cm^{-2}
C_{66}	18.12×10^{11}	dynes cm^{-2}

Table 3: Shell Parameters and Dielectric Constants

	<u>Model I</u>	<u>Model II</u>
Y(Pr)	0.0	0.0
K(Pr)	∞	∞
Y(Cr)	4.82	4.82
K(Cr)	41.6	37.3
Y(O)	-1.92	-1.92
K(O)	38.0	11.9
ϵ_0	11.6	19.85
ϵ_∞	2.7	3.2

Table 4: Defect Energies in PrCrO_3

	<u>Model I</u>	<u>Model II</u>
Pr^{3+} vacancy	46.11eV	45.73eV
Pr^{3+} interstitial	-20.17eV	-21.82eV
Pr^{3+} Frenkel defect	25.95eV	23.9eV
Cr^{3+} vacancy	64.66eV	63.96eV
Cr^{3+} interstitial	-39.47eV	-40.32eV
Cr^{3+} Frenkel defect	25.19eV	23.64eV
O^{2-} vacancy	17.72eV	15.69eV
O^{2-} interstitial	-8.35eV	-8.56eV
O^{2-} Frenkel defect	9.37eV	7.13eV
Schottky quintet	7.1eV	4.4eV

Table 5: Electronic Disorder in PrCrO_3

	<u>Model I</u>	<u>Model II</u>
HADES energy for electronic disorder, E_H	-11.84eV	-12.16eV
Ionisation energy for Cr^{3+} (Moore, 1952)	30.95eV	
Ionisation energy for Cr^{2+} (Moore, 1952)	49.6eV	
Energy of reaction as shown in the text	6.81eV	6.49eV

Table 6: Defect Migration Energies; Simple Vacancy Mechanism

	<u>Migration Energy</u>	
	<u>Model I</u>	<u>Model II</u>
Pr^{3+} in $\{100\}$ direction in Pr^{3+} sublattice	3.53eV	*
Cr^{3+} in $\{110\}$ direction in Cr^{3+} sublattice	20.9eV	20.0eV
O^{2-} in $\{100\}$ direction in O^{2-} sublattice	2.90eV	2.94eV

*The program does not give a stable minimum for this case. This could probably be overcome by a better potential.

BIBLIOGRAPHY

1. E. A. Wolicki, C. R. Gossett, K. W. Marlow, and M. E. Toms, "Capabilities for Nonnuclear Applications with Nuclear Facilities at NRL," NRL Report 6599, 17 October 1967.
2. I. Manning and D. Padgett, "Transport Theory of Penetration by Heavy Ions," NRL Memorandum Report 2631, August 1973.
3. I. Manning and G. P. Mueller, "Depth Distribution of Energy Deposition in Ion Bombardment," Comp. Phys. Comm. 7, 85 (1974).
4. G. P. Mueller, "Total Cross-Section Corresponding to the Differential Cross-Section of Lindhard, Nielsen and Scharff," Radiat. Eff. 21, 253 (1974).
5. J. W. Butler, "Ion Implantation and Tribology," Proceedings of ONR-NRL Tribology Workshop, Washington, DC, 14-16 October 1975.
6. H. W. Kugel, L. Eytel, G. K. Hubler, and D. E. Murnick, "The Temperature Dependence of Hyperfine Fields at Rare Earth Nuclei in Iron and Nickel," Phys. Rev. B13, 3697 (1976).
7. J. W. Butler, "Ion Implantation and Wear," Reports, Memoranda and Technical Notes of the Materials Research Council Summer Conference, La Jolla, CA (University of Michigan Document 005020, 1976) p. 255.
8. Irwin Manning, Mervine Rosen, and J. E. Westmoreland, "Adaptation of a Program for Depth Distribution of Energy Deposition by Ion Bombardment: Calculation of Ion Lateral Ranges," Comp. Phys. Comm. 12, 335 (1976).
9. I. Manning, M. Rosen, and J. E. Westmoreland, "Computer Code for the Calculation of Lateral Range of a PKA," NRL Memorandum Report 3358, September 1976.
10. J. M. Poate, J. A. Borders, A. G. Cullis, and J. K. Hirvonen, "Ion Implantation as an Ultrafast Quenching Technique for Metastable Alloy Production: The Ag-Cu System," Appl. Phys. Letters 30, 365 (1977).
11. G. P. Mueller and Mervine Rosen, "A Boltzmann Transport Code for Ion Penetration in Matter," NRL Memorandum Report 3556, July 1977.
12. J. K. Hirvonen, "Spinodal Decomposition in Amorphous Au-Implanted Pt," Appl. Phys. Letters 32, 25 (1978).
13. A. G. Cullis, J. A. Borders, J. K. Hirvonen, and J. M. Poate, "Metastable Alloy Layers Produced by Implantation of Ag⁺ and Ta⁺ Ions into Cu Crystals," Phil. Mag. B32, 615 (1978).
14. J. K. Hirvonen, "Ion Implantation in Tribology and Corrosion Science," J. Vac. Sci. Technol. 15, 1662 (1978).
15. Wen-Wei Hu, C. R. Clayton, H. Herman, and J. K. Hirvonen, "Fatigue-Life Enhancement by Ion Implantation," Scr. Met. 12, 697 (1978).

16. E. McCafferty and G. K. Hubler, "Electrochemical Behavior of Palladium-Implanted Titanium," *J. Electrochem. Soc.* **125**, 1892 (1978).
17. J. W. Butler, "Some Effects of Ion Implantation on Fluid-Solid Surface Interactions," Proceedings of the Fourth Symposium on Fluid-Solid Surface Interactions, sponsored by the U.S. Department of the Navy and the West Germany Federal Ministry of Defense, 18-20 October 1978, National Bureau of Standards, Gaithersburg, MD, p. 267.
18. J. K. Hirvonen, C. A. Carosella, R. A. Kant, I. L. Singer, R. Vardiman, and B. B. Rath, "Improvement of Metal Properties by Ion Implantation," *Thin Solid Films* **63**, 5 (1979).
19. G. K. Hubler, P. R. Malmberg, and T. P. Smith, III, "Refractive Index Profiles and Range Distributions of Silicon Implanted with High-Energy Nitrogen," *J. Appl. Phys.* **58**, 7147 (1979).
20. G. K. Hubler, C. N. Waddell, W. G. Spitzer, J. E. Fredrickson, J. Prussin, and R. G. Wilson, "High-Fluence Implantations of Silicon: Layer Thickness and Refractive Indices," *J. Appl. Phys.* **50**, 3294 (1979).
21. R. A. Kant, J. K. Hirvonen, A. R. Knudson, J. S. Wollam, "Surface Hardening of Beryllium by Ion Implantation," *Thin Solid Films* **63**, 27 (1979).
22. W. G. Spitzer, J. S. Ko, C. N. Waddell, G. K. Hubler, and J. E. Fredrickson, "Plasma Region in High-Fluence Implants of Phosphorus in Amorphized Silicon," *J. Appl. Phys.* **50**, 3775 (1979).
23. Y. F. Wang, C. R. Clayton, G. K. Hubler, W. H. Lucke, and J. K. Hirvonen, "Applications of Ion Implantation for the Improvement of Localized Corrosion Resistance of M50 Bearing Steel," *Thin Solid Films* **63**, 11 (1979).
24. J. K. Hirvonen, "Implantation Into Metals - Mechanical Property Changes," Proceedings of the 1st Conference on Ion Beam Modification of Materials, eds., J. Gyulai, T. Lohner, and E. Pasztor, Central Research Institute for Physics, H-1525, Budapest 114 POB 49, Hungary, Vol. III, p. 1753 (1979).
25. J. K. Hirvonen and J. W. Butler, "Improved Corrosion and Mechanical Behavior of Alloys by Ion Implantation," 1978 Science and Engineering Symposium Proceedings (Joint Air Force and Navy), Vol. IV (Basic Research), Navy Material Command and Air Force Systems Command, p. 981 (1979).
26. J. K. Hirvonen, J. W. Butler, T. P. Smith, III, R. A. Kant, and V. C. Westcott, "Sliding-Wear Reduction by Ion Implantation," Proceedings of the 1st Conference on Ion Beam Modification of Materials, eds., J. Gyulai, T. Lohner, and E. Pasztor, Central Research Institute for Physics, H-1525, Budapest 114, POB 49, Hungary, Vol. III, p. 1973 (1979).
27. J. K. Hirvonen, J. M. Poate, Z. L. Liao, and J. W. Mayer, "Sputtering Limitations for High-Dose Implantations," Proceedings of the 1st Conference on Ion Beam Modification of Materials, eds., J. Gyulai, T. Lohner, and E. Pasztor, Central Research Institute for Physics, H-1525, Budapest 114, POB 49, Hungary, Vol. III, p. 1519 (1979).

28. G. K. Hubler, P. R. Malmberg, C. A. Carosella, T. P. Smith, III, W. G. Spitzer, C. N. Waddell, and C. N. Phillippi, "Optical Effects Resulting from Deep Implants of Silicon with Nitrogen and Phosphorus," *Proceedings of the 1st Conference on Ion Beam Modification of Materials*, eds., J. Gyulai, T. Lohner, and E. Pasztor, Central Research Institute for Physics, H-1525, Budapest 114, POB 49, Hungary, Vol. II, p. 1323 (1979).
29. W. W. Hu, C. R. Clayton, H. Herman, J. K. Hirvonen, and R. A. Kant, "Fatigue-Life Enhancement of Steel by Nitrogen Implantation," *Proceedings of the 1st Conference on Ion Beam Modification of Materials*, eds., J. Gyulai, T. Lohner, and E. Pasztor, Central Research Institute for Physics, H-1525, Budapest 114, POB 49, Hungary, Vol. III, p. 1977 (1979).
30. D. J. Land, D. G. Simons, J. G. Brennan, M. D. Brown, and J. K. Hirvonen, "Range Distribution for 25-100 keV $^{14}\text{N}^+$ Ions," *Proceedings of the 1st Conference on Ion Beam Modification of Materials*, eds., J. Gyulai, T. Lohner, and E. Pasztor, Central Research Institute for Physics, H-1525, Budapest 114, POB 49, Hungary, Vol. I, p. 93 (1979).
31. E. McCafferty, G. K. Hubler, and J. K. Hirvonen, "Corrosion Control by Ion-Implantation," *Proceedings of the 1978 Tri-Service Conference on Corrosion*, ed. by M. Levy and J. Brown, *Materials and Ceramics Information Center*, Battelle, OH, p. 435, May 1979.
32. R. G. Vardiman, R. A. Kant, and T. W. Crooker, "The Effect of Ion Implantation on Fatigue Behavior of Ti/6Al/4V Alloy," *Report of NRL Progress*, p. 4, May 1979.
33. I. Manning, "Use of Range Distributions to Approximate Energy Distributions," F. A. Smidt and L. A. Beach, Coordinators, *Cooperative Radiation Effects Simulation Program (Annual Progress Report) NRL Memorandum Report 4630* (October 1979), p. 2.
34. I. Manning, "Approximation for Energy Deposition in Ion Beam Bombardment," F. A. Smidt and L. A. Beach, Coordinators, *Cooperative Radiation Effects Simulation Program (Annual Progress Report) NRL Memorandum Report 4080* (October 1979), p. 8.
35. M. Zamanzadeh, A. Allan, H. W. Pickering, and G. K. Hubler, "Effect of Helium-, Iron-, and Platinum-Ion Implantation on Permeation of Hydrogen Through Ion Membranes," *ONR Technical Report No. 10* (Contract No. N00-14-75-C-0264), July 1979.
36. G. K. Hubler and E. McCafferty, "The Corrosion Behaviour and Rutherford Backscattering Analysis of Palladium-Implanted Titanium," *Corros. Sci.* **20**, 103 (1980).
37. R. N. Bolster and I. L. Singer, "Surface Hardness and Abrasive Wear Resistance of Nitrogen-Implanted Steels," *Appl. Phys. Letters* **36**, 208 (1980).
38. I. L. Singer and J. S. Murday, "The Chemical State of Ion-Implanted Nitrogen in $\text{Fe}_{18}\text{Cr}_8\text{Ni}$ Steel," *J. Vac. Sci. Technol.* **16**, 330 (1980).
39. G. P. Mueller, "New Analytical Calculation of Displacement Damage," *Nucl. Instr. and Methods* **170**, 389 (1980).

40. G. P. Mueller, "Differential Cross Section and Related Integrals for the Moliere Potential," *Radiat. Eff. Letters* **50**, 87 (1980).
41. W. N. Allen, P. Brant, C. A. Carosella, J. J. DeCorpo, C. T. Ewing, F. E. Saalfeld, and D. C. Weber, "Ion Implantation Studies of (SN)_x and (CH)_x," *Synthetic Metals* **1**, 151 (1979/80).
42. L. Buene, J. M. Poate, D. C. Jacobson, C. W. Draper, and J. K. Hirvonen, "Laser Irradiation of Nickel Single Crystals," *Appl. Phys. Lett.* **37**, 385 (1980).
43. J. K. Hirvonen, J. M. Poate, A. Greenwald, R. Little, "Pulsed Electron Beam Irradiation of Ion Implanted Copper Single Crystals," *Appl. Phys. Lett.* **36**, 564 (1980).
44. G. K. Hubler, P. R. Malmberg, C. A. Carosella, T. P. Smith, III, W. G. Spitzer, C. N. Waddell, and C. N. Phillippi, "Optical Effects Resulting from Deep Implants of Silicon with Nitrogen and Phosphorus," *Radiat. Eff.* **48**, 81 (1980).
45. G. K. Hubler and E. McCafferty, "The Corrosion Behavior and Rutherford Backscattering Analysis of Pd-Implanted Titanium," *Corrosion Science* **20**, 103 (1980).
46. M. Zamanzadeh, A. Allam, H. W. Pickering, and G. K. Hubler, "Effect of Helium, Iron, and Platinum Implantation on the Absorption of Hydrogen by Iron," *J. Electrochem. Soc.* **127**, 1688 (1980).
47. C. A. Carosella, I. L. Singer, R. C. Bowers, and C. R. Gossett, "Friction and Wear Reduction of Bearing Steel via Ion Implantation," *Ion Implantation Metallurgy*, eds. C. M. Preece and J. K. Hirvonen, (The Metallurgical Society of AIME, 1980), p. 103.
48. C. R. Clayton, K. G. K. Doss, H. Herman, S. Prasad, Y-F. Wang, J. K. Hirvonen, and G. K. Hubler, "Modification of the Corrosion Behavior of 304 Stainless Steel by Phosphorus Implantation," *Ion Implantation Metallurgy*, eds. C. M. Preece and J. K. Hirvonen, (The Metallurgical Society of AIME, 1980), p. 65.
49. J. K. Hirvonen, "Introduction," *Ion Implantation*, Treatise on Materials Science and Technology **18**, 1-16, Academic Press (1980).
50. J. K. Hirvonen, ed., *Ion Implantation*, Treatise on Materials Science and Technology **18**, Academic Press (1980).
51. J. W. Mayer, S. S. Lau, B-Y Tsaur, J. M. Poate, and J. K. Hirvonen, "High-Dose Implantation and Ion-Beam-Mixing," *Ion Implantation Metallurgy*, eds., C. M. Preece and J. K. Hirvonen, (The Metallurgical Society of AIME, 1980), p.37.
52. W. W. Hu, H. Herman, C. R. Clayton, J. Kozubowski, R. A. Kant, J. K. Hirvonen, and R. K. MacCrone, "Surface-Related Mechanical Properties of Nitrogen-Implanted 1018 Steel," *Ion Implantation Metallurgy*, eds. C. M. Preece and J. K. Hirvonen, (The Metallurgical Society of AIME 1980), p.92.
53. C. M. Preece and J. K. Hirvonen, Editors, *Ion Implantation Metallurgy*, (The Metallurgical Society of the AIME, 1980).

54. I. L. Singer, R. N. Bolster, and C. A. Carosella, "Abrasive Wear Resistance of Ti and N Implanted 52100 Steel Surfaces," *Thin Solid Films* **73**, 283 (1980).
55. G. K. Hubler, J. K. Hirvonen, I. L. Singer, R. C. Bowers, C. R. Gossett, M. R. Weller, C. R. Clayton, and Y. A. Wang, "Application of Ion Implantation for the Improvement of Localized Corrosion Resistance of M50 Steel Bearings," *NAPC Progress Report*, Mar 1980.
56. I. L. Singer, J. S. Murday, H. Ravner, J. K. Hirvonen, and N. L. Jarvis, "New Opportunities in Tribology," *Naval Research Reviews* **32**, 4 (1980).
57. I. L. Singer and R. N. Bolster, "Surface Hardness and Abrasive Wear Resistance of Nitrogen-Implanted Steels," *Ion Implantation Metallurgy*, eds. C. M. Preece and J. K. Hirvonen, (The Metallurgical Society of AIME, 1980), p. 116.
58. J. H. Harding and R. H. Bassel, "A Theoretical Study of the Defect Structure of Praseodymium Chromite," TP.862, Theoretical Physics Division, AERE Harwell, Oxfordshire, United Kingdom, July 1980.
59. L. Buene, D. C. Jacobson, S. Nakahara, J. M. Poate, C. W. Draper, and J. K. Hirvonen, "Laser Irradiation of Ni: Defect Structures and Surface Alloying," pp. 583-590 in *Laser and Electron-Beam Interactions and Materials Processing*, eds. Gibbons, Hess, Sigmon, Elsevier North Holland, Inc., 1981.
60. R.G. Allas, A.R. Knudson, J.M. Lambert, P.A. Treado, and G.W. Reynolds, "Self-Ion Sputtering Yields for Copper, Nickel, and Aluminum," 9th International Conference on Atomic Collisions in Solids, Lyons, France, 6-10 Jul 1981.
61. G.K. Hubler, "Use of Ion Beam Analysis in Metal Modification By Means of Ion Implantation," *Nucl. Instrum. Methods* **191**, 101 (1981).
62. F. A. Smidt, J. K. Hirvonen, and S. Ramalingam, "Preliminary Evaluation of Ion Implantation as a Surface Treatment to Reduce Wear of Tool Bits," *NRL Memorandum Report 4616*, Naval Research Laboratory, 25 Sep 1981.
63. P. Trzaskoma, E. McCafferty, G. K. Hubler, and I. L. Singer, "Electrochemical Behavior of an Amorphous Fe-Ti-C Surface in Titanium-Implanted Steel," *Modification of the Surfaces by Ion Implantation Conference*, Manchester, UK, 23-26 Jun 1981.
64. R. G. Vardiman, D. Creighton, G. Saliver, A. Effatian, and B. B. Rath, "The Effect of Ion Implantation on Fretting Fatigue in Ti-6Al-4V," *Symposium on Materials Evaluation Under Fretting Conditions*, NBS, Gaithersburg, MD, 3 June 1981.
65. J. E. Fredrickson, C. N. Waddell, W. G. Spitzer, and G. K. Hubler, "Effects of Thermal Annealing on the Refractive Index of Amorphous Silicon Produced by Ion Implantation," **40**, 172 (1982).
66. G. K. Hubler, P. R. Malmberg, C. N. Waddell, W. G. Spitzer, and J. E. Fredrickson, "Electrical and Structural Characterization of Implantation Doped Silicon by Infrared Reflection," *Radiat. Eff.*, to be published.

D
FI
—